Chapter 9

Phase Manipulation of Ultrashort Soft X-Ray Pulses by Reflective Gratings

Fabio Frassetto, Paolo Miotti and Luca Poletto

Additional information is available at the end of the chapter

http://dx.doi.org/10.5772/63416

Abstract

In this chapter, we discuss the use of reflective diffraction gratings to manipulate the phase of ultrashort pulses in the extreme ultraviolet (XUV) and soft X-ray spectral regions. Gratings may be used to condition the spectral phase of ultrashort pulses, e.g., to compensate for the pulse chirp and compress the pulse, similarly to what is routinely realized for visible and infrared pulses. The chirped pulse amplification technique has been already proposed for soft X-ray free-electron laser radiation; however, it requires the use of a compressor to compensate for the pulse chirp and get closer to the Fourier limit. There are fundamental differences when operating the gratings at wavelengths shorter than ≈40 nm on a broad band: (a) the gratings are operated at grazing incidence; therefore, the optical design has to be consequently tailored to this peculiar geometry; (b) the grating efficiency is definitely lower; therefore, the number of diffractions has to be limited to two. We discuss the different configurations that can be applied to the realization of a grating stretcher/compressor.

Keywords: diffraction gratings, ultrafast optics, extreme ultraviolet, soft X-ray optics, chirped pulse amplification

1. Introduction

XUV and X-ray radiations have been used for many fundamental discoveries and outstanding applications in natural sciences. It has played a crucial role in basic research, medical diagnostics, and industrial development. In particular, the impressive developments in laser technology over the last decades lead to the generation of XUV and X-ray coherent ultra-

short and ultra-intense pulses in the femtosecond and sub-femtosecond time scale (1 fs = 10^{-15} s) [1–3]. Ultrafast short-wavelength radiation offers the unique capability to access and measure the structural arrangement and electronic structure inside the nucleus [4, 5]. The main available tools to generate ultrashort coherent pulses are presently high-order laser harmonics generated in gas and free-electron lasers [6].

High-order harmonics (HHs) are generated through the interaction between an ultrashort laser pulse and a gas in a cell or in a jet. Because of the strong peak power of the femtosecond laser pulse, a nonlinear interaction with the gas takes place and produces odd laser harmonics that may easily extend well above the order of several tens. The HH spectrum is described as a sequence of peaks corresponding to the odd harmonics of the fundamental laser wavelength and having an intensity distribution characterized by a plateau whose extension is related to pulse intensity and frequency. The use of advanced phase-matching mechanisms and interaction geometries has made possible the generation of HHs in the water window region between 2.3 and 4.4 nm, while still using a table-top laser source [7–9]. The radiation generated with the scheme of the HHs using few-optical-cycle laser pulses is currently the main tool for the investigation of matter with attosecond resolution (1 as = 10^{-18} s) [10–13]. Both trains [14, 15] and isolated [16–19] bursts of attosecond pulses have been experimentally demonstrated. The physical background of ultrashort pulses originates from the model of HH generation, i.e., the phase-matched emission of radiation results from the recombination of a tunnel-ionized electron with its parent ion. Once the conditions for such recombination are realized in only one occurrence per laser pulse, an isolated pulse is generated. Both trains and isolated attosecond pulses are positively chirped, resulting from the different duration of the quantum paths that contribute to the emitted spectrum [20]. Due to the nonzero chirp, the pulse temporal duration is longer than the Fourier limit. Positively chirped pulses may be temporally compressed by introducing a system that gives a compensating negative chirp. The compression has been achieved using a thin metallic filter with negative group-delay dispersion (GDD) as discussed in Refs. [15, 17] or broadband multilayer-coated optics with aperiodic layers [21].

Free-electron laser (FEL) sources generate radiation in the XUV and X-ray spectral regions with high spatial coherence, ultrashort time duration, and an increase of 6–8 orders of magnitude on the peak brilliance with respect to third-generation synchrotrons. FEL operation relies on a relativistic electron beam as the lasing medium which moves freely through a periodic magnetic structure (i.e., the undulator) that induces radiation [22]. There are presently four FEL user facilities operated at short wavelengths and dedicated to user-defined experiments: FLASH in Germany, SACLA in Japan, LCLS in USA, and FERMI in Italy. Presently, FEL pulses as short as 3 fs have been characterized at LCLS [23]. In order to increase the temporal resolution in pump-probe experiments, several approaches have been proposed for the generation of ultrashort FEL pulses in the femtosecond and sub-femtosecond regime, as the time slicing [24–26] or the reduction of the electron bunch charge [27]. Most of these methods rely on the selection of a small portion of the electron beam which undergoes FEL amplification, with a reduction of the amount of charge that contributes to the light amplification. A different possibility is the optical compression of the radiation pulse generated by

http://dx.doi.org/10.5772/63416

the whole electron beam that is required to have a nonzero energy chirp in order to generate a chirped pulse. As for optical lasers, where frequency chirping is introduced to stretch the pulse before its amplification and then compensated after amplification to recover the ultrashort duration and high peak power, chirped-pulse amplification (CPA) may also be applied to FELs [28, 29]. In case of seeded FELs, the seeding laser pulse has to be stretched in time before interacting with the electron beam. This solution allows the use of the whole electron beam charge obtaining a significantly higher number of photons.

Indeed, for both HH and FEL facilities, the availability of a compressor tunable in the spectral band of operation of the source, capable of changing the spectral phase of the pulses, is particularly attractive, either to compensate for the intrinsic chirp or to realize CPA.

Here we discuss the use of gratings at grazing incidence to realize a tunable device to manipulate the spectral phase of XUV and X-ray–chirped pulses. In designing instruments for photon handling in the XUV ultrafast domain, there are some basic differences with respect to the traditional optical schemes in the visible and infrared domain [30, 31]. The first is to exploit the very short duration of the pulse, the study of the optical length of the rays gathered by the pupil and their equalization is mandatory. Moreover, the very extended bandwidth of operation may be exploited only if the instrument has a rather flat spectral response. Finally, an overall high throughput of the instrument is often a crucial feature to maintain high peak intensity.

The use of gratings at grazing incidence to realize tunable monochromators for XUV ultrafast pulses is well established. Several monochromatic beamlines are presently in operation both with HHs [32–35] and FELs [36–39].

When using a grating for ultrafast pulses, the main problem faced with is the pulse-front tilt that is introduced by diffraction [40]. Indeed, each ray that is diffracted by two adjacent grooves is delayed by $m\lambda/c$, where m is the diffraction order, λ is the wavelength, and c is the speed of light in vacuum. The pulse-front tilt is given by the total difference in the optical paths of the diffracted beam, that is $\Delta\tau_G = m\lambda N/c$, where N is the total number of the illuminated grooves. This effect, that is totally negligible for picosecond or longer pulses, is noticeable in the femtosecond time scale, since it can dramatically degrade the instrumental ultrafast response. To overcome this effect, a double-grating configuration has to be adopted to compensate for the pulse-front tilt [41, 42]. The first grating is demanded to spectrally disperse the beam on an intermediate focal plane, where a slit performs the spectral selection, while the second grating compensates for the pulse-front tilt of the diffracted beam by equalizing the length of the optical paths. Double-grating instruments have been demonstrated to be very effective for HHs, with time resolution well below 10 fs [43–47]. Double-grating configurations, which are able to preserve the ultrafast duration of the pulse, have been also proposed as beam splitters for ultrafast intense pulses [48] and as infrared (IR)-XUV beam separators for HHs [49].

Here, we focus on the use of gratings to realize devices able to manipulate the spectral phase of chirped pulses, in particular to be used as XUV compressors.

2. Grating geometries for ultrashort pulses

Grazing incidence reflective gratings may be used either in the classical diffraction geometry (CDG) or in the off-plane geometry (OPG) [50].

The CDG is shown in **Figure 1(a)**. The grating equation is $\sin\alpha + \sin\beta = m\lambda\sigma_{CD}$, where α and β are, respectively, the incident and diffracted angles and σ_{CD} the groove density.

The OPG is shown in **Figure 1(b)**. The grating equation is $\sin\gamma\,(\sin\mu + \sin\nu) = m\lambda\sigma_{OP}$, where γ is the altitude angle, μ and ν are the azimuth angles as defined in the figure, and σ_{OP} is the groove density. The OPG, although seldom used, gives higher throughput than the classical mount, since it has been theoretically demonstrated and experimentally measured that the peak diffraction efficiency is close to the reflectivity of the coating at the altitude angle [51, 52]. Therefore, the OPG is suitable for the design of XUV grating instruments with high efficiency [53, 54].

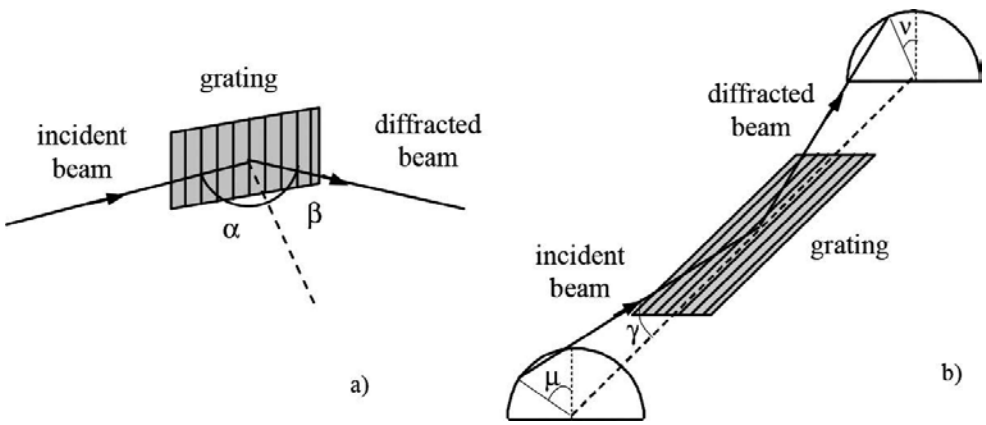

Figure 1. (a) Classical diffraction geometry; (b) off-plane geometry.

When realizing a grating compressor for ultrafast pulses, the main problem faced with is the pulse-front tilt given by the diffraction, as shown in **Figure 2** in the case of the CDG. Furthermore, different wavelengths are diffracted in different directions. The pulse-front tilt and the spectral angular dispersion have to be corrected by a second grating in a compensated configuration to fulfill the two following conditions: (1) the differences in the path lengths of rays with the same wavelength within the beam aperture that are caused by the diffraction from the first grating have to be compensated by the second grating; that is, the pulse-front tilt is corrected; (2) the angular spectral dispersion caused by the first grating has to be canceled by the second grating, that is, all the rays at different wavelengths exit the second grating with parallel directions. Both these conditions are satisfied by a scheme with two equal gratings mounted with opposite diffraction orders; that is, the incidence (incoming azimuth) angle on the second grating is equal to the diffraction angle (outcoming azimuth) from the first grating. The phase chirp introduced by the system is calculated as the difference in the optical

paths of rays at different wavelengths. This principle is well known for the realization of stretchers and compressors in the visible and near infrared [55, 56].

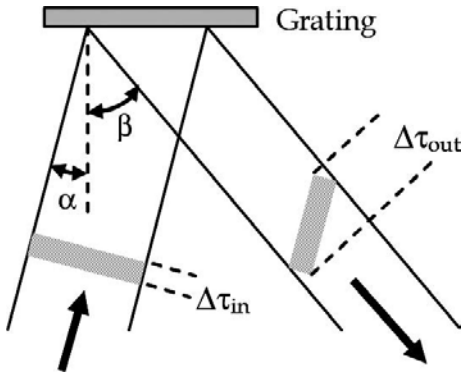

Figure 2. Pulse-front tilt of an ultrashort pulse diffracted by a grating in the CDG. $\Delta\tau_{in}$ and $\Delta\tau_{out}$ are the pulse duration at input and output, respectively. At the first diffracted order, the pulse-front tilt is $\Delta OP = N\lambda$, where N is the number of illuminated grooves.

3. Grazing incidence grating compressor

When applying the double-grating configuration to the phase manipulation of XUV pulses, all the optics have to be operated at grazing incidence. The simplest arrangement consists of two identical plane gratings mounted in the compensated configuration, as shown in **Figures 3** and **4**. Due to the symmetry of the configuration, the angular dispersion at the output is canceled, and the output rays are parallel to the input for all the wavelengths [57].

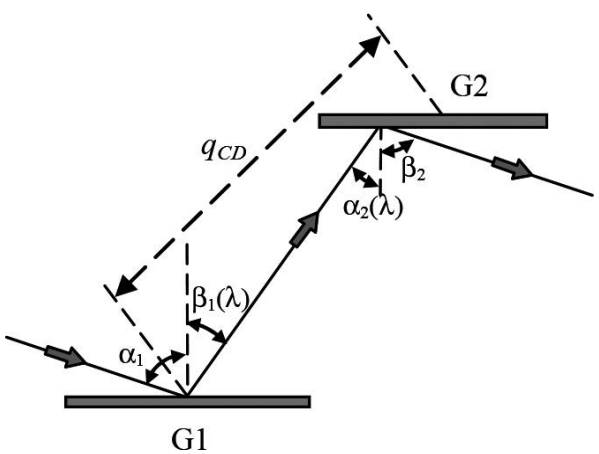

Figure 3. Double-grating compressor in the CDG. The diffraction angle from G2 is constant with the wavelength and equal to the incidence angle on G1, $\beta_2 = \alpha_1$.

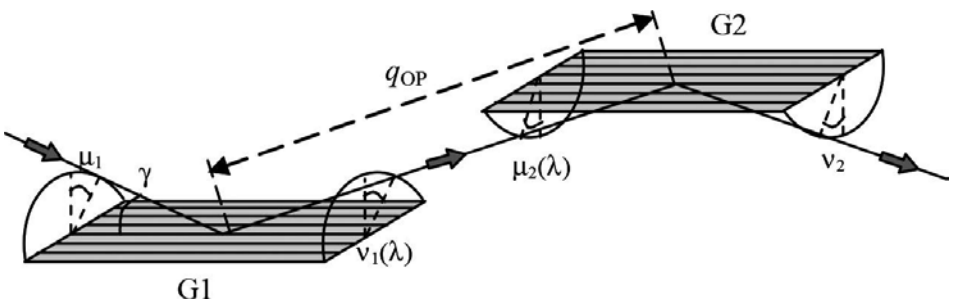

Figure 4. Double-grating compressor in the OPG. The outcoming azimuth from G2 is constant with the wavelength and equal to the incoming azimuth on G1, $\nu_2 = \mu_1$.

Since different wavelengths are diffracted by G1 at different angles, the rays do not make the same optical paths. In the case of the CDG, the optical path is analytically expressed (for less than a constant term) as

$$OP_{CD}(\lambda) = q_{CD}\frac{\cos\beta_c}{\cos\beta(\lambda)}\left[1-\sin\alpha\sin\beta(\lambda)\right] \tag{1}$$

where α is the incidence angle on G1, $\beta(\lambda)$ and β_c are, respectively, the diffraction angles from G1 at the generic wavelength λ and at the central wavelength of the interval of operation λ_c, and q_{CD} is the G1-G2 distance. The bandwidth of the pulse $\Delta\lambda$ is limited between λ_{min} and λ_{max}, $\Delta\lambda = \lambda_{max} - \lambda_{min}$, and $\underline{\lambda}_c = (\lambda_{min} + \lambda_{max})/2$. In case of a narrow-band pulse with $\lambda/\Delta\lambda < 20\%$, Eq. (1) is linearized in λ as

$$OP_{CD}(\lambda) = q_{CD}\lambda_c\left(\frac{m\sigma_{CD}}{\cos\beta_c}\right)^2\lambda \tag{2}$$

Similarly, in the case of the OPM, the optical path is expressed as

$$OP_{OP}(\lambda) = q\frac{\sin^2\gamma\cos\mu}{\cos\nu}\left(1+\sin\mu\sin\nu\right) \tag{3}$$

where μ is the incoming azimuth on G1 that has been chosen to have the central wavelength λ_c diffracted at $\nu_c = \mu$, i.e., $2\sin\gamma\sin\mu = \lambda_c\sigma_{OP}$, and q_{OP} is the G1-G2 distance. In case of a narrow-band pulse, Eq. (3) is linearized as

$$OP_{OP}(\lambda) = q_{OP}\lambda_c\left(\frac{m\sigma_{OP}}{\cos\mu}\right)^2\lambda \tag{4}$$

http://dx.doi.org/10.5772/63416

Note that in both cases the optical path increases with the wavelength, and this forces the group delay dispersion introduced by the double-grating configuration to be negative.

As usual, the group delay (GD) and the group delay dispersion (GDD) are expressed as a function of $\omega = 2\pi c/\lambda$: $GD(\omega) = \partial\varphi(\omega)/\partial\omega = OP(\omega)/c$ and $GDD(\omega) = \partial GD(\omega)/\partial\omega$. The central pulse frequency ω_c is defined as $\omega_c = 2\pi c/\lambda_c$.

For narrow-band pulses, the GD is also linear in frequency, and the GDD is constant and negative

$$GDD_{CD} = -\frac{q_{CD} c}{\omega_c^3}\left(\frac{2\pi\sigma_{CD}}{\cos\beta_c}\right)^2 \tag{5}$$

and

$$GDD_{OP} = -\frac{q_{OP} c}{\omega_c^3}\left(\frac{2\pi\sigma_{OP}}{\cos\mu}\right)^2 \tag{6}$$

Once the required GDD to manipulate the pulse has been defined, the above equations define the parameters of the grating compressor in both geometries.

Once the required GDD has been fixed, the two geometries give equivalent answer for $q_{OP}\,\sigma_{OP}^2/\cos^2\mu = q_{CD}\,\sigma_{CD}^2/\cos^2\beta_c$. In case of equal arms, i.e., $q_{OP} = q_{CD}$, since μ is typically below 20° and β_c above 80°, the groove density that would be required in the OPM is much higher than the CDM and may be not available from grating providers. Therefore, a compressor in the OPM is typically longer than the corresponding CDM, i.e., $q_{OP} > q_{CD}$.

The compressor introduces a spatial chirp of the pulse, i.e., rays with different wavelengths have the same output direction, but they are not exactly superimposed. In the conventional design of compressors for IR pulses, the spatial chirp is canceled by making the beam passing two additional times though the same gratings, so the output spatial dispersion is zero. This cannot be realized in grazing incidence, since it would require the insertion of two additional gratings that would make the configuration complex and inefficient. The spatial chirp $SC(\lambda)$ is expressed, in case of a narrow-band pulse, as

$$SC_{CD}(\lambda) = q_{CD}\sigma_{CD}\frac{\cos\alpha}{\cos^2\beta_c}\Delta\lambda \tag{7}$$

$$\mathrm{SC}_{\mathrm{OP}}(\lambda) = q_{OP}\sigma_{OP}\frac{1}{\cos^2\mu}\Delta\lambda \tag{8}$$

Since the rays are parallel, the spatial chirp does not influence the quality of the final spot size, since all the rays are focused on the same point.

In the following, we discuss the use of the double-grating configuration to the case of compression of FEL pulses and of attosecond pulses generated through HHs.

4. Grating compressor applied to FEL pulses

One of the main problems faced when manipulating intense FEL radiation is the use of robust optical components to be operated with the FEL pulses with minimum risk of damaging. From this point of view, grazing incidence elements are preferable. The double-grating compressor, whose optical elements are used at grazing incidence, is very suitable for FEL pulses. We assume FEL parameters already discussed in the literature [58] that may be a test case for the application to chirped-pulse amplification (CPA) of FEL pulses.

The scheme of the CPA applied to a seeded FEL is shown in **Figure 5**. The electron beam, being generated through a chirped laser seeding pulse, originates, after the radiator, a chirped optical pulse with positive GDD. The chirp is corrected by the grating compressor that introduces different optical paths for different wavelengths and shortens the pulse duration close to the Fourier limit.

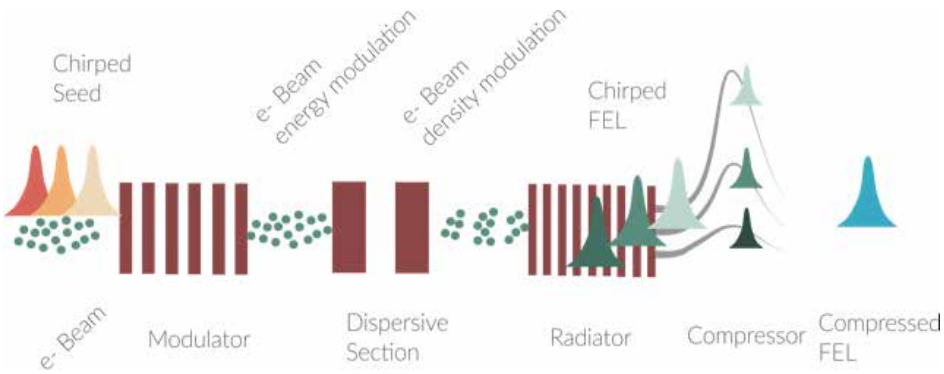

Figure 5. Schematic of the CPA applied to a seeded FEL.

Assuming a linear electron bunch energy spread at the entrance of the FEL radiator, the wavelength spread is evaluated as $\Delta\lambda/\lambda = -2\Delta E/E$. The photon chirp induced by the entrance energy spread is $2\alpha/E$, where α is the electron chirp. This has to be compensated to reduce the pulse time duration.

As a feasibility study, we want to define a configuration to compress an FEL pulse centered at 13.5 nm. **Table 1** resumes the FEL parameters used in the simulation. Using these parameters, the time to be compensated is calculated to be 310 fs for an FEL emission centered at 13.5

nm with a bandwidth $\Delta\lambda$ = 0.8 nm. If the GDD introduced by the compressor is opposite to the intrinsic GDD of the chirped pulse, the pulse time duration is reduced.

Beam energy	0.96 GeV
Charge	0.7 nC
Beam current	1 kA
Bunch duration	270 fs
Energy chirp	–0.15 MeV/ ▪ m

Table 1. FEL parameters used in the simulation.

The compressor parameters are summarized in **Table 2** for the two geometries. The GD of the configurations is shown in **Figure 6(a)**. The curve is almost the same for both geometries. As expected, for narrow-bandwidth pulses, the resulting GD is linear, and the GDD is constant: GDD ≈–37 fs^2.

Pulse central wavelength	13.5 nm
Bandwidth	0.8 nm
Stretching	310 fs
CDG	
Groove density	600 gr/mm
G1-G2 distance	285 mm
Subtended angle	164°
OPG	
Groove density	3600 gr/mm
G1-G2 distance	600 mm
Altitude angle	5°

Table 2. Parameters of the grating compressor in two geometries.

The spatial chirp calculated in the full-width-at-half-maximum (FWHM) bandwidth is 0.9 mm for both geometries. The compressor is typically inserted several tens of meters after the FEL source. As a typical angular divergence of the FEL source at 13.5 nm, 30 μrad (standard deviation) is assumed. The resulting beam diameter at the compressor input, that is assumed to be 50 m far from the source, is 3.6 mm FWHM, therefore much larger than the spatial chirp.

Note that the groove density required in the OPG is higher than the CDG and that the size of the instrument is longer for the OPG. On the basis of the efficiency measurements performed in the two geometries and already discussed in Ref. [54], the total efficiency in the OPG is expected to be higher than the CDG by a factor ≈2.5.

It can be shown that the FEL pulse duration is reduced by a factor of 10 at the output of the compressor, i.e., from 310 fs to about 30 fs. This gives a substantial increase in the temporal resolution of the FEL pulses when used for ultrafast experiments.

4.1. Tunability in wavelength and group delay

The compressor can be tuned in wavelength by rotating the gratings around an axis that is tangent to the surface, passes through the grating center, and is parallel to the grooves. The rotation changes the incidence angle α in the CDG at a constant subtended angle $K = \alpha + \beta$, or the azimuth angle μ in the OPM at constant altitude angle γ. The tuning in wavelength changes also the GD, since it depends on the incidence (azimuth) angles. The delays introduced in the bandwidth $\Delta\lambda$ = 0.8 nm when the central wavelength is tuned in the 10–18 nm interval are shown in **Figure 6(b)**.

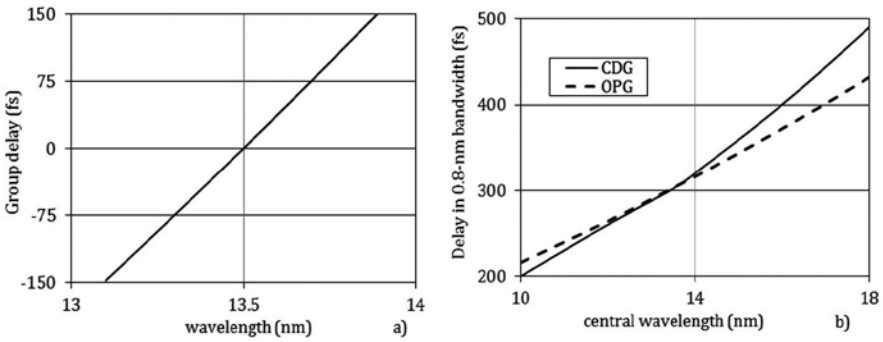

Figure 6. (a) GD of the compressor having the parameters of **Table 2**; (b) change of the delay in the bandwidth when the gratings are rotated to tune the wavelength in the 10–18 nm interval.

It is clear that the simple grating rotation is not sufficient to tune simultaneously the wavelength and the GD. An additional degree of freedom is required that may be the changing of the subtended angle K (the altitude angle γ) in the CDG (OPG), as shown in **Figure 6**. By acting simultaneously on grating rotation and subtended (altitude) angles, users can select simultaneously the wavelength and GD. This makes the design very flexible.

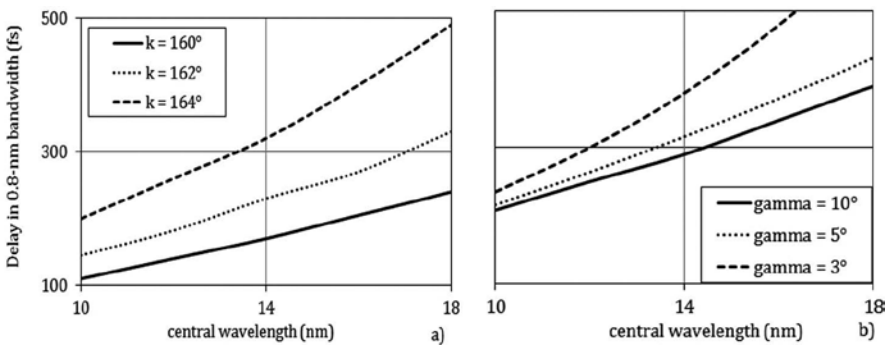

Figure 7. Delay in 0.8-nm bandwidth introduced by the compressor having the parameters of **Table 2** when the gratings are rotated to tune the wavelength in the 10–18 nm interval: (a) CDG, variable subtended angle; (b) OPG, variable altitude angle.

The optical setup of the compressor is shown in **Figure 7**. The instrument consists of two plane gratings and two plane mirrors. The two mirrors are used to deviate the FEL beam in the same direction as the input.

4.2. Operation with a diverging beam

The formulas calculated above assume to work with a collimated beam. In this case, the number of illuminated groove is the same for the two gratings when they are parallel, giving a corrected pulse-front tilt at the output. Indeed, in the real case of an FEL-divergent beam, this would require the use of an additional mirror at the input of the compressor to collimate the beam, namely a grazing-incidence parabola that makes the design complex. Indeed, the compressor, as presented in the previous paragraph, can be used in a divergent beam if the second grating is operated slightly out from the parallel condition, to have the same number of illuminated grooves.

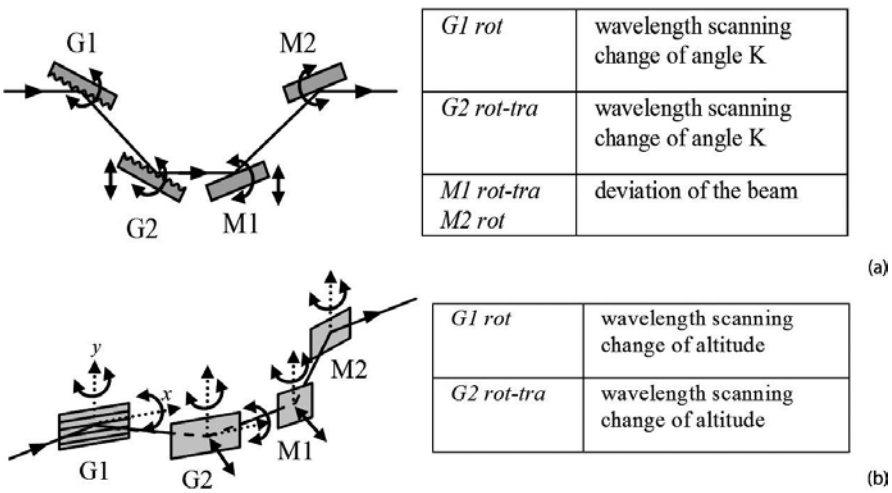

Figure 8. Optical setup of the compressor: (a) CDG; (b) OPG.

The geometry with a divergent beam is shown in **Figure 8** for CDG. The number of illuminated grooves is the same for both gratings if G2 is operated at a lower subtended angle, $k_2 < k_1$:

$$\cos\alpha_2 = \cos\beta_1 + \frac{q_{CD}\delta_1}{S_1}\frac{\cos^2\alpha_1}{\cos\beta_1} \tag{9}$$

where δ_1 is the divergence of the incoming beam, S_1 is the beam cross section at G1, α_1 and β_1 the incidence and diffraction angles on G1, and α_2 the incidence angle on G2.

In the case of OPM, the compensation of the pulse-front tilt is expressed by

$$\cos\mu_2 = \cos\mu_1 + \frac{q_{OP}\delta_1}{S_1} \tag{10}$$

where μ_1 and μ_2 are the azimuth angles on G1 and G2.

The asymmetry between G1 and G2 depends on the actual divergence of the FEL beam and on the distance between the two gratings. Let us assume the parameters of **Table 2**, with 30-μrad divergence (standard deviation). The compressor stage is supposed to be installed 50 m far from the source. In the case of CDG, the residual pulse-front tilt at 13.5 nm is 5 fs FWHM if the gratings are operated parallel and the correction to be applied to α_2 is 0.1°. If the compressor is used at longer wavelengths, the asymmetry to be applied is more remarkable because of the higher FEL divergence.

The spatial chirp, that does not influence the quality of the final spot size in case of a parallel beam, has to be evaluated in case of a divergent beam, since different wavelengths are focused in different points in the direction of the spectral dispersion. This gives a slight asymmetry in the spot profile that is broadened in the direction of spectral dispersion. Let us define M as the total demagnification of the FEL beamline, $M \approx 50$–100. The spatial chirp SC gives a limit to the minimum focal spot that can be achieved in the direction of the spectral dispersion, as SC/M. Assuming the same parameters of **Table 2** and $M = 75$, the minimum spot size that can be achieved in the direction of the spectral dispersion is 12 μm FWHM. The broadening due to the spatial chirp is generally negligible for spot sizes in the 20–50 μm range. However, the use of the compressor may degrade the quality of the final focus if the beamline is tailored to give micro-focusing. In such cases, the insertion of the compressor has to be carefully evaluated.

4.3. Efficiency of the compressor

The efficiency of the compressor depends on the geometry adopted for the gratings, since it is well known that the OPG gives efficiency higher than the CDG [59].

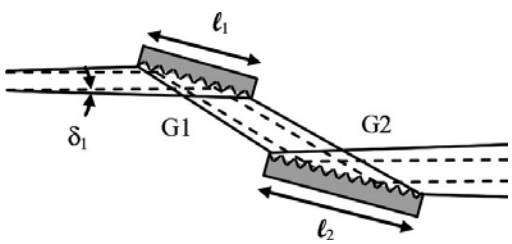

Figure 9. Grating compressor operated in divergent beam. The pulse-front tilt is corrected for $l_2 = l_1$.

To compare the two geometries, the first-order diffraction efficiency has been measured in the 25–35 nm (35–50 eV) region in the two different geometries. Both gratings are plane, gold-coated, and have 600 gr/mm groove density. The grating used in the CDG is blazed at 2°, and the grating used in the OPG is blazed at 7°. The results are shown in **Figure 9**. The efficiency

in the OPG is a factor ≈2 higher than the CDG that gives a factor 4 in the total efficiency of the compressor. The latter is expected to be ≈5% in the CDG and ≈20% in the OPG [60].

5. Grating compressor for attosecond pulses

Attosecond pulses generated with the scheme of HHs by the use of laser pulses of few optical cycles are positively chirped as a result of the different duration of the quantum paths that contribute to the different portions of the emitted spectrum. They can be compressed by introducing a suitable device with a negative GDD.

The simplest device that exhibits negative GDD is a thin metallic filter. Anomalous dispersion near absorption resonances can be exploited to compensate the positive chirp of the generated attosecond pulses. Aluminum or zirconium is normally used in the XUV range, depending on the spectral range of operation [61]. Furthermore, the filter is also useful to block the IR laser beam since it is totally solar blind. The main drawback of the filter is the strong XUV absorption that may even exceed one order of magnitude.

Aperiodic multilayer mirrors have also been developed and successfully tested for the dispersion control in the XUV [62–65]. The multilayer coating is designed to compensate for the attosecond chirp and reduce the pulse duration. Pulse compression and focusing are demanded to the same optical element that makes the design simple and compact. For a center-photon energy range of 100–120 eV, the mirror reflectivity is approximately 10% and the bandwidth 10–13 eV. Recently, also mirrors for the water-window region have been tested, although with reflectivity lower than 1% [66]. A metallic filter has to be inserted anyway in the optical path to block the IR laser light.

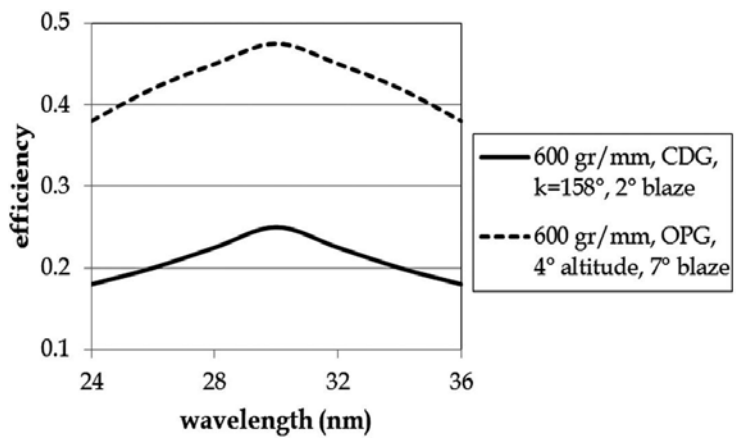

Figure 10. Comparison of efficiencies measured in CDG and OPG.

We discuss here the use of gratings to compress attosecond pulses by introducing a GDD that compensates for the intrinsic pulse chirp. Unfortunately, the configuration with plane gratings

discussed above is not suitable, since the G1-to-G2 distance q that is required to give the necessary GDD is too small to be realized in practice. Therefore, the plane-grating configuration has to be modified as shown in **Figure 10** for the OPG [67, 68], by adding an intermediate focal point between the two gratings. The case of CDG is analogous.

The design consists of six optical elements: four identical grazing incidence parabolic mirrors (P1-P4) and two identical plane gratings (G1, G2). The XUV source is located in the front focal plane of P1, and the rays are collected at the focus of the last parabolic mirror P4. The parabolic mirrors are used to collimate and refocus the XUV radiation with negligible aberrations, and the gratings are illuminated in parallel light. A spectrally dispersed image of the source is obtained in the intermediate plane. The two focusing mirrors placed between the gratings act as a telescopic arrangement. Differently from the plane-grating compressor discussed above, this makes it possible to: (i) continuously tune the GDD from negative to positive values and (ii) achieve the exceedingly small grating separations necessary to compensate the attosecond chirp.

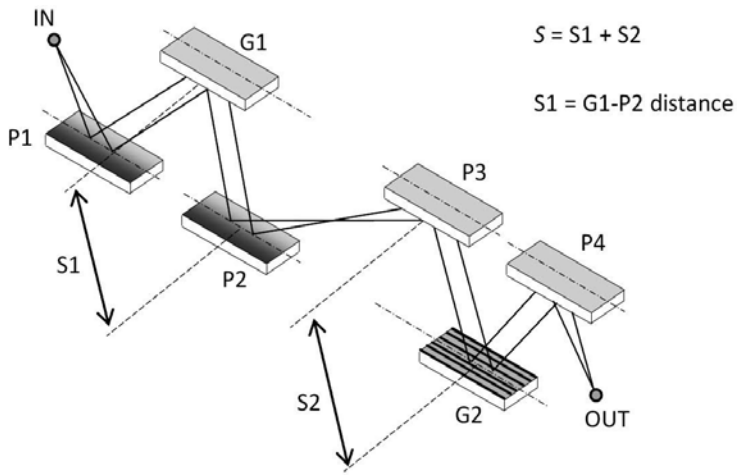

Figure 11. Grating compressor for attosecond pulses.

With reference to the symbols listed in **Figure 11**, the condition for zero GDD is to have G1 imaged on G2, that is realized when $S1 + S2 = 2f$. Since f is fixed, the GDD depends on $S1 + S2$: for $S1 + S2 < 2f$, G1 is imaged behind G2, and the resulting GDD is positive; for $S1 + S2 > 2f$, G1 is imaged before G2, and the resulting GDD is negative. Once the equivalent distance q that is required for compensation has been calculated, the effective displacement from the zero-dispersion case is $\Delta S = q/(\omega_0 \sin\gamma \cos\nu)$, where ω_0 is the center angular frequency. It can be noted that the design of the compressor is simplified if $S1$ is kept fixed, and only $S2$ is tuned to change the GDD. A suitable value for f is in the range of 200–300 mm, giving a total length of the compressor of ≈1.5 m.

As an application to ultrashort pulses, a compressor design for the 50–100 eV region is discussed here. The characteristics of the compressor are resumed in **Table 3**. The GD

introduced with the distance $S = S1 + S2$ is shown in **Figure 12**. An example of compression of a pulse with a positive GDD is presented in **Figure 13**, adapted from [69]. Note that the chirp introduced by the compressor is able to compensate the pulse chirp down to a nearly single-cycle pulse (**Figure 14**).

Pulse spectral interval	50-100 eV, 12-24 nm
Mirrors	**Off-axis parabola**
Input/output arms	300 mm
Grazing angle	3°
Gratings	**Plane**
Groove density	200 gr/mm
Altitude angle	1.5°
Distances	S1+S2 > 600 mm for negative GDD

Table 3. Parameters of the compressor for the 50–100 eV region.

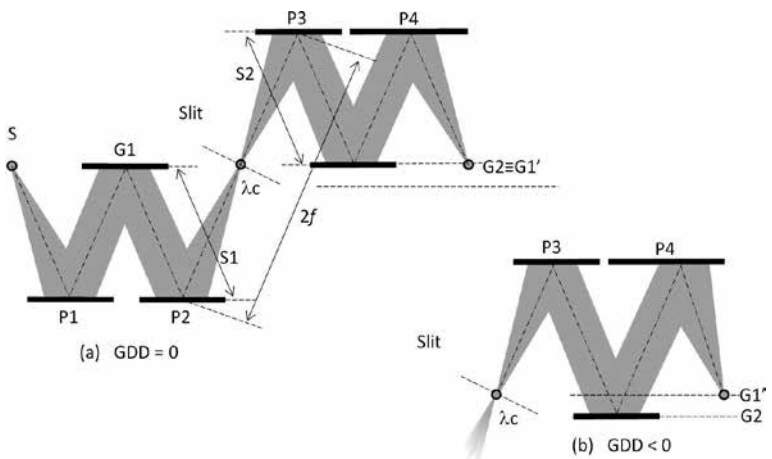

Figure 12. Operation of the attosecond compressor: (a) GDD = 0; (b) GDD < 0.

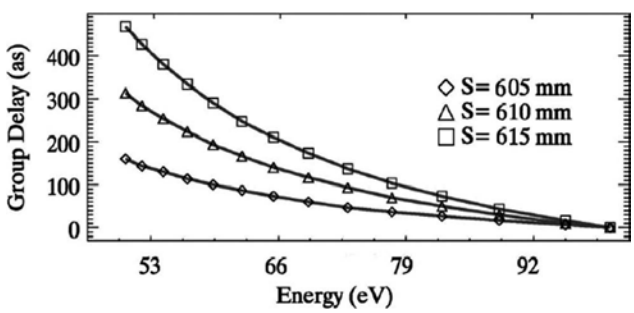

Figure 13. GD of the compressor with parameters listed in **Table 3**.

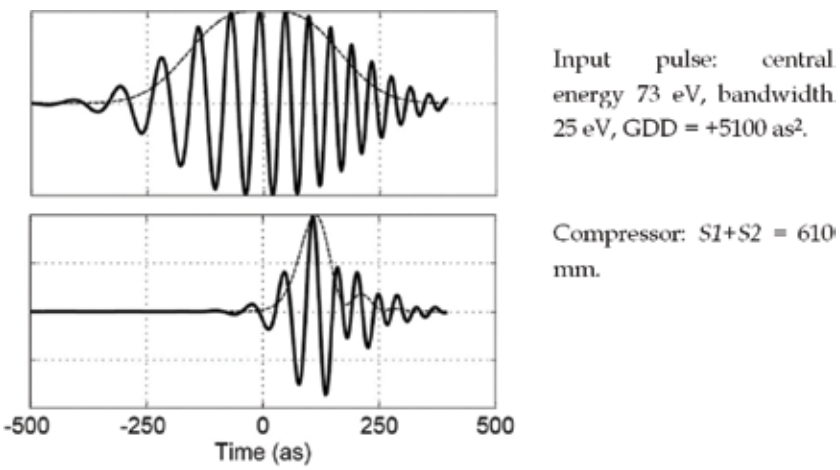

Figure 14. Simulation of the compression of a XUV pulse with the parameters of **Table 3**.

5.1. Example of application to attosecond pulses

A schematic view of an experiment using compressed attosecond pulses is shown in **Figure 15**. The XUV attosecond pulses are generated on a gas jet in a vacuum chamber and are intrinsically chirped. The XUV radiation is generated with the intrinsic attosecond chirp. Different wavelengths travel in different paths inside the compressor that compensates for the chirp and reduces the time duration of the pulse.

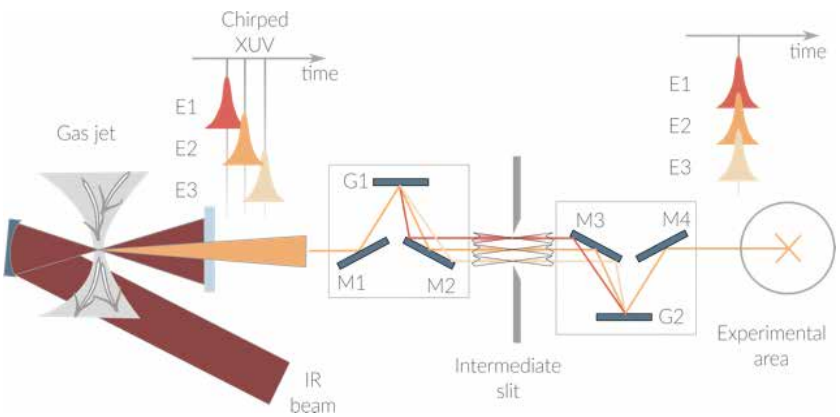

Figure 15. Schematic of the attosecond compressor.

Attosecond pulses are generated in different XUV spectral windows, depending on the interacting gas. Using argon and $\approx 2 \cdot 10^{14}$ W/cm^2 ultrafast laser intensity, radiation is generated in the 25–55 eV region, while with neon and $\approx 6 \cdot 10^{14}$ W/cm^2 intensity, radiation is generated in the 50–120 eV region. Attosecond pulses are generated from the short trajectory

components, since this is the part of the generated radiation that survives propagation in the generating medium. Aluminum and zirconium filters can be used, respectively, in the low- (i.e., argon) and high-energy range (i.e., neon) to introduce negative chirp to compensate for the intrinsic chirp of the attosecond pulses and compress them close to the Fourier limit.

Here, we discuss the parameters to be used for a grating compressor in the two different XUV regions. For the lower intensity case, the parameters are $\sigma = 100$ grooves/mm, $\gamma = 1.5°$, $\mu = 3.7°$, $\Delta S = 23$ mm. For the higher intensity case, the parameters are $\sigma = 200$ grooves/mm, $\gamma = 1°$, $\mu = 4.1°$, $\Delta S = 29$ mm.

Simulations of the generated and compressed pulses have been performed starting from 25-fs driving pulses at 790 nm [70]. The generated pulses have a duration of 270 as in argon and 200 in neon, while the Fourier-limited duration would be, respectively, 115 and 35 as. At the output of the grating compressor, the pulse duration results, respectively, 160 and 60 as, much closer to the Fourier limit. It is also shown that the optimal Al filter would reduce the pulse duration to 130 as, therefore shorter than the grating compressor, while the optimal Zr filter would reduce the pulse duration to 90 as, therefore longer than the grating compressor.

In general, the grating compressor is more versatile than metal filters and can be continuously tuned from negative to positive GDD with constant throughput.

6. Conclusions

The use of diffraction gratings to manipulate the spectral phase of XUV ultrashort pulses has been discussed. The system consists of two gratings to introduce the required phase chirp. Both the classical and the off-plane geometries have been discussed.

Both a simple design with two plane gratings working in collimated beam and a more complex design with two plane gratings and an intermediate focal point have been discussed. Both designs are tunable in wavelength range to cover the whole spectral extension of the source and operate at different wavelengths; furthermore, once the operating wavelength has been chosen, the GDD is tunable to compensate for the actual pulse chirp.

The use of elements at grazing incidence makes the system particularly suitable for the application to CPA of intense FEL pulses and to compression of attosecond pulses, playing an important role for the photon handling and conditioning of future ultrashort sources.

Acknowledgements

The results discussed here have been partially funded by Extreme Light Infrastructures (ELI) funds of the Italian Ministry for Education, University and Research.

Author details

Fabio Frassetto, Paolo Miotti and Luca Poletto*

*Address all correspondence to: luca.poletto@ifn.cnr.it

CNR-Institute of Photonics and Nanotechnologies, Padova, Italy

References

[1] Diels J-C, Rudolph W. Ultrashort Laser Pulse Phenomena. Oxford: Academic Press Inc.; 2006.

[2] Jaegle' P. Coherent Sources of XUV Radiation. Berlin: Springer; 2006.

[3] Marciak-Kozlowska J. From Femto-to Attoscience and Beyond. New York: Nova Science Publishers Inc; 2009.

[4] Vrakking M J J, Elsaesser T. X-Ray Photonics: X-rays Inspire Electron Movies. Nat. Photonics. 2012;6:645–647.

[5] Lépine F, Ivanov M Y, Vrakking, M J J. Attosecond Molecular Dynamics: Fact or Fiction?. Nat. Photonics. 2014;8:195–204.

[6] Canova F, Poletto L, editors. Optical Technologies for Extreme-Ultraviolet and Soft X-ray Coherent Sources. Berlin: Springer; 2015.

[7] Chang Z, Rundquist A, Wang H, Murnane M M, Kapteyn H C. Generation of Coherent Soft X Rays at 2.7 nm Using High Harmonics. Phys. Rev. Lett. 1997;79:2967–2970.

[8] Schnürer M, Spielmann Ch, Wobrauschek P, Streli C, Burnett N H, Kan C, Ferencz K, Koppitsch R, Cheng Z, Brabec T, Krausz F. Coherent 0.5-keV X-Ray Emission from Helium Driven by a Sub-10-fs Laser. Phys. Rev. Lett. 1998;80:3236–3239.

[9] Takahashi E J, Kanai T, Ishikawa K L, Nabekawa Y, Midorikawa K. Coherent Water Window X Ray by Phase-Matched High-Order Harmonic Generation in Neutral Media. Phys. Rev. Lett. 2008;101:253901.

[10] Corkum P, Krausz F. Attosecond Science. Nat. Physics. 2007;3:381–387.

[11] Krausz F, Ivanov M. Attosecond Physics. Rev. Mod. Phys. 2009;81:163–234.

[12] Sansone G, Poletto L, Nisoli M. High-Energy Attosecond Light Sources. Nat. Photonics. 2011;5:655–663.

[13] Krausz F, Stockman M I. Attosecond metrology: from electron capture to future signal processing. Nat. Photonics. 2014;8:205–213.

[14] Paul P M, Toma E S, Breger P, Mullot G, Auge F, Balcou P, Muller H G, Agostini P. Observation of a Train of Attosecond Pulses from High Harmonic Generation. Science. 2001;292:1689–1692.

[15] Lopez-Martens R, Varju K, Johnsson P, Mauritsson J, Mairesse Y, Salières P, Gaarde M B, Schafer K J, Persson A, Svanberg S, Wahlström C-G, L'Huillier A. Amplitude and Phase Control of Attosecond Light Pulses. Phys. Rev. Lett. 2005;94:033001.

[16] Kienberger R, Goulielmakis E, Uberacker M, Baltuska A, Yakovlev V, Bammer F, Scrinzi A, Westerwalbesloh T, Kleineberg U, Heinzmann U, Drescher M, Krausz F. Atomic Transient Recorder. Nature. 2004;427:817–822.

[17] Sansone G, Benedetti E, Calegari F, Vozzi C, Avaldi L, Flammini R, Poletto L, Villoresi P, Altucci C, Velotta R, Stagira S, De Silvestri S, Nisoli M. Isolated Single-Cycle Attosecond Pulses. Science. 2006;314:443–446.

[18] Zhao K, Zhang Q, Chini M, Wu Y, Wang X, Chan Z. Tailoring a 67 Attosecond Pulse Through Advantageous Phase-Mismatch. Opt. Lett. 2012;37:3891–3893.

[19] Chini M, Zhao K, Chang Z. The Generation, Characterization and Applications of Broadband Isolated Attosecond Pulses. Nat. Photonics. 2014;8:178–186.

[20] Mairesse Y, de Bohan A, Frasinski L J, Merdji H, Dinu L C, Monchicourt P, Breger P, Kovacev M, Auguste T, Carré B, Muller H G, Agostini P, Salières P. High-Harmonics Chirp and Optimization of Attosecond Pulse Trains. Laser Phys. 2005;15:863–870.

[21] Schultze M, Goulielmakis E, Uiberacker M, Hofstetter M, Kim J, Kim D, Krausz F, Kleineberg U. Powerful 170-Attosecond XUV Pulses Generated with Few-Cycle Laser Pulses and Broadband Multilayer Optics. New J. Phys. 2007;9:243–253.

[22] Saldin E L, Schneidmiller E A, Yurkov M V. The Physics of Free Electron Lasers. Berlin: Springer; 2000.

[23] Ding Y, Decker F-J, Emma P, Feng C, Field C, Frisch J, Huang Z, Krzywinski J, Loos H, Welch J, Wu J, Zhou F. Femtosecond X-Ray Pulse Characterization in Free-Electron lasers Using a Cross-Correlation Technique. Phys. Rev. Lett. 2012;109:254802.

[24] Emma P J, Bane K, Cornacchia M, Huang Z, Schlarb H, Stupakov G, Nalz D. Femtosecond and Sub-femtosecond X-Ray Pulses from a Self-Amplified Spontaneous-Emission–Based Free-Electron Laser. Phys. Rev. Lett. 2004;92:074801.

[25] Ding Y, Huang Z, Ratner D, Bucksbaum P, Merdji H. Generation of Attosecond X-Ray Pulses with a Multicycle Two-Color Enhanced Self-Amplified Spontaneous Emission Scheme. Phys. Rev. ST Accel. Beams. 2009;12:060703.

[26] Tanaka T. Proposal for a Pulse-Compression Scheme in X-Ray Free-Electron Lasers to Generate a Multiterawatt, Attosecond X-Ray Pulse. Phys. Rev. Lett. 2013;110:084801.

[27] Rosenzweig J B, Alesini D, Andonian G, Boscolo M, Dunning M, Faillace L, Ferrario M, Fukusawa A, Giannessi L, Hemsing E, Marcus G, Marinelli A, Musumeci P, O'Shea B,

Palumbo L, Pellegrini C, Petrillo V, Reiche S, Ronsivalle C, Spataro B, Vaccarezza C. Generation of Ultra-Short, High Brightness Electron Beams for Single-Spike SASE FEL Operation. Nucl. Instrum. Meth. A. 2008;593:39–44.

[28] Shu X, Peng T, Dou Y. Chirped Pulse Amplification in a Free-Electron Laser Amplifier. J. Elect. Spect. Rel. Phen. 2011;184:350–353.

[29] Feng C, Shen L, Zhang M, Wang D, Zhao Z, Xian D. Chirped Pulse Amplification in a Seeded Free-Electron Laser for Generating High-Power Ultra-Short Radiation. Nucl. Inst. Meth. Phys. Res. A. 2013;712:113–119.

[30] Poletto L, Tondello G, Villoresi P. High-order Laser Harmonics Detection in the EUV and Soft X-Ray Spectral Regions. Rev. Sci. Instr. 2001;72:2868–2874.

[31] Poletto L, Bonora S, Pascolini M, Villoresi P. Instrumentation for Analysis and Utilization of Extreme-Ultraviolet and Soft X-Ray High-order Harmonics. Rev. Sci. Instr. 2004;75:4413–4418.

[32] Frassetto F, Cacho C, Froud C, Turcu I C E, Villoresi P, Bryan W A, Springate E, Poletto L. Single-Grating Monochromator for Extreme-Ultraviolet Ultrashort Pulses. Opt. Express. 2011;19:19169–19181.

[33] Grazioli C, Callegari C, Ciavardini A, Coreno M, Frassetto F, Gauthier D, Golob D, Ivanov R, Kivimäki A, Mahieu B, Bučar B, Merhar M, Miotti P, Poletto L, Polo E, Ressel B, Spezzani C, De Ninno G. CITIUS: An Infrared-Extreme Ultraviolet Light Source for Fundamental and Applied Ultrafast Science. Rev. Sci. Instrum. 2014;85:023104.

[34] Poletto L, Miotti P, Frassetto F, Spezzani C, Grazioli C, Coreno M, Ressel B, Gauthier D, Ivanov R, Ciavardini A, de Simone M, Stagira S, De Ninno G. Double-Configuration Grating Monochromator for Extreme-Ultraviolet Ultrafast Pulses. Appl. Opt. 2014;53:5879–5888.

[35] Ojeda J, Arrell C A, Grilj J, Frassetto F, Mewes L, Zhang H, van Mourik F, Poletto L, Chergui M. Harmonium: A Pulse Preserving Source of Monochromatic EUV (30–110 eV) Radiation for Ultrafast Photoelectron Spectroscopy of Liquids. Structural Dynamics. 2016;3:023602.

[36] Martins M, Wellhöfer M, Hoeft J T, Wurth W, Feldhaus J, Follath R. Monochromator Beamline for FLASH. Rev. Sci. Inst. 2006;77:115108.

[37] Guerasimova N, Dziarzhytski S, Feldhaus J. The Monochromator Beamline at FLASH: Performance, Capabilities and Upgrade Plans. J. Mod. Opt. 2011;58:1480–1485.

[38] Heimann P, Krupin O, Schlotter W F, Turner J, Krzywinski J, Sorgenfrei F, Messerschmidt M, Bernstein D, Chalupský J, Hájková V, Hau-Riege S, Holmes M, Juha L, Kelez N, Lüning J, Nordlund D, Fernandez Perea M, Scherz A, Soufli R, Wurth W, Rowen M. Linac Coherent Light Source Soft X-Ray Materials Science Instrument Optical Design and Monochromator Commissioning. Rev. Sci. Inst. 2011;82:093104.

[39] Schlotter W F, Turner J J, Rowen M, Heimann P, Holmes M, Krupin O, Messerschmidt M, Moeller S, Krzywinski J, Soufli R, Fernández-Perea M, Kelez N, Lee S, Coffee R, Hays G, Beye M, Gerken N, Sorgenfrei F, Hau-Riege S, Juha L, Chalupsky J, Hajkova V, Mancuso A P, Singer A, Yefanov O, Vartanyants I A, Cadenazzi G, Abbey B, Nugent K A, Sinn H, Lüning J, Schaffert S, Eisebitt S, Le W-S, Scherz A, Nilsson A R, Wurth W. The Soft X-Ray Instrument for Materials Studies at the Linac Coherent Light Source X-Ray Free-Electron Laser. Rev. Sci. Inst. 2012;83:043107.

[40] Poletto L, Frassetto F. Time-Preserving Monochromators for Ultrafast Extreme-Ultraviolet Pulses. Appl. Opt. 2010;49:5465–5473.

[41] Villoresi P. Compensation of Optical Path Lengths in Extreme-Ultraviolet and Soft-X-Ray Monochromators for Ultrafast Pulses. Appl. Opt. 1999;38:6040–6049.

[42] Poletto L. Time-Compensated Grazing-Incidence Monochromator for Extreme-Ultraviolet and Soft X-Ray High-order Harmonics. Appl. Phys. B. 2004;78:1013–1016.

[43] Poletto L, Villoresi P. Time-Compensated Monochromator in the Off-Plane Mount for Extreme-Ultraviolet Ultrashort Pulses. Appl. Opt. 2006;45:8577–8585.

[44] Poletto L, Villoresi P, Benedetti E, Ferrari F, Stagira S, Sansone G, Nisoli M. Intense Femtosecond Extreme Ultraviolet Pulses by Using a Time-Delay Compensated Monochromator. Opt. Lett. 2007;32:2897–2899.

[45] Poletto L, Villoresi P, Frassetto F, Calegari F, Ferrari F, Lucchini M, Sansone G, Nisoli M. Time-Delay Compensated Monochromator for the Spectral Selection of Extreme-Ultraviolet High-order Laser Harmonics. Rev. Sci. Instrum. 2009;80:123109.

[46] Ito M, Kataoka Y, Okamoto T, Yamashita M, Sekikawa T. Spatiotemporal Characterization of Single-order High Harmonic Pulses from Time-Compensated Toroidal-Grating Monochromator. Opt. Express. 2010;18:6071–6078.

[47] Igarashi H, Makida A, Ito M, Sekikawa T. Pulse compression of Phase-Matched High Harmonic Pulses from a Time-Delay Compensated Monochromator. Opt. Express. 2012;20:3725–3732.

[48] Poletto L, Azzolin P, Tondello G. Beam-Splitting and Recombining of Free-Electron-Laser Extreme-Ultraviolet Radiation. Appl. Phys. B. 2004;78:1009–1011.

[49] Frassetto F, Villoresi P, Poletto L. Beam Separator for High-Order Harmonic Radiation in the 3–10 nm Spectral Region. J. Opt. Soc. Am. A. 2008;25:1104–1114.

[50] Poletto L, Frassetto F, Villoresi P. Ultrafast Grating Instruments in the Extreme Ultraviolet. IEEE J. Sel. Top. Quantum Electron. 2012;18:467–478.

[51] Werner W. X-Ray Efficiencies of Blazed Gratings in Extreme Off-Plane Mountings. Appl. Opt. 1977;16:2078–2080.

[52] Petit R. Electromagnetic Theory of Gratings. Berlin: Springer; 1980.

[53] Werner W, Visser H. X-Ray Monochromator Designs Based on Extreme Off-Plane Grating Mountings. Appl. Opt. 2006;20:487–492.

[54] Pascolini M, Bonora S, Giglia A, Mahne N, Nannarone S, Poletto L. Gratings in the Conical Diffraction Mounting for an EUV Time-Delay Compensated Monochromator. Appl. Opt. 2006;45:3253–3562.

[55] Martinez O. 3000 Times Grating Compressor with Positive Group Velocity Dispersion: Application to Fiber Compensation in 1.3–1.6 μm Region. IEEE J. Quantum Electron. 1987;23:59–64.

[56] Martinez O. Design of High-Power Ultrashort Pulse Amplifiers by Expansion and Recompression. IEEE J. Quantum Electron. 1987;23:1385–1387.

[57] Frassetto F, Poletto L. Grating Configurations to Compress Extreme-Ultraviolet Ultrashort Pulses. Appl. Opt. 2015;54:7985–7992.

[58] Frassetto F, Giannessi L, Poletto L. Compression of XUV FEL Pulses in the Few-Femtosecond Regime. Nucl. Instr. Meth. A. 2008;593:14–16.

[59] Poletto L, Bonora S, Pascolini M, Borgatti F, Doyle B, Giglia A, Mahne N, Pedio M, Nannarone S. Efficiency of Gratings in the Conical Diffraction Mounting for an EUV Time-Compensated Monochromator. In: Proc. SPIE Vol. 5534 Fourth Generation X-Ray Sources and Optics II; August 2004; Denver (USA). SPIE Publisher; 2004. p. 144–153.

[60] Poletto L, Frassetto F, Miotti P, Gauthier D, Fajardo M, Mahieu B, Svetina C, Zangrando M, Zeitoun P, De Ninno G. Grating-Based Pulse Compressor for Applications to FEL Sources. In: Proc. SPIE Vol. 9512, Advances in X-ray Free-Electron Lasers Instrumentation; April 2015; Prague (Czech Rep.). SPIE Publisher; 2015. p. 951210.

[61] Sola J, Mevel E, Elouga L, Constant E, Strelkov V, Poletto L, Villoresi P, Benedetti E, Caumes J-P, Stagira S, Vozzi C, Sansone G, Nisoli M. Controlling Attosecond Electron Dynamics by Phase-Stabilized Polarization Gating. Nat. Phys. 2006;2:319–322.

[62] Morlens A-S, Lopez-Martens R, Boyko O, Zeitoun P, Balcou P, Varju K, Gustafsson E, Remetter T, L'Huillier A, Kazamias S, Gautier J, Delmotte F, Ravet M-F. Design and Characterization of Extreme Ultraviolet Broadband Mirrors for Attosecond Science. Opt. Lett. 2006;31:1558–1560.

[63] Suman M, Monaco G, Pelizzo M-G, Windt D L, Nicolosi P. Realization and Characterization of an XUV Multilayer Coating for Attosecond Pulses. Opt. Express. 2009;17:7922–7932.

[64] Hofstetter M, Schultze M, Fie M, Dennhardt B, Guggenmos A, Gagnon J, Yakovlev V S, Goulielmakis E, Kienberger R, Gullikson E M, Krausz F, Kleineberg U. Attosecond Dispersion Control by Extreme Ultraviolet Multilayer Mirrors. Opt. Express. 2011;19:1767–1776.

http://dx.doi.org/10.5772/63416

[65] Bourassin-Bouchet C, de Rossi S, Wang J, Meltchakov E, Giglia A, Mahne N, Nannarone S, Delmotte F. Shaping of Single-Cycle Sub-50-Attosecond Pulses with Multilayer Mirrors. New J. Phys. 2012;14:023040.

[66] Guggenmos A, Rauhut R, Hofstetter M, Hertrich S, Nickel B, Schmidt J, Gullikson E M, Seibald M, Schnick W, Kleineberg U. Aperiodic CrSc Multilayer Mirrors for Attosecond Water Window Pulses. Opt. Express. 2013;21:21728–21740.

[67] Frassetto F, Villoresi P, Poletto L. Optical Concept of a Compressor for XUV Pulses in the Attosecond Domain. Opt. Express. 2008;16:6652–6667.

[68] Poletto L, Frassetto F, Villoresi P. Design of an Extreme-Ultraviolet Attosecond Compressor. J. Opt. Soc. Am. B. 2008;25:B133–B136.

[69] Poletto L, Villoresi P, Frassetto F. Diffraction Gratings for the Selection of Ultrashort Pulses in the Extreme-Ultraviolet. In: M. Grishin, editor. Advances in Solid-State Lasers: Development and Applications. INTECH, Croatia; 2010. p. 413–438.

[70] Mero M, Frassetto F, Villoresi P, Poletto L, Varju K. Compression Methods for XUV Attosecond Pulses. Opt. Express. 2011;19:23420–23428.

Section 5

Fiber-based Sources of Short Optical Pulse

Chapter 10

Fiber-Based High-Power Supercontinuum and Frequency Comb Generation

Qiang Hao, Tingting Liu and Heping Zeng

Additional information is available at the end of the chapter

http://dx.doi.org/10.5772/64209

Abstract

Ultrafast optics has been a rich research field, and picosecond/femtosecond pulsed laser sources seek many applications in both the areas of fundamental research and industrial life. Much attention has been attached to fiber lasers in recent decades as they offering various superiorities over their solid-state counterparts with compact size, low cost, and great stability due to the inherent stability and safety of the waveguide structures as well as high photoelectric conversion efficiency. Fiber-based sources of ultrashort and high-peak/high-average optical pulses have become extremely important for high-precision laser processing while sources whose carrier-envelop offset and repetition rate are stabilized can serve as laser combs with applications covering many research areas, such as precision spectroscopy, optical clock, and optical frequency metrology. For the application as laser combs, four parts as fiber laser, broadband supercontinuum, nonlinear power amplification, and repetition rate stabilization must be concerned. This chapter is intended to give a brief introduction about the achievement of the four technologies mentioned above with different experimental setups, recently developed such as divided-pulse amplification (DPA) in emphasize. Moreover, detailed descriptions of the experimental constructions as well as theoretical analyses about the phenomena they produced are also involved.

Keywords: fiber lasers, divided-pulse nonlinear amplification, four-wave mixing, frequency stabilized

1. Introduction

Ultrafast laser sources and their applications such as high-power supercontinuum and frequency comb have gained much attention in recent decades [1–7]. High-power fiber lasers

spur a rapid growth of industrial applications including laser cutting, laser marking, and so on [8]. Moreover, supercontinuum and frequency comb are considered as the breakthrough of laser field for their applications covering precision spectroscopy, astronomical observations, and optical frequency metrology [9, 10]. This chapter is intended to describe, from experimental point of view, the ultrashort pulse laser oscillators, high-power nonlinear fiber amplifiers, supercontinuum, and frequency combs. Section 2 shows the performance of two types of mode-locked lasers. The first one consisting of bulk and fiber optical components is mode-locked via nonlinear polarization rotation (NPR) mechanism at 1.03 μm. The other one, operating at 1.55 μm, is mode-locked by nonlinear amplified loop mirror (NALM) with polarization-maintaining (PM) fiber components in order to overcome environmental perturbation and thus maintain long-term operation. Section 3 introduces a practical method (spectral tailoring), which facilitates supercontinuum generation in single-mode fiber amplifier at 1.03 μm with a few picosecond laser pulses. The second part in this section introduced broadband supercontinuum generation (from 950 to 2200 nm) by injecting pulses with 72-fs temporal duration, 150-mW average power, and 60-MHz repetition rate at 1560 nm into 20-cm-long PM-HNLF. Section 4 gives a brief introduction of divided-pulse amplification (DPA). To generate transform-limited pulse at 1.55 μm, DPA with polarized pulse duplicating was employed to overcome the gain narrowing effect and control the nonlinear spectral broadening in anomalous dispersion Er-fiber amplifier. As high as 500-mW average power at 1560 nm is achieved by ×8 replicas. Moreover, the highest frequency-doubling conversion efficiency reached 56.3% by using a periodically poled lithium niobate (PPLN) crystal at room temperature. Section 5 discusses an all-optical control method via resonantly enhanced optical nonlinearity (or pump-induced refractive index change, RIC) for high-precision repetition rate stabilization. The standard deviation (SD) of repetition rate can be reduced to a record level of <100 μHz by using the RIC method in a PM figure-eight laser cavity.

2. Fiber laser

Fiber lasers offer several practical advantages, such as excellent spatial-mode quality, effective heat dissipation, and flexible optical path and, recently, are becoming attractive laser sources in both scientific researches and industry applications. Especially, mode-locked fiber lasers with ultrashort pulse duration and high-repetition rate have attracted a lot of attention for their applications in optical sensing, optical communication, optical metrology, and biomedical imaging and processing [11, 12]. Therefore, various femtosecond/picosecond mode-locked lasers have been constructed and developed. As mode-locked lasers are often affected by environmental perturbations (mechanical vibration and temperature fluctuation), robust and stable oscillator with compact design are urgently needed. In this section, we present a compact femtosecond fiber laser at 1.03 μm by using integrated fiber optical components. The shortest dechirped pulse duration reaches 81 fs for a net cavity dispersion value close to −0.001 ps^2. Another part of this section described a self-started Er-doped laser oscillator, which is mode-

locked by NALM with PM-fiber configuration. By optimizing the net dispersion, the buildup time can be reduced from 8 min to ~ms order of magnitude.

2.1. Operation regime of mode-locked lasers

As well known, the main features of mode-locked fiber laser depend on the pulse evolution process, which is relevant to the group-velocity dispersion (GVD) and the nonlinearity in optical fibers. According to the net intra-cavity dispersion, the pulse-shaping process can be roughly distinguished into the four different regimes, such as soliton regime, stretch-pulse regime, parabolic-pulse regime, and giant-chirp pulse regime, corresponding to all-anomalous dispersion, normal-anomalous dispersion, all-normal dispersion, and large-normal dispersion, respectively. Due to the equilibrium between Kerr nonlinearity and GVD, pulses that propagate in all-anomalous dispersion laser cavity keep unchanged in the form of fundamental soliton [13, 14]. While in dispersion-managed laser cavities, the negative dispersion is compensated by positive dispersion and thus stretch pulse forms. When the net cavity dispersion is optimized to zero, significant variations on pulse duration could be observed [15, 16]. As pulse operates in the all-normal dispersion regime, where laser gain, self-phase modulation, and dispersion co-effect, spectral/temporal filtering effects force linear chirping in the pulse, so that similariton forms [17–19]. While in ultra-long laser cavity, giant-chirped oscillating can be realized with ultralow repetition rate but at high-pulse energy [20–23].

2.2. NPR mode locking at 1.03 μm

In this section, we designed a compact ultra-fast Yb-doped fiber laser with integrated optical components. By integrating wavelength division multiplexer and optical isolator with

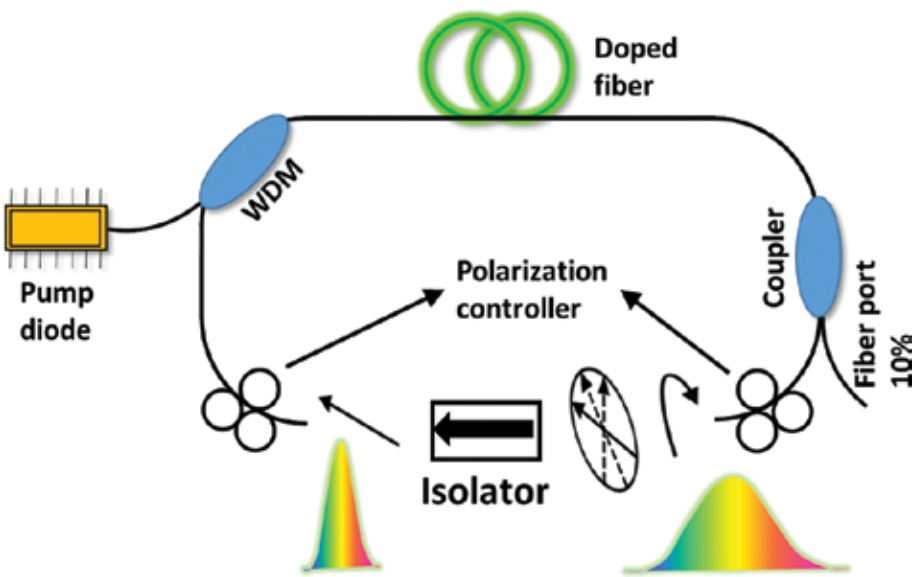

Figure 1. Schematic diagram of a passively mode-locked fiber laser via nonlinear polarization rotation mechanism.

collimators, the fiber loop was simplified. Self-started mode-locking could be realized by setting appropriate polarization angle of four intra-cavity wave plates. Due to the normal dispersion of fiber at 1.0 μm, transmission grating pair with 1250 l/mm was used to provide adjustable anomalous dispersion. As a result, 81-fs temporal duration with 65-MHz repetition rate and 0.5-nJ pulse energy was produced.

The mode-locking procedure can be explained in **Figure 1**. Two polarization controllers and a polarization-sensitive isolator (PSI) are used as the key elements for mode-locking. This combination acts as a virtual saturable absorber, which can absorb the low-intensity tail of pulse and transmit high-intensity part such that the pulse could be shortened. The pulse with linear polarization changes to elliptical polarization by twisting the polarization controller. As mentioned, self-phase modulation (SPM) or cross-phase modulation (XPM) can arouse energy coupling between two orthogonal polarizations. Moreover, serious nonlinear polarization rotation is produced by the high gain in the active fiber. Finally, another polarization controller is used to modify the polarization state to facilitate the central part of the pulse getting through the PSI [24].

In our experiment, a Yb-doped fiber laser shown in **Figure 2(a)** was firstly constructed without dispersion compensation elements. Three intra-cavity wave plates including two quarter-wave plates, QWP1 and QWP2, and one half-wave plate, HWP, were set with appropriate polarization angles to realize self-started mode-locking. The pigtails of fiber components are Hi1060 fiber with GVD of ~26 fs^2/mm and TOD of ~41 fs^3/mm, while the GVD for the active fiber is 39 fs^2/mm. The repetition rate and pulse duration were measured to be 70 MHz and 13 ps, respectively. By external-cavity dechirping, the pulse can be compressed to 170-fs duration, but with obvious pedestal. The autocorrelation of pulse before and after dechirping is shown in **Figure 3(a)** and **(b)**, respectively.

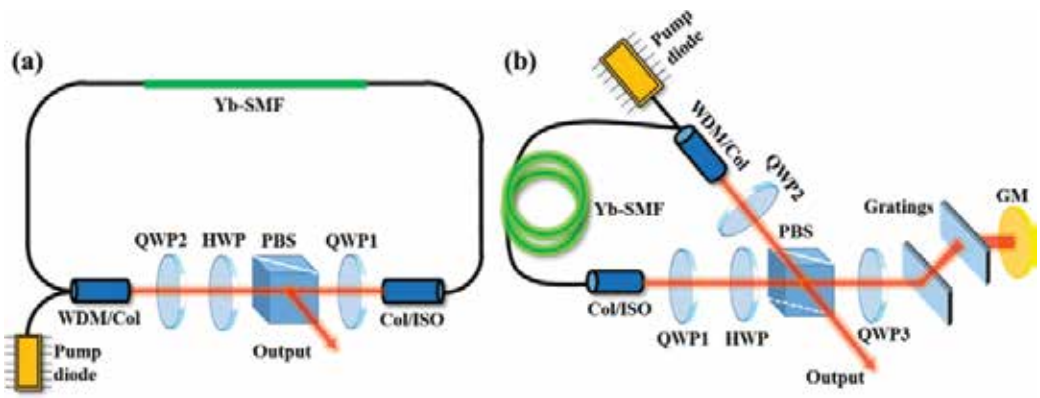

Figure 2. Structure of ultrafast Yb-doped fiber lasers without (a) and with (b) dispersion compensation. Pump diode: 400-mW laser diode at 976 nm; Yb-SMF: Yb-doped single-mode fiber; WDM/Col: the device combines WDM and collimator; Col/ISO: the device combines collimator and isolator; QWP1, QWP2, and QWP3: quarter-wave plate; HWP: half-wave plate; PBS: polarization beam splitter; GM: a gold-coated mirror.

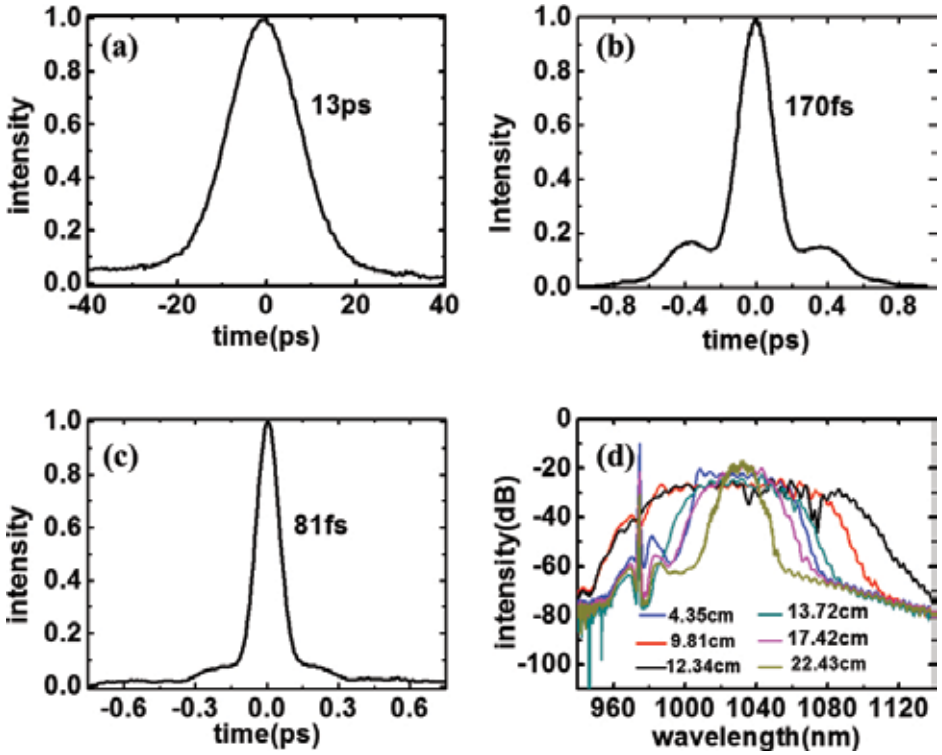

Figure 3. Autocorrelation trace of chirped pulses generated by picosecond fiber laser (a) and femtosecond fiber laser (c), (b) dechirped pulse of (a); (d) spectra generated by femtosecond fiber laser with different distances between gratings.

Secondly, a transmission grating pairs was used to manage the intra-cavity dispersion of the Yb-fiber laser, as shown in **Figure 2(b)**. The quarter-wave plate, QWP3, was used to impose 90° polarization rotation on laser pulses by double-passing the grating pairs. Soliton, stretch-pulse, and all-normal dispersion regime can be achieved by optimizing the distance between gratings. **Figure 3(d)** compares the various spectral shapes with different grating separations. As shown in **Figure 3(c)**, the shortest pulse duration was measured to be 81 fs. The black curve in **Figure 3(d)** represents the broadest spectra with a 10-dB bandwidth of 100 nm. The uncompensated phase was mainly caused by the accumulated high-order dispersion in fibers as well as intra- and extra-cavity grating pairs.

2.3. Polarization-maintaining figure-eight fiber laser at 1.55 μm

Compact size, low cost, and free maintenance fiber laser at 1.55 μm are desirable in many applications, such as eye surgery, Terahertz generation, and precision spectroscopy [25–28]. The standard repetition rate of commercial available fiber laser is typically 80 MHz with an optional design from 20 to 250 MHz. In order to combine both high pulse energy and high average power, a 10-MHz repetition rate is the best choice for applications. When the repetition

rate is lower than 10 MHz, a pulse picker has to be used between the laser oscillator and the succeeding amplifier.

In this section, we introduce a PM figure-eight laser cavity which is the best option for oscillator operated at 10-MHz repetition rate. **Figure 4(a)** shows the experimental setup of the figure-eight laser cavity. The linear loop comprises of a 980/1550 nm wavelength division multiplexer, a segment of Er-doped fiber (PM-ESF-7/125, Nufern), an isolator, a 2-nm bandpass filter at 1550 nm, and an output coupler CP2 with a splitting ratio of 20:80. The active gain applied in the linear loop is to compensate the cavity loses and facilitate self-started mode-locking. The band-pass filter is used to block longer wavelength (Raman self-frequency shift) and reduce the temporal width of the pulse to be self-consistent. Pulses from the linear loop are coupled into NALM via CP1 with a splitting ratio of 45:55.

Over-pump with three LDs was applied to provide enough power for self-started mode-locking. Interestingly, the buildup time of mode-locking was found to be closely related to the net cavity dispersion. When the net dispersion was set to −0.115 ps^2, as long as 8-min buildup time was observed. After optimizing the net dispersion to about −0.062 ps^2, the time dramatically decreased to ~ms of magnitude.

Furthermore, we recorded the mode-locked pulse trains triggered by a square wave with 5-Hz modulation frequency which is simultaneously used to drive LD3. **Figure 4(c)** shows two

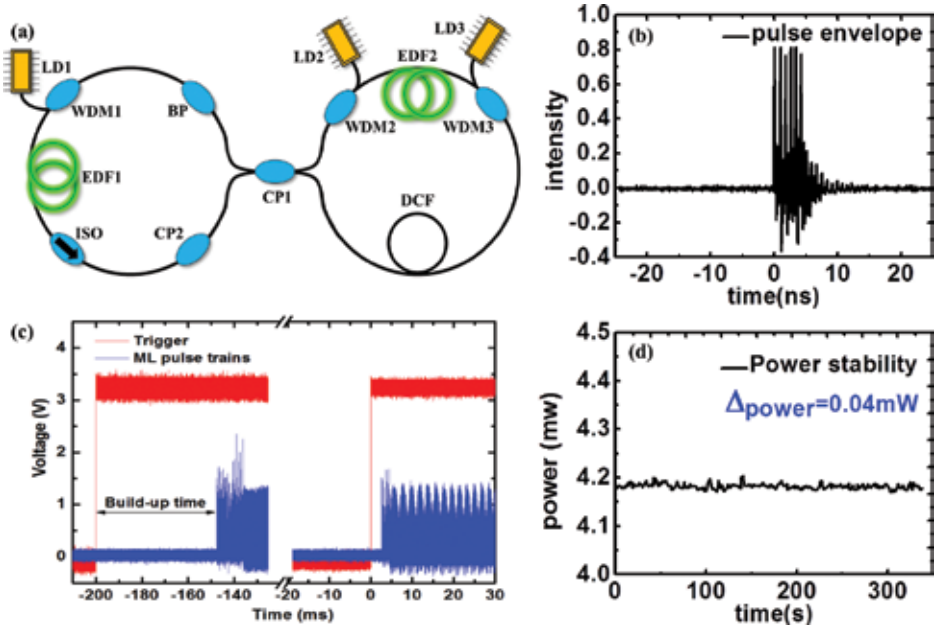

Figure 4. (a) Schematic of a polarization-maintaining figure-eight erbium-doped fiber laser. WDM1, WDM2, and WDM3: 980/1550 nm wavelength division multiplexers; ISO: isolator; EDF1 and EDF2: erbium-doped fiber; BP: 2-nm bandpass filter at 1550 nm; DCF: dispersion compensation fiber; CP1 and CP2: 1550 nm coupler with splitting ratio of 45:55 and 20:80. (b) The initial pulse that polarization-maintaining figure-eight erbium-doped fiber laser generated. (c) The buildup time measured by an oscilloscope. (d) The measurement of power stabilization once mode-locked.

adjacent periods with 50-ms pump duration, and the corresponding buildup time was measured to be 53 and 6 ms, respectively, exhibiting certain randomness. From experimental results point of view, the mode-locking buildup time is a random value in a certain range, which is related to the net cavity dispersion.

Interestingly, multiple-pulse operation was observed as the mode-locking is established, as shown in **Figure 4(b)**. Peak power clamping effect originating from sagnac mechanism resulted in the formation of pulse bunching [29]. Stable single pulse could be obtained by decreasing the pump power. In single-pulse regime, the 5-min power stability was measured to be 0.26%, as shown in the inset of **Figure 4(d)**.

3. Broadband supercontinuum

Recent years, supercontinuum generation (SC) has attracted much attention for its applications in optical coherence tomography, stimulated emission depletion microscopy, dense wavelength-division-multiplexing (DWDM) optical networks, and frequency comb generation [30–33]. In this section, several nonlinear optical effects such as SPM, XPM, four-wave mixing (FWM), and stimulated Roman scattering (SRS) that facilitate SC generation would be firstly discussed. Secondly, spectral filtering method is demonstrated to be an effective way for broadband supercontinuum generation in picosecond region [34]. By spectral filtering, a linear-chirped picosecond pulse with a 1-nm bandwidth filter installed between two Yb-doped single-mode preamplifiers, pulse shortening, and high peak power is achieved, so that an octave-spanning SC with bandwidth of 650 nm from 750 to 1400 nm and 10-dB peak-to-peak flatness was obtained at an output average power of 190 mW. Thirdly, SC covering from 950 to 2200 nm is generated in a 20-cm-long PM HNLF by injecting 72-fs pulse with 150-mW average power and 60-MHz repetition rate at 1.56 μm. Furthermore, an inline f-2f interferometer, including a PPLN for frequency doubling and a PM-fiber delay line, is used to generate carrier-envelop offset signal (f_{ceo}).

3.1. Nonlinear effects in optical fibers

Most of nonlinear effects in optical fibers attribute to nonlinear refraction, which refer to the intensity dependence of the refractive index. Especially, the lowest order nonlinear effects in optical fibers originate from the third-order susceptibility $\chi^{(3)}$, which governs the four-wave mixing, Raman effect, third-harmonic generation, and polarization properties [24].

This section does not thoroughly focus on the discussion of theoretical issues. In simple, the refractive index of the optical fiber can be described by the following equation

$$n = n_0 + n_1 \left| E(t) \right|^2 \tag{1}$$

where n_0 is the linear part and $n_1 | E(t) |^2$ is the nonlinear part.

An interesting phenomenon of the intensity dependence of the refractive index change in optical fiber occurs through SPM. When the input pulse is of low intensity, the corresponding refractive index remains a constant n_0. As the input pulse increases, the corresponding refractive index becomes nonlinear change with power intensity I. Hence, an additional phase shift is produced:

$$\delta\varphi(t) \propto |E(t)|^2 \tag{2}$$

This can be understood as an instantaneous optical frequency change from its central frequency:

$$\delta\omega(t) = -\frac{\partial}{\partial t}\delta\varphi(t) \tag{3}$$

Therefore, new spectral components are generated and time dependent frequency chirping is produced.

Another most widely studied nonlinear effect is XPM, which leads to asymmetric spectral and temporal changes for two co-propagating optical fields with different wavelength or orthogonally polarization. The contribution of the nonlinear phase shift induced by XPM is twice that of SPM. Therefore, the nonlinear part Δn_j induced by the third-order nonlinear effects is given by (j = 1, 2)

$$\Delta n_j \approx n_2\left(|E_j|^2 + 2|E_{3-j}|^2\right) \tag{4}$$

Eq. (4) shows the refractive index of the optical media seen by an optical field inside a single-mode fiber depends not only on the intensity of that field but also on the intensity of the other co-propagating fields [35]. As the optical field propagates inside the fiber, an intensity-dependent nonlinear phase shift shows up

$$\phi_j^{NL}(z) = n_2(\omega_j / c)\left(|E_j|^2 + 2|E_{3-j}|^2\right)z \tag{5}$$

The first term is related to SPM while the second term is related to XPM.

Stimulated Raman scattering (SRS) is an important nonlinear process that can produce red-shifted spectral components. Once the spectrum of the input pulse is broad enough, the Raman gain can amplify the long-wavelength components of the pulse with the short-wavelength components acting as pumps, and the energy appears red-shifted. The longer the propagating fiber, the more red-shifted spectral components can be generated. The red-shifted components are called Stokes wave. The initial growth of the Stokes wave can be described by

$$\frac{dI_s}{dz} = g_R I_p I_s \tag{6}$$

where I_s is the Stokes wave intensity, I_p is the pump-wave intensity, and g_R is the Raman-gain coefficient, which is related to the cross section of spontaneous Raman scattering.

The Raman-gain coefficient g_R (Ω) is the most important factor to describe SRS. Ω represents the frequency difference between the pump wave ω_p and Stokes wave ω_s. In the case of silica fibers, the Raman-gain spectrum is found to be very broad, extending up to approximately 40 THz. Assuming the pump wavelength is 1.5 μm and, peak gain is $g_R = 6 \times 10^{-14}$ m/W, the frequency downshift can be calculated to be 13.2 THz.

When supercontinuum is generating in an optical fiber, the SPM, XPM, and SRS are always accompanied by FWM. In optical fibers, FWM transfers energy from pump wave (ω_p) to two other waves in frequency domain, blue-shifted (anti-Stokes wave, ω_{as}) and red-shifted (Stokes wave, ω_s). Once the phase-matching condition $\Delta k = 2k(\omega_p) - k(\omega_s) - k(\omega_{as}) = 0$ is satisfied, the Stokes and anti-Stokes waves can be amplified from noise or an incident signal at ω_s or ω_{as}, respectively [36, 37]. Therefore, FWM process is used to produce spectral sidebands for supercontinuum generation.

3.2. Supercontinuum generation

SC is a powerful laser sources for many applications, such as nonlinear microscopy, optical coherence tomography, and frequency metrology [38–40]. Nowadays, more than one octave SC can be easily generated with a length of PCF, and the average power can reach tens of Watts [41, 42]. When ultrashort optical pulses propagate through a PCF fiber, the combination of SPM, XPM, SRS, and FWM is responsible for the spectral broadening. Generally speaking, the feature of SC depends on whether the incident laser wavelength λ located is below, closed to, or above the Zero-dispersion wavelength λ_D of the PCF. In the anomalous-dispersion regime ($\lambda > \lambda_D$) where $\beta_2 < 0$, soliton affects. If the λ nearly coincides with λ_D, $\beta_2 \approx 0$, β_3 dominant and the phase-matching condition of FWM are approximately satisfied. While in the normal-dispersion regime, $\beta_2 > 0$, GVD and SPM effects dominant SC generation. From the time domain of view, SPM and soliton effects dominant SC generation for femtosecond (typically <1 ps) pump pulses, while FWM and SRS contribute to spectral broadening for tens of picoseconds pulses.

3.2.1. Spectrally filtered seed for broadband supercontinuum generation in single-mode fiber amplifiers

There are several methods to extend the SC spectrum. Considerable spectral broadening could be observed with high-power incident laser. High-average/high-peak powers facilitate CW and pulse SC generation [43–45]. Besides, the SC bandwidth could also be increased by tapering PCFs. A flat (3 dB) spectrum from 395 to 850 nm was achieved in a tapered fiber with a continuously decreasing ZDW [46]. In this section, we demonstrate an effective method for broadband SC generation, which is valid in normal-dispersion fiber amplifiers. By spectral filtering of upchirped pulse at 1028 nm with 1-nm bandpass filter, as broad as 650-nm

bandwidth from 750 to 1400 nm within 10-dB peak-to-peak flatness is obtained with an output power of 190 mW.

The experimental setup is shown in **Figure 5(a)**. The SC laser source is consisted of a picosecond mode-locked laser oscillator, a spectral filter, two-stage single-mode amplifiers, and 2-m-long PCF with ZDW at 1.02 μm. The laser oscillator operated in an all-normal-dispersion regime with repetition rate of 20 MHz. With 100 mW pumping power, 25 mW average output power laser is exported from the 30% port of the coupler. The pulse duration of highly up-chirped pulse was measured to be 10 ps.

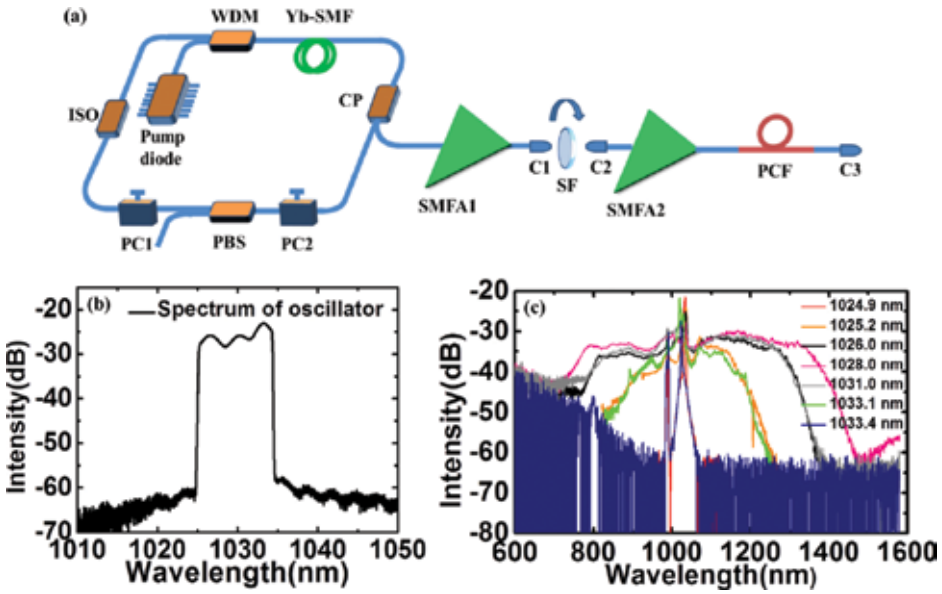

Figure 5. (a) Experimental setup for SC generation. Pump diode: 400 mW laser diode at 976 nm; WDM: 980/1040 nm wavelength division multiplexer; Yb-SMF: ytterbium-doped single-mode fiber; CP: 30:70 coupler; PC1 and PC2: polarization controller; PBS: polarization beam splitter; ISO: isolator; SMFA1 and SMFA2: single-mode fiber amplifiers; C1, C2, and C3: three collimators; SF: spectral filter; PCF: photonics crystal fiber. (b) The output spectrum of the laser oscillator. (c) SC with different filtering windows.

A bandpass spectral filter with 1-nm bandwidth at 1036 nm is installed between two single-mode fiber amplifiers. The transparent wavelength of the filter could be tuned from 1024 to 1036 nm by varying the incident deflection angle. For the large up-chirp with 10-nm spectral width (see **Figure 5(b)**) and 10-ps temporal duration, corresponding to a time-bandwidth product of 28.3, pulse can be greatly shortened by the filter. The shortest pulse duration of 2.9 ps was obtained with filtering window at 1028 nm. After the second-stage amplifier, the laser pulses could be amplified to an average power up to 190 mW with 400 mW pumping power.

A 2-m length of silica-based PCF with ZDW at 1024 nm is directly spliced to the fiber end of SMFA2. **Figure 5(c)** shows the output spectrum with different filtering window. The spectra

keep unchanged when the filtering window is at the shoulder of the spectrum, shown as the red curve (1024.9 nm) and blue curve (1033.4 nm) in **Figure 5(c)**. When filtering window is located at the central wavelength of 1028 nm, the 10-dB bandwidth of SC is extended to 650 nm (from 750 to 1400 nm), shown as the pink curve in **Figure 5(c)**. Besides, filtering windows above or below the central wavelength produce a less broad SC.

3.2.2. One octave supercontinuum for frequency comb generation

Broadband supercontinuum of bandwidth up to 1250 nm can also be provided by HNLFs with spectral-tailored femtosecond pump pulses produced by erbium-doped power amplifiers. The schematic diagram of the experiment is shown in **Figure 6(a)**.

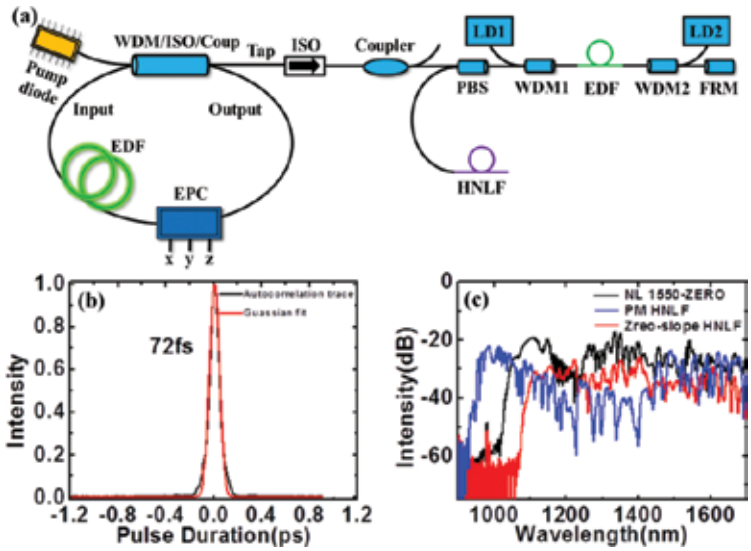

Figure 6. (a) Schematic diagram for SC generation. Pump diode: 400-mW pump at 976 nm; WDM/ISO/Coup: the device combines wavelength division multiplexer, isolator, and coupler; EDF: erbium-doped fiber; EPC: electric polarization controller; ISO: isolator; coupler: 30:70 polarization-maintaining coupler; PBS: polarization beam splitter; HNLF: high nonlinear fiber; LD1 and LD2: pumps at 976 nm; WDM1 and WDM2: 980/1550 nm wavelength division multiplexer; FRM: Faraday rotation mirror. (b) Autocorrelation trace of chirped pulses poured into HNLFs. (c) SC generated by different kinds of HNLFs on logarithmic coordinate.

The laser system consisted of an erbium-doped mode-locking fiber oscillator, a single-mode fiber amplifier (SMFA), and 20-cm-long PM-HNLF. To improve the mode-locking stability, an electric polarization controller (EPC) is utilized to replace the conventional mechanical polarization controller such that automatic and active control of mode-locking is accessible. By applying the voltage on three axes (x, y, and z) of EPC, accurate control of the temporal duration, spectral shape, f_{rep}, and f_{ceo} can be achieved [47, 48].

With the help of a PBS and a FRM, a dual-pass single-mode fiber amplifier with bidirectional pump configuration was used to boost the laser average power to more than 150 mW average power and reduce the environmental disturbance on SMFA. The pulse duration at the output

port was measured to be 2.84 ps. Additional PM-1550 fiber was used to dechirp the pre-amplified pulse to 72 fs (shown in **Figure 6(b)**). Therefore, considering a repetition rate of 60 MHz, the pulse peak power achieved as high as 34.7 kW. Three types of HNLFs, such as NL 1550-ZERO, PM-HNLF, and Zero-slope HNLF, were applied to generate the supercontinuum by splicing the HNLFs to the dechirping fiber directly.

As shown in **Figure 6(c)**, 20-cm-long PM-HNLF with nonlinearity of 10.5 W^{-1} km^{-1} achieved the broadest spectrum, covering from 950 to 2200 nm, which is sufficient broad to produce f_{ceo} signal. The HNLF type should be taken into consideration as it influences the SC generation. We used three kinds of HNLFs: 25-cm-long NL 1550-ZERO with nonlinear coefficient of 10.4-W^{-1} km^{-1} and effective mode area of 13-μm^2, 20-cm-long PM-HNLF with nonlinear coefficient of 10.5-W^{-1} km^{-1} and effective mode area of 12.7-μm^2, 25-cm-long Zero-slope HNLF with nonlinear coefficient of 10.8-W^{-1} km^{-1} and effective mode area of 12.4-μm^2, and the corresponding SC was depicted in **Figure 6(c)**. Obviously, PM-HNLF produces broader spectrum than other two HNLFs.

As shown in **Figure 7**, a collinear setup was established for the detection of f_{ceo} signal. The SC generated by 20-cm-long PM-HNLF was coupled into free space via a lens (L1) with adjustable focal length. An inline f-2f interferometer, including a PPLN, several wave plates and lens, and a PM-fiber delay line, is used to produce the temporal overlapped components at 1.0 μm. The long-wavelength component of SC at 2092 nm was frequency doubled to match with the short-wavelength component at 1046 nm. After the PPLN, two lenses, L3 and L4, were used to couple the two components at 1046 nm back to PM-980 fiber. A half-wave plate, HWP2, is used to adjust the energy ratio on the fast and slow axes of PM-980 fiber. The pulse transmitted along the slow axis experiences a delay relative to the pulse on fast axis. With an optimized fiber length of 3.4 m, the differential delay between the fast and slow axes could be fully compensated [49]. Subsequently, a half-wave plate, HWP3, as well as a PBS were used to selected pulses to generate f_{ceo} signal on APD. Finally, with 28-dB signal-to-noise ratio was generated by using this setup.

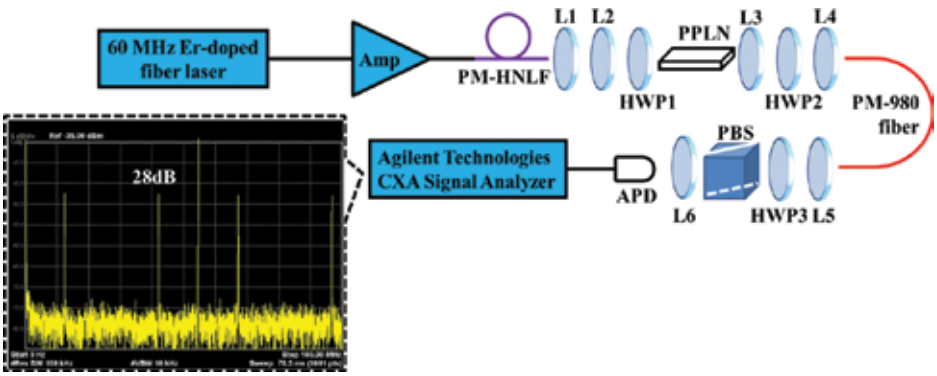

Figure 7. Setup for f_{ceo} detection. Amp: fiber amplifier; L1, L4, and L5: optical lens with adjustable focal length; L2, L3, and L6: optical lens with focal length of 50 mm; HWP1, HWP2, and HWP3: half-wave plates; PPLN: periodically poled lithium niobate; PBS: polarization beam splitter; APD: avalanche photodiode.

4. Nonlinear fiber amplifier

With the increasing applications in frequency metrology, THz generation, and in cataract surgery, the development for high-energy transform-limited pulse generation around 1.55 μm is still a fascinating area [50–53]. Owing to the limited available output power from laser oscillator, erbium-doped fiber amplifiers (EDFAs) are commonly used. Nevertheless, high-power amplification in EDFA is inevitably accompanied by several unwanted effects, such as SRS and amplified spontaneous emission (ASE), which would significantly deteriorate the temporal and spectral duration of pulse [54]. Chirped-pulse amplification (CPA) provides an effective way to decrease pulse peak power and avoid the nonlinearity in optical fibers [55–58]. In CPA, strong stretching and compression occurs to extract more energy and avoid nonlinear distortion as well as damage. However, CPA is inevitably accompanied by the gain-narrowing effect and therefore hardly produces pulse with temporal duration less than 400 fs [59].

Even though CPA has many advantages over the other techniques in amplifying pulses around 1.55 μm, ~100-fs pulse duration with above 10-nJ pulse energy is still a challenge because of the spectral gain-narrowing effects and nonlinear phase accumulation. Moreover, due to the involvement of bulk media, CPA is not suited for applications that require compact size and alignment-free laser source. A recent developed technique, divided-pulse amplification (DPA), opens up a new way for high-power laser pulse amplification [60–62]. In the configuration of DPA, the initial pulse is divided into a sequence of lower-intensity pulse with orthogonal polarization for successive replicas, and subsequently, the low-energy pulse is amplified and then recombined to create a high-energy pulse [61, 63].

In this section, we mainly focus on DPA at 1.56 μm where pulse amplification and compression can be simultaneous carried out so that a separate compressor is no longer necessary. The

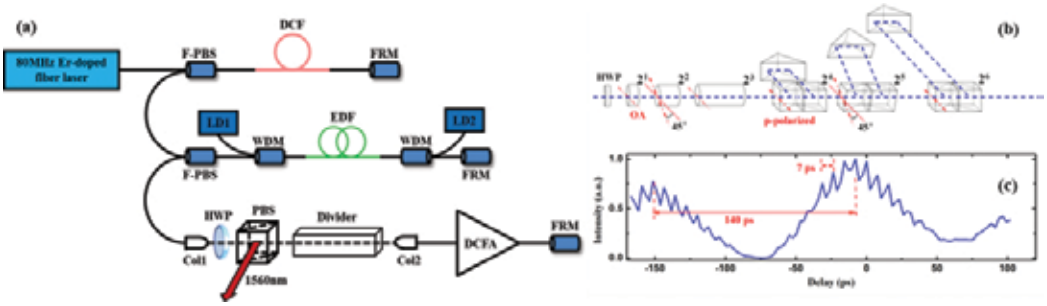

Figure 8. (a) Schematic diagram for laser system. F-PBS: fiber-coupled polarization beam splitter; DCF: dispersion compensation fiber; FRM: Faraday rotation mirror; LD1, LD2: pump diodes at 976 nm; WDM: wavelength division multiplexer; EDF: erbium-doped single-mode fiber; Col1, Col2: high-power collimators; HWP: half-wave plate; PBS: polarization beam splitter cube; DCFA: double-clad fiber amplifier. (b) Schematic of the pulse divider. The left-hand three cylinders (21, 22, and 23) represent YVO4-based dividers with given direction of crystal optical axes (OAs) shown as the red dash dot lines. The right-hand three parts (24, 25, and 26) represent PBS-based dividers with p-polarized direction shown as red dash dot lines. The red dot lines represent the horizontal plane, which is the same direction as the OA of 21 and 23 and the p-polarized direction of 24 and 26. (c) The measured autocorrelation trace of the divided replicas.

schematic diagram of DPA is shown in **Figure 8(a)**. The experimental setup is composed of a mode-locked fiber laser, a fiber stretcher, a single-mode fiber amplifier for preamplifying, and a pulse-divider as well as a double-clad fiber amplifier for main amplification. The Er-doped fiber laser with 80-MHz repetition rate shared the same configuration as **Figure 6(a)**, which takes the advantage of EPC to actively control the mode-locking. A photodiode and an electric loop were applied to monitor and feedback control the EPC for long-term stable operation. The fiber oscillator consisted of 1.74-m SMF28-e fiber with dispersion parameter of 19 ps/nm/km and 0.82-m Er-doped fiber with dispersion parameter of −51 ps/nm/km. There, the laser operated in the stretched-pulse regime and produced positively chirped pulses. As a result, with 200-mW pumping power at 976 nm, the laser oscillator produces 5-mW output average power with 1.5-ps pulse duration and 28-nm spectral bandwidth, corresponding to a time-bandwidth product of 5.2.

A fiber stretcher is spliced to the output of the fiber oscillator to stretch laser pulse and control the quantity of frequency up-chirp. However, over-long fiber could inevitably introduce too much high-order dispersion which is hardly compensated by the pulse-compressing stage. For the current configuration, a double-pass fiber stretcher consisting of a fiber-coupled PBS with PM fiber at input/output port and non-PM fiber at common port, a segment of non-PM dispersion compensation fiber with 6.0-μm-mode field diameter and −38 ps/nm/km dispersion at 1550 nm, and a FRM is used to reduce the environmental perturbation.

In our experiment, 6-m dispersion compensation fiber was applied to stretch pulses from the fiber oscillator. A dual-pass bidirectionally pumped single-mode fiber preamplifier was used to boost the average power to more than 100 mW to ensure efficient operation of the subsequent amplifiers. A FRM reflected the incident pulse to suppress ASE noise and rotated the polarization of the pulses by 90° to cancel all birefringence effects in the dual-pass amplifier. A fiber-based polarization beam splitter (F-PBS) was used to couple the seed laser to the preamplifier and reflected preamplified pulses to subsequent components. The output characters of the preamplifier were shown as the blue curves in **Figure 9(a)** and **(b)**. The FWHM temporal duration and spectrum bandwidth of the preamplified pulses is 4 ps and 15 nm, respectively, generating a time-bandwidth product of 7.4. Dramatic decrease in spectral bandwidth was

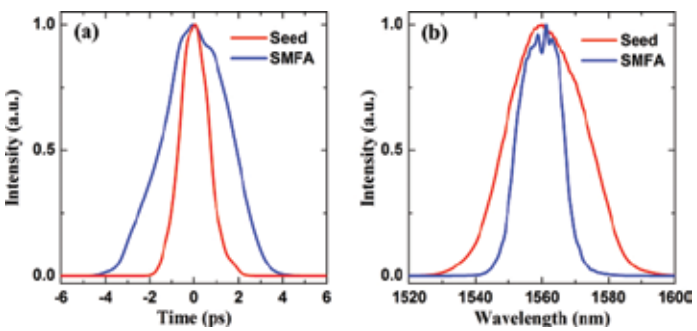

Figure 9. The temporal duration (a) and spectral bandwidth (b) of laser pulses from laser oscillator (red curves) and SMFA (blue curves).

observed due to the limited transmission bandwidth of WDM and FRM as well as spectral-narrowing effect in fiber amplifier.

Then, the concept of DPA was carried out to boost the laser to Watt-level average power. The preamplified laser is coupled into free space by collimator C1 and rotated to horizontal polarization to reach maximum transmission on PBS. The pulse division and combination were achieved by applying cascaded YVO_4-based and PBS-based dividers with the help of a FRM to reflect the replicas passing through the same divider but in the opposite direction. Each divider (YVO_4-based or PBS-based) can divide a single pulse into two cross-polarized replicas; hence, a single seed pulse could be temporally divided into 2^N (where N is the stage number of the divider) replicas. Ideally, each replica has identical pulse energy after division. As depicted in **Figure 8(b)**, three YVO_4 crystals with lengths of 10, 20, and 40 mm divided the initial pulse into $N = 8$ replicas. A half-wave plate (HWP) was used to produce the desired polarization of input pulses. The first (2^1) and third (2^3) YVO_4 crystals had their crystal optical axes (OA) oriented in the same direction as the horizontal plane, while the OA of the second (2^2) YVO_4 crystal oriented at a 45° angle to the horizontal plane. The polarization-mode delay between ordinary and extraordinary waves in YVO_4 is 0.7 ps/mm at 1560 nm. The shortest crystal length for our system was chosen to split the input pulse into replicas with 7 ps separation, about twice of the seed pulse duration.

To mitigate the nonlinearity in main amplifier, the string of pulse ($N = 8$) was further divided by three PBS-based dividers, resulting in a final pulse number of 64. For PBS-based divider, each incoming pulse was divided into an s-polarized beam and a p-polarized beam. All p-polarized components were directly transmitted the PBS, while the s-polarized components were reflected to the folded delay line. For the sake of simplicity, the second PBS-based divider (2^5) had its p-polarized direction oriented 45° to the direction of the horizontal plane, while the first (2^4) and third (2^6) PBS-based oriented in the same direction as the horizontal plane, such that separate half-wave plates were no longer necessary.

Owing to the delay length of 10, 20, 40, 26.8, 53.6, and 107.2 mm, the 2^1, 2^2, 2^3, 2^4, 2^5, and 2^6 stages approximately provided time delay of 7, 14, 28, 130, 260, and 520 ps, respectively. **Figure 8(c)** shows the measured autocorrelation trace of the pulse string which matches well with the designed time delays. The 7-ps interval between adjacent peaks in the same envelope was consistent with the expected time delay with 10-mm increment length of YVO_4, and the ~140-ps spacing between two adjacent envelopes was consistent with the expected time delay introduced by the PBS-based divider.

Intuitively, for simultaneous pulse amplification and compression in EDFAs, a positively pre-chirping seed pulse is desired. Numerical simulations show that there exists an equilibrium position that can not only restrict excessive nonlinear effects to ensure high-quality temporal integrity but also produce sufficient optical nonlinearity to broaden the spectrum around the wavelength of 1.55 μm. The generalized nonlinear Schrödinger equation (7) with the split-step Fourier method was used to carry out the simulation [24].

$$\frac{\partial A}{\partial z} = \frac{\alpha}{2}A + \sum_{n\geq 2}\frac{i^{n+1}}{n!}\beta_n\frac{\partial^n A}{\partial T^n} + i\gamma A\int_{-\infty}^{\infty} R(T')\left|A(z,T-T')\right|^2 dT' \tag{7}$$

where $A = A(z, t)$ is the complex amplitude of the pulse envelope of pulses, α is the laser gain coefficient, β_n is the dispersion parameter at ω_0 (1560 nm), and γ (3 W^{-1} km^{-1}) is the nonlinear coefficient. The right-hand side of Eq. (7) models laser gain, dispersion, and nonlinearity. Pulse of 2.5-ps temporal duration and 19.9-nm spectral width (corresponding to 0.16 ps^2 prechirping on 180-fs transform-limited pulse) and a pulse energy of 0.05 nJ were applied in the simulation.

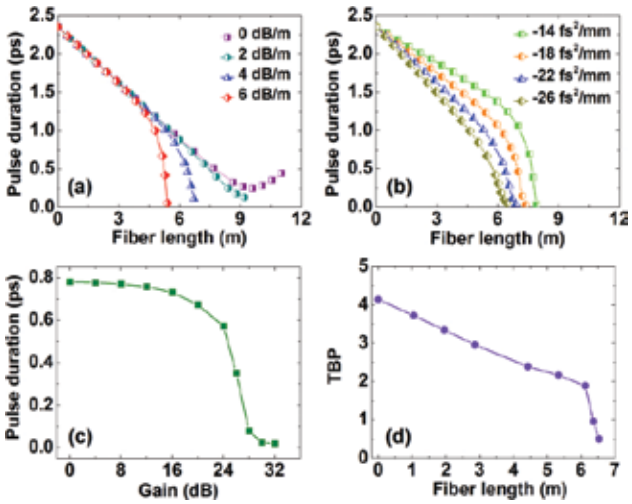

Figure 10. Amplified output pulse duration versus propagation length for the cases of different α (a) and β_2 (b). (c) Pulse duration versus the total gain provided by 6.5-m fiber. (d) Time-bandwidth product at different position of gain fiber.

The interplay of the SPM and group-velocity dispersion (GVD) as well as laser gain can lead to a qualitatively different behavior compared with that expected from them alone. SPM broadened the spectrum with increase in pulse energy, and simultaneously, the anomalous dispersion of the fiber compressed the new spectral components resulting in temporal shortening. **Figure 10(a)** compares the simulation results with different α but a fixed β_2 (−22 fs^2/mm). It is clear that pulse compression operates in linear regime when the laser gain is low, then it enters in nonlinear regime when the laser gain gradually increased. The shortest transform-limited pulse duration decreased from 180 fs at 7.0 m (α = 0 dB/m) to 60 fs at 4.3 m (α = 3 dB/m). **Figure 10(b)** compares the pulse compression with different β_2 but a fixed α (3 dB/m). The maximum pulse energies with respect to fiber length of 4.65, 5.07, and 5.53 m reached 1.24, 1.66, and 2.28 nJ, respectively. Therefore, higher α and smaller $|\beta_2|$ are benefit to overcome spectral bandwidth limitation for high-energy pulse amplification. For reference, the blue curves in **Figure 10(a)** and **(b)** present pulse evolution with the same parameters.

Next, we focus on pulse amplification and compression in a fixed fiber length by way of guiding the subsequent experiment. About 5.0-m-long fiber with $\beta_2 = -22$ fs^2/mm was introduced to simulate the output pulse duration and the time-bandwidth product (TBP) at different position along the fiber. As shown in **Figure 10(c)**, when the total gain is smaller than 16 dB, the output pulse duration deceases linearly owing to the GVD and insufficient nonlinearity. As the total gain is greater than 24 dB, the output pulse duration dramatically decreases owing to strong nonlinear compression. Theoretically, pulse as short as 80-fs duration can be achieved with a total gain of nearly 28 dB. Although the pulse duration could be further decreased to 20 fs with 32-dB gain, considerable pedestal as well as wave breaking appears due to excessive nonlinearity. Meanwhile, the TBP of the pulse along the fiber gradually decreases from 4.1 at the input port to 0.5 at the output port.

Experimentally, the divider first operated with ×8 replicas. A dual-pass double-cladding fiber amplifier (DCFA) was used to boost the divided pulses. The DCFA consisted of 1.2-m 12/130 Er-doped double-clad fiber and 2.5-m SMF fiber. With a pump power of 4.3 W at 976 nm, the DCFA delivered 600 mW output power at 1560 nm, as measured at PBS output port. Along the first pass of DCFA, pulse evolution worked in the near-linear regime. Subsequently, as the pulse reflected by the FRM and passed through DCFA again, SPM and anomalous dispersion brought the pulse amplification into the moderate nonlinearity regime. **Figure 11(a)** and **(b)** shows pulse duration and spectral bandwidth of the combined pulse measured by an FROG (15-100-USB, Swamp Optics). The linear spectral phase indicates a nearly transform-limited pulse with the FWHM duration of 97 fs if a Gaussian pulse shape is assumed. The output power limitation was resulted from splicing losses of different type fibers and the insertion loss of FRM.

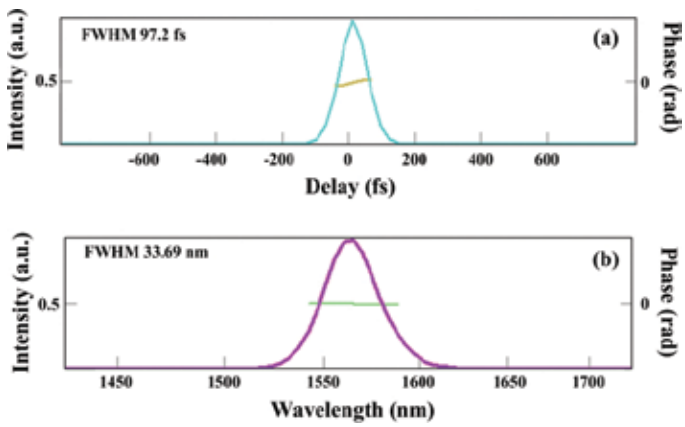

Figure 11. The measured pulse duration (a) and spectral width (b) of pulses from the nonlinear fiber amplifier.

Furthermore, a PPLN with 20.9-μm poling period and 0.3-mm length was used for frequency-doubling the amplified laser and checking the available peak power at 1560 nm. A pair of lens was used to focus and collimate the input and output beam on the PPLN, respectively. The output average power at 1560 nm and the corresponding SHG is shown in **Figure 12**. The

highest SHG conversion efficiency was obtained as 56.3% with 302 mW incident power at 1560 nm. Further increasing the power at 1560 nm induced decay of conversion efficiency, shown as the black squares in **Figure 12**.

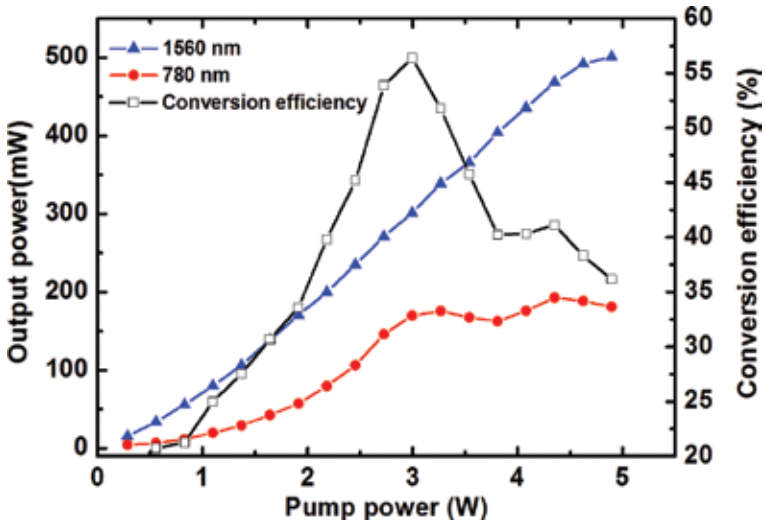

Figure 12. The output average power of 1560 nm (blue triangles) and 780 nm (red circles), and the SHG conversion efficiency.

To extract more energy from the double-pass amplifier, we will increase the number of the replicas from 8 to 16 and 32. The results for ×16 and ×32 replicas are still under investigation.

In conclusion, a divided fiber laser fiber amplifier delivering 500 mW average power at 1560 nm by the interplay between divided prechirped pulse amplification and nonlinear pulse compression. A small core double-clad erbium-doped fiber with anomalous dispersion carries out the pulse amplification and simultaneously compresses the laser pulses such that a separate compressor is no longer necessary. A numeric simulation reveals the existence of an optimum fiber length for producing a transform-limited pulse. Furthermore, frequency doubling to 780 nm with 170-mW average power is realized by using a PPLN at room temperature.

5. Repetition rate stabilization

Fiber-based frequency comb is recognized as the key breakthrough in the field of optics for it brings high accuracy in frequency domain as well as low jitter in time domain [49, 64–67]. Principally, as a frequency comb, two RF frequencies, f_{ceo} and f_{rep}, are required to be stabilized to external references. Therefore, the optical frequencies can be written as $\nu = m \times f_{rep} + f_{ceo}$, where m is a large integer of order 10^6 that indexes the comb line. Nevertheless, recent developments in adaptive dual-comb spectroscopy successfully employed free-running mode-locked lasers where the f_{ceo} instabilities could be compensated by data acquisition and

electronic signal processing [68, 69]. Therefore, high accuracy f_{rep} stabilization of passively ML lasers is of great importance.

The relatively mature method for f_{rep} locking is to use a piezoelectric ceramic transducer (PZT) to control the geometrical length L of the laser cavity, and the best locking accuracy is in the range of ±0.5 mHz with the corresponding SD of 220 μHz [70]. However, the PZT-based stabilization encounters many limitations, such as significant positioning errors, hysteresis effect, bulky-design, and the need for time-consuming alignment.

In this section, we focus on the f_{rep} stabilization by using optical pumping scheme which can be achieved via resonantly enhanced optical nonlinearity or so-called pump-induced refractive index change (RIC) in doped fibers. In optical pumping scheme, the f_{rep} is stabilized by modulating the refractive index n, while keeping the geometrical cavity length L fixed. In the past, this method has been successfully applied in fiber switch where a low pump power and a short length doped fiber are sufficient for the switching [71]. Moreover, the validity of this concept has also been achieved in coherent combining and adaptive interferometry [72]. In 2013, Rieger et al. reported all-optical stabilized repetition rate by using the RIC-based method. With the help of thermos-electric element, over 12-h long-term stabilization was achieved in an NPE-mode-locked Er-doped fiber laser, while the SD of repetition rate drift was measured

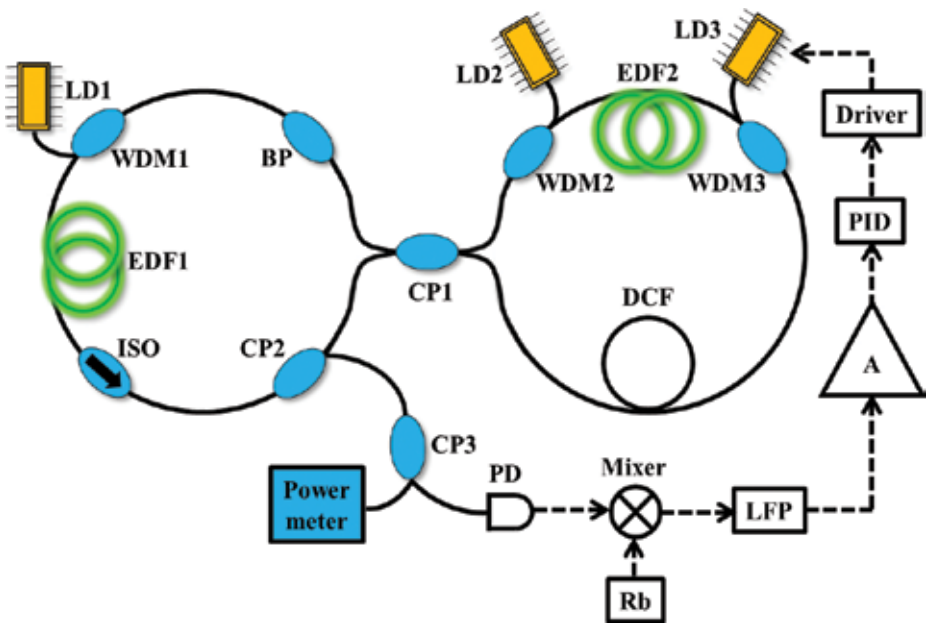

Figure 13. Experimental setup. LD1, LD2, and LD3: pump diodes at 976 nm; WDM1, WDM2, and WDM3: 980/1550 nm wavelength division multiplexers; EDF1, EDF2: erbium-doped fiber; BP: 2-nm bandpass filter centered at 1550 nm; CP1, CP2, and CP3: 1550 nm couplers with splitting ratio of 45:55, 30:70, and 50:50, respectively; DCF: dispersion compensation fiber; PD: photodiode detector; Rb: Rubidium clock; LFP: low-pass filter; A: electronic amplifier; PID: proportional–integral–derivative controller; Driver: precision current source.

to be 22 mHz. A recent experiment extends this concept to Yb-fiber laser and achieves 1.39-mHz SD of residual fluctuation in an hour measurement [73].

As reported in Ref. [74], a commercial available pump current supply can provide a minimum resolution of pump power as 1.5 μW and thus achieve a controlling accuracy of 0.05 Hz, which is more than two orders of magnitude than PZT-based method. Therefore, an interesting experiment worth to do is to use RIC-method to achieve high-precision f_{rep} stabilization. So far, the RIC method has been fully investigated in NPR mode-locked lasers, which applied non-PM fibers and components [73–75], and the locking accuracy limited to ~mHz. Considering the environmental perturbation on non-PM fiber, a straightforward idea is to implement RIC method in a PM fiber laser. Therefore, the following part will discuss high-precision repetition rate stabilization by using RIC method in a PM figure-eight laser cavity.

The laser setup shown in **Figure 13** is same as **Figure 4(a)**, except the net dispersion of laser cavity. In the current experiment setup for all-optical repetition stabilization, a 56-cm-long Er^{3+}-doped fiber (EDF2) is spliced asymmetrically in the NALM to act as a frequency controller, while the LD3, which is controlled by the error signal from frequency mixer, provides the feedback modulating pump power via WDM3 on EDF2. Besides, a segment of DCF38 is used to compensate the anomalous dispersion of PM1550 fiber. The dispersion of linear loop and the NALM was estimated numerically to be −0.208 and 0.025 ps^2, producing −0.183 ps^2 net dispersion for the whole cavity. Self-started mode-locking in multiple-pulse regime can be achieved by over-pumping method, and stable single-pulse operation can be obtained by decreasing the pump power of LD1 and LD2. At fundamental repetition rate of 11.9 MHz, the figure-eight laser cavity delivers 1.5-mW average power via CP2.

The repetition rate was detected by PD3 and successively compared with standard reference (Rb clock) in a frequency mixer to produce the error signal. Subsequently, the error signal was filtered and amplified by low-noise voltage preamplifier with frequency cutoff at 1 MHz and a maximum voltage gain of 5×10^4 and further processed by a proportional-integral-derivative (PID) controller.

The long-term stabilization was depicted in **Figure 14**. As low as 27-μHz accuracy is achieved within 16-h measurement. The inset of **Figure 14** magnifies the measured dates from 30,000 to 31,000 s and shows fluctuation range within ±0.1 mHz. Typically, thermal effect, Kerr nonlinear effect, pump-induced nonlinear effect, and random acoustic perturbations contribute to the precision of f_{rep} stabilization. For our experiment, a temperature-controlled incubator with a ripple of 0.2°C was used to take the laser cavity to isolate environmental perturbation. As for Kerr-nonlinearity, the RIC is proportional to the traveling power of resonant laser. Assuming 5-mW traveling power in NALM, the Kerr-induced RIC is estimated as 1.2×10^{-7}/mW, having the same order of magnitude of the pump-induced RIC (2.1×10^{-7}/mW). However, when the pump power of LD3 increased from 30 to 205 mW, only 1.6% of output power change was observed, which means little change on the dynamic process of pulse evolution in NALM. Thus, the Kerr-induced RIC is near ~1% of the RIC by pump-induced nonlinearity. Therefore, we postulate that the nonlinearity on the RIC of fibers owes to pump-induced nonlinear effect and thermal effect rather than Kerr effect.

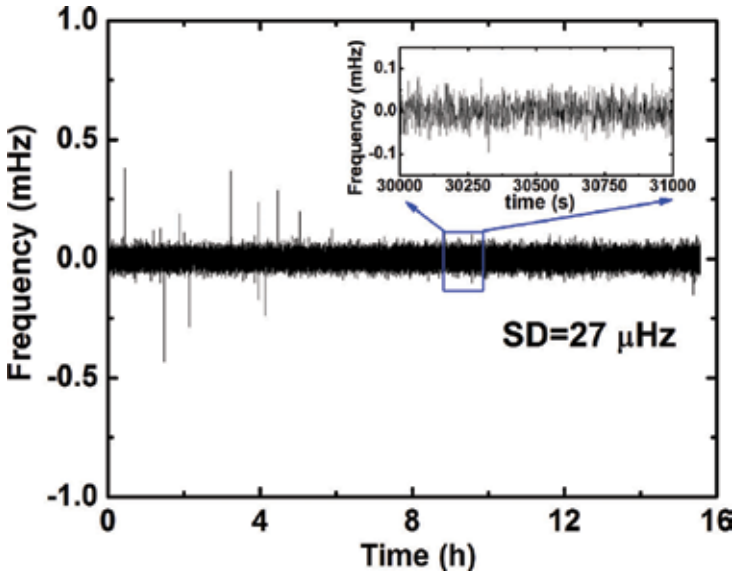

Figure 14. The long-time stabilization of repetition rate.

6. Conclusion

In this chapter, we first present several types of mode-locked fiber lasers, as well as their derivatives for SC generation. Second, an effective method named DPA was applied in Er-doped fiber laser system allowing simultaneous pulse amplification and compression so that additional pulse compressor is no longer needed. With ×8 replicas in DPA, as high as 500-mW average power was achieved and the highest SHG conversion efficiency was measured to be 56.3%. Third, an all-optical method, named as pump-induced nonlinearity, is applied to stabilize the repetition rate of a figure-eight Er-doped fiber laser, achieving as low as 27-μHz accuracy within 16-h measurement.

Author details

Qiang Hao, Tingting Liu and Heping Zeng*

*Address all correspondence to: hpzeng@phy.ecnu.edu.cn

Shanghai Key Laboratory of Modern Optical System, Engineering Research Center of Optical Instrument and System (Ministry of Education), School of Optical-Electrical and Computer Engineering, University of Shanghai for Science and Technology, Shanghai, China

References

[1] Hao, Q.; Li, W. & Zeng, H. (2007). Double-clad fiber amplifier for broadband tunable ytterbium-doped oxyorthosilicates lasers, *Opt. Express*, Vol. 15(25), 16754–16759.

[2] Xu, J.; Wu, S.; Liu, J.; Li, Y.; Ren, J.; Yang, Q. & Wang, P. (2014). All-polarization-maintaining femtosecond fiber lasers using graphene oxide saturable absorber, *IEEE Photon. Technol. Lett*., Vol. 26(4), 346–348.

[3] Albert, A.; Couderc, V.; Lefort, L. & Barthelemy, A. (2004). High-energy femtosecond pulses from an ytterbium-doped fiber laser with a new cavity design, *IEEE Photon. Technol. Lett*., Vol. 16(2), 416–418.

[4] Morin, F.; Druon, F.; Hanna, M. & Georges, P. (2009). Microjoule femtosecond fiber laser at 1.6 microm for corneal surgery applications, *Opt. Lett*., Vol. 34(13), 1991–1993.

[5] Kieu, K.; Mehravar, S.; Gowda, R.; Norwood, R. A. & Peyghambarian, N. (2013). Label-free multi-photon imaging using a compact femtosecond fiber laser mode-locked by carbon nanotube saturable absorber, *Biomed. Opt. Express*, Vol. 4(10), 2187.

[6] Li, W.; Hao, Q.; Yan, M. & Zeng, H. (2009). Tunable flat-top nanosecond fiber laser oscillator and 280 W average power nanosecond Yb-doped fiber amplifier, *Opt. Express*, Vol. 17(12), 10113–10118.

[7] Xu, C. & Wise, F. W. (2013). Recent advances in fiber lasers for nonlinear microscopy, *Nat. Photonics*, Vol. 7(11), 875–882.

[8] Shi, W.; Fang, Q.; Zhu, X.; Norwood, R. A. & Peyghambarian, N. (2014). Fiber lasers and their applications [Invited], *Appl. Opt*., Vol. 53(28), 6554–6568.

[9] Yang, K.; Li, W.; Yan, M.; Shen, X.; Zhao, J. & Zeng, H. (2012). High-power ultra-broadband frequency comb from ultraviolet to infrared by high-power fiber amplifiers, *Opt. Express*, Vol. 20(12), 12899–12905.

[10] Dudley, J. M. & Coen, S. (2002). Coherence properties of supercontinuum spectra generated in photonic crystal and tapered optical fibers, *Opt. Lett*., Vol. 27(13), 1180–1182.

[11] Wan, P.; Yang, L. & Liu, J. (2013). All fiber-based Yb-doped high energy, high power femtosecond fiber lasers, *Opt. Express*, Vol. 21(24), 29854.

[12] Nicholson, J. W. & Andrejco, M. (2006). A polarization maintaining, dispersion managed, femtosecond figure-eight fiber laser, *Opt. Express*, Vol. 14(18), 8160–8167.

[13] Baumgartl, M.; Ortaç, B.; Limpert, J. & Tünnermann, A. (2012). Impact of dispersion on pulse dynamics in chirped-pulse fiber lasers, *Appl. Phys. B*, Vol. 107(2), 263–274.

[14] Iii, I. N. (1991). All-fiber ring soliton laser mode locked with a nonlinear mirror, *Opt. Lett*., Vol. 16(8), 539–541.

[15] Tamura, K.; Ippen, E. P.; Haus, H. A. & Nelson, L. E. (1993). 77-fs pulse generation from a stretched-pulse mode-locked all-fiber ring laser, *Opt. Lett*., Vol. 18(13), 1080.

[16] Tamura, K.; Doerr, C. R.; Nelson, L. E.; Haus, H. A. & Ippen, E. P. (1994). Technique for obtaining high-energy ultrashort pulses from an additive-pulse mode-locked erbium-doped fiber ring laser, *Opt. Lett*., Vol. 19(1), 46–48.

[17] Herda, R. & Okhotnikov, O. G. (2004). Dispersion compensation-free fiber laser mode-locked and stabilized by high-contrast saturable absorber mirror, *IEEE J. Quantum Elect*., Vol. 40(7), 893–899.

[18] Runge, A. F. J.; Aguergaray, C.; Provo, R.; Erkintalo, M. & Broderick, N. G. R. (2014). All-normal dispersion fiber lasers mode-locked with a nonlinear amplifying loop mirror, *Opt. Fiber Technol*., Vol. 20(6), 657–665.

[19] Oktem, B.; Ulgudur, C. & Ilday, F. O. (2010). Soliton-similariton fibre laser, *Nat. Photon*., Vol. 4(5), 307–311.

[20] Abdelalim, M. A.; Logvin, Y.; Khalil, D. A. & Anis, H. (2009). Properties and stability limits of an optimized mode-locked Yb-doped femtosecond fiber laser, *Opt. Express*, Vol. 17(4), 2264–2279.

[21] Zhao, L. M.; Tang, D. Y.; Cheng, T. H.; Tam, H. Y. & Lu, C. (2007). Bound states of dispersion-managed solitons in a fiber laser at near zero dispersion, *Appl. Opt*., Vol. 46(21), 4768–4773.

[22] Chong, A.; Renninger, W. H. & Wise, F. W. (2007). All-normal-dispersion femtosecond fiber laser with pulse energy above 20 nJ, *Opt. Lett*., Vol. 32(16), 2408–2410.

[23] Erkintalo, M.; Aguergaray, C.; Runge, A. & Broderick, N. G. (2012). Environmentally stable all-PM all-fiber giant chirp oscillator, *Opt. Express*, Vol. 20(20), 22669–22674.

[24] Agrawal, G. P. (2001). *Applications of nonlinear fiber optics* (1st edn): Academic Press; 525 B Street, Suite 1900, San Diego, California 92101–4495, USA.

[25] Senoo, Y.; Nishizawa, N.; Sakakibara, Y.; Sumimura, K.; Itoga, E.; Kataura, H. & Itoh, K. (2010). Ultralow-repetition-rate, high-energy, polarization-maintaining, Er-doped, ultrashort-pulse fiber laser using single-wall-carbon-nanotube saturable absorber, *Opt. Express*, Vol. 18(20), 20673–20680.

[26] Hofer, M.; Fermann, M. E.; Galvanauskas, A.; Harter, D. & Windeler, R. S. (1998). High-power 100-fs pulse generation by frequency doubling of an erbium ytterbium-fiber master oscillator power amplifier, *Opt. Lett*., Vol. 23(23), 1840–1842.

[27] Takayanagi, J.; Kanamori, S.; Suizu, K.; Yamashita, M.; Ouchi, T.; Kasai, S.; Ohtake, H.; Uchida, H.; Nishizawa, N. & Kawase, K. (2008). Generation and detection of broadband coherent terahertz radiation using 17-fs ultrashort pulse fiber laser, *Opt. Express*, Vol. 16(17), 12859–12865.

[28] Gaponov, D. A.; Kotov, L. V.; Likhachev, M. E.; Bubnov, M. M.; Cabasse, A.; Oudar, J. L.; Fevrier, S.; Lipatov, D. S.; Vechkanov, N. N.; Guryanov, A. N. & Martel, G. (2012).

High power all-fibered femtosecond master oscillator power amplifier at 1.56 μm, *Opt. Lett*., Vol. 37(15), 3186–3188.

[29] Tang, D. Y.; Zhao, L. M.; Zhao, B. & Liu, A. Q. (2005). Mechanism of multisoliton formation and soliton energy quantization in passively mode-locked fiber lasers, *Phys. Rev. A*, Vol. 72(4), 043816.

[30] Takayanagi, J.; Nishizawa, N.; Nagai, H.; Yoshida, M. & Goto, T. (2005). Generation of high-power femtosecond pulse and octave-spanning ultrabroad supercontinuum using all-fiber system, *IEEE Photonic. Technol. Lett*., Vol. 17(1), 37–39.

[31] Chen, Y.; Räikkönen, E.; Kaasalainen, S.; Suomalainen, J.; Hakala, T.; Hyyppä, J. & Chen, R. (2010). Two-channel hyperspectral LiDAR with a supercontinuum laser source, *Sensors*, Vol. 10(7), 7057–7066.

[32] Kaminski, C. F.; Watt, R. S.; Elder, A. D.; Frank, J. H. & Hult, J. (2008). Supercontinuum radiation for applications in chemical sensing and microscopy, *Appl. Phys. B*, Vol. 92(3), 367–378.

[33] Rulkov, A.; Vyatkin, M.; Popov, S.; Taylor, J. & Gapontsev, V. (2005). High brightness picosecond all-fiber generation in 525–1800 nm range with picosecond Yb pumping, *Opt. Express*, Vol. 13(2), 377–381.

[34] Hao, Q.; Guo, Z.; Liu, Y.; Li, W.; Zhang, Q. & Zeng, H. (2014). Spectrally tailored supercontinuum generation from single-mode-fiber amplifiers, *Appl. Phys. Lett*., Vol. 104(20), 201112.

[35] Tao, Z.; Yan, W.; Liu, L.; Li, L.; Oda, S.; Hoshida, T. & Rasmussen, J. C. (2011). Simple fiber model for determination of XPM effects, *J. Lightwave Technol*., Vol. 29(7), 974–986.

[36] Kudlinski, A.; Pureur, V.; Bouwmans, G. & Mussot, A. (2008). Experimental investigation of combined four-wave mixing and Raman effect in the normal dispersion regime of a photonic crystal fiber, *Opt. Lett*., Vol. 33(21), 2488–2490.

[37] Nodop, D.; Jauregui, C.; Schimpf, D.; Limpert, J. & Tünnermann, A. (2009). Efficient high-power generation of visible and mid-infrared light by degenerate four-wave-mixing in a large-mode-area photonic-crystal fiber, *Opt. Lett*., Vol. 34(22), 3499–3501.

[38] Hao, Q. & Huang, Y. C. (2013). Two-octave polarized supercontinuum generated from a Q-switched laser pumped doubly resonant parametric oscillator, *Opt. Lett*., Vol. 38(11), 1863–1865.

[39] Brown, W. J.; Kim, S. & Wax, A. (2014). Noise characterization of supercontinuum sources for low-coherence interferometry applications, *J. Opt. Soc. Am. A Opt. Image Sci. Vis*., Vol. 31(12), 2703–2710.

[40] Klose, A.; Ycas, G.; Maser, D. L. & Diddams, S. A. (2014). Tunable, stable source of femtosecond pulses near 2 μm via supercontinuum of an erbium mode-locked laser, *Opt. Express*, Vol. 22(23), 28400.

[41] Wadsworth, W.; Joly, N.; Knight, J.; Birks, T.; Biancalana, F. & Russell, P. (2004). Supercontinuum and four-wave mixing with Q-switched pulses in endlessly single-mode photonic crystal fibres, *Opt. Express*, Vol. 12(2), 299–309.

[42] Holdynski, Z.; Napierala, M.; Mergo, P. & Nasilowski, T. (2015). Experimental investigation of supercontinuum generation in photonic crystal fibers pumped with sub-ns pulses, *J. Lightwave Technol*., Vol. 33(10), 2106–2110.

[43] Cumberland, B. A.; Travers, J. C.; Popov, S. V. & Taylor, J. R. (2008). 29 W high power CW supercontinuum source, *Opt. Express*, Vol. 16(8), 5954–5962.

[44] Qiang, H. & Heping, Z. (2014). Cascaded four-wave mixing in nonlinear Yb-doped fiber amplifiers, *IEEE J. Sel. Top. Quant*., Vol. 20(5), 900205.

[45] Chen, K. K.; Alam, S.; Price, J. H. V.; Hayes, J. R.; Lin, D.; Malinowski, A.; Codemard, C.; Ghosh, D.; Pal, M.; Bhadra, S. K. & Richardson, D. J. (2010). Picosecond fiber MOPA pumped supercontinuum source with 39 W output power, *Opt. Express*, Vol. 18(6), 5426–5432.

[46] Kudlinski, A.; George, A. K.; Knight, J. C.; Travers, J. C.; Rulkov, A. B.; Popov, S. V. & Taylor, J. R. (2006). Zero-dispersion wavelength decreasing photonic crystal fibers for ultraviolet-extended supercontinuum generation, *Opt. Express*, Vol. 14(12), 5715–5722.

[47] Shen, X.; He, B.; Zhao, J.; Liu, Y.; Bai, D.; Yang, K.; Wang, C.; Liu, G.; Luo, D.; Liu, F.; Hao, Q.; Li, W. & Zeng, H. (2015). Repetition rate stabilization of an erbium-doped all-fiber laser via opto-mechanical control of the intracavity group velocity, *Appl. Phys. Lett*., Vol. 106(3), 31117.

[48] Xuling, S.; Wenxue, L.; Ming, Y. & Heping, Z. (2012). Electronic control of nonlinear-polarization-rotation mode locking in Yb-doped fiber lasers, *Opt. Lett*., Vol. 37(16), 3426–3428.

[49] Sinclair, L. C.; Coddington, I.; Swann, W. C.; Rieker, G. B.; Hati, A.; Iwakuni, K. & Newbury, N. R. (2014). Operation of an optically coherent frequency comb outside the metrology lab, *Opt. Express*, Vol. 22(6), 6996.

[50] Lee, C.; Chu, S. T.; Little, B. E.; Bland-Hawthorn, J. & Leon-Saval, S. (2012). Portable frequency combs for optical frequency metrology, *Opt. Express*, Vol. 20(15), 16671–16676.

[51] Reichel, S. & Zengerle, R. (1999). Effects of nonlinear dispersion in EDFA's on optical communication systems, *J. Lightwave Technol*., Vol. 17(7), 1152–1157.

[52] Mahran, O. & Aly, M. H. (2016). Performance characteristics of dual-pumped hybrid EDFA/Raman optical amplifier, *Appl. Opt*., Vol. 55(1), 22–26.

[53] Ju, H. L.; You, M. C.; Young, G. H.; Haeyang, C.; Sang, H. K. & Sang, B. L. (2005). A detailed experimental study on single-pump Raman/EDFA hybrid amplifiers: static,

dynamic, and system performance comparison, *J. Lightwave Technol*., Vol. 23(11), 3484–3493.

[54] Varallyay, Z. & Jasapara, J. C. (2009). Comparison of amplification in large area fibers using cladding-pump and fundamental-mode core-pump schemes, *Opt. Express*, Vol. 17(20), 17242–17252.

[55] Eidam, T.; Hanf, S.; Seise, E.; Andersen, T. V.; Gabler, T.; Wirth, C.; Schreiber, T.; Limpert, J. & Tünnermann, A. (2010). Femtosecond fiber CPA system emitting 830 W average output power, *Opt. Lett*., Vol. 35(2), 94–96.

[56] Galvanauskas, A.; Cho, G. C.; Hariharan, A.; Fermann, M. E. & Harter, D. (2001). Generation of high-energy femtosecond pulses in multimode-core Yb-fiber chirped-pulse amplification systems, *Opt. Lett*., Vol. 26(12), 935–937.

[57] Ancona, A.; Roser, F.; Rademaker, K.; Limpert, J.; Nolte, S. & Tünnermann, A. (2008). High speed laser drilling of metals using a high repetition rate, high average power ultrafast fiber CPA system, *Opt. Express*, Vol. 16(12), 8958–8968.

[58] Kuznetsova, L. & Wise, F. W. (2007). Scaling of femtosecond Yb-doped fiber amplifiers to tens of microjoule pulse energy via nonlinear chirped pulse amplification, *Opt. Lett*., Vol. 32(18), 2671–2673.

[59] Sobon, G.; Kaczmarek, P.; Gluszek, A.; Sotor, J. & Abramski, K. M. (2015). μJ-level, kHz-repetition rate femtosecond fiber-CPA system at 1555 nm, *Opt. Commun*., Vol. 347, 8–12.

[60] Guichard, F.; Hanna, M.; Zaouter, Y.; Papadopoulos, D. N.; Druon, F. & Georges, P. (2014). Analysis of limitations in divided-pulse nonlinear compression and amplification, *IEEE J. Sel. Top. Quant*., Vol. 20(5), 619–623.

[61] Kong, L. J.; Zhao, L. M.; Lefrancois, S.; Ouzounov, D. G.; Yang, C. X. & Wise, F. W. (2012). Generation of megawatt peak power picosecond pulses from a divided-pulse fiber amplifier, *Opt. Lett*., Vol. 37(2), 253–255.

[62] Hao, Q.; Zhang, Q.; Sun, T.; Chen, J.; Guo, Z.; Wang, Y.; Guo, Z.; Yang, K. & Zeng, H. (2015). Divided-pulse nonlinear amplification and simultaneous compression, *Appl. Phys. Lett*., Vol. 106(10), 101103.

[63] Kienel, M.; Klenke, A.; Eidam, T.; Baumgartl, M.; Jauregui, C.; Limpert, J. & Tünnermann, A. (2013). Analysis of passively combined divided-pulse amplification as an energy-scaling concept, *Opt. Express*, Vol. 21(23), 29031.

[64] Cingoz, A.; Yost, D. C.; Allison, T. K.; Ruehl, A.; Fermann, M. E.; Hartl, I. & Ye, J. (2012). Direct frequency comb spectroscopy in the extreme ultraviolet, *Nature*, Vol. 482(7383), 68–71.

[65] Hsieh, Y. D.; Iyonaga, Y.; Sakaguchi, Y.; Yokoyama, S.; Inaba, H.; Minoshima, K.; Hindle, F.; Araki, T. & Yasui, T. (2014). Spectrally interleaved, comb-mode-resolved spectroscopy using swept dual terahertz combs, *Sci. Rep*., Vol. 4, 3816.

[66] Heinecke, D. C.; Bartels, A. & Diddams, S. A. (2011). Offset frequency dynamics and phase noise properties of a self-referenced 10 GHz Ti:sapphire frequency comb, *Opt. Express*, Vol. 19(19), 18440–18451.

[67] Locke, C. R.; Ivanov, E. N.; Light, P. S.; Benabid, F. & Luiten, A. N. (2009). Frequency stabilisation of a fibre-laser comb using a novel microstructured fibre, *Opt. Express*, Vol. 17(7), 5897–5904.

[68] Ideguchi, T.; Poisson, A.; Guelachvili, G.; Picque, N. & Hansch, T. W. (2014). Adaptive real-time dual-comb spectroscopy, *Nat. Commun*., Vol. 5, 3375.

[69] Schliesser, A.; Picqué, N. & Hänsch, T. W. (2012). Mid-infrared frequency combs, *Nat. Photon*., Vol. 6(7), 440–449.

[70] Zhang, W.; Han, H.; Zhao, Y.; Du, Q. & Wei, Z. (2009). A 350 MHz Ti:sapphire laser comb based on monolithic scheme and absolute frequency measurement of 729 nm laser, *Opt. Express*, Vol. 17(8), 6059–6067.

[71] Pantell, R. H.; Sadowski, R. W.; Digonnet, M. J. & Shaw, H. J. (1992). Laser-diode-pumped nonlinear switch in erbium-doped fiber, *Opt. Lett*., Vol. 17(14), 1026–1028.

[72] Fotiadi, A. A.; Zakharov, N.; Antipov, O. L. & Megret, P. (2009). All-fiber coherent combining of Er-doped amplifiers through refractive index control in Yb-doped fibers, *Opt. Lett*., Vol. 34(22), 3574–3576.

[73] Yang, K.; Hao, Q. & Zeng, H. (2015). All-optical high-precision repetition rate locking of an Yb-doped fiber laser, *IEEE Photon. Technol. Lett*., Vol. 27(8), 852–855.

[74] Bo, N.; Dong, H.; Peng, D. & Jianye, Z. (2013). Long-term repetition frequency stabilization of passively mode-locked fiber lasers using high-frequency harmonic synchronization, *IEEE J. Quantum Electron*., Vol. 49(6), 503–510.

[75] Rieger, S.; Hellwig, T.; Walbaum, T. & Fallnich, C. (2013). Optical repetition rate stabilization of a mode-locked all-fiber laser, *Opt. Express*, Vol. 21(4), 4889–4895.

Chapter 11

High-Energy and Short-Pulse Generation from Passively Mode-Locked Ytterbium-Doped Double-Clad Fiber Lasers

Yuzhai Pan

Additional information is available at the end of the chapter

http://dx.doi.org/10.5772/63900

Abstract

Mode-locked ytterbium-doped fiber lasers capable of producing nanosecond-, picosecond- or femtosecond-level pulses with high energy or power have many advantages for various applications such as material processing and laser surgery. Firstly, in this chapter, the principles and methods used in passively mode-locked fiber lasers are briefly described. Secondly, mathematical modeling of all normal dispersion ytterbium-doped fiber lasers for analyzing the pulse generation and propagation has been established and simulated with the generalized nonlinear Schrödinger equation. Thirdly, short pulses generated from passively mode-locked fiber lasers have been demonstrated with carbon nanotube– deposited D-shaped fiber as the saturable absorber. Different pulse width can be realized with different parameters of the laser cavity. Finally, the main amplification methods for short laser pulses have been discussed, and a broad prospect for applications of various technologies using short-pulse fiber lasers is further introduced.

Keywords: Ultra-short pulse, passively mode-locked fiber laser, carbon nanotube saturable absorber, double-clad ytterbium-doped fiber

1. Introduction

Optical fiber lasers gained by rare-earth-ions-doped fibers with broad gain spectrum of tens of nanometers make them very attractive for ultrashort-pulse generation via the mode-locking mechanisms [1, 2]. They are under a growing interest because of their unique features of high efficiency and low consumption, good beam quality, high stability, naturally fiber coupled

and providing a powerful tool for high-speed optical communications, precise micromachining, biomedical imaging, and other applications [3].

Mode locking refers to phase locking of many different frequency modes in a laser cavity, which induces a laser to produce a continuous train of extremely short pulses. Unlike the Q-switched pulses, the mode-locked pulses are phase coherent with each other. Active and passive mode locking are two different methods of mode locking. Active mode-locking methods typically involve using external modulators, for example, electro-optical modulator, which induce a phase or amplitude modulation of the intra-cavity light including lots of longitudinal modes with a periodic duration according to the cavity length to generate the mode-locked pulses, whereas in passive mode locking, the generation of the mode-locked pulse is controlled by the saturable absorber (SA), that is a nonlinear optical element whose loss depends on the laser pulse intensity and causes self-modulation of the light.

Optical pulses generated from passive mode locking have the phase locking being carried out automatically in the cavity without external electrical components required, which results in extremely short and high stability. A number of potential operating and applying characteristics of passively mode-locked fiber lasers have been attractively demonstrated that produce laser pulses with durations from nanosecond to femtosecond, ultrawide bandwidth (~100 nm) at repetition rates ranging from several kHz to hundreds GHz. The research field in passive mode-locking fiber laser goes beyond the generation mechanisms and pulse behaviors that can be found in their operation. A lot of attempts and explores have been made to optimize the operation of the laser to suit for the particular application.

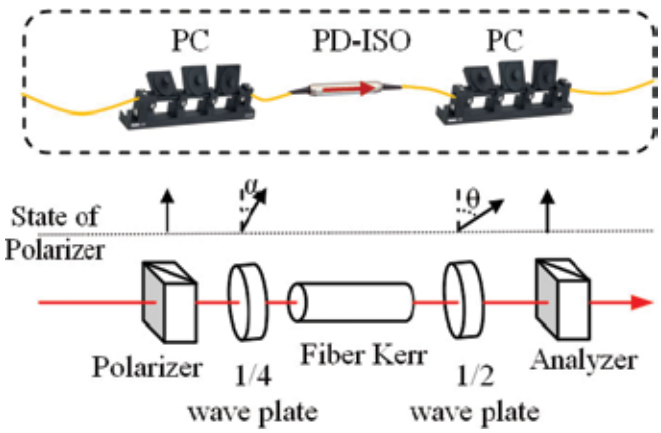

Figure 1. Basic configuration of fiber-based nonlinear polarization rotation. Top, basic configuration; bottom, principle model. PC, polarization controller; PD-ISO, polarization-dependent isolator.

The first passively mode-locked fiber laser was demonstrated in 1983 [4]. An all-fiber, unidirectional, mode-locked ring laser was first constructed using a type of artificial saturable absorber, which uses the effect of intensity-dependent polarization mode coupling in the fiber, that is, nonlinear polarization rotation effect [5]. Since self-phase modulation and other

http://dx.doi.org/10.5772/63900

nonlinearity effects contribute to changing the refractivity index by field intensity, as well the change of the state of polarization as shown in **Figure 1**. Another type of common saturable absorber is based on the nonlinear interference between two polarization modes, that is, the so-called nonlinear optical loop mirror [6] and nonlinear amplifying loop mirror [7]. Nonlinear optical loop mirror relies on the nonlinear interference of the fields that counter-propagate, so the intensity of the pulse is determined by the product of loop length, peak power, and splitting ratio. The longer the loop length, the smaller the peak power required to reach the first transmission maximum. For passively mode-locked fiber lasers operating at large normal dispersion, a short loop length is preferred for ultrashort-pulse generation, while nonlinear amplifying loop mirror is designed with a gain medium placed asymmetrically in the Sagnac loop that is a ring-cavity interferometer. To date, this artificial saturable absorber continues to be an effective approach to generate ultrashort pulses from passively mode-locked fiber lasers [8].

Other methods of the use of new materials have been extensively investigated. Most commonly passive mode-locking devices used in research laboratories and commercial fiber or solid-state lasers are semiconductor saturable absorber mirror (SESAM) [9]. A semiconductor absorber mirror consists of semiconductor heterostructures embedded by a multiple-quantum-well structure like GaInNAs/GaAs. Such a semiconductor absorber mirror can achieve a recovery time of less than 1ns, but has some restrictions on the relatively narrow bandwidth operation, the lower antidamage threshold. Even so, semiconductor absorber mirrors have become widely commercially available and popularly utilization for environmentally robust and stable mode locking.

Various kinds of low-dimensional materials exhibiting the advantages of ultrafast recovery time and broadband saturable absorption have been presented for mode-locked fiber lasers, including carbon-based nanomaterials, such as carbon nanotubes [10], graphenes [11]. Recently, many two-dimensional (2D) layered materials have been investigated as broadband saturable absorbers for the mode locking [12–14]. Almost at the same time, another kind of nanomaterials, that is, the so-called topological insulators (TI), are characterized by a linear dispersion band structure with the Dirac point similar to graphene, which possess inherent features of broad response with a flat broadband wavelength absorption as well as high flexibility. This type of material includes bismuth telluride (Bi_2Se_3) and antimony telluride (Sb_2Te_3) [15, 16]. The manufacturing technique of these low-dimensional materials may have more simple process, easy integration, higher modulation depth, higher damage threshold, a broadband wavelength operation.

Most of passively mode-locked fiber lasers are based on a ring-cavity configuration, which conventionally contains a wavelength division multiplexer for the delivery of the pump energy to the cavity, a segment of gain fiber with the core doped by rare-earth ions, an isolator that provides the unidirectional travelling wave inside the cavity, a beam splitter for the output, a polarization controller, and a saturable absorber for the mode locking. In addition, a spectral filter or other optical elements may be inset into the cavity for the lasing stabilization. In an all-fiber scheme, the cavity contains the active medium and few fiber elements, which offer lower loss for laser pulses. For mode-locked ring-cavity fiber lasers, the fundamental repeti-

tion rate is determined by its cavity length L, the relation expression is as follows: *repetition rate* $=c/nL$, where c and n represents the speed of light, and refractive index respectively. On the state of the so-called harmonic mode locking (HML), the repetition rate can be two or more integer times of the fundamental repetition rate.

To improve the performance of the interaction of nanomaterials and light in fibers, various types of nanomaterial-based saturable absorbers have been demonstrated. For instance, a transmission-mode film-like saturable absorber is fabricated by nanomaterial-polymer composites sandwiched between two fiber ferrules in a standard fiber connector [10, 11]. **Figure 2(a)** shows the typical configuration of a transmission-type saturable absorber. This composite can be constituted by several easy fabrication and integration methods of sputtering, direct synthesis or deposition on the end surfaces of optical fibers, whereas there is a direct physical contact, that is, the laser light is directly transmitted through the nanomaterial film. It is noticed that there may be thermal and mechanical damages within the limited interaction length for high-energy pulsed fiber lasers. A promising alternative is lateral interaction with the evanescent waves of the fiber. The saturable absorbers with the evanescent wave interaction have been demonstrated by several fiber structures including tapered fiber [11], D-shaped fiber [13], etc. The structures and lateral interaction process of the tapered and D-shaped fibers are shown in **Figure 2(b)** and **(c)**. The evanescent wave is generated by total internal reflection of rays at the boundary of the fiber core with a lower index of clad medium. The nanomaterials like carbon nanotubes that contained in the lower-index region can raise the nonlinear reflection coefficient due to evanescent wave absorption along the fiber in a longer nonlinear interaction length in a centimeter scale. This configuration is compatible with the fiber format and easy to add the saturable absorber in the cavity by using simple fiber fusing splicing technique.

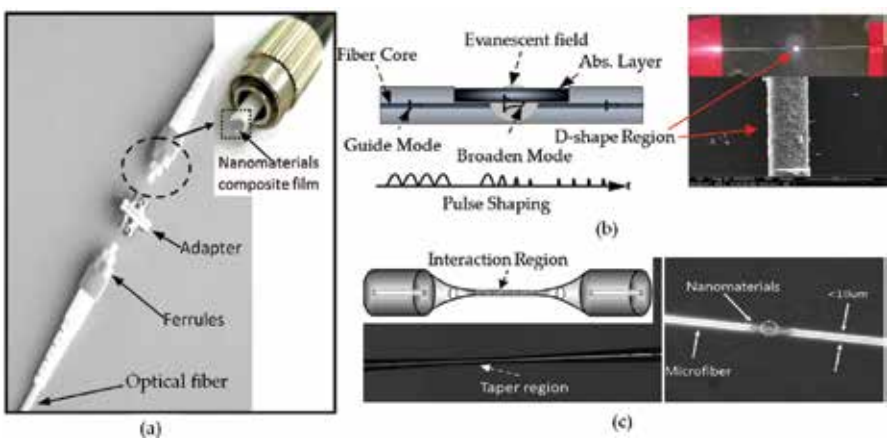

Figure 2. Typical configuration of transmission-type saturable absorber (a), evanescent field interaction of the D-shaped fiber (b), and tapered fiber (c).

http://dx.doi.org/10.5772/63900

Mode-locked silicate-based fibers lasers doped by rare-earth ions have been demonstrated directly operating around 1 μm, 1.5 μm, and 2 μm with very high optical efficiencies. There have also been reported that mode-locked fiber lasers based on Raman cascading, frequency conversion, and other nonlinear processes. The group velocity dispersion of silica fiber is normally positive at 1 μm. Many studies have demonstrated that all-normal dispersion passively mode-locked fiber lasers can generate various kinds of pulses [17], like dissipative solitons, similaritons, noise-like solitons, and soliton rains.

Dissipative soliton pulses refer to those confined wave packets of light in nonlinear optical systems with the balance of nonlinear gain, loss mechanisms. Dissipative solitons generally show large linear chirp with high pulse energies due to the large dispersion experienced in the fiber cavity and possible realization of larger compression ratio by means of simple chirp pulse compression techniques. Dissipative solitons offer highly desirable properties for some direct application and as the seed laser for pulse amplifier system, such as short light pulses of high pulse energies and the improved output stability with compactness, efficiency, and reliability.

An effective method of reducing the repetition rate of passively mode-locked fiber laser is to elongate the cavity by simply adding fiber lengths, and at this time, high-energy ultrashort pulses can be obtained by this effective approach. This method is well suited for fiber lasers where the resonator cavity may reach length in excess of one mile and generate higher energy pulse while maintaining a compact structure [18]. All-normal dispersion passively mode-locked ytterbium-doped fiber laser in a sense offers an ideal laser source of low repetition rate, long duration, and high-energy pulses suitable for a range of applications.

Passively mode-locked fiber laser yields a relatively lower pulse energy in the ultrashort duration because of mode confinement of conventional single-mode fiber. Also, the longer fiber enhances nonlinearities like stimulated Raman scattering and self-phase modulation, which lead to the distortions of the pulse and instability of the mode locking. Today, for the sake of the high-energy laser pulses with available pump power in many application fields like micromachining, many researchers pay their attentions to the use of double-clad fiber for high-power fiber amplifiers and lasers. The double-clad fiber can be pumped by high power laser diodes to get the higher gain [19–21], where the pump light is coupled into the larger inner cladding with a higher numerical aperture.

2. Simulation of passively mode-locked ytterbium-doped fiber laser

Ultrashort-pulse propagation in optical fiber can be accurately modeled by one or more coupled partial differential equations. Various of simulation methods with different theoretical models have been introduced to study laser pulse phenomenon and dynamic processes in the cavity with the parameters of dispersion, nonlinearity, gain, loss, etc. The well-known master mode-locking equation first proposed by H. A. Haus [22], which being a perturbation from the nonlinear Schrödinger equation, has the capacity of describing both the energy saturation and the pulse stabilization process. To prove the possibility of stable pulse gener-

ation in the presented cavity, numerical simulation of the generalized nonlinear Schrödinger equation is performed here, which provides an insights into the mode-locking dynamics of ytterbium-doped fiber lasers and directs to the performance optimization for the pulses.

The whole cavity is schematically shown as an analytical model in **Figure 3**. The main parameters of each fiber can be found in **Table 1**. Firstly, we have numerically simulated the pulse propagation and formation in the cavity governed by the following equation [23]:

$$\frac{\partial \mathrm{A}}{\partial \mathrm{z}} = \frac{\mathrm{g}-\alpha}{2}\mathrm{A} + \frac{\mathrm{g}}{2\Omega_{\mathrm{g}}^2}\frac{\partial^2 \mathrm{A}}{\partial \tau^2} + \mathrm{i}\gamma\left|\mathrm{A}\right|^2\mathrm{A} - \mathrm{i}\frac{\beta_2}{2}\frac{\partial^2 \mathrm{A}}{\partial \tau^2} + \mathrm{i}\frac{\beta_2}{2}\frac{\partial^3 \mathrm{A}}{\partial \tau^3} \tag{1}$$

where A is the slowly varying envelope of the optical field, z is the axial distance, τ is the local time, α accounts for the loss, γ is the nonlinear coefficient of fiber, which accounts for the self-phase modulation effect, and β_2 is the second-order derivative of the propagation constant. During each cavity round-trip time, the pulse goes through different cavity components, and the output from one component is used as the input to the other, as described in **Figure 3**. Also, the pulse goes through the saturable absorber with a nonlinear loss and through the coupler with a fraction of the pulse energy outputted. The fiber parameters were chosen to match the measured or specified parameters of different elements used in the experiment.

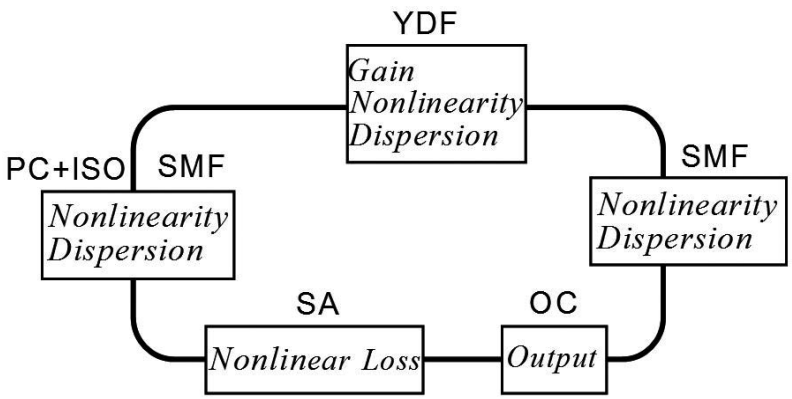

Figure 3. Proposed model of passively mode-locked fiber laser. YDF, ytterbium-doped fiber; SMF, single mode fiber; OC, output coupler; SA, saturable absorber.

Fiber type	β_2 (ps^2 m^{-1})	β_3 (fs^3 m^{-1})	γ (W^{-1} m^{-1})	Length (m)
Ytterbium-doped fiber	0.021	0.0254	0.0048	10
Other fiber elements	0.022	0.0254	0.0044	5
Hi1060 fiber	0.022	0.0254	0.0044	20 or Var.

Table 1. Summary of the fiber parameters used in the simulation.

http://dx.doi.org/10.5772/63900

The parameter g denotes the gain coefficient of ytterbium-doped fiber, which can be described as the gain function and approximately expressed by:

$$g_i = \frac{g_0}{1 + E_{pulse} / E_{sat}} \tag{2}$$

where E_{sat} is the saturation energy due to the limited pump power, which is defined as $E_{sat}=(h\nu/\sigma)A_{eff}$ with the dependence of pump power. The pulse energy E_{pulse} is given by $E_{pulse}=\int_{T_R/2}^{-T_R/2} |A(z,\tau)|^2 d\tau$, where T_R is the cavity round-trip time. The same small signal gain g_0, depending on the doping concentration, can be assumed to be constant if only a small fraction of the pump light is absorbed provided an approximation of uniform pumping. Ytterbium-doped fiber is modeled with a total unsaturated gain of 30 dB, corresponding to these parameters: $g_0=6.9m^{-1}$ and $E_{sat}=1nJ$. Ω_g is the gain bandwidth of ytterbium-doped fiber, which is related to the bandwidth $\Delta\lambda$ through $\Omega_g=|2\pi c/\lambda^2|\Delta\lambda$, where $\Delta\lambda$ is chosen to be 55nm bandwidth.

The parameter β_2 represents dispersion of the group velocity contributing to time-domain broadening of laser pulse, that is, the so-called group velocity dispersion, which is commonly used by physicists in units of $ps^2\Delta m^{-1}$. For optical fibers, the group velocity dispersion usually refers to the chromatic dispersion parameter D that defined as a derivative $d\beta_1/d\lambda$, which is also used in practice with the relation of β_2 and n as: $\beta_2=-(\lambda^2/2\pi c)\Delta D$, where λ is the operating wavelength. The higher order dispersion and higher order nonlinear effects were ignored in simulations. Fiber nonlinear parameter γ relates the wavelength λ and effective area A_{eff} to the nonlinear index n_2 with an expression as: $\gamma=2\pi n_2/\lambda_0 A_{eff}$, when the radial field distribution is known.

Nonlinear transmission of the saturable absorber can be described by $T=\exp[-(\alpha_1+\alpha_{nl})]$, where α_1 is nonsaturable absorption loss, and α_{nl} denotes power-dependent nonlinear absorption loss, which is given by $\alpha_{nl}=\alpha_0/(1+P(\tau)/P_{sat})$, where α_0 is the saturable loss due to the absorption, that is, the modulation depth. $P(\tau)$ is the instantaneous pulse power and P_{sat} is the saturation power of the saturable absorber. The saturable loss, which acts as an equivalent-filtering effect, has a significant impact on the pulse duration and bandwidth of laser pulse. It is expected, for high power/energy pulse, that the saturable absorber with a larger modulation depth can be used in a fiber laser with large normal dispersion and strong nonlinearity. The further increase of the modulation depth should be carefully designed due to the limitation of the nonsaturable loss. One probable way for the increase of modulation depth is to reduce the evanescent field leaking of D-shaped fiber and enlarge the evanescent field interaction with the saturable absorber by lengthening the fiber D-shaped domain. Here, the parameters of the saturable absorber in the simulation model are as follows: $\alpha_1=45\%$, $\alpha_0=27\%$, and $P_{sat}=1000W$.

2.1. Numerical simulation and results

All optical fibers in the model above have normal dispersion within the laser spectral range. A 20 m length of Hi1060 fiber was inserted into the cavity aiming to increase the cavity length. The total dispersion is calculated to be about 0.75 ps^2. Eq. (1) has been solved with the standard split-step Fourier method. The simulation field is represented on a temporal grid (and via the Fourier transform on a frequency grid) consisting of 2^{11} points with a width of 0.2 ns. One initialized weak signal was introduced into the round-trip propagation in the cavity, and this pulse consecutively experiences each action of cavity components along the routes.

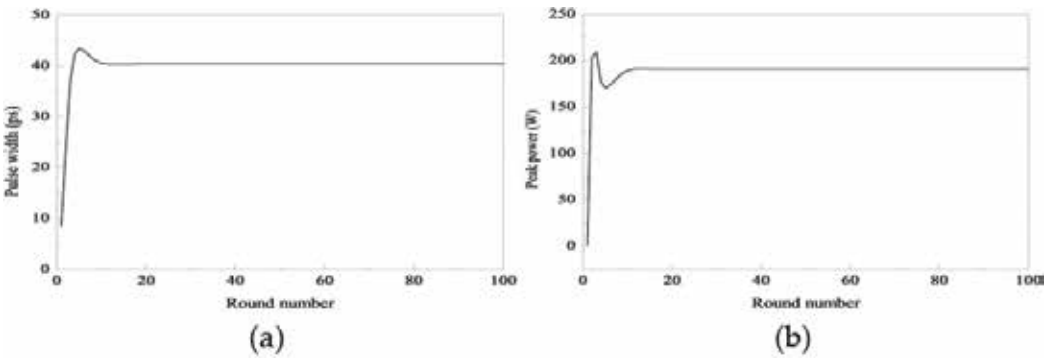

Figure 4. Transient evolution of the pulse width (a) and peak power (b).

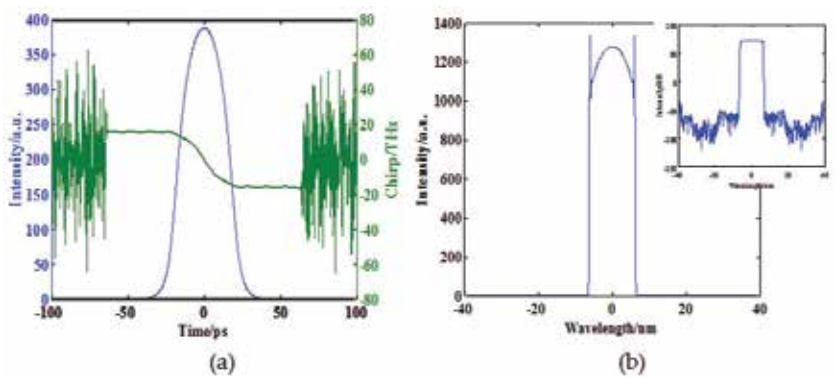

Figure 5. Pulse profile and chirp (a), and spectrum (b) of mode-locked laser. The inset is the spectrum in decibel scale.

After a finite number of round trips, the pulse started to converge into stable dissipative soliton solutions. The simulation results indicate that stable solutions do exist in such a laser, which can be confirmed from the peak power and pulse duration evolutions as shown in **Figure 4**. The pulse duration is ~40.6 ps and the spectral edge-to-edge bandwidth is 11.2 nm as shown in **Figure 5**, which both evidently indicate that the pulses are highly chirped. As shown in **Figure 5(b)**, the spectrum on a linear scale and a logarithmic scale is characterized by their

http://dx.doi.org/10.5772/63900

steep edges, that is, the so-called M-shaped optical spectra. The higher peak power of the pulse after amplification by gain fiber induces a substantial nonlinear phase shift in the single-mode fiber, which results in sharp peaks on the spectrum edges. The gain and loss coexist in the dissipative system and play an essential role in the formation of dissipative solitons. Thus, dissipative soliton must be self-organized and its dynamics differ from that of the conventional soliton. It is noted that the saturable absorber has a nonlinear transmission depending on the light intensity, and the nonlinear phase shift is gradually varied in the process of gain saturation when an initial pulse is circulating in the cavity [24].

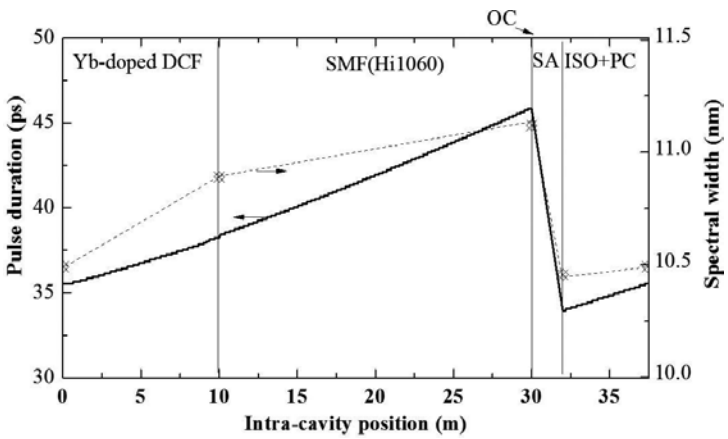

Figure 6. Evolution of the pulse width and spectral bandwidth in one cavity round trip.

The evolutions of the pulse duration and spectral edge-to-edge bandwidth in one cavity round trip are shown in **Figure 6**. It can be seen that the significant broadening of the duration and spectral width of the pulse after passing through the gain fiber. The large normal dispersion of a long segment of single-mode fiber induces large and positive chirp. The nonlinear phase shift broadens the spectrum of the pulse, while strong chirping induced by normal cavity dispersion enlarges the pulse pedestals, which are the lower intensity red-shifted and blue-shifted spectral weights located at both pulse edges in time-domain. When the pulse is travelling throughout the saturable absorber, pulse duration and spectrum width could be compressed. Here, the saturable absorber plays a key role of providing an effective filtering function to stabilize the mode locking.

When the cavity length was increased to 60m, the total cavity dispersion is up to ~1.3 ps^2. The laser works on a larger normal dispersion regime without dispersion compensation in this model as the same above. Simulation results showed that the stable pulse obtained with the pulse duration of 76.5 ps and the corresponding spectral width of 9.6 nm. With the larger positive dispersion, the stable pulses have been obtained again but highly chirp. Comparing the pulse characteristics of these two cavities, the broadened pulse induced mainly by self-phase modulation in the longer cavity has lower peak power, and both of the equivalent filter effect and lower self-phase modulation result in the narrower spectrum.

For the deliverable high energy of the pulse, the stabilization of mode locking should be ensured in a normal and large cavity dispersion accompanied with a high nonlinearity. A spectral filter, which is added in such a laser cavity, can be considered as an effective absorber in the spectral domain to cut off the temporal wings of the pulse and stable the mode locking. It is assumed that the spectral filter has a Gaussian profile, so the spectral filter is numerically implemented in the model by a function as: $T(\omega)=\exp[-(\omega/\Omega_f)^2]$, where ω is the angular frequency, and Ω_f is the bandwidth of the spectral filter. The influence of the spectra filtering on pulse shaping could be investigated for the stabilization of the mode locking, as well as the performance optimization of the pulses [25].

3. Mode-locked ytterbium-doped fiber laser with carbon nanotubes

Single-walled carbon nanotube is an enrolled two-dimensional graphene honeycomb sheet with a diameter of typically 0.6–2 nm and a length distribution ranging from tens of nanometers to several micrometers. Depending on their chirality [26], single-walled nanotubes exhibit two different electrical properties, metallic or semiconducting. Semiconducting nanotubes have an energy band gaps like those in ordinary semiconductors; thus, photons having corresponding wavelength are absorbed. Single-walled nanotubes are a kind of promising material as saturable absorber for passive mode locking because the bandgap energy can be controlled by the tube diameter, which would be applied for different spectral ranges.

The absorption loss and modulation depth of the nanotubes-based saturable absorber can be adjusted by changing the concentration of nanotubes, the interaction length of light with nanotubes, nonsaturable loss of fiber structure, and substrate materials. To study the effect of modulation depth on the mode locking in a larger normal dispersion cavity with high nonlinearity, the evanescent field used here is from the D-shaped fiber that was fabricated by ablating part of the cladding of single mode fiber by the femtosecond laser-induced water breakdown method [27]. Top- and side-view microscope images of the as-prepared D-shaped fiber are shown in **Figure 7(a)**. Averaged distance between the core and the flat face of the fiber is about 7 μm, and the entire length of D-shaped fiber is 900 μm. Measured insertion loss of the D-shaped fiber is about 0.6 dB which guarantees the lower loss in the cavity. Secondly, the commercial solution of single-walled carbon nanotubes with the purity of approximately 95% was used in the experiments. The diameter distribution of nanotubes is around 1.5 nm. The nanotube solution was further diluted to be a concentration of 0.05 wt% with a ten-hour ultrasonically agitated process to minimize bundling of nanotubes. Finally, the well-dispersed aqueous solution was sprayed on the D-shaped surface of the fiber. These devices were dried out in a vacuum oven at the temperature of 40 °C for 30 min carefully adjusted to reduce agglomeration and detaching of nanotubes. Simple encapsulation for these saturable absorbers was performed to avoid unexpected damage. A microscope image of the nanotube–deposited D-shaped fiber is shown in **Figure 7(b)**. The transmission values of the saturable absorber were recorded by using the ultrashort-pulse fiber laser with a MHz repetition rate at different average power. The results for both the D-shaped fiber with nanotubes and with-

http://dx.doi.org/10.5772/63900

out nanotubes are presented in **Figure 7(c)**. The result shows that the transmissivity can be changed with the increase of the input power indicating the existence of saturable absorption. The power-dependent transmissivity induced by nanotubes can be decreased to ~28%. Nonsaturable loss induced by both D-shaped fiber and other impurities is about 21%. The modulation depth of about 51% can be provided, which is higher and sufficient.

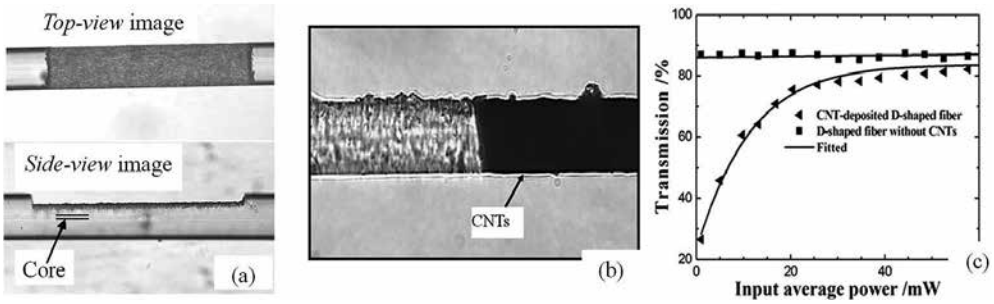

Figure 7. (a) Top-view and side-view microscope images of a D-shaped zone in fiber, (b) microscope image of carbon nanotube–deposited D-shaped fiber, and (c) transmissivity curves of saturable absorber and D-shaped fiber versus the input power.

3.1. Ultrashort-pulse generation

The presented experimental setup is schematically shown in **Figure 8(a)**. A side-pumping scheme of ytterbium-doped fiber was taken as the gain fiber pumped by 915-nm laser diode through a fiber combined with a coupling efficiency of 90%.

A lower absorption coefficient of gain fiber could suppress thermal effects to some extent, a 10-m-long ytterbium-doped double-clad fiber (Nufern SM-YDF-5/130) with a cladding absorption coefficient of 1.16 m^{-1} at 915 nm. The dispersion and nonlinear coefficients of ytterbium-doped fiber are $0.02 ps^2 \cdot m^{-1}$ and $0.0048 W^{-1} \cdot m^{-1}$, respectively. A 20-m-long single-mode fiber was employed to extend the cavity length, which correspondingly decreased the repetition rate. An optical coupler (OC) provided a 20% output ratio. The dispersion and nonlinear coefficients of single-mode fiber are $0.022\ ps^2 \cdot\ m^{-1}$ and $0.0047\ W^{-1} \cdot m^{-1}$, respectively. The total length of laser cavity is ~36.5 m with the all-normal cavity dispersion of $\sim 0.76\ ps^2$.

Self-starting mode locking has been achieved at the pump power of ~0.6 W by appropriately adjusting polarization controller. The self-consistent pulse evolution and stable mode locking indicate that the saturable absorber performs a filtering-equivalent function by the loss depending on light intensity to promote and stabilize the mode-locking operation in all-normal dispersion cavity as we expected. The pulse train generated has been observed by the oscilloscope trace as shown in **Figure 8(b)**. The pulse sequence was traced up to 2.5 μs by an oscilloscope connected with a high-speed photodetector (3 GHz). The figure exhibits the round-trip time of ~178.7 ns corresponding to the repetition rate of 5.59 MHz, which is consistent with the cavity length.

The temporal profile and spectral of the pulse recorded at the pump power of 2 W are shown in **Figure 8(c)** and **(d)**. The spectrum was measured by a spectrometer with the resolution of 1 nm (Ocean Optics Inc., HR4000). The operation wavelength is around 1085 nm, which indicated nearly four energy-level lasing behavior of ytterbium ions. The pulse duration is 46.6 ps, and the spectrum has an approximately M-shaped profile on a linear scale with a bandwidth of ~12.8 nm, which implies that the mode-locking operation in the dissipative soliton regime. The pulse duration could be further decreased to 941 fs from the outside cavity simple compression by using a segment of single-mode fiber with negative dispersion. The near Gaussian fitting shape of the pulse suggests that linear chirp dominates across the pulse in the cavity.

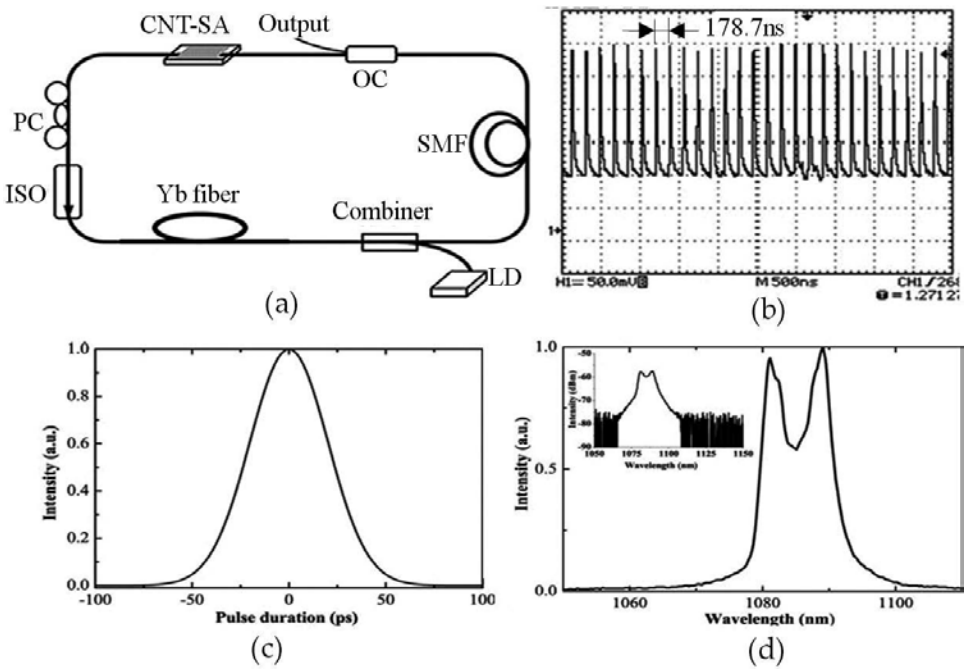

Figure 8. (a) Schematic diagram of mode-locked fiber laser, (b) oscilloscope traces of pulse train, (c) pulse profile trace of the pulse, and (d) output spectrum (the inset is the spectrum in a log scale).

When the pump power was increased to 3.5 W, the corresponding pulse duration was enlarged to 62.6 ps, and the spectral width was broadened to 16.3 nm. The output power was almost linearly increased to 162 mW, and the corresponding pulse energy was raised to ~29 nJ. The experimental results manifest that the evanescent-field interaction scheme and large modulation depth of the saturable absorber would be preferentially chosen for the achievement of high-energy pulses. Mode-locked fiber lasers could be robust against optical wave breaking due to the linear chirp across the pulse, showing a stretched pulse with the duration up to a few or even several hundred picoseconds.

http://dx.doi.org/10.5772/63900

Unlike nonlinear polarization rotation effect, various new nanomaterials hardly generate fs-level ultrashort pulses directly from the laser oscillators [28]. A robust self-starting picoseconds ytterbium-doped fiber laser is easy to be realized by using one of other 2D materials or topological insulators, at the aspect of characteristics of the pulses, those results are similar to these of carbon nanotubes yet. The pulse duration is limited by large normal dispersion, while the larger linear chirp dissipative solitons pulses are easy to be compressed. So the research interests are focused on various pulses dynamics of stable, self-starting mode locking of the fiber lasers in all-normal dispersion regime.

3.2. Nanosecond-level pulse generation

Carbon nanotubes have been demonstrated it suitable for stable long-duration pulse mode locked in all-normal dispersion regime [29]. Absence of nonlinear polarization evolution dynamics gives giant chirped pulses that can be suitable for compression. Here, an ultralong cavity ytterbium-doped fiber laser mode locked by nanotubes-based saturable absorber has been experimentally investigated. It is used a saturable absorber with the unsaturated loss of ~57.8% and the modulation depth of ~4.7%. The ring cavity was elongated by an one-kilometer-long single-mode fiber (YOFC, C1060), which results in an ultralong laser cavity with the length of 1021 m.

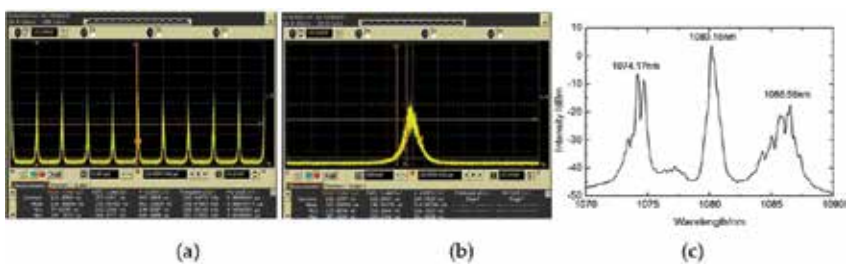

Figure 9. Characteristics of noise-like pulses. Train trace (a), single pulse (b) and optical spectrum (c).

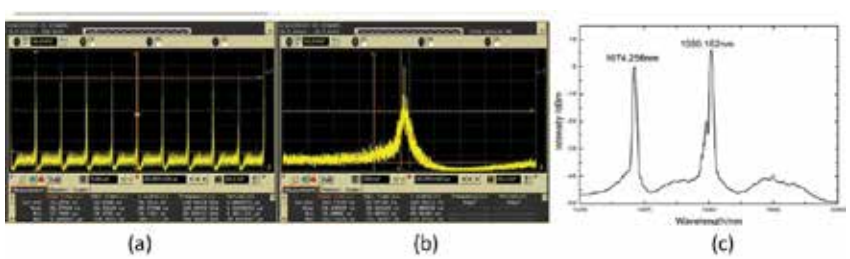

Figure 10. Characteristics of soliton rains. Train trace (a), single pulse (b), and optical spectrum (c).

Stable mode-locked pulses were obtained by slightly adjusting PC at the pump power of 0.81 W. The amplitude of the pulse was increased with the increase of pump power until the

power of 1.81 W, which changing into a state of multipulses. The pulse sequence and single pulse, which is a typical noise-like pulse, have been measured and shown in **Figure 9(a)** and **(b)**, respectively. The repetition period of the pulse is approximately 5 μs. The pulse duration is approximately 292.6 ns. When the pump power was 1.81 W, another stable state, that is, soliton rains, could be obtained with carefully adjusting the polarization controller. **Figure 10** shows the pulse train, single pulse, and the spectrum of the fiber laser at the pumping power of 1.93 W. Within each pulse period, the pulse contains background noise, drifted pulse, and phase-condensed soliton. The intensity of the drifted pulse is about 10% of the phase-condensed soliton. The pulse width of phase condensation soliton is about 102.5 ns at 3 dB, as shown in **Figure 10(b)**. The steady soliton rains cannot be maintained once the pump power is above 1.93 W. The maximum output power is ~40.3 mW with single pulse energy of ~201.5 nJ. Output spectra of the noise-like pulses and soliton rains have been measured and shown in **Figures 9(c)** and **10(c)**. It can be seen that both spectra have several central wavelengths indicating that the presence of filtering effect in the cavity could be used as a multiwavelength short-pulse fiber laser.

Recently, it has been reported that the generated pulses of an ultralong cavity fiber laser can deliver microjoule-level energy in the nanosecond range [30]. In the all-normal dispersion fiber laser systems, the stable mode-locking pulses exhibits that the formation of pulse shaping is the product of complicated processes of energy conversion. Various nonlinear effects such as self-phase modulation, dispersion wave, peak clamping, which have strong influence on the stability of mode locking, and combining with high cavity dispersion can lead to complex pulsing phenomena, like wave-breaking of the soliton pulse as noise-like pulses in the results above. On the other hand, the Raman-induced noise-like pulses can be realized by the Raman effect in a fiber laser with high nonlinearity and dispersion [31].

4. Amplification of short-pulse fiber lasers

Because laser pulses that extracted from the master oscillator are generally of relatively low energies, an additional external amplifier is required for the enhancement of the pulse energy, which is of key importance of power scaling of fiber lasers for the wide applications. Ytterbium-doped fiber laser systems are excellently suited to generate and amplify ultrashort laser pulses due to their large amplification bandwidth supporting pulse durations of few hundred femtoseconds. This approach is benefited from the simple fiber connection between the oscillator and the amplifier. There are mainly two methods, that is, the chirped pulse amplification (CPA) and the master oscillator power amplification (MOPA).

For the CPA technique, ultrashort pulses are amplified by time stretching of the original pulses and later recompress them back into a short duration after the fiber amplifier [32]. The chirped pulse amplifier system, as schematically shown in **Figure 11**, is composed of a seed laser, a pulse stretcher, amplifier chains, and a pulse compressor. The duration of laser pulses is firstly increased temporally to a much longer duration of the order of 1ns, that is chirped by using a pulse stretcher, for example a grating pair, fiber chirped Bragg grating, etc., which reduces the

http://dx.doi.org/10.5772/63900

peak power to a level so that the nonlinear effects in the gain medium can be avoided. The stretched pulse was amplified in next amplifier system, which typically consisted of large-mode area single-mode fiber or photonic crystal fiber (PCF) gained by multimode laser diodes, allowing more peak power generation below the limit of nonlinear optical intensity effects. Finally, a low-loss compressor is used to temporally compress the pulses to a duration similar to the input pulse duration. The pulse stretcher is necessary for the amplification of ultra-short pulses. Or otherwise, high nonlinearities in the fiber induced by high optical peak power in ultrashort pulses would affect the recompression to an ideal short pulse in the final compression part. Of course, the compressor also needs to tolerate high peak powers without introducing nonlinear distortions.

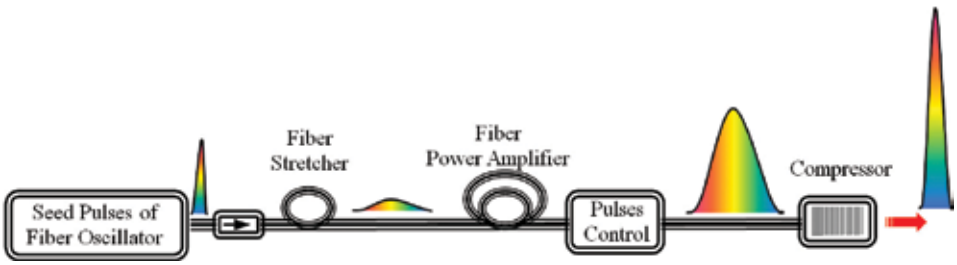

Figure 11. Schematic diagram of the chirped pulse amplifier for ultrashort-pulse fiber laser.

Femtosecond fiber amplifier systems have the potential for millijoule pulse energies at megahertz repetition rate. Fox example, a ytterbium-doped fiber amplifier system has delivered millijoule level pulse energy at repetition rates above 100 kHz corresponding to an average power of more than 100 W, the compressed pulse is as short as 800 fs [33], where a short-length PCF with 80-μm core diameter is employed, which allows the pulse energies up to 1.45 mJ with a stretched pulse duration of 2 ns. Scaling up of pulse energy in an ultrafast fiber laser has been demonstrated that the simultaneous generation of 60 W of compressed average power at 100 kHz, together with 320 fs and 600 μJ pulses [34].

Highly chirped pulse fiber oscillators may create powerful all-fiber generator-amplifier systems, that is, the so-called master oscillator power amplifier (MOPA), which is an attractive technology to achieve picoseconds-level laser pulses with higher average output power and peak power [35–38]. The master oscillator power amplifier, as shown in **Figure 12**, generally consists of a laser oscillator that produces the weak seed pulse and series of amplifiers that increase the laser power to the required level. Chirped pulses from the generator are directly fed to an amplifier without the use of a stretcher or a modulator and compressed after one or more amplifying stages. In addition, the chirped pulses coming out of the master oscillator in the normal dispersion regime, like dissipative solitons, whose energy exceeds the energy of classical solitons by tens or hundreds of times because of longer duration at the same peak power, can be further increased to the required level in one power amplifier, as well compressed by an external compressor.

Double-clad fibers have been extensively used to build fiber amplification systems, exhibiting desirable characteristics such as high gain, good efficiency, and excellent beam quality. A diode-pumped mode-locked ytterbium-doped fiber seed laser followed by two fiber amplifiers has been demonstrated [36], where both fiber amplifiers with the design of large-mode area were cladding pumped. The oscillator produced 30 pJ, 1.8 ps pulses. After two-scales amplifying, the output pulses compressed by 830 grooves/mm gratings produced high-quality 400 nJ pulses with a pulse duration of 110 fs at average power levels in excess of 25 W. A carbon-nanotube-based master oscillator power amplifier has also been reported that a compact picosecond-level pulse fiber laser with high average power [37]. The seed laser that is the nanotube-based mode-locked Nd:YVO_4 laser is further amplified with a single-stage fiber amplifier. An amplified pulse with a pulse width of 15.7 ps, pulse energy of 244 nJ, has been achieved with an average power of 20 W at a repetition rate of 82 MHz. A fiber amplifier contains a seed source and two-scale amplifiers in that the gain fibers are different size double-clad fibers to suppress the nonlinear effects, and single pulse energy of 4.56 μJ with a pulse width of 0.62 ns at 26.3 MHz has been realized [38]. These systems present simple and practical fiber-based solutions for high-average-power ultrashort-pulse laser applications.

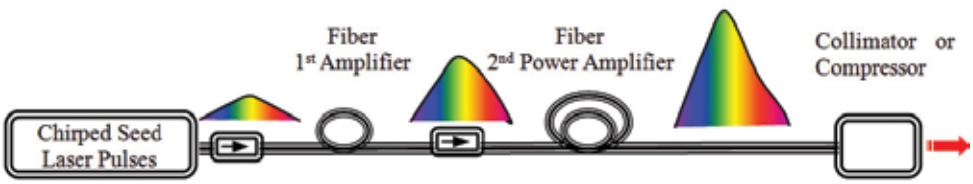

Figure 12. Schematic diagram of a master oscillator power amplifier system.

Fiber nonlinearity is proportional to the length of fiber and inversely proportional to the fiber core size. The developed large-mode area double-clad photonic crystal fiber can be considered as a possible approach to overcome many of the difficulties as mentioned above. These amplifiers enabled by advancements in photonic crystal fiber manufacturing technology can generate kilowatts to multigigawatts of peak power using direct amplification showing excellent conversion efficiency, diffraction-limited beam quality.

5. Typical applications of short-pulse mode-locked fiber lasers

Fiber laser sources with nanosecond pulses have great potential in a variety of applications requiring low temporal coherence, such as optical metrology, or sensor interrogation based on low-coherence spectral interferometry technology. Furthermore, the applications of fiber-based master oscillator power amplifier sources can also extend to industrial fields, such as laser marking, engraving, and other micromachining in various materials, particularly suitable for cutting high reflectivity materials like titanium, copper [39], silver [40]. Other successfully commercial examples include the high-resolution 3D imaging lidar system [41], nonlinear

http://dx.doi.org/10.5772/63900

frequency conversion [42], etc. The pulse duration of ultralong cavity mode-locked fiber laser may be up to several or even hundreds of nanoseconds with higher energy. In contrast to the Q-switched lasers, obviously, there would be the limited range of direct applications. For this reason, the interests would focus on the high-chirp solitons or dissipative solitons resonance with the duration as long as nanoseconds that can further be compressed into a picosecond level.

All-fiber subnanosecond lasers have great potential application in the generation of wide-band supercontinuum (SC) source [38]. The supercontinuum laser source is the widely broadened spectrum generated by strong nonlinear effects using highly nonlinear fibers. The output power of this novel supercontinuum light source is high by using the small core fibers, so that the supercontinuum source is of interest to many kinds of applications. For example, an ultrahigh-resolution optical coherence tomography (OCT) has been investigated by using the ultrashort-pulse fiber supercontinuum source as fiber-based, high-power, wideband sources [43].

Laser beam at the output of the fiber can be easily focused in a spot with a radius of ~μm, a few nanojoules of energy in a tens femtoseconds pulse resulting in intensities on the order of ~GW/cm^2. So, ultrashort laser pulses would not induce heat diffusion during the fast interaction with objects such as various materials and living structures, that is, free from cracks and melting and other thermal effects [44]. For ultrashort laser pulses with the duration below several picoseconds, the pulses interacting period is generally shorter than the lattice heating time, which is necessary for energy diffusion processes for most materials. Ultrashort-pulse fiber lasers presently have provided a stable and reliable platform for many applications.

Material micro- and nano-machining has been for a long time identified as an important and the largest market for high-power/energy ultrashort-pulse fiber lasers [45]. High pulse intensities are widely used for permanent transparent material modification. In addition, these extremely high power densities of the pulses resulting in a highly localized disruption of the material matrix with very little energy deposited and few heat transferred to the surrounding material. This is a so-called laser cold process. A clear processing edge formed by laser ablation is of key importance for medical, photovoltaic, and semiconductor industry, especially for thermally sensitive material, like nitinol shape memory alloys, bio-absorbable polymers like polylactic acids, glass, etc. [46]. In comparison, nanosecond laser pulses micromachining in glass or other materials would leave an undesirable heat-affected zone, numerous stress fractures, and micro-cracks around the processing edge.

Although known as a cold ablation process, by precisely controlling localized heat accumulation to melt material accompanying with the inhibition of shrinkage stress by producing embedded molten pool by nonlinear absorption process, ultrashort laser pulses at high repetition rates (hundreds of kHz and above) have been applied into micro-welding of materials including glass and plastic, silicon and glass, and medical piece part [47].

Ultrashort-pulse laser make them ideal sources for time resolved measurement of the faster physical and chemical phenomenon. By controlling the optical carrier frequency and the carrier phase of ultrafast lasers, optical frequency combs, spectroscopy and precision metrology of

optical frequency transitions and natural constants have been realized. Pump-probe measurements can use ultrashort laser pulses to measure and determine the evolution of a series of ultrafast processes in many kinds of materials, molecules or even in internal states of atoms, with the advantage of shortening the transient behavior resulting from the optical excitation [48]. Femtosecond laser pulses with modest energies generating the intensities above 10^{15} W/cm^2 are used to determine the elements of the sample in a technique called femtosecond laser-induced breakdown spectroscopy (fs-LIBS) [49].

Ultrashort fiber lasers are developing rapidly in the medical and biology applications. These laser pulses can be used as a laser scalpel directly to medical treatment on the one hand. The advantages of accuracy, absence of thermal interaction, and safety have been accepted by a wide customer. On the other hand, the indirect applications refer to high precision and high-quality medical devices, such as stents, implants, and catheters, requiring sophisticated manufacturing techniques, which are available from medical industrial manufacturing processes. An example has been reported in 2014, the multifunctional biochips for realizing high-performance biochemical analysis and cell engineering [50].

In conclusion, passively mode-locked ytterbium-doped fiber lasers operating in the normal dispersion regime have been firmly established in the field of various short-duration pulses, and attracted increasing attention due to their compactness, low cost, and widespread applications. Various technologies have been developed with the aim to realize short-pulse all-fiber laser sources with the desirable energies, durations, average powers and beam quality, as well the environmental stabilization and reliability. This chapter is intended to smoothly understand each topic on this field and has the interest to further read and explore high-energy short-pulse generation and their applications.

Acknowledgements

This work was partially supported by Shandong Graduate Teaching Innovation Project (SDYY15003) and HIT Graduate Teaching Reform Project(JGYJ201436 & WH2015008).

Author details

Yuzhai Pan*

Address all correspondence to: panyzh2002@163.com

Department of Optoelectronic Science, Harbin Institute of Technology at Weihai, Hi-Tech District, Weihai, China

http://dx.doi.org/10.5772/63900

References

[1] S M Swift. Q-switched and mode locked short pulses from a diode pumped, Yb-doped fiber Laser. BiblioScholar; 2012

[2] M J F Digonnet. Rare-earth-doped fiber lasers and amplifiers. 2nd edn. Boca Raton, FL: CRC Press; 2001

[3] H Endert, A Galvanauskas, G Sucha and R Patel. Novel ultrashort pulse fiber lasers and their applications. Proceedings of SPIE. 2002; 4426:483–488

[4] M I Dzhibladze, Z G Esiashvili, E S Teplitskii, S K Isaev and V R Sagaradze. Mode-locking in a fiber laser. Kvantovaya Elektron. 1983; 10:432–434

[5] V J Matsas and T P Newson. Self starting passively mode locked fibre ring soliton laser exploiting nonlinear polarization rotation. Electron Lett. 1992; 28(15):1391–1393

[6] Doran N J and Wood D, Nonlinear-optical loop mirror. Opt. Lett. 1988; 13(1):56–58

[7] M. E. Fermann, F. Haberl, M. Hofer, and H. Hochreiter, Nonlinear amplifying loop mirror. Opt. Lett. 1990; 15(13):752–754

[8] X Jin, X Wang, X Wang, and P Zhou, Tunable multiwavelength mode-locked Tm/Ho-doped fiber laser based on a nonlinear amplified loop mirror. Appl. Opt. 2015; 54(28): 8260–64

[9] U Keller, K J Weingarten, F X Kartner, et al. Semiconductor saturable absorber mirrors (SESAM's) for femtosecond to nanosecond pulse generation in solid-state lasers. IEEE J. Sel. Top. Quantum Electron. 1996; 2(3):435–453

[10] S Y Set, H Yaguchi, Y Tanaka, and M Jablonski, Ultrafast fiber pulsed lasers incorporating carbon nanotubes. IEEE J. Sel. Top. Quantum Electron. 2004; 10(1):137–146

[11] J Du, Q Wang, G Jiang, et al. Ytterbium-doped fiber laser passively mode locked by few-layer molybdenum disulfide (MoS_2) saturable absorber functioned with evanescent field interaction. Sci. Rep. 2014; 4(4):6346

[12] D Mao, Y Wang, C Ma, L Han, B Jiang, X Gan, S Hua, W Zhang, T Mei, and J Zhao, WS_2 mode-locked ultrafast fiber laser. Sci. Rep. 2015; 5:7965

[13] Y Chen, G Jiang, S Chen, et al. Mechanically exfoliated black phosphorus as a new saturable absorber for both Q-switching and Mode-locking laser operation. Opt. Express. 2015; 23(10):12823–12833

[14] Z Luo,Y Huang, J Weng, et al. 1.06 μm Q-switched ytterbium-doped fiber laser using few-layer topological insulator Bi_2Se_3 as a saturable absorber. Opt. Express. 2013; 21(24) :29516–29522

[15] J Sotor, G Sobon, K Grodecki, et al. Mode-locked erbium-doped fiber laser based on evanescent field interaction with Sb_2Te_3 topological insulator. Appl. Phys. Lett. 2014; 104(25):251112

[16] K Kashiwagi and S Yamashita. Deposition of carbon nanotubes around microfiber via evanescent light. Opt. Express. 2009; 17(20):18364–18370

[17] Z Cheng, H Li, and P Wang. Simulation of generation of dissipative soliton, dissipative soliton resonance and noise-like pulse in Yb-doped mode-locked fiber lasers. Opt. Express. 2015; 23(5):5972–5981

[18] A Ivanenko, S Turitsyn, S Kobsev, and M Dubov. Mode-locking in 25-km fibre laser. in Optical Communication (ECOC), 2010 36th European Conf. and Exhibition on. 2010:1–3

[19] A Hideur, T Chartier, M Brunel, S Louis, C Özkul, and F Sanchez. Generation of high energy femtosecond pulses from a side-pumped Yb-doped double-clad fiber laser. Appl. Phys. Lett. 2001; 79:3389

[20] K Kieu, W H Renninger, A Chong, and F. W. Wise. Sub-100 fs pulses at watt-level powers from a dissipative-soliton fiber laser. Opt. Lett. 2009; 34(5):593–595

[21] Y Huang, Z Luo, F Xiong, Y Li, M Zhong, Z Cai, H Xu, and H Fu. Direct generation of 2 W average-power and 232 nJ picosecond pulses from an ultra-simple Yb-doped double-clad fiber laser. Opt. Lett. 2015; 40(6):1097–1100

[22] H A Haus. Mode-locking of lasers,. IEEE J. Sel. Top. Quant Electron. 2000; 6(6):1173–1185

[23] G P Agrawal. Nonlinear Fiber Optics. 4th ed. San diego, CA. Academic Press; 2009

[24] Z Zhang and G Dai. All-normal-dispersion dissipative soliton ytterbium fiber laser without dispersion compensation and additional filter. IEEE Photon. J. 2011; 3(6):1023–1029

[25] B Sonia, F Christophe, K Huseyin, and P Periklis. Pulse shaping in mode-locked fiber lasers by in-cavity spectral filter. Opt. Lett. 2014; 39(3):438–441

[26] S Yamashita. A tutorial on nonlinear photonic applications of carbon nanotube and graphene. J. Lightwave Technol. 2012; 30(4):427–447.

[27] Y Li and S L Qu. Femtosecond laser-induced breakdown in distilled water for fabricating the helical microchannels array. Opt. Lett. 2011; 36(21):4236–4238

[28] Z Sun, T Hasan, F Wang, A G. Rozhin, I H. White, and A C. Ferrari. Ultrafast stretched-pulse fiber laser mode-locked by carbon nanotubes. Nano Res. 2010; 3:404–411

[29] E J R Kelleher, J C Travers, Z Sun, A G Rozhin, A C Ferrari, S V Popov, and J R Taylor. Nanosecond-pulse fiber lasers mode-locked with nanotubes. Appl. Phys. Lett. 2009; 95(11):111108

[30] S Kobtsev, S Kukarin, and Y Fedotov. Ultra-low repetition rate mode-locked fiber laser with high-energy pulses. Opt. Express. 2008; 16(26):21936–21941

[31] T North and M Rochette. Raman-induced noiselike pulses in a highly nonlinear and dispersive all-fiber ring laser. Opt. Lett. 2013; 38(6):890–892

[32] D Strickland and G Mourou. Compression of amplified chirped optical pulses. Opt. Commun. 1985; 56(6):447–449

[33] M E Fermann and I Hartl. Ultrafast fibre lasers. Nature Photon. 2013; 7:868–874

[34] Y Zaouter, F Guichard, C Hoenninger, et al. High average power 600 uJ ultrafast fiber laser for micromachining application. Journal of Laser Applications. 2015; 27: S29301

[35] G A Ball, C E Holton, G Hull-Allen, and W W Morey. 60 mW 1.5 μm single-frequency low-noise fiber laser MOPA. IEEE J. Photon. Technol. Lett. 1994; 6(2):192–194.

[36] A Malinowski, A Piper, J H V Price, K Furusawa, Y Jeong, J Nilsson, and D J Richardson. Ultrashort-pulse Yb^{3+}-fiber-based laser and amplifier system producing>25-W average power. Opt. Lett. 2004; 29(17):2073–2075

[37] L Zhang, Y G Wang, H J Yu, et al. 20 W high-power picosecond single-walled carbon nanotube based MOPA laser system. J. Lightwave Technol. 2012; 30(16):2713–17

[38] J J Chi, P X Li, H Hu, et al. 120W subnanosecond ytterbium-doped double clad fiber amplifier and its application in supercontinuum generation. Laser Phys. 2014; 24(8): 085103

[39] http://www.ipgphotonics.com/apps_mat_lab_cutting.htm

[40] J Gabzdyl. Application versatility of nanosecond pulsed fiber lasers. Ind Laser Solut. 2014; 29 (1):p4

[41] J Yun, C Gao, S Zhu, C Sun, H He, L Feng, L Dong, et al. High-peak-power, single-mode, nanosecond pulsed, all-fiber laser for high resolution 3D imaging LIDAR system. Chin. Opt. Lett. 2012; 10(12):121402

[42] A Liu, M A Norsen and R D Mead. 60W green output by frequency doubling of polarized Yb-doped fiber laser. Opt. Lett. 2005; 30(1):67–69

[43] N Nishizawa, H Kawagoe and M Yamanaka. Highly functional ultrashort pulse fiber laser sources and applications for optical coherence tomography. CPMT Symposium Japan (ICSJ) 2015, IEEE. Kyoto. 2015: 85–87.

[44] M E Fermann, A Galvanauskas, and G Sucha. Ultrafast lasers: technology and applications. 1st edn. Marcel Dekker AG: CRC Press; 2002

[45] K Sugioka and Y Cheng. Ultrafast lasers—reliable tools for advanced materials processing. Light: Science & Applications. 2014; 3: e149

[46] L Rihakova1 and H Chmelickova. Laser micromachining of glass, silicon, and ceramics. Adv Mater Sci Eng 2015; 2015:584952

[47] I Miyamoto, K Cvecek, Y Okamoto, et al. Internal modification of glass by ultrashort laser pulse and its application to microwelding, Appl. Phys. A. 2014; 114:187–208

[48] N A Inogamov, V V Zhakhovsky, S I Ashitkov, et al. Pump-probe method for measurement of thickness of molten layer produced by ultrashort laser pulse. AIP Conf. Proc. 1278. 2010; 590–599

[49] J M Vadillo and J J Laserna. Laser-induced plasma spectrometry: truly a surface analytical tool. Spectrochim. Acta Part B Atomic Spectroscopy. 2004; 59(2):147–161

[50] D Wu, S Z Wu, J Xu, et al. Hybrid femtosecond laser micro-fabrication to achieve true 3D glass/polymer composite biochips with multiscale features and high performance: the concept of ship-in-a-bottle biochip. Laser Photon. Rev. 2014; 8(3):458–467

Section 6

Applications of Short Pulse Lasers

Chapter 12

Effects of Different Laser Pulse Regimes (Nanosecond, Picosecond and Femtosecond) on the Ablation of Materials for Production of Nanoparticles in Liquid Solution

Abubaker Hassan Hamad

Additional information is available at the end of the chapter

http://dx.doi.org/10.5772/63892

Abstract

Ultra-short laser pulse interaction with materials has received much attention from researchers in micro- and nanomachining, especially for the generation of nanoparticles in liquid environments, because of the straightforward method and direct application for organic solvents. In addition, the colloidal nanoparticles produced by laser ablation have very high purity—they are free from surfactants and reaction products or by-products. In this chapter, nanosecond, picosecond and femtosecond laser pulse durations are compared in laser material processing. Due to the unique properties of the short and ultra-short laser pulse durations in material processing, they are more apparent in the production of precision material processing and generation of nanoparticles in liquid environments.

Keywords: lasers, laser ablation, nanoparticles, pulse duration, nanosecond lasers, picosecond lasers, femtosecond lasers

1. Introduction

Different laser pulse regimes (nanosecond, picosecond and femtosecond) were used not only to generate nanoparticles but also to manipulate them. Different laser wavelengths were selected to reduce the size of the nanoparticles and change their morphology. The study in this filed focuses on using different laser types and parameters to generate and manipulate of micro- and nanomaterials. Researchers have used different types of lasers not only to produce new materials

but also for precise micro- and nanomachining. Generating lasers with short and ultra-short pulse duration leads to high-precision laser processing. Lasers with pulse durations in the femtosecond to picosecond range demonstrate a significant development in quality for different materials in comparison with nanosecond or longer laser pulses [1]. In addition, using pulsed lasers to produce nanoparticles in liquid environments is a promising alternative to chemical methods for the production of totally ligand-free colloidal nanoparticles [2].

In general, for laser material processing, two different laser pulse duration regimes are used: long pulse duration, such as nanosecond pulse duration, which generates quite a significant heat-affected zone in the material because "the pulse duration is longer than the thermalisation time of most metals" [3]. This type of laser is suitable for removing materials or ablation. Short pulse duration (picosecond laser) and ultra-short pulse duration (femtosecond laser) yield better results, suited to the production of high-precision micro- and nanomachining. Typical laser pulse durations for precise laser material processing are 10 ps or less. It has been shown that suitable laser pulse durations for the micromachining of copper and stainless steel are in the range of 10–100 ps [3].

However, there is little evidence that researchers have approached the issue of lasers in nanotechnology in terms of precise and controllable ablation and their ability to generate nanoparticles from different materials. Consequently, the aim of this chapter is to provide an overview of how different laser pulses can be used in laser-material interaction and the production of nanoparticles.

Two important parameters used to describe lasers are their pulse duration (width) and pulse repetition rate (PRR). As shown in **Figure 1a**, laser pulse duration can also be described as full-width at half of the maximum (FWHM) amplitude of the laser pulse. Pulse repetition rate or pulse repetition frequency refers to the number of pulses emitted per second. For 1 kHz of PRR, the time period T would be 0.001 s (see **Figure 1b**).

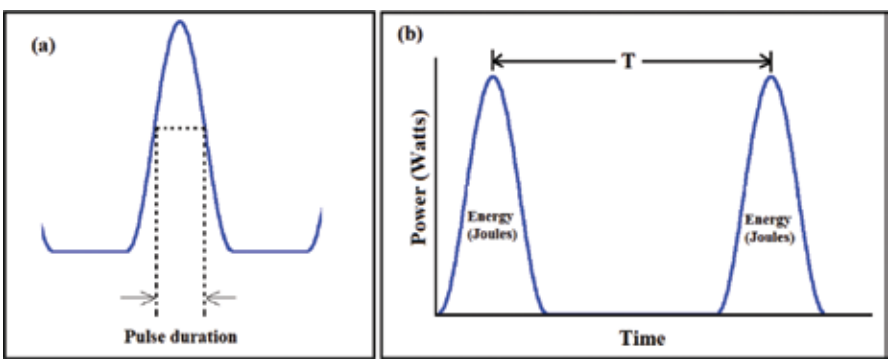

Figure 1. Pulse width or pulse duration (a) and pulse repetition rate (b) of a laser.

Two further parameters of pulsed lasers, which are especially relevant for ultrafast lasers, are the laser's peak power (P_{peak}), which is equal to the laser pulse energy divided by laser pulse

duration ($P_{peak} = E_p/\tau$) and the average laser power, which is equivalent to the laser pulse energy multiplied by the pulse repetition rate ($P_{ave.} = E_p \times PRR$) [4].

In this chapter, the author shows the effects of different laser pulse interactions (nanosecond, picosecond and femtosecond lasers) with materials and the ablation of nanoparticles in a liquid environment in terms of their size, size distribution, morphology and production rate (productivity).

2. Pulsed laser ablation

Ultra-short laser pulse duration in the range of femtosecond laser pulses and a few picoseconds can be used to produce high-quality and precise material processing. Ultra-short pulse duration can only interact with electrons but longer pulse duration interacts with lattice. It is worth mentioning that during the interaction of an ultra-short laser pulse with materials, heat conduction is limited [5]. As a result of this, the material will be ablated within a spatial or well-defined area with minimised mechanical and thermal damage of the ablated area on the target. In contrast, longer (nanosecond) pulse duration irradiation on the materials leads to continuously heating the target material. The laser pulse energy will then be spread by heat conduction to an area outside the laser spot size, causing the irradiated target to boil and evaporate. Boiling and evaporation of the target material leads to the production of an uncontrollable melt layer [6]. In the case of nanosecond laser pulse duration, this problem may be caused by imprecise machining or marking.

There is existing research on laser-material interaction [6–8]; however, these show how differently pulsed lasers can be used for material processing, especially in nanotechnology. Furthermore, there are relevant findings concerning laser ablation of nanoparticles in liquid environments [9–12], and they are somewhat showing the effects of different laser pulse durations on the ablation of nanoparticles. Even most previous research on laser-material interaction and laser-generated nanoparticles tends to highlight laser beam parameters and experimental setups to produce small and well-distributed nanoparticles and to precision material processing, there is little emphasis on the optimal laser parameters to apply in laser material processing. Moreover, little attention has been given to the conceptualisation of the structure and phase of the nanoparticles produced by laser ablation in a liquid solution. Consequently, an understanding of the optimal pulse regime for these applications is critical in order to support and enhance the performance of laser material processing in nanotechnology.

3. Laser-material interaction at different laser pulse durations

Laser ablation of the materials starts with photon absorption, followed by the heating and photoionisation of the subjected area on the target by the laser beam. Subsequently, the ablated materials released from the target surface as solid fragments, vapours, liquid drops or as an expanding plasma plume. The amount of ablated material and phase depends on the absorbed

energy by the target material [13]. After laser-material interaction with short pulses and low intensity, due to the inverse Bremsstrahlung, the laser beam energy will be absorbed by free electrons from the material followed by thermalisation within the electrons, and energy transfer to the lattice. Finally, energy will be lost due to electron heat transfer to the target material. The energy transfer from the laser beam to the target material can be described using 1D and 2D diffusion models when this is considered rapid thermalisation in the electron subsystem and if both lattice and electron subsystems are characterised by their temperatures (T_i lattice temperature and T_e electron temperature) [5]:

$$C_e \frac{\partial T_e}{\partial t} = -\frac{\partial Q(z)}{\partial z} - \gamma\left(T_e - T_i\right) + S \tag{1}$$

$$C_i \frac{\partial T_i}{\partial t} = \gamma\left(T_e - T_i\right) \tag{2}$$

$$Q(z) = -k_e\left(\frac{\partial T_e}{\partial z}\right) \tag{3}$$

$$S = I(t) A\alpha\, e^{-\alpha z} \tag{4}$$

where $Q(z)$ is the heat flux along the z-axis perpendicular to the target material surface, S is the laser heating source, $I(t)$ is the laser intensity as a function of time, A is the surface transmissivity ($A = 1 - R$), R is the reflectivity of the target material, α is the absorption coefficient of the target material, C_e is the heat capacity of the electrons per unit volume, C_i is the lattice heat capacity per unit volume, γ is the parameter characterising the electron-lattice coupling, and k_e is the thermal conductivity of the electrons. Two non-linear differential Eqs. (1) and (2) are used to model the cooling dynamics for T_e and T_i, which account for the electron-phonon coupling and thermal conductivity of the sample material [14]. In addition, these equations can be used to model the time evolution of the electron and lattice temperatures, T_e and T_i [15]. Eqs. (1)–(4) can be written as:

$$C_e \frac{\partial T_e}{\partial t} = k_e\left(\frac{\partial^2 T_e}{\partial z^2}\right) - C_i \frac{\partial T_i}{\partial t} + I(t) A\alpha e^{-\alpha z} \tag{5}$$

The lattice heat capacity (C_i) is considerably higher than the electronic heat capacity (C_e); in this case, the electrons have a very high temperature. When the Fermi energy is higher than the electron energy, the non-equilibrium thermal conductivity and heat capacity of the electron can be written as $k_e = k_o\,(T_i).T_e/T_i$ and $C_e = C'_e T_e$, respectively, where $k_o(T_i)$ is the conventional equilibrium thermal conductivity of a material and C'_e is a constant. In Eq. (5), a thermal

conductivity in the lattice subsystem (phonon component) is neglected, and it has three characteristic timescales; τ_e is the electron cooling time ($\tau_e = C_e/\gamma$), τ_i is the lattice heating time ($\tau_e << \tau_i$) ($\tau_i = C_i/\gamma$), and τ_L is the laser pulse duration. In laser-material interaction, these parameters define three different interaction regimes: nanosecond, picosecond and femtosecond [5].

Zimmer [16] proposed a model for the analytical solution of the laser-induced temperature distribution across internal solid-liquid interfaces (see **Figure 2a**). It was shown that high solid surface temperature can be obtained with short laser pulse durations, sufficient interface absorption and high absorption liquids. As shown in **Figure 2b**, in the case of using a nanosecond laser (20 ns), the temperature of the liquid environment is quite higher than that of the transparent solid material.

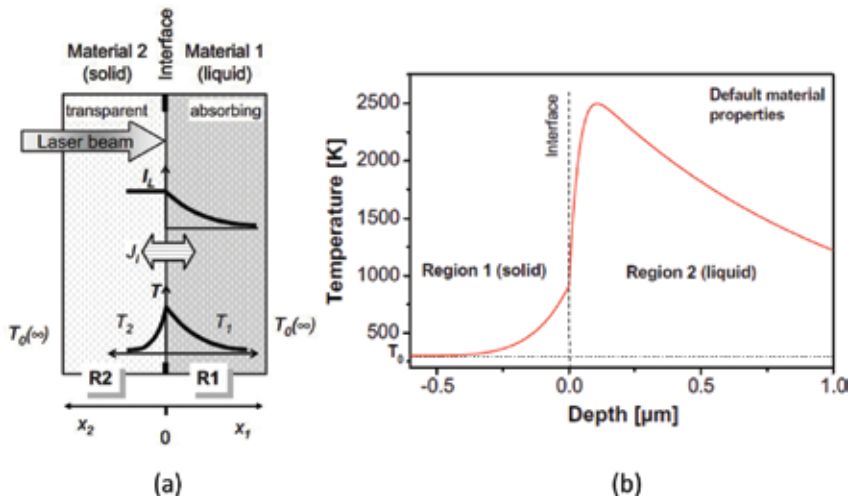

Figure 2. Diagram showing laser heating of a solid-liquid interface. I_L is the laser absorption, T is the temperature distribution in both materials, and J_I is the heat conduction across the interface [16].

3.1. Nanosecond laser

It was shown that the laser pulse duration has an effect on both the material ablation thresholds and penetration depths. Long pulse duration or increasing laser pulse duration increases the threshold fluence and decreases the effective energy penetration depth [1]. Low-intensity long laser pulse interaction with a target material firstly heats the surface of the target due to the absorbed energy, which leads to melting and vaporisation. It should be noted that vaporisation of the target requires much more energy than melting. "In case of low laser intensities the created vapour remains transparent for the laser radiation". The electron and lattice (ion) temperatures are equal ($T_e = T_i = T$) [6]. In other words, if the laser pulse duration is long in comparison with the electron-phonon energy-transfer time ($\tau_L >> \tau_i$), the electrons and lattice temperatures will remain at the same thermal equilibrium point ($T_e = T_i = T$) [5, 17]; as such, Eq. (5) reduces to the heat equation:

$$C_i \frac{\partial T}{\partial t} = k_o \left(\frac{\partial^2 T}{\partial z^2} \right) + I_\alpha \alpha e^{-\alpha z} \tag{6}$$

In nanosecond laser beam interaction with material, the surface of the target material will be heated to melting point and then to vaporisation temperature. During the laser-material interaction, energy will be lost as heat conduction into the target material; the heat penetration depth (l) is given by $l \sim (D_i)^{1/2}$, where D is the heat diffusion coefficient and is given by ($D = k_o/C_i$). It can be noted that for this regime of lasers, the condition $D\tau_L\alpha^2 >> 1$ is fulfilled, for example the thermal penetration depth is quite larger than the optical penetration depth [18]. The energy deposited in the target material per unit mass is given by $E_m \sim I_\alpha t/pl$; at a specific time ($t = t_{th}$), this energy becomes higher than the specific heat of evaporation Ω, at which point considerable evaporation will occur. When $E_m \sim \Omega$, the results are $t_{th} \sim D(\Omega\varrho/I)^2$. Consequently, for strong evaporation conditions, $E_m > \Omega$ or $\tau_L > f_{th}$ can be written for laser intensity as [5, 6]:

$$I > I_{th} \sim \frac{\rho \Omega D^{1/2}}{\tau_L^{1/2}} \tag{7}$$

and for laser fluence as:

$$F > F_{th} \sim \rho \Omega D^{1/2} \times \tau_L^{1/2} \tag{8}$$

The threshold laser fluence increases as $\tau_L^{1/2}$. In nanosecond laser ablation regimes, there is enough time for thermal waves to propagate into the target material and to create a relatively large layer of melted material target [5, 6]. Nanosecond laser pulses can ablate the target materials even at low laser intensities in both the vapour and liquid phases, so a recoil pressure that expels the liquid will be created due to the vaporisation process [6]. Evaporation occurrence makes challenge to precise laser processing with nanosecond laser pulses [18].

At long laser pulse duration, interaction with materials usually fulfils the condition $L_{th} >> \alpha^{-1}$, L_{th} being the heat-penetration depth which is given by $L_{th} \approx (2D\tau_p)^{1/2}$, where $D = k/\rho c$, D is the heat-diffusion coefficient. So, long laser pulse duration creates sufficient time for thermal waves to propagate within the target material, and the absorbed energy will be stored in a layer with a thickness of about L_{th}. In this case, the target material needs much more energy to vaporise than to melt; in other words, evaporation will occur, while the energy absorbed per unit volume into the vaporised layer becomes higher than the latent heat of evaporation per unit volume, namely [19].

$$\Delta z_\upsilon \approx \frac{A\left(F_L - F_{th}\right)}{\rho L_\upsilon} \tag{9}$$

where F_{th} is the laser fluence threshold which represents the minimum energy above which appreciable evaporation occurs from liquid metals. This figure is approximately given by the energy required to melt a surface layer of the target material of the order of L_{th} [19]:

$$F_{th} \approx \frac{\rho c \Delta T_m L_{th}}{A} \tag{10}$$

where $\Delta T_m = T_m - T_o$ and T_m and T_o are the melting and initial target temperature, respectively.

3.2. Picosecond laser

At low-intensity, short laser pulse interactions with a target material, due to the inverse Bremsstrahlung most of the laser energy will be absorbed by the free electrons of the target. This result can be described by the difference between the electron and lattice temperatures ($T_e > T_i$) in a transient nano-equilibrium state. In spite of a small energy exchange between the lattice and the electron heat conduction, the electrons are cooled [6]. For picosecond laser ablation, time t is much greater than τ_e ($t \gg \tau_e$), which is equivalent to $C_e T_e / t \ll \gamma T_e$. In addition, when the condition $\tau_e \ll \tau_L \ll \tau_i$ is fulfilled, Eq. (1) becomes quasi-stationary for the electron temperature [5]. In other words, when the laser pulse duration is shorter than the electron-phonon energy-transfer time, then the electron and lattice have different temperatures, meaning that they will be in a non-thermal equilibrium state. In this case, Eq. (5) becomes the following equations [5, 17]:

$$k_e \left(\frac{\partial^2 T_e}{\partial z^2} \right) - \gamma \left(T_e - T_i \right) + I_\alpha \alpha e^{(-\alpha z)} = 0 \tag{11}$$

$$T_i = T_o + \frac{1}{\tau_i} \int_0^t e^{\left(\frac{t-\theta}{\tau_i} \right)} T_e(\theta) d\theta \tag{12}$$

This method represents the lattice temperature in integral from. The above equations describe heating of metal targets by the laser pulses when the laser pulse duration $\tau_L \gg \tau_e$. By neglecting T_o and when $t \ll \tau_i$, because of the quasi-stationary character of the electron temperature, Eq. (12) can be reduced as follows [5, 18]:

$$T_i \simeq T_e \left(1 - e^{\left(-\frac{t}{\tau_i} \right)} \right) \simeq \left(\frac{t}{\tau_i} \right) T_e \tag{13}$$

It can be noted from the last equation that during picosecond laser ablation, the lattice temperature remains notably lower than the electron temperature, and thus, the lattice temperature in Eq. (11) can be neglected.

When $k_e T_e \alpha^2 \ll \gamma T_e$, from Eqs. (11) and (13), it can be concluded that the electron cooling is due to an exchange of energy with the lattice of the material target. Finally, both the lattice and electron temperature at the end of the laser pulse can be expressed by the following equation [5]:

$$T_e \simeq \frac{I_\alpha \alpha}{\gamma} e^{(-\alpha z)} \; and \; T_i \simeq \frac{F_\alpha \alpha}{C_i} e^{(-\alpha z)} \tag{14}$$

It can be noted that when the condition $\tau_e \ll \tau_L$ is fulfilled, at the end of the pulse, both lattice temperature and attainable lattice temperature are approximately equal.

3.3. Femtosecond laser

For femtosecond lasers, if the laser pulse duration τ_L is assumed to be shorter than the electron cooling time $\tau_{e'}$. ($\tau_L \ll \tau_{e'}$.) and when $t \ll \tau_e$, it is equivalent to $C_e T_e / t \gg \gamma T_e$. In this case, the electron-lattice coupling can be neglected and Eq. (1) can be solved easily. When $D_e \tau_L < \alpha^2$ (where $D_e = k_e / C_e$ is the electron thermal diffusivity) is fulfilled, to simplify the solution of the equation, the electron heat conduction term can be neglected. Thus, Eq. (1) can be written as [5]:

$$C_e^{'} \left(\frac{\partial T_e^2}{\partial t^2} \right) = 2 I_\alpha \alpha e^{(-\alpha z)} \tag{15}$$

which gives

$$T_e(t) = \left(T_o^2 + \frac{2 I_\alpha \alpha}{C_e^{`}} t e^{(-\alpha z)} \right)^{1/2} \tag{16}$$

where $I(t) = I_o$ is assumed constant, and $I_\alpha = I_o A$, and $T_o = T_e(0)$ refer to the initial temperature.

It has been shown that heat conduction of the target material can be neglected at the very short timescales of picosecond and femtosecond laser pulse durations; thus the target temperature at the end of the pulse within the target material can be given by [19].

$$T(z, \tau_L) \approx \left(\frac{\alpha A F_\alpha}{\rho c} \right) e^{(-\alpha z)} \tag{17}$$

where $F_\alpha = I_o \tau_L$ is the laser pulse fluence, and τ_L is the laser pulse duration.

The evolution of the electron temperature (T_e) and lattice temperatures (T_i) after the laser pulse is described by Eq. (5) with S = 0. In addition, the electron temperature and lattice temperature initial conditions are given by Eq. (17) and $T_i = T_o$. Due to the energy transfer to the lattice and heat conduction of the bulk material, the electrons are rapidly cooled after the laser pulse. Since the electron cooling time is quite short, then Eq. (2) can be written as $T_i \simeq T_e(\tau_L)t/\tau_i$. It should be noted that the initial lattice temperature is neglected here. On the other hand, the attainable lattice temperature is determined by the average cooling time of the electrons $\tau_e^{\alpha} = C_e^{`} T_e(\tau_L)/2\gamma$ and is given by the following equation [5]:

$$T_i \simeq T_e^2(\tau_L)\frac{C_e^{`}}{2C_i} \simeq \frac{F_\alpha \alpha}{C_i} e^{(-\alpha z)} \tag{18}$$

Fann et al. [20] and Wang et al. [14] have shown that the time scale for significant energy transfer and fast electron cooling is about 1 ps. In the case of $C_i T_i >> \varrho\Omega$, where ϱ is the density and Ω is the specific heat of evaporation per unit mass, considerable evaporation will occur. From Eq. (18), the conditions for strong evaporation can be given in the form:

$$F_\alpha \geq F_{th}\, e^{(\alpha z)} \tag{19}$$

where $F_{th} = \varrho\Omega/\alpha$ is the threshold fluence laser evaporation by femtosecond laser pulses. Then, the ablation depth per laser pulse (or ablation rate) L can be written as [5, 21]:

$$L \simeq \alpha^{-1} \ln\left(\frac{F_\alpha}{F_{th}}\right) \tag{20}$$

The logarithmic dependence of the ablation depth on the laser pulse fluence is well known for the laser ablation of organic polymers and metal targets with femtosecond pulse duration [5].

It can be noted that Eqs. (14) and (18) give the same expressions for the lattice temperature in both picosecond and femtosecond laser regimes. Therefore, the condition for strong evaporation given by (19), the fluence threshold and the ablation depth per pulse given by (20) remain unchanged [5, 18]. Thus, in the picosecond laser range, it is possible that logarithmic dependence of the ablation depth on the fluence exists. Here, electron heat conduction inside the target material is neglected. In this case, laser ablation is accompanied by the electron heat conduction and production of a melted area in the target material. Even evaporation can be considered as a direct solid-vapour transition process, whereby the existence of a liquid phase in the target material reduces the precision of laser material processing. Femtosecond laser ablation effects a direct solid-vapour transition due to the short timescales in this laser regime; as a result of this, the lattice is heated on a picosecond timescale, leading to the production of vapour and plasma phases followed by a rapid expansion in vacuum. Here, in a first approximation,

thermal conduction into the target material can be neglected during all of the aforementioned processes. Due to the advanced properties of picosecond laser ablation, highly precise and pure laser material processing can be achieved, as has been experimentally demonstrated by Chichkov et al. [5].

4. Comparison of different pulse durations for the ablation of materials and production of nanoparticles

A comparison of the characteristics of nano-, pico- and femtosecond lasers produced nanoparticles and materials processing have been studied [5, 22]. Even the comparison is not a like-for-like; the experimental work should be assumed as a fare comparison between these types of commercial lasers operating at their usual operating conditions [22]. Nanosecond laser ablation of materials occurs due to "melt expulsion driven by the vapour pressure and the recoil pressure of light". The melted material will solidify again because of the instability of this process, in which the fluid phase dynamics and the driving vapour conditions are very complex. As a result of this, the ablated area on the surface of the material target is not precise and uniform in comparison with that produced by a femtosecond laser (see **Figure 3**). Furthermore, nanosecond laser ablation creates a heat-affected zone (HAZ) [4]. It was shown that the HAZ of Al sample for the nanosecond laser ablation was about 40 mm wide, whereas for the femtosecond laser there was not observable because it was <2 mm wide [23].

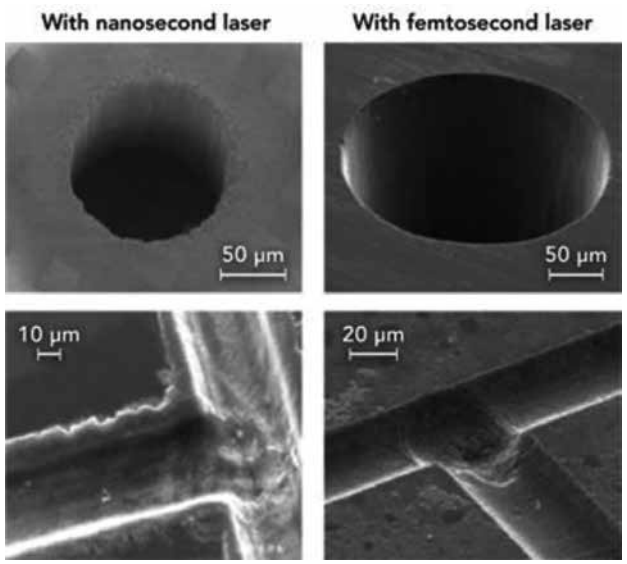

Figure 3. Laser material processing of a glass target by nanosecond laser (left) and femtosecond laser (right) ablation [4].

In the case of short (picosecond laser) and ultra-short laser pulses (femtosecond lasers), their pulse duration (τ) is considerably shorter than the timescale required for energy transfer between the lattice and the free electrons of the material target. As a result of this, very high temperatures and pressures are produced at a very shallow depth in the range of microns. Conversely, irradiated material is heated rapidly by pulsed laser and directly reaches the vapour phase with high kinetic energy without passing through the melting point temperature due to the absorbed energy. In other words, the material ablation will take place by vaporisation without producing a recast layer on the ablated area. As shown in **Figure 3**, the ablated area is very precise and smooth without forming any observable heat-affected zone (HAZ) [4]. The target materials with a high thermal conductivity are very important for the femtosecond laser ablation process because of the stable properties and chemical composition of the area ablated with femtosecond laser ablation [24].

For ultrafast lasers, laser beam energy deposition happens on a timescale that is quite short in comparison with atomic relaxation processes. After the laser energy is absorbed by the electrons, cold ions will be produced, leading to the occurrence of thermalisation at the end of the laser pulse. In addition, the femtosecond laser intensity is quite high and is sufficient to drive highly non-linear absorption processes in the target materials which the laser wavelength cannot absorb. At these high intensities, multi-photon ionisation becomes considerably strong [4]. Because of the very high flux of the femtosecond laser photons, several photons collide and become bound electrons; this is multi-photon ionisation. When the amount of total photon energies absorbed is higher than the ionisation potential, the bound electrons will absorb several photons. As a result, the bound electrons become free from the valence band. The multi-photon ionisation process is higher at very high laser intensities. When the laser intensity (photon flux) is above 10^{13} W/cm^2, multi-photon ionisation becomes very strong and seed electrons are not required to initialise ionisation in high-energy band gap materials or wide band gap materials (see **Figure 4a**) [4].

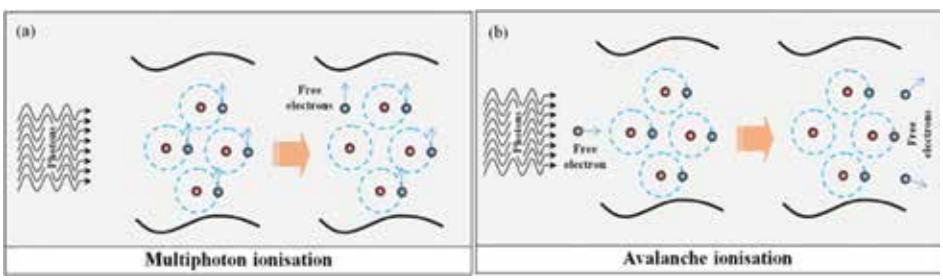

Figure 4. Non-linear ionisation processes of multi-photon absorption (a) and avalanche ionisation (b).

If the kinetic energy of the free electron is very high, some of the energy might be transferred to a bound electron in the target material by collision, thus overcoming the ionisation potential and generating two free electrons; this process is known as (collisional) impact ionisation. Thus, more free electrons will be produced from the bound electrons after the free electrons have absorbed photons. This is called avalanche ionisation, in which free electron density

exponentially increases. It is worth mentioning that avalanche ionisation is highly dependent upon free electron density. Energy loss by phonon emission and energy gain by inverse Bremsstrahlung competition indicate the efficiency of this process. It is responsible for the high-energy gap transition materials at laser intensities below 10^{12} W/cm^2 (see **Figure 4b**) [4]. For femtosecond lasers, avalanche ionisation plays an essential role in the optical breakdown. Briefly, avalanche ionisation produces a macroscopic breakdown of the target materials and multi-photon ionisation produces seed electrons at a critical density of about 10^{20} cm^{-3} [25].

The amount of material removed during laser ablation depends on the amount of energy absorbed by the bulk material target. The dissipation of the absorbed laser energy will usually occur after the laser pulse duration. There are two major mechanisms to explain material removal by laser ablation: thermal vaporisation, where the local temperature increases to above the vaporisation point due to the electron-phonon collisions, and the occurrence of a Coulomb explosion, where the bulk materials release the excited electrons and produce a relatively strong electric field which revokes the ions inside the impact area [4, 26]. According to these mechanisms, femtosecond laser material removal can be classified in two ways: the first is "strong ablation dominated by thermal vaporisation at intensities significantly higher than the ablation threshold" and the second is "gentle ablation governed by the Coulomb explosion near the ablation threshold" [4]. As shown in **Figure 5**, the long-pulse lasers have more heat-affected zones and shock waves in comparison with the shorter picosecond and femtosecond lasers. The main differences between them are due to the mechanism or the basic principles of laser-induced target material removal processes [27].

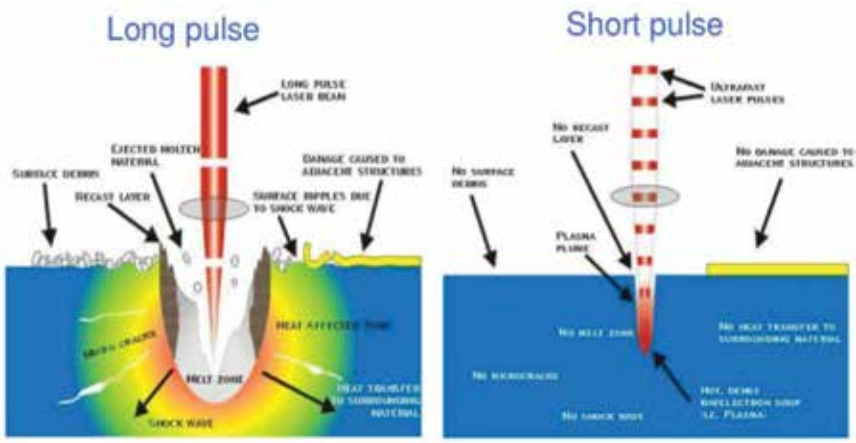

Figure 5. Long-pulse and ultrafast-pulse laser interaction with target material [27].

Laser pulse duration is an important parameter in the laser ablation process. There are quite large differences between the long pulse duration (nanosecond laser) and ultra-short laser pulse duration (femtosecond laser) for the ablation of materials [26]. As shown in **Figure 6**, during nanosecond laser ablation, plasma will be produced during the laser pulse, but during femtosecond laser ablation, it will be produced after the laser pulse has ended. During

nanosecond laser ablation, plasma is a part of the pulse duration, so the pulse serves to reheat the plasma. This leads to higher persistence of the plasma for nanosecond laser ablation than for femtosecond laser ablation [26].

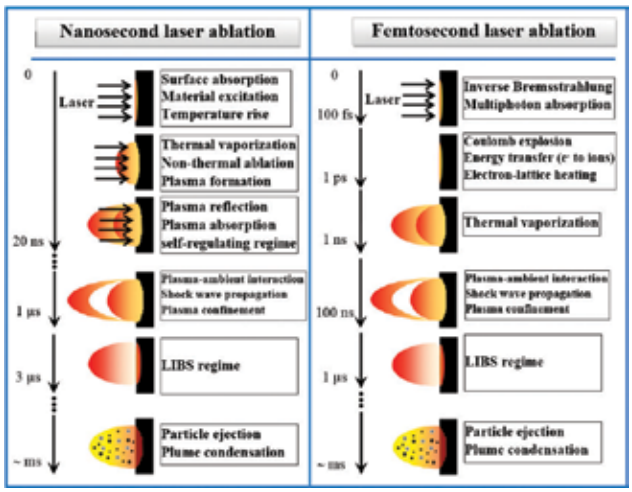

Figure 6. Approximate timescale comparison of pulsed laser energy absorption and ablation, along with the various processes, for nanosecond laser (10 ns) and femtosecond laser (50 fs) ablation in an ambient gas.

As shown in the schematic diagram in **Figure 7**, Lescoute et al. [28] showed that during subpicosecond laser ablation three phases occur behind the shock: liquid, vapour and plasma. The shock waves produced can compress the solid target material. The plasma plume effect is more predominant in picosecond laser ablation than in femtosecond laser ablation [22]. In general, laser-plasma interaction during laser-material ablation is strongly dependent on laser wavelength and the excitation wavelength is a very important parameter in nanosecond laser ablation, as in femtosecond laser ablation. The production of nanoparticles through plasma plume condensation occurs in the microsecond-millisecond timescales.

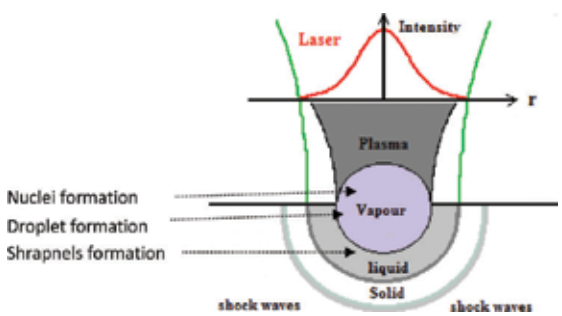

Figure 7. Schematic diagram of ablated matter depicted in an ultra-short, that is subpicosecond, laser-material interaction.

Another advantage of the femtosecond laser is its short timescale which prevents the material target from being heated; this leads to a reduction in the thermal effects in comparison with the nanosecond laser ablation. The duration of the energy transfer process from electron to ion (τ_{ei}) is approximately 1–10 s of a picosecond; this is in the same order as the heat conduction time (τ_{heat}). In an ideal femtosecond laser ablation case, this is considerably longer than the laser pulse duration (t_p). ($\tau_{ei} \sim \tau_{heat} >> t_p$) [26]. This will depend on the type of material sample.

Femtosecond laser energy transfer in the material for ablation will occur through energy absorption by electrons, leading to ionisation and then redistribution of the laser energy to the lattice. Ionisation is either produced by multi-photon ionisation or collisional impact. These processes can be labelled multi-photon ionisation (MPI) and collisional impact ionisation (CII) [26]. Multi-photon ionisation (MPI) occurs when multiple photons provide sufficient energy to the electrons in the valance band; as a result, the electrons are free to reach metastable quantum states by excitation. Collisional impact ionisation (CII) will take place when bound electrons gain energy from free electrons by collision; as a result, the bound electrons will be released.

As shown in **Figure 8**, when a single high fluence fs laser pulse is incident onto a material, the timescale of the physical phenomena involved in laser-material interaction can take place as follows: after 1 fs, photo-ionisation, such as multi-photon absorption and/or tunnelling ionisation, will occur; after 50 fs, avalanche ionisation will occur; and after 100 fs, thermalisation of the electrons of the metal target will take place. Longer laser pulse durations lead to more physical phenomena; after 1 ps, energy transformation from electron to lattice will result, then after 10 ps, some thermodynamic processes such as thermal diffusion, fusion and explosion will occur. In much longer laser pulses, after 1 ns, photochemical processes such as chemical reactions and phase transformation will take place [29].

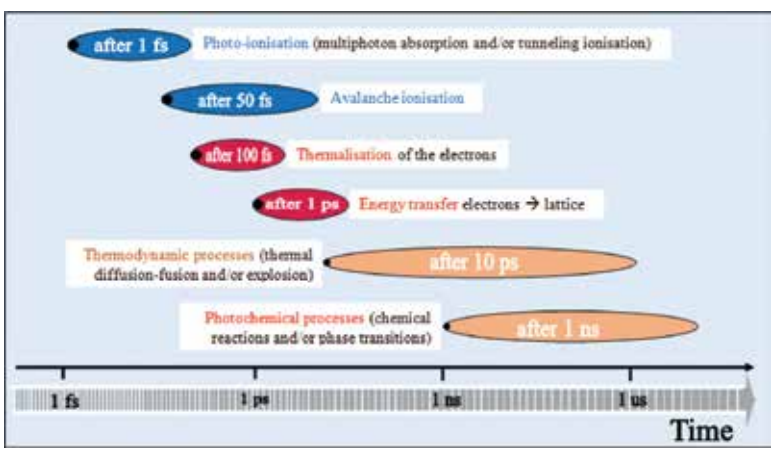

Figure 8. Occurrence of different physical phenomena during different timescales involved in laser-material interaction.

Different types of nanoparticles have been produced by nanosecond [30, 31], picosecond [32, 33] and femtosecond [28, 34, 35] lasers in different liquid environments, vacuum and gas media. A physical aspect of laser ablation in liquid environments is the liquid breakdown phenomena; it has been shown that the conversion efficiency of the radiation energy to a cavitation bubble during radiation focusing of different wavelengths in water is much lower for femtosecond lasers (at 100 fs, efficiency 1–2%) than for nanosecond lasers (at 76 ns, efficiency 22–25%). Femtosecond lasers (120 fs and 800 nm) can produce controllable size and size distribution of nanoparticles, while nanosecond laser produces relatively large, quite widely dispersed particles [36].

The generation of large nanoparticles in a liquid environment by nanosecond laser pulse durations and longer is due to the essential target material melting and laser pulse interaction with the cavitation bubbles that are then produced in the liquid environment [37]. The long pulse duration is sufficient to allow photon coupling with both the electronic and vibrational modes of the sample material. This case will be more predominant when the target material has low reflectivity at the laser wavelength, a large absorption coefficient, a low thermal diffusion coefficient and a low boiling point [38]. Long pulse duration heats the target material continually during the pulse duration. This causes the target material to start boiling and subsequently leads to evaporation, which produces a considerable melt layer. As a result, heat will be transferred to the target that prevents the production of very small structures and small nanoparticles. In nanosecond laser ablation, the laser power heats the target material to melting point and then vaporisation temperature; as such, this process can be considered an indirect solid-vapour transition but a solid-melt-vapour transition [19]. Nanosecond laser ablation ejects an ablation plume which creates a shielding on the surface of the material target, leading to a reduction in the laser power induced to the target. Chemistry material responses, cumulative changes in the target material's surface texture and morphology will occur due to surface melting and a combination of ablation and thermally activated processes [7].

However, the generation of small nanoparticles by short laser pulse duration is due to minimisation of both the thermal effects and the laser pulse interaction with the cavitation bubble [37]. Here, thermal conduction of the target material can be neglected because of the very short timescale and the heated area of the material being of the order of the laser absorption length α^{-1}, where α is the target material absorption coefficient [19]. At short and ultra-short laser pulse durations, because the laser interacts with materials due to very quick excitation of the electron distribution, electron-electron coupling leads to a rapid rise in the electron temperature, followed by lattice heating "at a rate dependent upon the electron-phonon coupling strength, and eventual vaporisation of the transiently heated target". Electronic contributions "can manifest themselves as unexpectedly large ion yields and/or supra-thermal propagation velocities within the expanding plasma plume" [38]. At short and ultra-short pulse durations, because the energy transfer from the electrons to the lattice happens on a longer timescale than for the short or ultra-short pulses, the pulses do not heat the target material continually. This limits the heat conduction within the target material and produces a superheated layer the size of the irradiated volume. This leads to ablation in a

specific area, resulting in minimal thermal damage. Both picosecond and femtosecond laser ablation can be viewed as a direct solid-vapour transition [19].

At short and ultra-short laser pulse durations, the ablation threshold fluence of the target materials decreases and becomes very sharply defined. In addition, the excess energy in the target still can produce thermal effects on the ablation area after the pulse has ended. Furthermore, at ultra-short laser pulse duration, the optical absorption depth reduces due to an optical breakdown caused by the ultra-short laser pulse duration; this can also cause strong absorption in otherwise transparent wide-energy band gap materials. Another advantage of picosecond and femtosecond laser ablation is that they are "separated in time from material response and ejection" [7]. In contrast, for laser production of nanoparticles in a liquid solution, the picosecond laser performs better than the femtosecond laser [37]. It can be seen that only the femtosecond laser avoided the laser-bubble interaction [22].

The size and the morphology of the nanoparticles depend on the laser pulse duration, such as whether a nano-, pico- and femtosecond laser regime is being used and the nature of the target material [39]. Hamad et al. [22] showed that the picosecond laser (10 ps and 1064 nm wavelength) produced more spherical silver nanoparticles than those produced by both nanosecond (5 ns and 532 nm wavelength) and femtosecond (100 fs and 800 nm wavelength) lasers. Under the same conditions, smaller gold nanoparticles were produced in comparison with the silver and titania, with the latter being the largest. It was also concluded that the average size of the nanoparticles was smaller for the shorter wavelength (532 nm) nanosecond laser in relation to picosecond and femtosecond lasers, showing that the role of the laser wavelength is more significant than the laser pulse duration to control the size of the nanoparticles. It is worth mentioning that some silver nanoparticles produced by nanosecond laser have irregular (non-spherical) shapes. Dudoitis et al. [40] showed that the specific nanosecond and picosecond laser parameters can be used to produce controllable particle size distribution of nickel and aluminium in argon gas.

Lescoute et al. [28] observed two groups of particles of two different sizes after femtosecond laser ablation caused by the temperature achieved in the plasma plume: these could be classified into micrometer-size fragments and nanometre-size particles for temperatures lower than the critical temperature and for higher temperatures, respectively. Kabashin and Meunier [34] used femtosecond laser ablation to produce Au nanoparticles in deionised water. The researchers observed two different groups of nanoparticles: the small (about 3–10 nm) and monodispersed particles were produced due to a mechanism which, "associated with thermal-free femtosecond ablation, manifests itself at relatively low laser fluences F, 400 J/cm^2". The second group of particles was of a larger size and a broad size distribution, produced due to plasma-induced heating and ablation that occurs at high laser fluencies. Itina [41] showed that the ultra-short laser pulses produce small nanoparticles and a stable size distribution at optimal experimental parameters. This is because while using short and ultra-short laser pulse duration, laser radiation will not be absorbed by created plasma plume. This leads to transfer much more energy into the target material during very short time. Finally, the target ejected the cluster precursors directly to the liquid solution and the plasma plume is confined to a smaller volume. Chakravarty et al. [42] concluded that the smaller size of silver and copper

nanoparticles can be produced by ultra-short laser pulse duration in comparison with the subnanosecond laser pulse duration. It was shown that broader surface plasmon resonance (SPR) and smaller reflection/transmission of silver and copper nanoparticles deposited by femtosecond laser in comparison with those deposited by subnanosecond laser indicating smaller size particle generation by ultra-short pulse durations. In contrast, Hubenthal et al. [43] concluded that the tailoring the size and shape of nanoparticles with nanosecond pulsed laser is more achieved in comparison with both continuous wave (CW) and femtosecond pulsed lasers.

5. Conclusions

Pulsed laser ablation for material processing and production of nanoparticles in liquid environments have been used due to the unique properties of the laser beam in marking and machining materials. There is a lack of knowledge of the optimal laser beam parameters in this field, as different laser pulse durations respond differently to different materials. A critical comparison of different laser pulse durations in micro- and nanomaterial processing was therefore sought in order to obtain higher quality and productivity. Femtosecond and picosecond lasers were found to be superior to the nanosecond laser for precision material processing. In addition, in spite of the short and ultra-short duration of their laser pulses, these lasers were observed to be more effective for the production of nanoparticles than those with longer pulse durations. Finally, laser wavelength was found to play significant role in the production of nanoparticles. The advantages of femtosecond laser ablation for micro- and nanotechnology are due to non-thermal interaction with solid target materials.

Author details

Abubaker Hassan Hamad*

Address all correspondence to: abubaker.hamad75@yahoo.co.uk

Laser Processing Research Centre, School of Mechanical, Aerospace and Civil Engineering, The University of Manchester, Manchester, UK

References

[1] Le Harzic, R., D. Breitling, M. Weikert, S. Sommer, C. Föhl, S. Valette, C. Donnet, E. Audouard and F. Dausinger, *Pulse width and energy influence on laser micromachining of metals in a range of 100 fs to 5 ps*. Applied Surface Science, 2005. 249(1): pp. 322–331. doi: 10.1016/j.apsusc.2004.12.027

[2] Rehbock, C., J. Jakobi, L. Gamrad, S. van der Meer, D. Tiedemann, U. Taylor, W. Kues, D. Rath and S. Barcikowski, *Current state of laser synthesis of metal and alloy nanoparticles as ligand-free reference materials for nano-toxicological assays*. Beilstein Journal of Nanotechnology, 2014. 5(1): pp. 1523–1541. doi:10.3762/bjnano.5.165

[3] Jaeggi, B., B. Neuenschwander, M. Schmid, M. Muralt, J. Zuercher and U. Hunziker, *Influence of the pulse duration in the ps-regime on the ablation efficiency of metals*. Physics Procedia, 2011. 12: pp. 164–171. doi:10.1016/j.phpro.2011.03.118

[4] Lucas, L. and J. Zhang, *Femtosecond laser micromachining: a back-to-basics primer*. 2012, http://www.industrial-lasers.com/

[5] Chichkov, B.N., C. Momma, S. Nolte, F. von Alvensleben and A. Tünnermann, *Femtosecond, picosecond and nanosecond laser ablation of solids*. Applied Physics A, 1996. 63(2): pp. 109–115. doi:10.1007/bf01567637

[6] Momma, C., B.N. Chichkov, S. Nolte, F. von Alvensleben, A. Tünnermann, H. Welling and B. Wellegehausen, *Short-pulse laser ablation of solid targets*. Optics Communications, 1996. 129(1): pp. 134–142. doi:10.1016/0030-4018(96)00250-7

[7] Brown, M.S. and C.B. Arnold, *Fundamentals of laser–material interaction and application to multiscale surface modification*, in *Laser Precision Microfabrication*. 2010, Springer. pp. 91–120. doi:10.1007/978-3-642-10523-4__4

[8] Han, J. and Y. Li, *Interaction Between Pulsed Laser and Materials*. Lasers-Applications in Science and Industry, K. Jakubczak, Ed. InTech, 2011. doi:10.5772/25061

[9] Sukhov, I.A., G.A. Shafeev, V.V. Voronov, M. Sygletou, E. Stratakis and C. Fotakis, *Generation of nanoparticles of bronze and brass by laser ablation in liquid*. Applied Surface Science, 2014. 302(0): pp. 79–82. doi:10.1016/j.apsusc.2013.12.018

[10] Tyurnina, A.E., V.Y. Shur, R.V. Kozin, D.K. Kuznetsov and E.A. Mingaliev, *Synthesis of stable silver colloids by laser ablation in water*. Proceedings of SPIE 2013. 9065: p. 8. doi: 10.1117/12.2053557

[11] Yan, Z. and D.B. Chrisey, *Pulsed laser ablation in liquid for micro-/nanostructure generation*. Journal of Photochemistry and Photobiology C: Photochemistry Reviews, 2012. 13(3): pp. 204–223. doi:10.1016/j.jphotochemrev.2012.04.004

[12] Amans, D., C. Malaterre, M. Diouf, C. Mancini, F. Chaput, G. Ledoux, G. Breton, Y. Guillin, C. Dujardin and K. Masenelli-Varlot, *Synthesis of oxide nanoparticles by pulsed laser ablation in liquids containing a complexing molecule: impact on size distributions and prepared phases*. The Journal of Physical Chemistry C, 2011. 115(12): pp. 5131–5139. doi: 10.1021/jp109387e

[13] Amendola, V. and M. Meneghetti, *Laser ablation synthesis in solution and size manipulation of noble metal nanoparticles*. Physical Chemistry Chemical Physics, 2009. 11(20): pp. 3805–3821. doi:10.1039/B900654K

[14] Wang, X., D.M. Riffe, Y.-S. Lee and M. Downer, *Time-resolved electron-temperature measurement in a highly excited gold target using femtosecond thermionic emission*. Physical Review B, 1994. 50(11): p. 8016. doi:10.1103/PhysRevB.50.8016

[15] Schoenlein, R., W. Lin, J. Fujimoto and G. Eesley, *Femtosecond studies of nonequilibrium electronic processes in metals*. Physical Review Letters, 1987. 58(16): p. 1680. doi:10.1103/PhysRevLett.58.1680

[16] Zimmer, K., *Analytical solution of the laser-induced temperature distribution across internal material interfaces*. International Journal of Heat and Mass Transfer, 2009. 52(1): pp. 497–503. doi:10.1016/j.ijheatmasstransfer.2008.03.034

[17] Fujimoto, J., J. Liu, E. Ippen and N. Bloembergen, *Femtosecond laser interaction with metallic tungsten and nonequilibrium electron and lattice temperatures*. Physical Review Letters, 1984. 53(19): p. 1837. doi:10.1103/PhysRevLett.53.1837

[18] Stafe, M., A. Marcu and N. Puscas, *Pulsed Laser Ablation of Solids: Basics, Theory and Applications*. Vol. 53. 2013: Springer Science & Business Media. doi: 10.1007/978-3-642-40978-3

[19] Amoruso, S., R. Bruzzese, N. Spinelli and R. Velotta, *Characterization of laser-ablation plasmas*. Journal of Physics B: Atomic, Molecular and Optical Physics, 1999. 32(14): p. R131. doi:10.1088/0953-4075/32/14/201

[20] Fann, W., R. Storz, H. Tom and J. Bokor, *Electron thermalization in gold*. Physical Review B, 1992. 46(20): p. 13592. doi:10.1103/PhysRevB.46.13592

[21] Izawa, Y., Y. Setuhara, M. Hashida, M. Fujita and Y. Izawa, *Ablation and amorphization of crystalline Si by femtosecond and picosecond laser irradiation*. Japanese Journal of Applied Physics, 2006. 45(7R): p. 5791. doi:10.1143/JJAP.45.5791

[22] Hamad, A., L. Li and Z. Liu, *A comparison of the characteristics of nanosecond, picosecond and femtosecond lasers generated Ag, TiO_2 and Au nanoparticles in deionised water*. Applied Physics A, 2015. 120(4): pp. 1247–1260. doi:10.1007/s00339-015-9326-6

[23] Le Harzic, R., N. Huot, E. Audouard, C. Jonin, P. Laporte, S. Valette, A. Fraczkiewicz and R. Fortunier, *Comparison of heat-affected zones due to nanosecond and femtosecond laser pulses using transmission electronic microscopy*. Applied Physics Letters, 2002. 80(21): pp. 3886–3888. doi:10.1063/1.1481195

[24] Hirayama, Y. and M. Obara. *Molecular dynamics simulation of heat-affected zone of copper metal ablated with femtosecond laser*. in *Lasers and Applications in Science and Engineering*. 2005: International Society for Optics and Photonics. doi:10.1117/12.589513

[25] Musaev, O., A. Midgley, J. Wrobel and M. Kruger, *Laser ablation of alumina in water*. Chemical Physics Letters, 2010. 487(1): pp. 81–83. doi:10.1016/j.cplett.2010.01.011

[26] LaHaye, N.L., S.S. Harilal, P.K. Diwakar and A. Hassanein, *The effect of laser pulse duration on ICP-MS signal intensity, elemental fractionation, and detection limits in fs-LA-*

ICP-MS. Journal of Analytical Atomic Spectrometry, 2013. 28(11): pp. 1781–1787. doi: 10.1039/c3ja50200g

[27] *Machining with Long Pulse Lasers, Machining with Ultrafast Laser Pulses*. 2011 [cited 2016; Available from: http://www.cmxr.com/Education/Short.html, http://www.cmxr.com/Education/Long.html

[28] Lescoute, E., L. Hallo, D. Hébert, B. Chimier, B. Etchessahar, V. Tikhonchuk, J.-M. Chevalier and P. Combis, *Experimental observations and modeling of nanoparticle formation in laser-produced expanding plasma*. Physics of Plasmas (1994–present), 2008. 15(6): p. 063507. doi:10.1063/1.2936267

[29] Royon, A., Y. Petit, G. Papon, M. Richardson and L. Canioni, *Femtosecond laser induced photochemistry in materials tailored with photosensitive agents [Invited]*. Optical Materials Express, 2011. 1(5): pp. 866–882. doi:10.1364/OME.1.000866

[30] Damian, V., C. Udrea, M. Bojan, C. Luculescu, A. Armaselu and I. Apostol. *Aluminum nanoparticles production by laser ablation in liquids*. in *International Conference on Applications of Optics and Photonics*. 2011: International Society for Optics and Photonics. doi: 10.1117/12.894525

[31] Gondal, M., T.F. Qahtan, M. Dastageer, T.A. Saleh and Y.W. Maganda. *Synthesis and characterization of copper oxides nanoparticles via pulsed laser ablation in liquid*. in *10th International Conference on High Capacity Optical Networks and Enabling Technologies (HONET-CNS)*. 2013: IEEE. doi:10.1109/HONET.2013.6729774

[32] Hamad, A., L. Li, Z. Liu, X.L. Zhong and T. Wang, *Picosecond laser generation of Ag–TiO_2 nanoparticles with reduced energy gap by ablation in ice water and their antibacterial activities*. Applied Physics A, 2015. 119(4): pp. 1387–1396. doi:10.1007/s00339-015-9111-6

[33] Giorgetti, E., A. Giusti, S. Laza, P. Marsili and F. Giammanco, *Production of colloidal gold nanoparticles by picosecond laser ablation in liquids*. Physica Status Solidi (a), 2007. 204(6): pp. 1693–1698. doi:10.1002/pssa.200675320

[34] Kabashin, A.V. and M. Meunier, *Synthesis of colloidal nanoparticles during femtosecond laser ablation of gold in water*. Journal of Applied Physics, 2003. 94(12): pp. 7941–7943.

[35] Torres-Mendieta, R., R. Mondragón, E. Juliá, O. Mendoza-Yero, J. Lancis and G. Mínguez-Vega, *Fabrication of high stable gold nanofluid by pulsed laser ablation in liquids*. Advanced Materials Letters, 2015. 6(12): p. 6. doi:10.5185/amlett.2015.6038

[36] Perrière, J., E. Millon and E. Fogarassy, *Recent advances in laser processing of materials*. 2006, Elsevier.

[37] Intartaglia, R., K. Bagga and F. Brandi, *Study on the productivity of silicon nanoparticles by picosecond laser ablation in water: towards gram per hour yield*. Optics Express, 2014. 22(3): pp. 3117–3127. doi:10.1364/OE.22.003117

[38] Ashfold, M.N., F. Claeyssens, G.M. Fuge and S.J. Henley, *Pulsed laser ablation and deposition of thin films*. Chemical Society Reviews, 2004. 33(1): pp. 23–31. doi:10.1039/B207644F

[39] Kuzmin, P.G., G.A. Shafeev, G. Viau, B. Warot-Fonrose, M. Barberoglou, E. Stratakis and C. Fotakis, *Porous nanoparticles of Al and Ti generated by laser ablation in liquids*. Applied Surface Science, 2012. 258(23): pp. 9283–9287. doi:10.1016/j.apsusc.2011.08.108

[40] Dudoitis, V., V. Ulevičius, G. Račiukaitis, N. Špirkauskaitė and K. Plauškaitė, *Generation of metal nanoparticles by laser ablation*. Lithuanian Journal of Physics, 2011. 51(3): pp. 248–259.

[41] Itina, T.E., *On nanoparticle formation by laser ablation in liquids*. The Journal of Physical Chemistry C, 2010. 115(12): pp. 5044–5048. doi:10.1021/jp1090944

[42] Chakravarty, U., P. Naik, C. Mukherjee, S. Kumbhare and P. Gupta, *Formation of metal nanoparticles of various sizes in plasma plumes produced by Ti: sapphire laser pulses*. Journal of Applied Physics, 2010. 108(5): p. 053107. doi:10.1063/1.3475512

[43] Hubenthal, F., M. Alschinger, M. Bauer, D.B. Sánchez, N. Borg, M. Brezeanu, R. Frese, C. Hendrich, B. Krohn and M. Aeschliman. *Irradiation of supported gold and silver nanoparticles with continuous-wave, nanosecond, and femtosecond laser light: a comparative study*. in *Microtechnologies for the New Millennium 2005*. 2005: Proceedings of SPIE 5838, Nanotechnology II. doi:10.1117/12.608560

Chapter 13

Application of PLD-Fabricated Thick-Film Permanent Magnets

Masaki Nakano, Takeshi Yanai and
Hirotoshi Fukunaga

Additional information is available at the end of the chapter

http://dx.doi.org/10.5772/64235

Abstract

Isotropic Nd-Fe-B thick-film magnets have been prepared using a pulsed laser deposition (PLD) method with the control of laser energy density (LED) followed by post-annealing. The characteristics of the method are a high deposition rate up to several tens of microns per hour together with a reliability of magnetic properties due to the good transfer of composition from an Nd-Fe-B target to a film. Several micro-machines comprising the isotropic Nd-Fe-B films such as a miniaturized DC motor and a swimming machine in liquid were demonstrated. Furthermore, the deposition of isotropic Nd (or Pr)-Fe-B thick-film magnets on a Si or glass substrate was carried out to apply the films to various micro-electro-mechanical-systems (MEMS). We also introduced the preparation of isotropic Sm-Co, Fe-Pt, and nano-composite Nd-Fe-B+α-Fe film magnets synthesized using the PLD.

Keywords: pulsed laser deposition, thick-film magnet, isotropic, post-annealing

1. Introduction

Much research on anisotropic Nd-Fe-B film magnets thicker than several microns was carried out in order to advance miniaturized electronic devices including micro-electro-mechanical-systems (MEMS) [1–7]. It is generally known that the $(BH)_{max}$ value of an isotropic Nd-Fe-B film [8, 9] is smaller than that of an anisotropic Nd-Fe-B one; however, the flexibility of magnetization of the isotropic films is attractive in practical and various applications. Töpfer et al. demonstrated a multipolarly magnetized isotropic Nd-Fe-B film using a screen printing method

[10]. Yamashita et al. also reported that the torque of a milli-size motor comprising a multipolarly magnetized isotropic thick film exceeded the torque of a motor using an anisotropic one [11].

In Sm-Co thick-film magnets, we have difficulty in overcoming the values of $(BH)_{max}$ for Nd-Fe-B films due to the low saturation magnetization. However, several researchers have demonstrated Sm-Co thick films because of their high Curie temperature and good corrosion resistance [12–19]. For example, Cadieu et al. reported in-plane anisotropic Sm-Co films with a thickness above 100 μm using sputtering together with pulsed laser deposition (PLD) methods [16, 17]. In addition, Budde and Gatzen demonstrated a magnetic micro-actuator comprising a sputtering-made 30-μm-thick Sm-Co film [19].

Fe-Pt magnet is a promising material to use in the medical field owing to its outstanding biocompatibility [20]. In order to advance medical MEMS, the miniaturization of Fe-Pt magnets is necessary [21]. Aoyama and Honkura [22] and Liu et al. [23] reported isotropic Fe-Pt film magnets thicker than several microns using a sputtering method from the medical application point of view.

Here, we show the properties of isotropic Nd-Fe-B [24–28] thick-film magnets prepared using the PLD method and several miniaturized machines [24, 25, 28] comprising the Nd-Fe-B thick film. Moreover, PLD-fabricated isotropic Sm-Co, Fe-Pt, and nano-composite Nd-Fe-B+α-Fe thick films were introduced.

2. Experimental

A target such as Nd-Fe-B, Pr-Fe-B, Sm-Co, and Fe-Pt was ablated with an Nd-YAG pulse laser with a wavelength of 355 nm together with a frequency of 30 Hz in a vacuum atmosphere. The chamber was evacuated to approximately 4×10^{-5} Pa with a vacuum equipment before the deposition. During the deposition, each target was rotated and the distance between the target and the substrate (*T-S* distance) varied from 5 to 20 mm. In the experiment, a laser power was measured with a power meter in front of the entrance lens of the chamber. The laser energy density (LED) varied by controlling the laser power (LP) together with a spot size of laser beam which could be changed by moving the distance between the focal lens and the target intentionally (see **Figure 1**). Here, the spot size was expressed as a defocusing rate (DF rate) = (TD − FD)/FD × 100(%), where TD is the distance between the condensing lens and the target and FD is the focal length. In the experiment, the control of the defocusing rate (DF rate) enabled us to change LED widely compared with the variation of LP.

In some experiments, the post-annealing of a conventional annealing (CA) and a pulse annealing (PA), respectively, was carried out as shown in **Figure 2**. After magnetizing each sample up to 7 T with a pulse magnetizer, M-H loops were measured by using a vibrating sample magnetometer (VSM) which could apply a magnetic field up to approximately 1800 kA/m reversibly. The average thickness was mainly measured with a micrometer. In some samples, the thickness was estimated from hysteresis loops of as-deposited films [29]. Surface observation and composition analysis were carried out by using a scanning electron microscope (SEM) and an SEM-energy-dispersive X-ray spectroscopy (EDX), respectively.

http://dx.doi.org/10.5772/64235

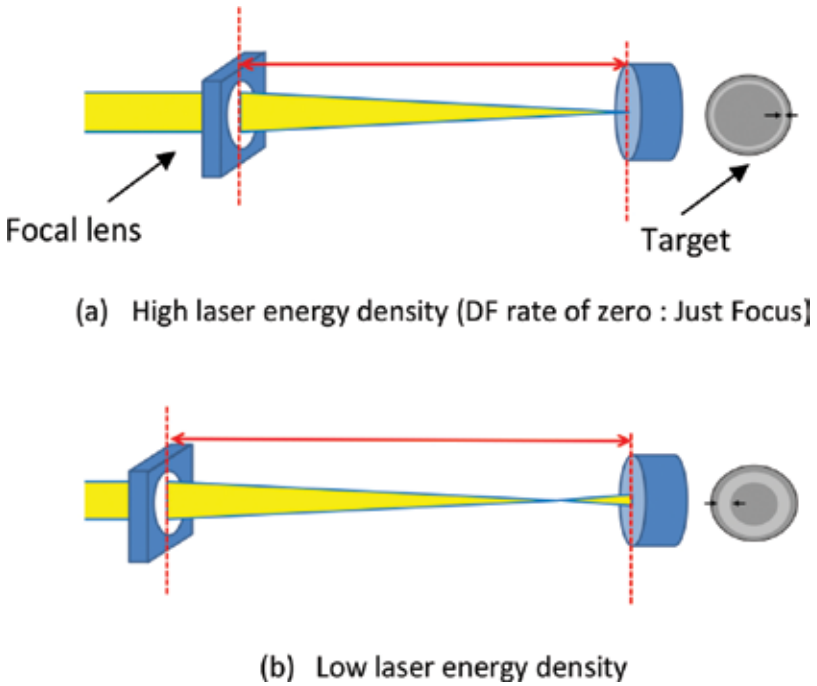

Figure 1. Schematic diagrams of deposition process with several values of the laser energy density (LED) which was controlled by changing the laser power and DF rate independently. (a) High laser energy density (DF rate of zero: just focus) and (b) low laser energy density.

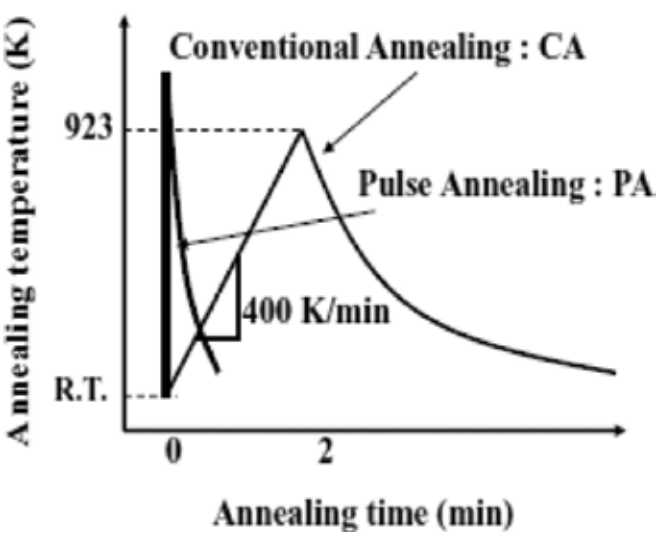

Figure 2. Schematic diagram of conventional annealing (CA) and pulse annealing (PA) methods.

3. Results

3.1. PLD-fabricated isotropic Nd-Fe-B thick-film magnets

Figure 3 shows the in-plane demagnetization curves of isotropic Nd-Fe-B thick-film magnets after the crystallization using two methods of CA and PA with each optimum condition. Both samples were prepared using an $Nd_{2.4}Fe_{14}B$ target under the deposition rate higher than 40 μm/h. The annealing duration of PA was approximately 1.8 s and the ramping rate of CA was 400 K/min (see **Figure 2**). The coercivity value of the annealed film using PA method was larger by approximately 300 kA/m than the annealed 673 K/min sample using CA method. On the other hand, the remanence and $(BH)_{max}$ values of the two samples were almost the same. Transmission electron microscopy (TEM) observation revealed that the use of PA method enabled us to reduce the size of $Nd_2Fe_{14}B$ grains compared with that of the sample annealed using CA method. We considered that the enhancement in coercivity is due to the increases in the domain pinning sites. From these results, a high-speed crystallization annealing process (PA method) is a promising method to refine $Nd_2Fe_{14}B$ grains of PLD-fabricated Nd-Fe-B thick-film magnets.

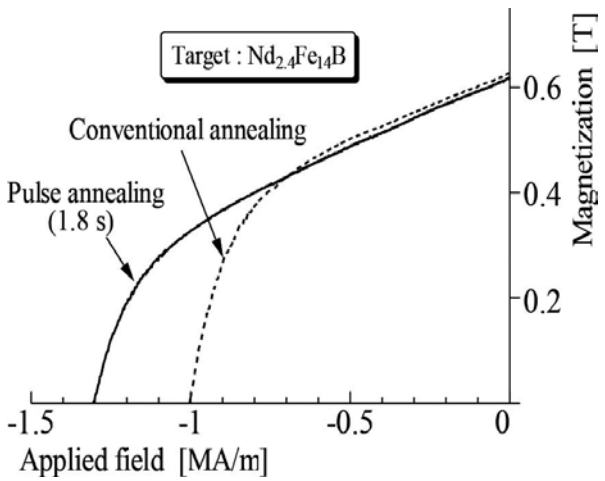

Figure 3. Demagnetization curves (in-plane) of PLD-made Nd-Fe-B thick films crystallized by two methods of CA and PA.

Figure 4 shows the relationship between the LED and magnetic properties of annealed Nd-Fe-B film magnets deposited on Ta substrates prepared using an $Nd_{2.6}Fe_{14}B$ target. All the samples were annealed using PA method. As the inset in each figure shows, the laser power LP and DF rate were controlled independently. In low energy density, high coercivity (H_c) and low remanence (M_r) were obtained, respectively. The samples with low H_c and high M_r were prepared in high energy density. In order to obtain the high deposition rate above 40 μm/h, LED less than 30 mJ/mm^2 was used. In this chapter, PA method was used in the results of

Sections 3.1–3.5. On the other hand, energy density above 200 mJ/mm^2 was used in the results of Sections 3.5 and 3.6.

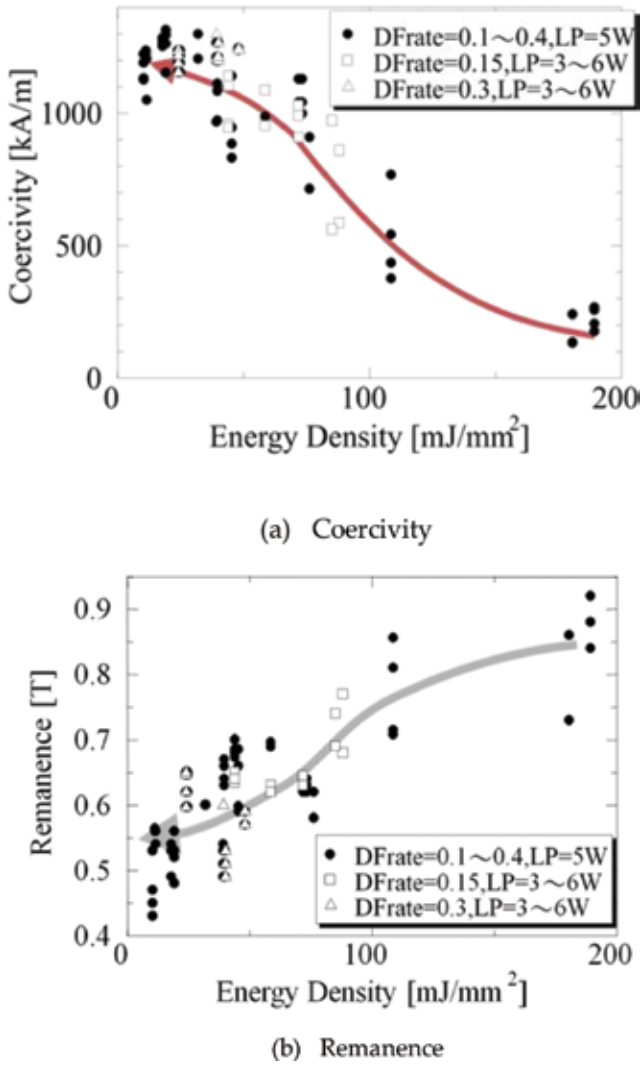

Figure 4. Effects of energy density of laser beam on (a) coercivity and (b) remanence. The laser power LP and DF rate varied independently. (a) Coercivity and (b) Remanence.

3.2. Applications comprising isotropic Nd-Fe-B thick-film magnets

Several miniaturized devices comprising the above-mentioned isotropic Nd-Fe-B thick films were demonstrated [24, 25, 28]. **Figure 5(a)** shows a small DC brushless motor with a 200-μm-thick isotropic PLD-made Nd-Fe-B film magnet. The values of coercivity and remanence of the film deposited on an Fe substrate were approximately 970 kA/m and 0.6 T, respectively. It

was confirmed that the motor with a thickness of 0.8 mm and diameter of 5 mm rotates at approximately 15,000 rpm under no-load test. The torque constant of 0.0236 mNm/A showed at the gap of 0.1 mm between a rotor and a stator.

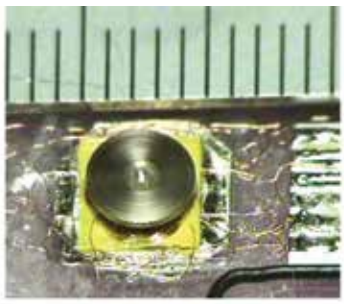

(a) DC brush-less motor

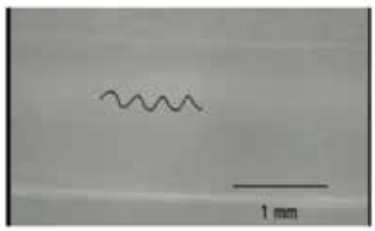

(b) Swimming machine in liquid

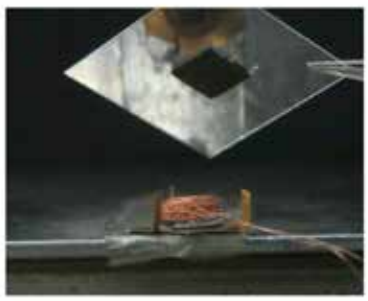

(c) Electromagnetic friction-drive micro-motor

Figure 5. Three micro-machines comprising PLD-made Nd-Fe-B thick films. (a) DC brushless motor, (b) swimming machine in liquid, and (c) electromagnetic friction-drive micro-motor.

A spiral-type micro-machine with 0.14 mm in outer diameter and 1.0 mm in length was fabricated as seen in **Figure 5(b)**. In the machine, an isotropic PLD-made Nd-Fe-B film magnet was deposited on a tungsten (W) wire. After magnetizing the film magnet in the circumferential direction, the machine rotated in sync with the rotating external magnetic field and the

http://dx.doi.org/10.5772/64235

spiral structure generated the propellant force. In the experiment, three types of liquids with kinematic viscosity of 1, 10, and 100 mm^2/s, respectively, were used. In order to move the wireless micro-machine, an external magnetic field of 8 kA/m was applied under the frequency range between 2 and 10 Hz. It was confirmed that the machine swam at the speed of 0.2–1.6 mm/s under various conditions.

A micro-motor using a PLD-made Nd-Fe-B film magnet with a thickness of 384 μm deposited on a Ta substrate was demonstrated as shown in **Figure 5(c)**. The stator is a coil with a ferrite core in the center together with a ferrite disc at the bottom. As an alternating voltage was applied to the coil, pulling and reacting forces worked alternatively between the film and the ferrite core, and as a result the rotor of the film magnet vibrated. The rotor is magnetically mounted onto the stator without mechanical attachments. The motor rotated at approximately 300 rpm with a starting torque of approximately 2 μNm. We confirmed that the electromagnetic friction-drive motor had a large torque together with a low rotational speed.

3.3. Isotropic Nd-Fe-B thick-film magnets deposited on Si substrates

As mentioned earlier, increase in thickness of an Nd-Fe-B film magnet is indispensable to provide a sufficient magnetic field. Here, the deposition of isotropic Nd-Fe-B thick-film magnet on Si substrates was carried out in order to apply the film magnet to various MEMS. It is generally known that we had difficulty in suppressing the peeling phenomenon due to the different values of a linear expansion coefficient for a Si substrate and an Nd-Fe-B film. Even if a buffer layer such as a Ta film was used, the maximum thickness was less than 200 μm. Here, we reported that a control of microstructure of Nd-Fe-B thick films enabled us to increase the thickness above 100 μm without a buffer layer on Si substrates [30].

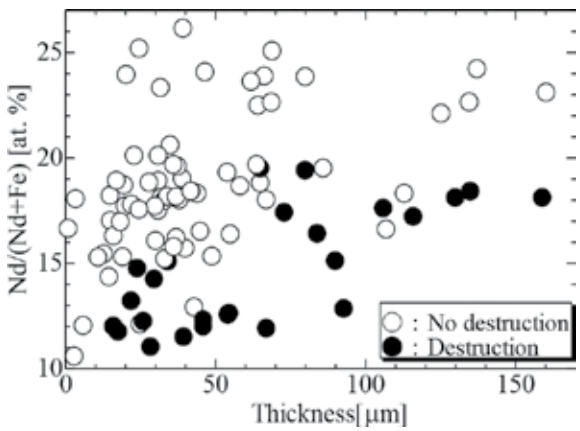

Figure 6. Relationship between thickness and Nd contents in isotropic Nd-Fe-B thick-film magnets deposited on Si substrates after an annealing process. Increase in Nd contents enabled us to increase the thickness up to 160 μm without mechanical destruction.

We investigated the relationship between thickness and Nd contents in annealed isotropic Nd-Fe-B thick films deposited on SiO_2/Si substrates as seen in **Figure 6**. After all the samples were

annealed using PA method, many samples displayed by the symbol "○" could be prepared without mechanical destruction. All the other samples plotted as "●" were broken. As the Nd content exceeded by approximately 22 at.%, the thickness of the sample symbolized "○" could be enhanced up to approximately 160 μm. The thickness of Nd-Fe-B films deposited on Si substrates increased without the deterioration of mechanical properties. It was considered that the precipitation of Nd element at the boundary of Nd-Fe-B grains together with the triple junctions due to the composition adjustment of $Nd_2Fe_{14}B$ phase is effective to suppress the destruction of the samples through an annealing process.

3.4. Isotropic Pr-Fe-B thick-film magnets deposited on glass substrates

The laser beam was focused on the surface of a $Pr_XFe_{14}B$ (X = 1.8–2.4) target under a high deposition rate of approximately several tens of microns per hour (see **Figure 1(b)**). **Figure 7** shows the magnetic properties as a function of Pr contents in each film with a thickness above 10 μm. Coercivity increased and residual magnetic polarization decreased with an increase in the amount of Pr. As displayed in **Figure 6**, Nd(or Pr)-Fe-B thick films with rare-earth amount less than 15 at.% deposited on Si substrates were mechanically broken after a post-annealing process. On glass substrates, the Pr amounts could be reduced down to approximately 13 at.% without the deterioration of mechanical properties. It was also confirmed that an approximately 100-μm-thick Pr-Fe-B thick film with $(BH)_{max}$ of about 80 kJ/m^3 could be deposited on a glass substrate.

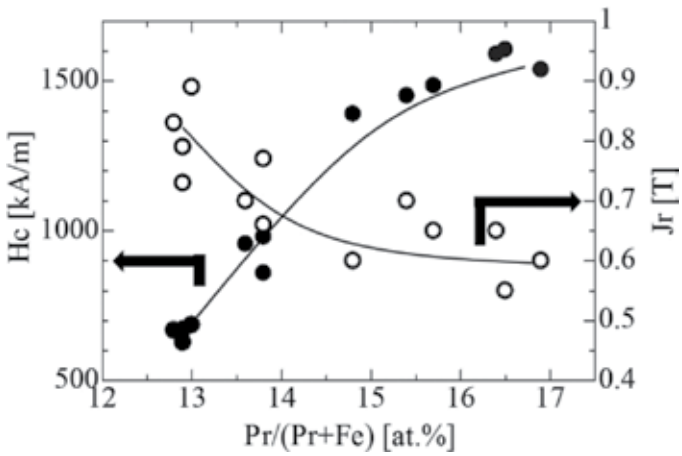

Figure 7. Remanence and coercivity as a function of Pr contents in Pr-Fe-B thick-film magnets deposited on glass substrates.

3.5. PLD-fabricated isotropic Sm-Co thick-film magnets

In this section, a high-speed PLD method with a deposition rate of approximately several tens of microns per hour was applied to fabricate Sm-Co thick-film magnets by using an $Sm_{1.2}Co_5$ target. In-plane and perpendicular M-H loops of a sample annealed by CA method are shown

in **Figure 8**. The perpendicular M-H loop was corrected by a demagnetization factor of 1.0. The structure of as-deposited films prepared using an $SmCo_5$ target without a substrate heating system was amorphous as seen in **Figure 9**; therefore, the samples were post-annealed at a temperature of 973 K with a heating rate of 673 K/min (CA method). After the post annealing, not only $SmCo_5$ but also Sm_2Co_{17} phases were observed. In the present stage, we demonstrate the fabrication nano-composite Sm-Co/α-Fe multilayered film magnets using the PLD method [31].

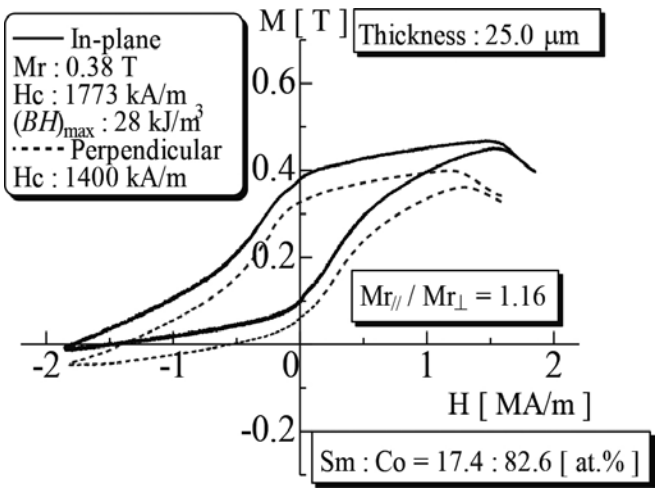

Figure 8. In-plane and perpendicular M-H loops of a PLD-fabricated Sm-Co thick film after a post-annealing process.

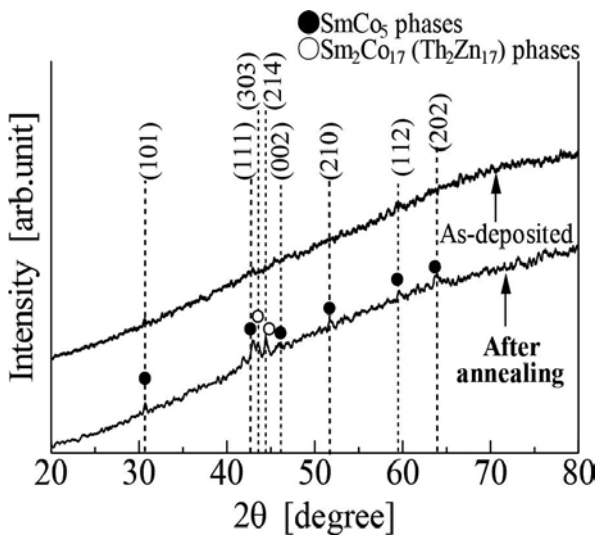

Figure 9. X-ray diffraction patterns of a PLD-fabricated Sm-Co thick film before and after a post-annealing process.

3.6. PLD-fabricated isotropic Fe-Pt thick-film magnets

In this section, a $Fe_{70}Pt_{30}$ target was ablated with an Nd-YAG pulse laser under LED above 200 mJ/mm^2 in a vacuum atmosphere (see **Figure 1(a)**). **Figure 10** shows coercivity values of the as-deposited films as a function of laser power. The values drastically increased at a power of 3 W and then gradually decreased with increase in power. We confirmed that the substrate temperature was proportional to the laser power due to the rise of a radiation heat from a target. As a result, it was found that $L1_0$ ordered phase together with relatively high coercivity could be obtained using a suitable laser power without using a substrate heating system and a post-annealing process. **Figure 11** shows in-plane M-H loop of a Fe-Pt film fabricated at a power of 3 W. The values of coercivity, remanence, and $(BH)_{max}$ were 378 kA/m, 0.94 T, and 104 kJ/m^3, respectively [32]. We, therefore, considered that remanence enhancement occurred in the sample because the saturation magnetization of 1.43 T for $Fe_{50}Pt_{50}$ ordered phase [33].

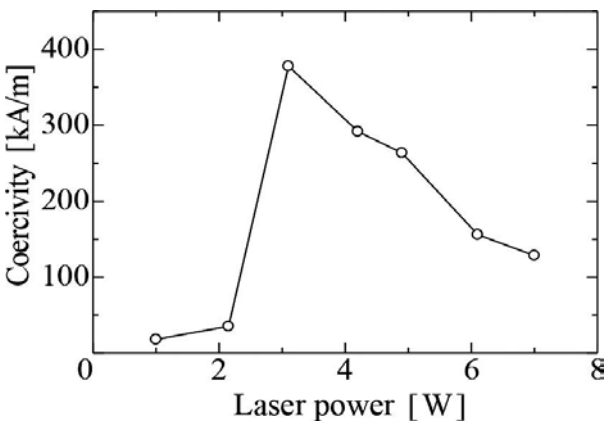

Figure 10. In-plane coercivity values for as-deposited Fe-Pt film magnets prepared from $Fe_{70}Pt_{30}$ target as a function of laser power.

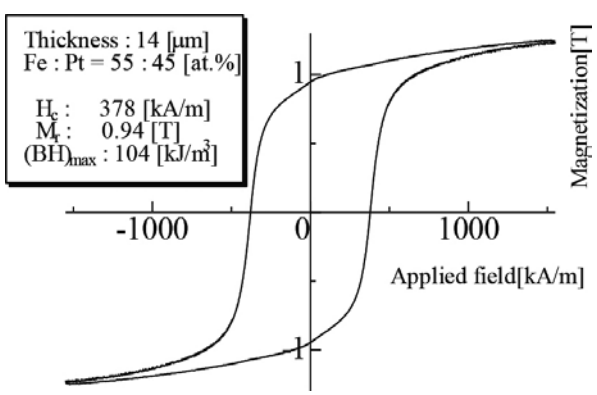

Figure 11. In-plane and perpendicular M-H loops of an as-deposited Fe-Pt film magnet prepared from a $Fe_{70}Pt_{30}$ target.

http://dx.doi.org/10.5772/64235

3.7. PLD-fabricated isotropic nano-composite Nd-Fe-B + α-Fe thick-film magnets

In this section, we focus on the use of high LED above 200 mJ/mm^2 in order to adopt a different deposition process by taking account of the explosively emitting process of atoms from a target. The as-deposited films had amorphous phase including α-Fe grains, and a nano-composite structure could be obtained after the pulse annealing [34].

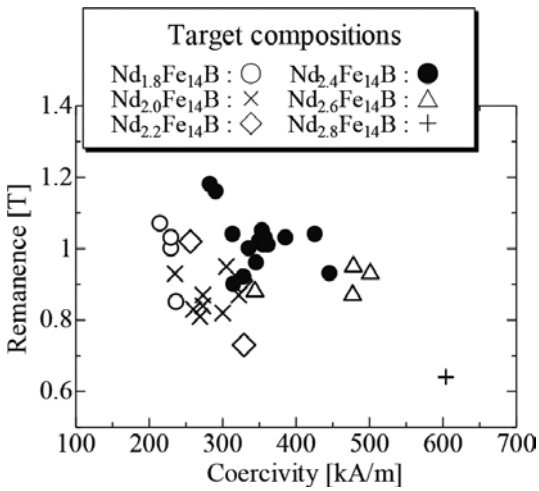

Figure 12. Relationship between remanence and coercivity values of films thicker than 10 μm by using six targets with various compositions. Use of an $Nd_{2.4}Fe_{14}B$ target is effective to obtain good magnetic properties.

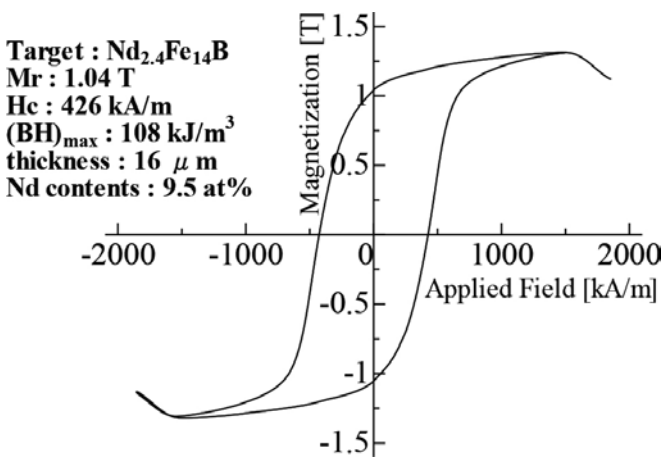

Figure 13. M-H loop of a 16-μm-thick Nd-Fe-B film magnet prepared using laser energy density above 200 mJ/mm^2 together with an $Nd_{2.4}Fe_{14}B$ target.

Investigation on the relationship between coercivity and remanence of each sample thicker than 10 μm prepared by six Nd-Fe-B targets with various compositions under LED above

200 mJ/mm^2 (see **Figure 12**). In all the targets, the deposition rate was higher than 20 μm/h and the reduction in the Nd contents of each film by several atomic percentages was observed compared with that of the corresponding target. The samples prepared by using an $Nd_{2.4}Fe_{14}B$ target had relatively large values of coercivity and remanence. **Figure 13** shows an in-plane M-H loop of a 16-μm-thick Nd-Fe-B + α-Fe thick-film magnet prepared using LED higher than 200 mJ/mm^2 together with an $Nd_{2.4}Fe_{14}B$ target.

4. Conclusion

In this chapter, we introduced the preparation of rare-earth thick-film magnets using a PLD method and their applications. The PLD-made Nd-Fe-B thick-film magnets thicker than 10 μm deposited on metal substrates could be applicable to miniaturized devices by taking account of the relatively good magnetic and mechanical properties. In addition, Nd(or Pr)-Fe-B thick films with a thickness above 100 μm without a buffer layer on a Si or glass substrate. Preparation of Sm-Co, Fe-Pt, and nano-composite Nd-Fe-B + α-Fe thick-film magnets was also carried out.

Author details

Masaki Nakano*, Takeshi Yanai and Hirotoshi Fukunaga

*Address all correspondence to: mnakano@nagasaki-u.ac.jp

Graduate School of Engineering, Nagasaki University, Nagasaki, Japan

References

[1] F. Dumas-Bouchat, L. F. Zanini, M. Kustov, N. M. Dempsey, R. Grechishkin, K. Hasselbach, J. C. Orlianges, C. Champeaux, A. Catherinot, and D. Givord, *Appl. Phys. Lett*. 96, 102511 (2010).

[2] A. Walther, C. Marcoux, B. Desloges, R. Grechishkin, D. Givord, and N. M. Dempsey, *J. Magn. Magn. Mater*. 321, 590 (2009).

[3] N. M. Dempsey, A. Walther, F. May, D. Givord, K. Khlopkov, and O.Gutfleisch, *Appl. Phys. Lett*. 90, 092509 (2007).

[4] M. Uehara, *J. Magn. Magn. Mater*. 284, 281 (2004).

[5] L. K. B. Serrona, A. Sugimura, N. Adachi, T. Okuda, H. Ohsato, I. Sakamoto, A. Nakanishi, M. Motokawa, D. H. Ping, and K. Hono, *Appl. Phys. Lett*. 82, 1751 (2003).

[6] B. A. Kapitanov, N. V. Kornilov, Ya. L. Linetsky, and V. Yu. Tsvetkov, *J. Magn. Magn. Mater*. 127, 289 (1993).

[7] S. Yamashita, J. Yamasaki, M. Ikeda, and N. Iwabuchi, *J. Appl. Phys*. 70, 6627 (1991).

[8] T. Spelitos, D. Niarchos, V. Skumryev, Y. Zhang, and G. Hadjipanayis, *J. Magn. Magn. Mater*. 272–276, e877(2004).

[9] A. Melsheimer, and H. Kronműller, *Phys. B*. 299, 251 (2001).

[10] J. Töpfer, B. Pawlowski, and B. Pawlowski, *Proceedings of the 18th Int. Workshop on High Performance Magnets and Their Applications*, 828 (2004).

[11] F. Yamashita, S. Nishimura, N. Menjo, O. Kobayashi, M. Nakano, H. Fukunaga, and K. Ishiyama, *IEEE Trans. Magn*. 46, 2012 (2010).

[12] S. Fahler, V. Neu, U. Hannemann, S. Oswald, J. Thomas, B. Holzapfel, and L. Schultz, Annual report 2001 in IFW Dresden, 21 (2001).

[13] K. Chen, H. Hegde, S. U. Jen, and F. J. Cadieu, *J. Appl. Phys*. 73, 5923 (1999).

[14] S. Takei, X. Liu, and A. Morisako, *Phys. Stat. Sol.(a)* 204, 12, 4166(2007).

[15] L. N. Zhang, J. S. Chen, J. Ding, and J. F. Hu, *J. Appl. Phys*. 103, 043911 (2008).

[16] F. J. Cadieu, H. Hegde, E. Schloemann, and H. J. Van Hook, *J. Appl. Phys*. 76, 6059 (1994).

[17] F. J. Cadieu, R. Rani, X. R. Qian, and Li Chen, *J. Appl. Phys*. 83, 6247 (1998).

[18] F. J. Cadieu, R. Rani, T. Theodoropoulos, and Li Chen, *J. Appl. Phys*. 85, 5895 (1999).

[19] T. Budde, and Hans H. Gatzen, *J. Appl. Phys*. 99, 08N304 (2006).

[20] T. Nakayama, M. Watanabe, M. Homma, T. Kanno, K. Kimura, and O. Okuno, *J. Magn. Soc. Jpn*. 21, 377 (1997). (in Japanese).

[21] A. Yamazaki, M. Sendoh, K. Ishiyama, K. I. Arai, R. Kato, M. Nakano, and H. Fukunaga, *J. Magn.Magn. Mater*. 272–276, e1741 (2004).

[22] H. Aoyama, and Y. Honkura, *J. Magn. Soc. Jpn*. 20, 237 (1996). (in Japanese).

[23] W. F. Liu, S. Suzuki, D. S. Li, and K. Machida, *J. Magn. Magn. Mater*. 302, 201 (2006).

[24] M. Nakano, S. Sato, H. Fukunaga and F. Yamashita, *J. Appl. Phys*. 99, 08N301 (2006).

[25] M. Nakano, S. Sato, F. Yamashita, T. Honda, J. Yamasaki, K. Ishiyama, M. Itakura, J. Fidler, T. Yanai, and H. Fukunaga, *IEEE Trans. Magn*. 43, 2672 (2007).

[26] M. Nakano, H. Takeda, F. Yamashita, T. Yanai, and H. Fukunaga, *IEEE Trans. Magn*. 44, 4229 (2008).

[27] H. Fukunaga, T. Kamikawatoko, M. Nakano, T. Yanai, and F. Yamashita, *J. Appl. Phys*. 109, 07A758 (2011).

[28] M. Nakano, T. Honda, J. Yamasaki, S. Sato, F. Yamashita, J. Fidler, and H. Fukunaga, *Sens. Lett*. 5, 48 (2007).

[29] M. Nakano, S. Tsutsumi, and H. Fukunaga, *IEEE Trans. Magn*. 38, 2913 (2002).

[30] M. Nakano, Y. Chikuba, M. Oryoshi, A. Yamashita, T. Yanai, R. Fujiwara, T. Shinshi, and H. Fukunaga, *IEEE Trans. Magn*. 51, #2102604 (2015).

[31] H. Fukunaga, A. Tou, M. Itakura, M. Nakano, and T. Yanai, *IEEE Trans. Magn*. 50, 2101504 (2014).

[32] M. Nakano, W. Oniki, T. Yanai, and H. Fukunaga, *J. Appl. Phys*. 109, 07A723 (2011).

[33] O. Gutfleisch, J. Lyubina, K. H. Műller, and L. Schultz, *Adv. Eng. Mater*. 7, 208 (2005).

[34] M. Nakano, K. Motomura, T. Yanai, and H. Fukunaga, *IEEE Trans. Magn*. 50, 2101404 (2014).

Chapter 14

Obtaining a Thin and Flexible Dental Film of Hydroxyapatite

Lucia Marin Biolan, Andrei Bedros Agop and Doriana Forna

Additional information is available at the end of the chapter

http://dx.doi.org/10.5772/63955

Abstract

The deposition of hydroxyapatite thin films has become a topic of interest in medical applications. This dental film applied on the surface of the tooth may act as a highly resistant and flexible artificial enamel, protecting teeth and removing tooth sensitivity. Other possibilities include whitening and coating enamel-deficient structures. We obtained this flexible film of hydroxyapatite using laser ablation. The plasma plumes were generated by an Nd:YAG nanosecond laser in a vacuum chamber. We used the pulsed laser deposition (PLD) technique and conducted investigations using optical emission spectroscopy (OES), laser-induced breakdown spectroscopy (LIBS), and Raman spectroscopy. Initially, a thin film of HA was deposited on a soluble substrate and heated, followed by immersion into pure water to dissolve the substrates. The originality of our approach consists in the fact that the flexible HA film can be obtained in pure state, because it grows without a substrate, using just a base and lateral supports between, on which it will grow vertically. In order to verify the compatibility and the "stickiness" of HA on the teeth, we chose to grow the film between the roots of a tooth. In this case, besides the film, we also obtained HA microfibers. We tried to bind the film on an extracted tooth. A protocol must be established in order to allow the bonding of the film to the surface of the tooth, knowing that contaminants such as saliva or sulcular fluid increase bonding strength to enamel or dentin. We realized an efficient bonding as HA absorbs protein, the mineral also participates in this ionic exchange, and we strengthened the tooth structure. The main purpose of our research is to rebuild the dentine layer or enamel and close the dental channels. Our experiments led to the creation of an HA foil that has the role of protecting teeth against cariogenic bacteria and could even have cosmetic effects by teeth whitening. This dental plaster acts as an artificial HA enamel, very resistant and flexible, protecting the tooth and eliminating

dental sensitivity. Being very thin, it is invisible once applied on teeth and can be observed only by examination under a strong light.

Keywords: hydroxyapatite, biocompatibility, films, biomaterials, laser, tooth

1. Introduction

This chapter describes a unique way to obtain a flexible pure hydroxyapatite film. In the past years, the nanocomposites have been in the center of attention due to their unique physical and chemical properties.

Specifically, the biomaterials have been widely studied, motivated by their clinical applications. Among these, the hydroxyapatite has been studied due to its remarkable properties, such as biocompatibility, osteoconductivity, and bioactivity. This material is naturally found in the human body, being one of the major constituents of bones and teeth. As a consequence, HA has been widely used in many fields, including biomedical applications. Our experiments led to the creation of a thin HA film that has the role of protecting teeth against cariogenic bacteria and could even have cosmetic effects by teeth whitening. This dental plaster acts as an artificial HA enamel, very resistant and flexible, protecting the tooth and eliminating dental sensitivity. Being very thin, it is invisible once applied on teeth and can be observed only by examination under a strong light. The plaster, produced by pulsed laser deposition (PLD), can be manipulated with tweezers and applied on the tooth. The originality of our approach consists in the fact that the flexible HA film can be obtained in pure state, because it grows without a substrate, using just a base and lateral supports between which it will grow on vertical direction.

2. Experimental methods

The deposition of hydroxyapatite thin films has become a topic of interest in medical applications. This dental film applied on the surface of the tooth may act as a(n) artificial, highly resistant, and flexible enamel, protecting teeth and removing tooth sensitivity. There is also a possibility for whitening and covering deficient enamel structure. We obtained this flexible film of hydroxyapatite using laser ablation. We also tried to apply the film on an extracted tooth. The plasma plumes were generated by an Nd:YAG nanosecond laser in a vacuum chamber with 10^{-6} Torr. We used the pulsed laser deposition technique and for the investigations we opted for optical emission spectroscopy (OES) and Raman spectroscopy.

In this work, we studied the evolution of plasma plumes resulting from enamel and hydroxyapatite ablation. The plasma plumes were generated by an Nd:YAG nanosecond laser and the depositions were performed in a cylindrical stainless steel vacuum chamber (10 L volume, 30 cm height, 20 cm diameter) (**Figure 1**). The chamber is evacuated to a base pressure of 10^{-6}

Torr by a 550 L/s turbomolecular pump (Agilent Technologies TV-551) placed in a vertical position at the bottom of chamber. The target (HA) is placed on a micrometric precision XYZ stage and can be rotated with a motorized vacuum feedthrough (Caburn MDC). The target is placed on a metallic target holder, which is electrically isolated from the rest of the experiment by an alumina block. The substrate (salt) is placed parallel to the target. The target-substrate distance was 1.4 cm. The ablation laser beam was usually at 45° on the target surface (**Figure 2**).

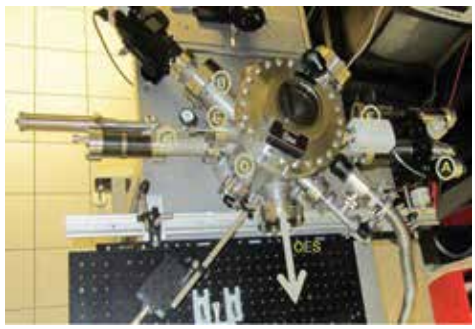

Figure 1. Vacuum chamber.

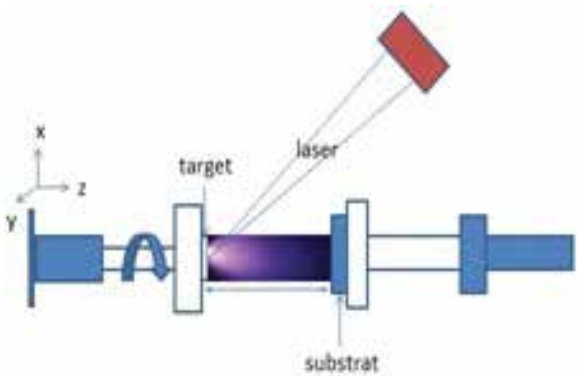

Figure 2. Experimental setup of an Nd:YAG nanosecond laser (Continuum Surelite III-10) (gw = 1 μs, gd = 25 ns).

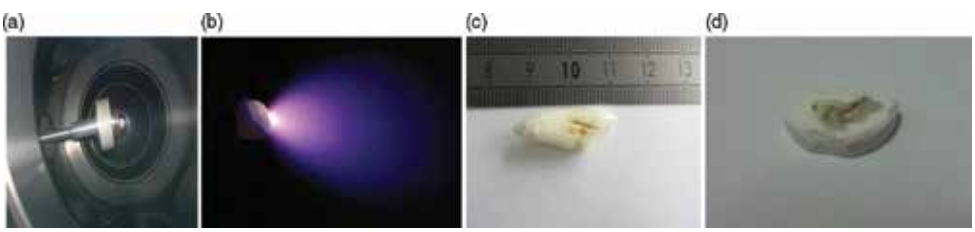

Figure 3. (a) Vacuum chamber with target; (b) 1 plasma tooth; (c) 1 tooth after ablation; (d) 1 HA after ablation.

2.1. Experimental data

We used λ = 266 nm, 10 ns, 10 Hz, E = 40 mJ/pulse, fluence 2.1 J/cm^2. The materials used in these studies were hydroxyapatite and a human tooth (**Figure 3a–d**).

2.2. Results and discussions

The dynamics of the plasma plume has been studied by means of a high-resolution monochromator (Acton SP 2500i) and intensified charge-coupled device (ICCD) camera (Roper Scientific PI MAX2-1003-UNIGEN2, 1024 × 1024 pixels). The monochromator has an alternative exit port fitted with a photomultiplier (PM, Hamamatsu) in order to record fast temporal profiles of a given spectral line. The PM output is sent to a fast digital oscilloscope (GHz, LeCroy). In order to obtain preliminary insight into the dynamics of the laser ablation plasma plume, ICCD sequential pictures of the spectrally unresolved plasma optical emission were recorded at various delays with respect to the laser pulse. We used the PLD technique to produce flexible films of hydroxyapatite deposited on glass or NaCl (salt) substrates, followed by a space-and-time-resolved optical emission spectroscopy (OES) investigation on selected spectral lines, the properties of the deposited films were investigated by Raman spectroscopy.

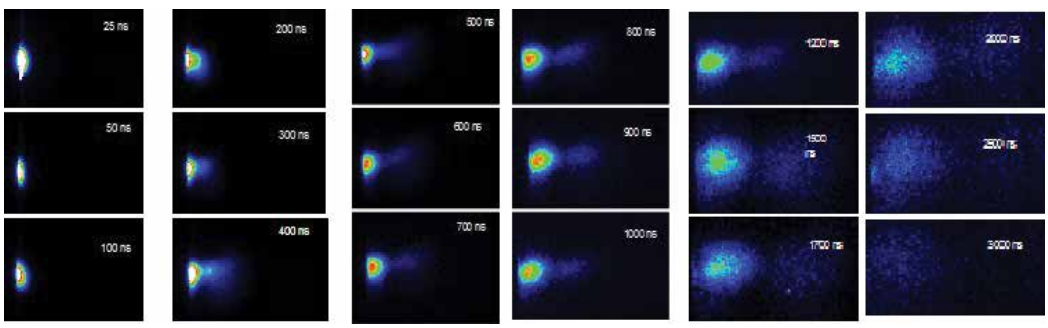

Figure 4. Temporal evolution of the plasma produced by irradiation of HA sample.

We used the ICCD camera to record the global template evolution of the plasma (**Figure 4**) and we observed the presence of two main structures: a fast one, represented by the spectral lines of ions, and a slower one, mainly due to the contribution of neutrals (the first one, plume-like-shaped, expands at a velocity of about 2 × 10^4 m/s; the second one, which looks like a small plasma cloud close to the target surface, shows an expansion velocity of about 2 × 10^3 m/s). OES allowed us to obtain information on the contribution of each species present in the plasma, the processes of formation and expansion of the plume. Identification of spectral lines observed in the OES was performed using the NIST database and CFA (**Figure 5**).

Emission is dominated by Ca I, Ca II ions but O II, H I, and contaminants such as Na I, Mg III, Hg I ions were also found. Raman analysis of HA deposition on glass and Raman analysis of HA deposition on salt are presented in **Figures 6** and **7**, respectively.

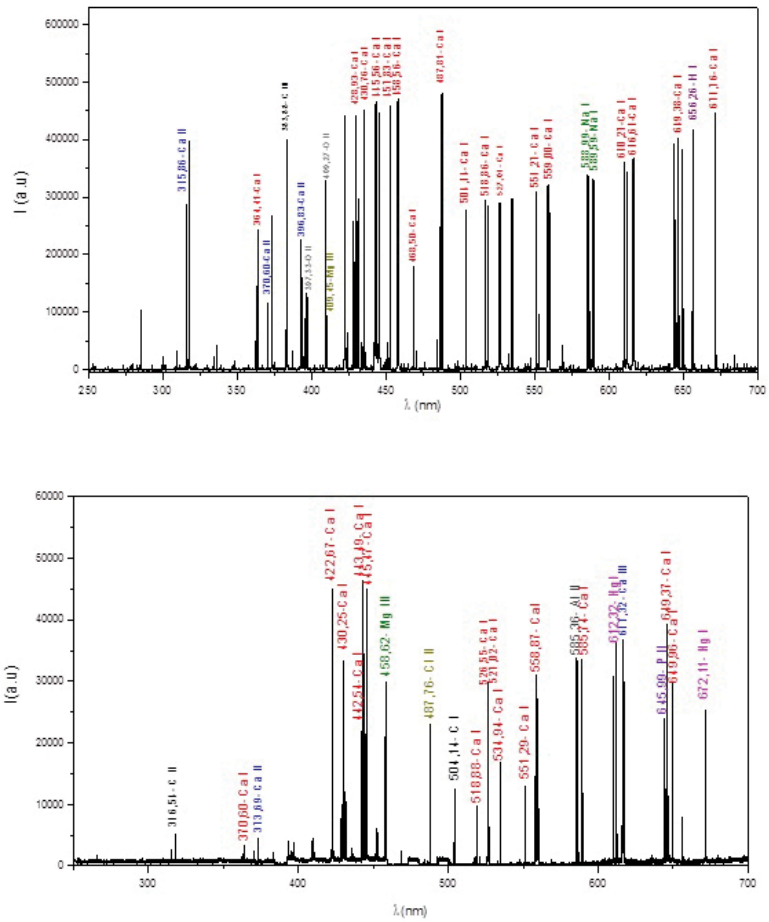

Figure 5. OES hydroxyapatite/OES enamel tooth.

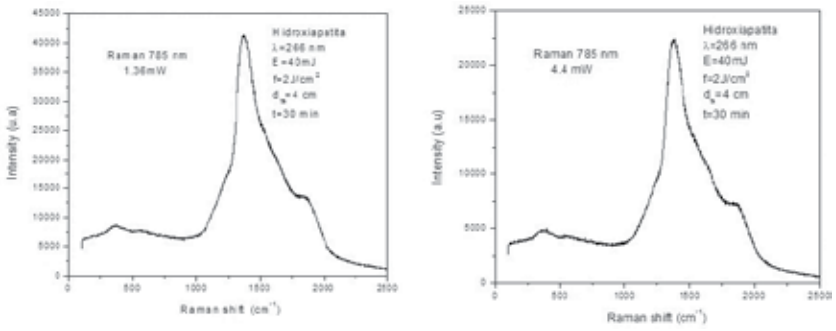

Figure 6. Raman analysis of HA deposition on glass. Experimental data: 785 nm, object 50×, 10 acc, 10 s, 1.36 mW/785 nm, 50×, 10 acc, 10 s, 4.4 mW.

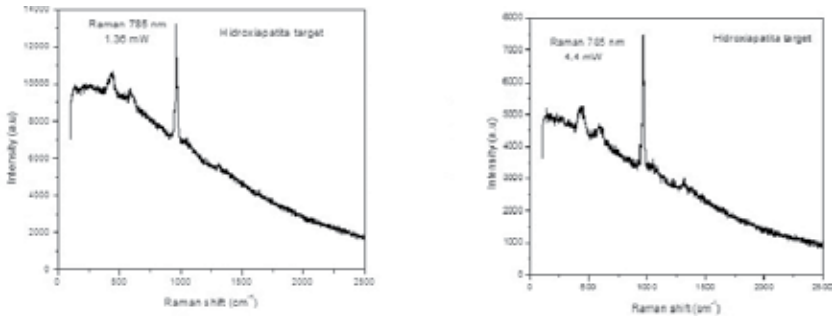

Figure 7. Raman analysis of HA deposition on salt. Experimental data: 785 nm, object 50×,10 acc, 10 s, 1.36 mW/785 nm, 50×, 10 acc, 10 s, 4.4 mW.

A starting point in the investigation of the thin HA film is to obtain information on the surface morphology of the deposited samples. For the study of the thin film discussed here, we used a confocal optical microscope (Olympus) coupled to the Raman spectroscopy setup (Renishaw). Our images were obtained using the 50× objective (**Figure 8**).

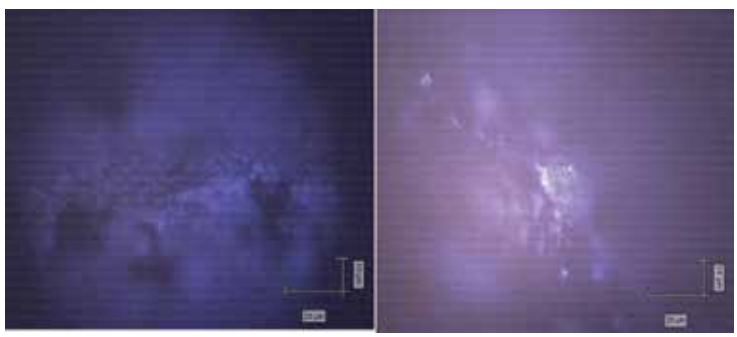

Figure 8. Optical microscopy for deposition: on glass/on salt.

Figure 9. Thin film of hydroxyapatite on the salt after heated/thin and flexible film of HA.

A thin film of Hap was deposited on a soluble substrate by a pulsed laser deposition (PLD) technique. The substrates were then dissolved using a solvent and the thin Hap films were

collected as freestanding sheets. The HA film was deposited on salt single crystals (**Figure 9**) and heated at 400°C, t = 30 min. These HA sheets were crystallized. Thereafter, the thin films were collected as freestanding sheets by immersing the NaCl substrates into pure water to dissolve the substrates. This procedure gave rise to flexible HA films.

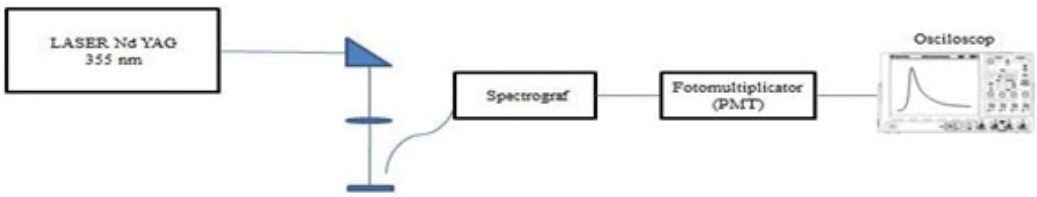

Figure 10. Schema of the LIBS setup.

Laser-induced breakdown spectroscopy (LIBS) uses a short laser pulse (≈10 ns) focused on the surface of a solid sample to vaporize a very small quantity of material. The ejected material forms a plasma plume and the optical radiation emitted by the plasma species is collected through an optical fiber exactly where the plasma was produced, meaning that this method can be used for *in situ* analysis. Because the quantity of ejected material is in the order of 20–200 ng, this method is considered microdestructive because the crater formed on the surface of the sample is practically invisible to the naked eye. LIBS can be used for elemental analysis of materials and it allows the measurement of fluorescence lifetime of the species identified in the plasma. For the LIBS analysis, we used the third harmonic of an Nd:YAG (BMI LT-1233) laser (355 nm, 10 ns) focused by a 5 cm focal distance lens. The optical radiation emitted by the plasma plume was collected using an optical fiber and analyzed using a monochromator and detected with a photomultiplier (H9305-02 Hamamatsi) connected to a 500 MHz oscilloscope (Agilent Technologies) (**Figure 10**). This way, we were able to measure the intensity of the radiation emitted at various wavelengths and to record the time evolution of each signal.

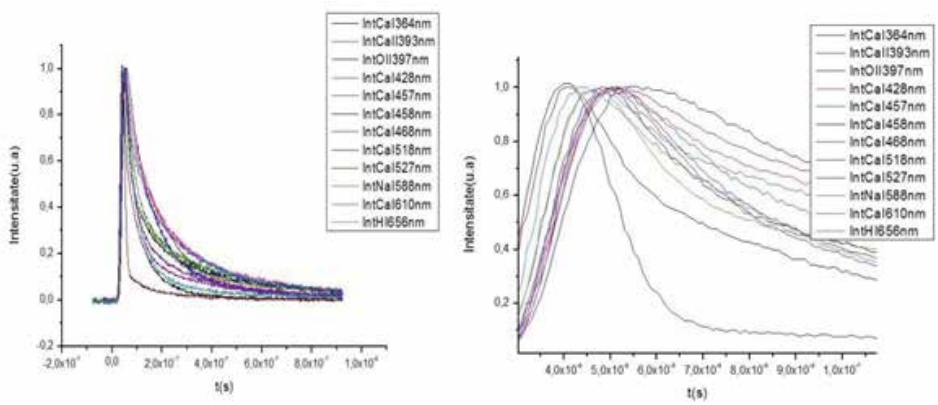

Figure 11. Fluorescence lifetime of HA species/normalized graph.

The measurements have been performed at IESL-FORTH (Institute of Electronic Structure and Laser-Foundation for Research and Technology-Hellas), Greece. The HA pellet was placed 1 cm before the focal point in order to avoid laser focusing in the air and air breakdown. The laser fluence could be adjusted by changing the area of the laser spot at the surface of the sample by modifying the lens-sample distance. Experiments were performed at 1.47 J/cm^2 (fluence) (E = 7.4 mJ, 10 Hz, D = 0.8 mm, S = 0.50 mm^2).

The main species identified are Ca I, then HI and OII, but also the main contaminant, Na I. The fluorescence lifetime of Ca I and oxygen is considerably larger (**Figure 11**).

2.3. Vertical growth methods for flexible HA films

In order to obtain flexible HA films, we used PLD starting from a solid pure HA pellet as a target. The powdered HA was processed in the form of solid pellets of 14–15 mm diameter and 4–6 mm thickness using a hydraulic press (15–25 tones) at "Gheorghe Asachi" Technical University of Iasi (**Figure 12**).

Figure 12. Manual press.

The hydroxyapatite thin films were obtained by nanosecond PLD. This method proved to be competitive for growing high-quality thin films because it has the capacity to preserve the stoichiometry of deposed compounds [4]. Obtaining thin films using PLD offers many advantages compared with other techniques, such as the laser source is external to the deposition chamber, most materials can be laser ablated and deposed in thin films, and the

growth rate can be precisely controlled (10^{-2} to 10^{-1} nm/pulse)nm/pulse); the ablated material is localized in the volume of the generated plasma; the stoichiometry of the film is identical with that of the target and the high energy of ablated species allows one to obtain very adherent films [5–8]. The film depositions were performed using an Nd:YAG laser, BMI Industries, at IESL-FORTH (Institute of Electronic Structure and Laser-Foundation for Research and Technology-Hellas, Heraklion) Greece, at $\lambda = 266$ nm, repetition rate 10 Hz (**Figure 13**). Various fluencies were used and the target substrate distance was also adjustable (**Table 1**). As previously explained, the fluence can be varied by changing the distance between the focusing lens and the target surface.

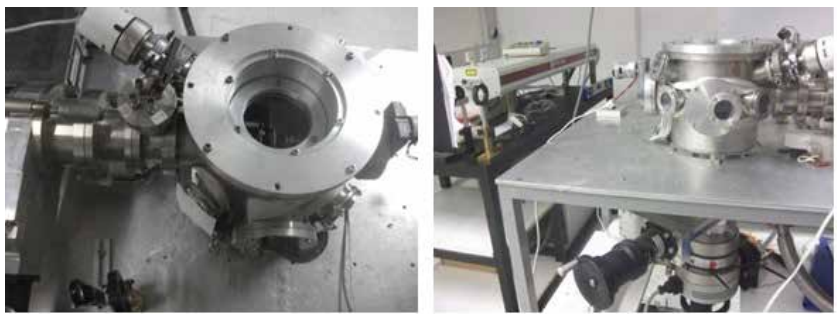

Figure 13. PLD experimental setup.

Diameter (mm)	Area (mm^2)	Area (cm^2)	Measured power (mW)	Repetition rate (Hz)	Energy (mJ)	Fluence (mJ/cm^2)	Fluence (J/cm^2)
0.8	0.502655	0.005027	74	10	7.4	1472.183	1.472183
1	0.785398	0.007854	66	10	6.6	840.3381	0.840338
1.5	1.767146	0.017671	200	10	20	1131.768	1.131768

Table 1. Laser fluence.

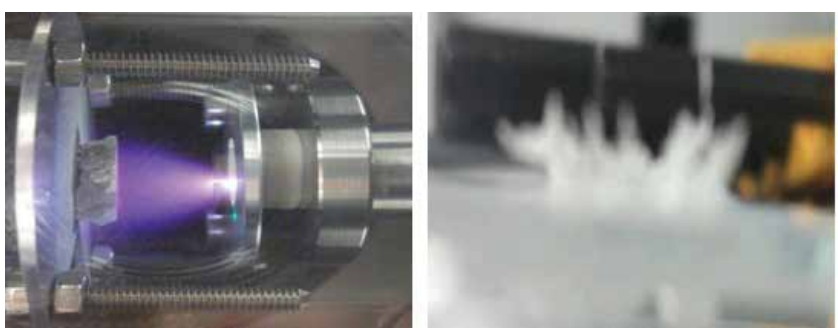

Figure 14. HA ablation plasma/HA vertical film obtained on salt substrate.

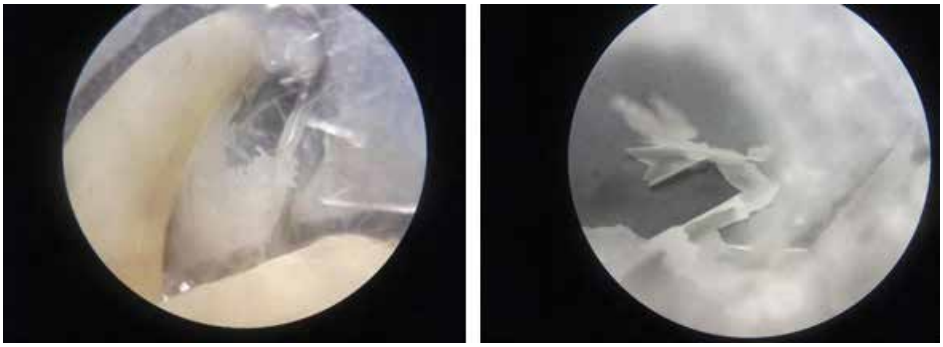

Figure 15. HA film formed between two lateral supports/vertical HA film attached only at the base.

Figure 16. HA microfibers attached to the tooth surface.

Figure 17. Optical microscope 15×, Brunel microscopes.

Figure 18. The oven used for thermal treatment, IESL, Greece.

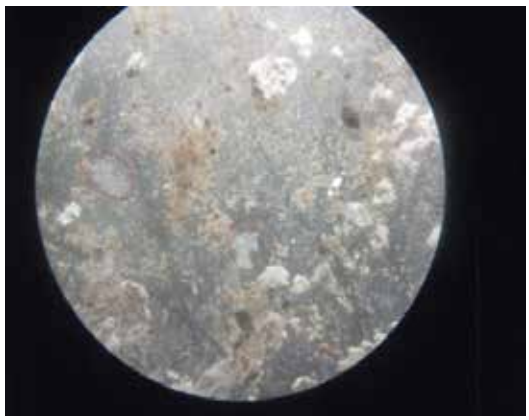

Figure 19. Free HA films, obtained by deposing on salt substrate, after thermal treatment.

Initially, we made a deposition on a salt (NaCl) substrate and it led to the formation of some HA vertical structures (**Figure 14**). The next step was to obtain films that were not completely attached to the substrate by growing them between two lateral supports. In order to verify the compatibility and the "sticking" of HA on the teeth as well, which corresponds to the intended application, we chose to grow the film between the roots of a tooth (**Figure 15**). In this case, besides the film, we also obtained HA microfibers attached only at one end on the tooth enamel (**Figure 16**). We used for these experiment Optical microscope (**Figure 17**).

In order to improve the crystallinity and biocompatibility of the films, they were thermally treated for 30 min at 400°C (**Figures 18** and **19**).

2.4. Methods of HA adhesion on enamel

This flexible HA film can be handled with tweezers and applied to the tooth. We tried to bind the film on an extracted tooth.

Adhesion to enamel is the hard process (**Figure 20**). A protocol must be established in order to allow the bonding of the film on the surface of the tooth knowing that contaminants such as saliva or sulcular fluid increase bonding strength to enamel or dentin. We realized an efficient bonding as HA absorbs protein, the mineral also participates in this ionic exchange and we strengthened the tooth structure.

Figure 20. Methods of HA adhesion on enamel.

Using the PLD technique, we can obtain a flexible film of hydroxyapatite, a biocompatible dental material that can be immediately and directly attached to the tooth surface for restoration and conservation of teeth.

For the experimental part, we have attached a theoretical model [8–16].

We proposed a new approach for the analysis of dynamics in nanostructures. The dynamics of nanostructure quasiparticles takes place on continuous but nondifferentiable curves. Consequently, the standard properties of nanostructures, such as quasiparticles generation through self-structuring, interferential capacities through self-similar solutions of Kirchhoff type equations, etc., are controlled through nondifferentiability of motion curves.

The standard theoretical models of nanostructures dynamics are sophisticated and ambiguous. However, such situation can be simplified if we consider that complexities in interaction processes impose various time resolution scales and the evolution pattern leads to different freedom degrees. To develop new theoretical models, we have to admit that the nanostructures with chaotic behaviors can achieve self-similarity (space-time structures can appear) associated with strong fluctuations at all possible space-time scales. Then, for time scales that prove to be larger if compared with the inverse of the highest Lyapunov exponent, the deterministic trajectories are replaced by a collection of potential routes. In its turn, the concept of "definite positions" is replaced by that of probability density.

Thus, the nondifferentiability appears as a universal property of nanostructures and, moreover, it is necessary to create nondifferentiable physics of nanostructures. Under such circumstances, if we consider that the complexity of interactions in the dynamics of nanostructures is replaced by nondifferentiability, it is no longer necessary to use the whole classical "arsenal" of quantities from standard physics (differentiable physics).

This topic was developed using either the scale relativity theory (SRT) or scale relativity theory with arbitrary constant fractal dimension. According to these models, the dynamics of

nanostructure quasiparticles takes place on continuous but nondifferentiable curves (fractal curves) so that all physical phenomena involved depend not only on space-time coordinates but also on space-time scale resolution. That is why physical quantities describing the dynamics of nanostructures can be considered as fractal functions. Moreover, according to geodesics in a nondifferentiable (fractal) space, the nanostructure quasiparticles may be reduced to, and identified with, their own trajectories (i.e., their geodesics) so that the nanostructure should behave as a special "fluid" lacking interactions—fractal fluid.

Various theoretical aspects of nanostructure dynamics (self-structuring, phenomena through quasiparticles generation, interferential capacities through self-similar solutions of Kirchhoff type equations, etc.) were analyzed using the SRT with arbitrary constant fractal dimension.

Any particle can take part in a permanent interaction with the "subfractal level" through the fractal potential, Q. The "subfractal level" is identified with a nonrelativistic fractal fluid described by momentum and state density conservation laws. The nondifferentiable hydrodynamics implies a quantum hydrodynamics model (QHM). Indeed, for motions described by fractal curves with fractal dimension $D_F = 2$, at Compton scale, the Non-differentiable hydrodynamics (NDH) reduces to quantum hydrodynamics model. Moreover, the "subfractal level" can be identified with "subquantum level." The fractal potential comes from the nondifferentiability and must be considered as a kinetic term and not as a potential one. Moreover, the fractal potential can generate a viscosity stress tensor type.

The main conclusions of the theoretical model are the following: (i) the nanostructure dynamics was theoretically analyzed assuming that the quasiparticle moves on continuous and nondifferentiable curves; (ii) a nondifferentiable hydrodynamic model containing the density and momentum conservation equations was built. The fractality is introduced via fractal potential; (iii) supposing that the fractal potential implies an isentropic-type behavior of the fractal fluid, the self-structuring phenomena are analyzed through numerical simulations; (iv) in the absence of convection, interferential properties are induced in nanostructures; (v) this chapter deals with the standard properties of nanostructures, such as quasiparticles generation through self-structuring or interferential capacities through self-similar solutions of Kirchhoff-type equations. In the literature, there are also other descriptions of the forms of organization of the matter. The quantum theory is used in each of these descriptions of the forms of organization of matter. However, the interpretation of modern quantum theory is still an open question as shown in the Reference [1–3].

3. Conclusions

We created a flexible HA film, a dental plaster grown vertically, thus improving its quality: there are no contaminations and impurities from the substrate. The crystalline structure can be improved by thermal treatment. The main purpose of our research is to rebuild the dentine layer or enamel and close the dental channels.

Author details

Lucia Marin Biolan[1*], Andrei Bedros Agop[2] and Doriana Forna[3]

*Address all correspondence to: luciamarin2015@yahoo.com

1 Faculty of Physics, "Alexandru Ioan Cuza" University of Iaşi, Iaşi, România

2 Faculty of Material Science and Engineering, "Gheorghe Asachi" Technical University of Iaşi, Iaşi, România

3 Faculty of Dental Medicine, "Grigore T. Popa" University of Medicine and Pharmacy of Iaşi, Iaşi, România

References

[1] Agop M, Forna N, Casian-Botez I, Bejenariu C. New theoretical approach of the physical processes in nanostructures. *Journal of Computational and Theoretical Nanoscience* 2008;5(4):483–489.

[2] Croca JR, de Lemos e Silva Cordovil JL. Nonlinear quantum physics. *Reviews in Theoretical Science* 2014;2(3):181–200.

[3] Casian-Botez I, Vrajitoriu L, Rusu C, Agop, M. *Interferential behaviors in nanostructures via non-differentiability.* Journal of Computational and Theoretical Nanoscience 2015;12:1–7.

[4] Mazilu N, Agop M, Axinte CI, Radu E, Jarcău M, Gârţu M, Răuţ, M, Pricop M, Boicu M, Mihăileanu D, Vrăjitoriu L. A Newtonian message for quantization. *Physics Essays* 2014;27:204–214.

[5] Landi E, Tampleri A, Celotti G, Spio S. Densigication behavior and mechanisms of synthetic hydroxyapatites. *Journal of European Ceramican Society* 2000;20(14–15):2377.

[6] Gurlui S, Agop M, Nica P, Ziskind M, Focsa C. Experimental and theoretical investigations of aluminium expanding laser-plasma. *Physical Review E* 2008;78:026405.

[7] Nica P, Vizureanu P, Agop M, Gurlui S, Focsa C, Forna N, Ioannou P, Borsos Z. *Japanese Journal of Applied Physics* 2009;48:066001.

[8] Baurle D. Laser Processing and Chemistry. Springer, Berlin; 2000.

[9] Serra P, Morenza JL. Imaging and spectral analysis of hydroxiapatite laser ablation plumes. *Applied Surface Science* 1998;127–129:662–667.

[10] Kokkinaki O, Mihesan C, Velegrakis M, Anglos D. Comparative study of laser-induced breakdown spectroscopy and mass spectrometry for the analysis of cultural heritage materials. *Journal of Molecular Structure* 2013;1044:160–166.

[11] Buonocore MG, Matsui A, Gwinnett AJ. Penetration of resin dental materials into enamel surfaces with reference to bonding. *Archives of Oral Biology* 1968;13:61–70.

[12] Raskin A, Michotte-Theall B, Vreven J, Wilson NH. Clinical evaluation of a posterior composite 10-year report. *Journal of Dentistry* 1999;27(1):13–19.

[13] Tesloianu D, Vrajitoriu L, Costin A, Vasincu D, Timofte D. Dispersive behaviours in biological fluids. Applications (II), *The Bulletin of the Polytechnic Institute of Jassy* 2014; Pg.12. Tomul LX(Fasc. 3), Sectia matematica, mecanica teoretica, fizica.

[14] Marin L, Mereuţă VD. Obtaining a thin and flexible dental film of hydroxiapatite using a PLD technique. Bulletin of the Polytechnic Institute of Iaşi; 2015.

[15] Marin L, Mihesan C, Velegrakis M. Obtaining hydroxiapatite flexible thin films without using a substrate. Bulletin of the Polytechnic Institute of Iaşi; 2015.

[16] Marin L, Mereuţă VD, Agop M. Nonlinear effects in complex systems. Publisher Ars Longa, Iasi, October 2015.

Chapter 15

High-Energy Nanosecond Laser Pulses for Synthesis of Better Bone Implants

Amirkianoosh Kiani and Mitra Radmanesh

Additional information is available at the end of the chapter

http://dx.doi.org/10.5772/63770

Abstract

The main objective of this chapter is to introduce high-energy nanosecond laser pulse treatment for enhancing the surface bioactivity of titanium for bone and tissue implant fabrication. Improvement to the implant performance could immensely benefit the human patient. Bioactivity enhancement of materials is currently an essential challenge in implant engineering. Laser micro/nano surface texturing of materials offers a simple, accurate, and precise method to increase the biocompatibility of materials in one single step. In this chapter, the effects of laser power, scanning parameters, and frequency on surface structure and topographic properties are studied. Through bioactivity assessment of treated titanium substrates, it was found that an increase in power and frequency increases the bioactivity of titanium, while a decrease in scanning speed of laser could lead to an increase in the cell adhesion ability of titanium.

Keywords: titanium, bone implant, laser surface treatment, micro- and nanotexturing, bioactivity, biocompatibility

1. Introduction: biomaterials and implant engineering

Biomaterials and implant engineering have become vital fields in the medical and surgical industries. These disciplines can enhance the quality and length of human life, and have an immense effect on the health of numerous individuals. The technologies associated with biomaterials and implant engineering, particularly in the fields of surgical implants such as dental, bone, and tissue implant applications, have led to the creation of numerous research opportunities [1–3]. In today's society, with the continuous growth in population and education, there is a preference for an improved life style, better body functionality, and more appealing

aesthetics. This leads to ongoing expansion and discovery in the technology and science associated with biomaterials and implant engineering [3–6].

This chapter describes a research opportunity for the investigation and improvement of the effects of laser surface texturing on enhancing the biocompatibility and bioactivity of titanium. Titanium substrates are used to examine the effects of key laser process parameters, including power, scanning parameters, and frequency on their surface topography properties and biocompatibility.

1.1. Main challenge in implant engineering

Cell adhesion and biocompatibility are important parameters for implant fabrication and the production of biomedical devices. Improvements to an implant's performance in the implantation site could benefit the patient's quality of life. Low biocompatibility is often caused by poor integration of the implant with surrounding tissues. Cell behaviour on biomaterial surfaces depends upon implant-cell interactions, which are correlated with surface properties such as hydrophilicity, roughness, texture, chemical composition, charge, and topography properties [6–8]. Although there is a great range in the design and function of various implants, the one common factor for all of them is their biocompatibility, which affects overall implant performance. Biocompatibility enhancement of materials used in implants is currently an essential challenge in implant engineering [8]. This property is essential in order to avoid any infections and immune system rejection. It can also affect the healing process by reducing the healing time. A reduced healing time is desirable in implant applications, since the sooner the body accepts the implant organ, the sooner the user can function normally [7, 9, 10].

The implant's surface is the main area in contact with the body at an implantation site. Therefore, to increase the biocompatibility of a material, various methods of surface treatment are currently being used in industry [9, 11, 12].

1.2. Fabrication methods of biocompatible materials

One method to affect the surface properties of a material is to alter the surface topography properties. There are multiple conventional methods used commercially for processing and surface texturing of materials for bone and tissue implant applications [9, 11]. The most common mechanical methods for altering surface topography properties include sandblasting and machining, while acid etching and oxidation are common chemical methods. Although these methods are effectively used in industry, there are major disadvantages associated with them. Slow production time, complex control processes, and chemical contaminations are only a small number of the challenges presented by these commonly used processing techniques [13]. The newly developing method of laser surface texturing of materials addresses these disadvantages in a simple and effective manner. Lasers are able to deliver very low to high energy with extreme precision in dimension, spatial distribution, and temporal distribution. Lasers offer better control and precision, offer more feasibility, and are environmentally friendly [14–16]. Decreased processing time makes lasers particularly suitable for mass production, rapid prototyping, and custom-scale manufacturing for a wide variety of

http://dx.doi.org/10.5772/63770

applications, such as microwelding, drilling, cutting, and heat treatment of metals and alloys. Laser treatment is known for its fast and precise manner in the processing of materials, and for the variety of scales offered by lasers, including micro-, submicro-, and nanofabrication [8, 15].

1.3. Physics of laser surface texturing

Laser processing can be applied in two categories based on the energy requirements: first, applications requiring relatively low energy with limited structural and physical changes; second, applications calling for high-energy transformations for significant structural changes over a large volume, such as welding. Energy transformation in applications involving lasers requires the coupling of the laser radiation with the electrons of the interacting surface, such as metals or semiconductors [17, 18]. In return, the speed of energy transformation from the laser beam to the surface becomes fully dependent on the nature of the interacting material and its chemical bonding. There have been significant improvements in energy transformation of lasers through the development of ultrashort lasers [19–23].

Ultrashort lasers decrease the interaction time (pulse duration) between the laser and the material, which reduces the effects on the bulk material. Despite these improvements, ultrashort laser systems are relatively expensive and cannot be utilized in industries. Hence, depending on the nature of the application, less expensive yet advanced laser systems, with pulse durations in the range of nanoseconds, are more popular among manufacturers because they are more widely available in manufacturing sectors. An understanding of the laser irradiation mechanism is required to utilize the more common lasers to their fullest capability, therefore, choosing the laser parameters is essential to the final quality of a particular application [24–27].

2. Laser-enhanced topography properties

Micro/submicro-treated surfaces are popularly used in scaffold systems for bone and tissue implant applications. The surface topography properties of a material, particularly roughness, are influential on the cell adhesion rate of bone-like apatite to surfaces. Increasing the cell adhesion rate to the surface of a material increases the biocompatibility of the material. Thus, surface texturing of materials to enhance their biocompatibility is an effective method in the fabrication of implant devices [26–28]. The effects of laser irradiation on the surface topography properties of materials are the main advantage of laser surface texturing. Laser parameters, including frequency, power, and laser scanning parameters, can influence these material properties greatly [27].

The irradiated surface area of a material has increased surface irregularities. In return, the exposed area is more readily available for cell attachment, which enhances the apatite-inducing ability and cell adhesion rate of the material [27–31]. Furthermore, laser treatment of the materials increases the surface temperature up to oxidation temperature, and results in the creation of thin layers of oxide upon the surface. An increase in the oxidation of the surfaces

increases the wettability of surface of the material. Consequently, this leads to an increase in the apatite-inducing ability of the material and greatly improves the biocompatibility of the implant surfaces [30–35].

2.1. Laser system

The nanosecond laser used for obtaining all the results discussed in this chapter was a Nd:YAG pulsed laser system (SOL-20 by Bright Solutions Inc). The maximum output power is 20 W with a wavelength of 1064 nm and a repetition rate ranging between 10 and 100 kHz. This laser emits pulses of 6–35 ns pulse duration. The diameter of circular output beam from the laser is around 9 mm. The diameter of beam is reduced to 8mm by using an iris diaphragm before entering to galvo-scanner. A two-axis galvo-scanner (JD2204 by Sino Galvo) with the input aperture of 10 mm and beam displacement of 13.4 mm was used for beam scanning since it has a high scanning speed (to 3000 mm/s). In order to focus the normal beam to the surface of Ti, scan lens of a focal length of 63.5 mm was used. The theoretical focused laser spot diameter (d_0) is calculated to be 20 μm. During the experiment, the spot size may be bigger due to scatter and misalignment. The average laser fluence was 900 μJ at the frequency of 10 kHz.

The scanning parameters including scanning speed, and scanning configurations can be adjusted through the software operating the laser. When the combination of parameters is adjusted with this software, along with power and frequency set for laser irradiation, the desired pattern is irradiated across the surface of the selected material.

3. Effects of laser power

Power is one of the most influential laser parameters when surface treating a material. Adjusting the power increases the surface irregularities of the material and therefore enhances the topography properties of the substrate [25, 33]. In this chapter, the effects of four different powers on surface topographic and oxidation properties of titanium substrates are investigated, and the bioactivity of the treated substrates is examined through the use of simulated body fluid (SBF). Simulated body fluid (SBF), or formally known as hydroxyapatite, is a supersaturated insoluble calcium phosphate mineral, with the chemical composition of $Ca_{10}(PO_4)_6(OH)_2$. This fluid has a close similarity with human blood plasma and is the essential component of the biological hard tissues such as bones. Due to the high absorbance and catalytic properties of SBF, this fluid is commonly used to estimate the biocompatibility level of materials used in implant productions.

To treat the titanium substrates, a range of low to high average laser powers from 6 to 12W was used, while frequency and scanning speeds were kept constant in all cases. The effective number of pulses for all results was kept constant to be 25 pulses for frequency of 100 kHz [36, 37]. **Table 1** introduces the parameters used in more detail.

http://dx.doi.org/10.5772/63770

Average laser power (W)	Total number of laser pulses	Pulse energy (mJ) at 100 kHz	Pulse width (ns)	Total delivered energy (mJ)
6	25	0.06	35	1.5
8	25	0.08	35	2
10	25	0.10	35	2.5
12	25	0.12	35	3

Table 1. Laser parameters used in surface treating of Ti substrates.

3.1. Surface topography analysis

Once treated, there is often more available exposed surface area of the material because of the increase in surface roughness, which, in return, enhances the apatite-inducing ability and cell adhesion rate of that material. **Figure 1** displays the variation in the treated substrates using the stated powers.

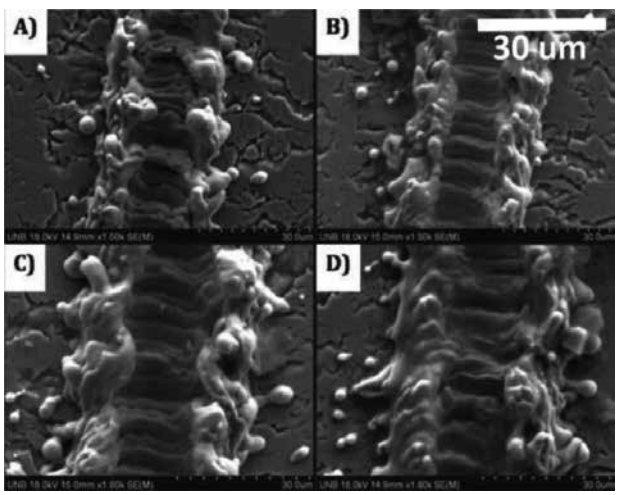

Figure 1. Surface of treated titanium (A) 6 W, (B) 8 W, (C) 10 W, (D) 12 W.

Although the number of pulses delivered to each of these substrates is the same, as indicated in **Table 1**, the images shown in **Figure 1** clearly indicate different surface topography after laser treatment. With an increase in power, the energy delivered to the surface of the material increases as well, hence, more ablation and topography changes occur. Substrates treated with a power of 12 W have a larger surface affected by laser irradiation as opposed to 6 W.

During laser irradiation, a plasma plume with radial surface tension is formed surrounding the irradiated area due to the high temperature gradient caused by laser energy transfer. Immediately following irradiation, a high temperature difference exists between the surface of the material and the generated plasma plume. Thus, a high cooling rate results, which causes rapid re-solidification of the ablated material. Consequently, the tension within the laser plume

causes shooting of the molten titanium to outside of the ablated zones [37]. The micro re-solidified particles observed outside the crater in **Figure 1** have been formed due to the same reason.

Using 3D microscopy, the surface profile of the treated substrates can be compared; this is introduced in **Figure 2**. This study used the Zeta-20 optical profiler to scan the surface of the samples in order to obtain the surface topography results across each sample.

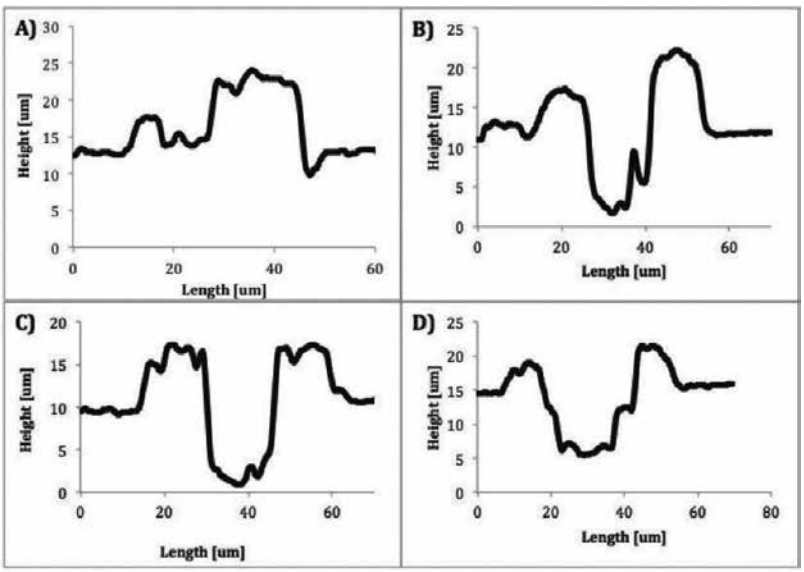

Figure 2. Surface profiles of Ti (A) 6 W, (B) 8 W, (C) 10 W, (D) 12 W.

As shown, an increase in laser power clearly affects the surface topography profile of titanium substrates. Different laser powers create different surface irregularities across the surface of the treated titanium substrates.

3.2. Surface temperature analysis

Different power levels deliver various amounts of energy to the surface of the substrate, and, therefore, increase the surface temperature of the titanium. This increase in the surface temperature could affect the surface structure, topographic properties, and oxidation of the titanium substrates. Oxidation is an important factor when considering bioactivity of a material. With higher oxidation, a higher surface energy is present, which results in more interaction between the implant and the body. Therefore, generating larger amounts of titanium oxide across the surface substrates consequently increases the biocompatibility of the treated work pieces. However, after a certain power threshold, the energy delivered to the surface of the titanium increases the surface temperature beyond the oxidation limit. Therefore, the material develops less titanium oxide as the surface undergoes larger ablation [32, 34, 38].

http://dx.doi.org/10.5772/63770

In order to calculate the surface temperature in this chapter, a theoretical calculation has been conducted according to the previous published results [25, 36, 39]; in this method, we assumed that the laser energy is absorbed in a much thinner layer compared to the penetration depth of the heat wave. Finally, the average surface temperature of the Ti substrate can be obtained as fully discussed in [25, 39]:

$$T_n = 2\alpha \frac{\left[1-\frac{2}{3}\alpha\right]}{(1+\alpha^2)} \frac{T_m}{(1-\alpha)} \left[1+\frac{\alpha^n-\alpha}{n(1-\alpha)}\right] \quad (1)$$

where T_m is the maximum temperature calculated at the end of first pulse, n is the pulse numbers, and α is the constant ratio for the previous maximum and the following minimum temperatures and equal to $\alpha = (t_p/t_{pp})^{1/2}$, where t_{pp} is the pulse interval and equal to $t_{pp} = 1/f$ (f is pulse repetition rate) and t_p is pulse duration. The analytical results obtained in this study are associated with possible errors due to multiple assumptions made throughout the study.

Upon completion of the analytical analysis, the temperature profile for both cases with 8 and 10 W powers, and a pulse number range of 2 pulses to 50 pulses is obtained.

The trend of average surface temperature of the treated titanium substrates is shown in **Figure 3**.

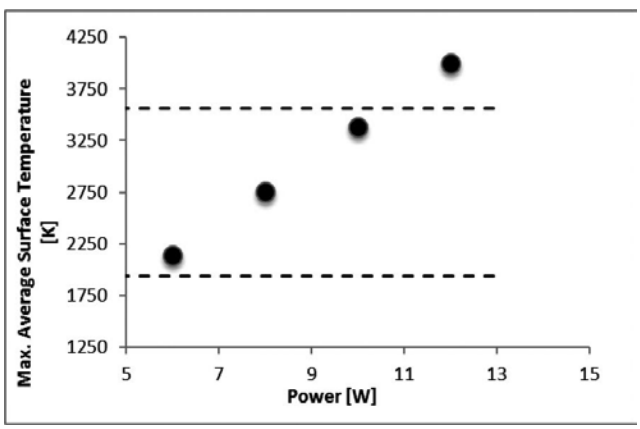

Figure 3. Maximum average surface temperature in each power.

As evident, with 12 W of power, the maximum average surface temperature of the titanium exceeds its evaporation point, and therefore less concentration of titanium oxide is generated along the surface of the substrates. Also, more ablation occurs, which agrees with the observations. Having a larger concentration of titanium oxide across the surface results in better cell interactions. To further investigate the oxidation of treated substrates, energy dispersive X-ray (EDX) analysis was conducted to detect the amount of oxygen available across the surface of substrates treated using the stated powers.

Figure 4 indicates the results.

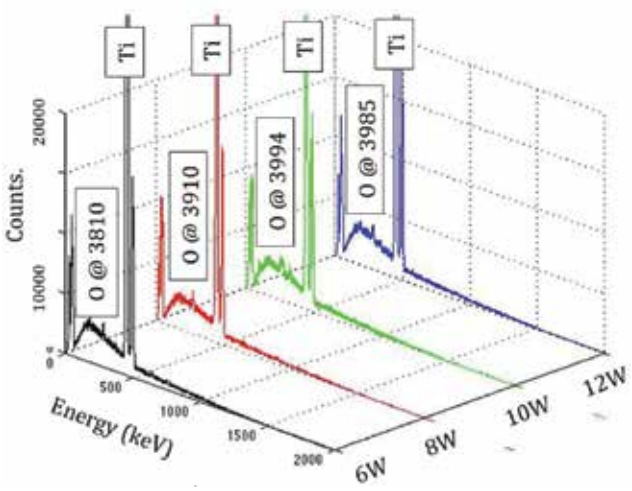

Figure 4. EDX analysis of the irradiated Ti at 6, 8, 10, and 12 W.

Comparing the trace of oxygen across the surface of all four substrates, it is observed that with an increase in power, the oxygen concentration increases slightly as well, until a power of 12 W is reached, which shows slightly a lower trace of oxygen. This is in agreement with the average temperature results observed in **Figure 3**. Considering the results shown in **Figures 4** and **5**, it is expected that powers of 8 and 10 W would result in a better biocompatibility compared to other two powers. This conclusion is assessed through the use of simulated bodily fluids (SBF).

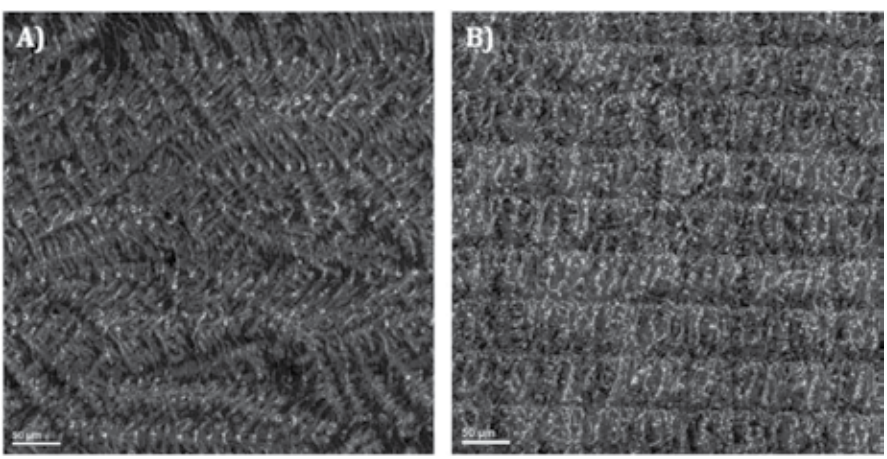

Figure 5. SBF-soaked substrates. (A) 8 W, (B) 10 W.

http://dx.doi.org/10.5772/63770

3.3. Biocompatibility assessment

To determine how the differences in surface topography affect the biocompatibility of titanium, the treated substrates using powers of 8 and 10 W were immersed in SBF for 7 days. **Figure 5** shows the scanning electron microscopy (SEM) photographs of the substrates after the completion of the assessment.

In **Figure 5**, the white layers across the induced line patterns indicate the bone-like apatite deposition on the surface of the titanium. These microscopy images show that generally with an increase in power, apatite-inducing ability across the surface of treated titanium increases as well. Looking closely into **Figure 5**, the EDX results for 10 W curve indicate a larger amount of apatite deposition compared to the 8 W curve. This is further observed in the EDX analysis conducted on these titanium substrates shown in **Figure 6**. Detecting larger amount of oxygen, calcium, and phosphorous elements indicates a higher apatite-inducing ability for the substrates.

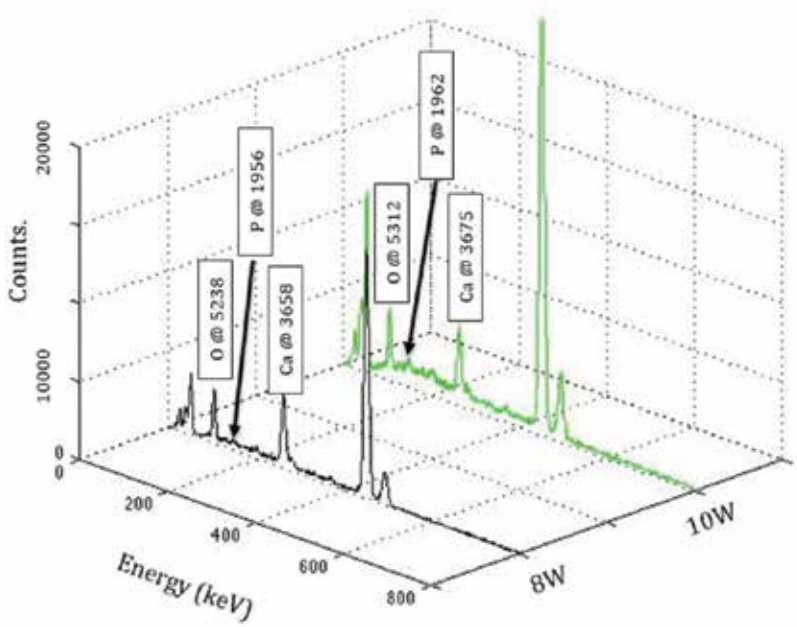

Figure 6. EDX analysis at 8 and 10 W.

As shown, the apatite-inducing ability of substrates treated with a power of 10 W is higher than the substrates treated with 8 W. This is in agreement with results observed with oxidation and SEM photography analysis.

Overall, the biocompatibility was highest for substrates treated with 10 W. This power provides adequate surface topography and the energy delivered is within the oxidation temperature range, hence creating a desirable environment for cell attachment to take place.

4. Effects of number of laser pulses

The total number of laser pulses delivered to the substrate is related to the scanning speed and laser frequency used while irradiation is taking place [40–42]. Effects of scanning speed on the number of laser pulses delivered to surface of the titanium substrates during laser irradiation are examined. Similar to power, scanning parameters have a direct effect on the surface topography and oxidation of treated titanium substrates. These effects are monitored using various scanning parameters, while keeping power and frequency constant. **Table 2** displays the parameters used.

Scanning speed (μm/ms)	Frequency (kHz)	Average power (W)	Total number of laser pulses	Total delivered energy (mJ)
50	100	10	167	16.7
200	100	10	41	4.1
400	100	10	21	2.1
500	100	10	17	1.7

Table 2. Scanning speed and pulse numbers used in surface treating of Ti substrates (pulse width, 35 ns; pulse energy, 0.1 mJ).

Scanning speed and the number of laser pulses are indirectly related. With an increase in scanning speed, the pulse number decreases. This is because with a lower scanning speed, more time is given to the laser to induce a pattern across the surface; hence, more pulses are delivered to the substrates.

4.1. Surface topography analysis

Similar to power, the effects of different scanning speeds on surface topographic properties of the treated substrates are examined using SEM photography. **Figure 7** displays these results.

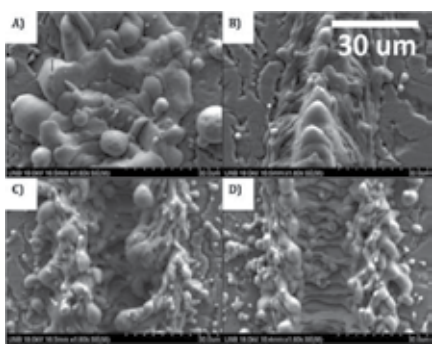

Figure 7. Surface of treated titanium (A) 50 μm/ms, (B) 200 μm/ms, (C) 400 μm/ms, (D) 500 μm/ms.

http://dx.doi.org/10.5772/63770

As shown in this figure, with an increase in scanning speed, the surface irregularities decrease in size; therefore, fewer topographic changes take place on those samples. This is in agreement with expectations, since **Figure 7(A)** with a scanning speed of 50 μm/ms has a larger number of pulses compared to **Figure 7(B)** with a scanning speed of 500 μm/ms.

The surface profile of these substrates is shown in more detail in **Figure 8**.

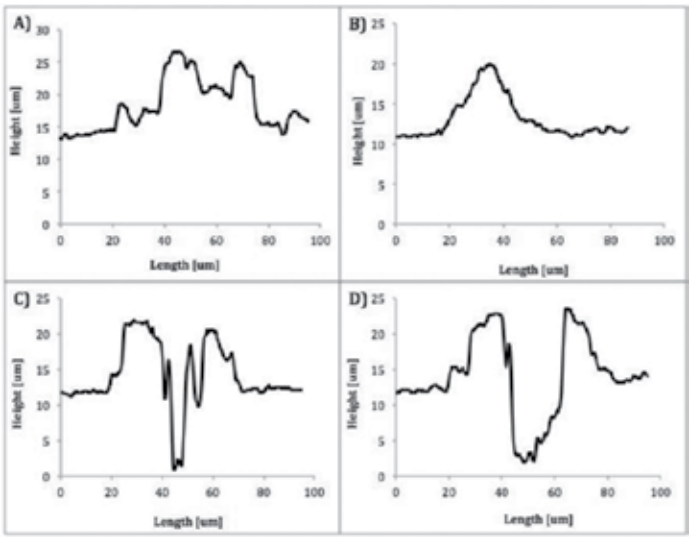

Figure 8. Surface profile of Ti (A) 50 μm/ms, (B) 200 μm/ms, (C) 400 μm/ms, (D) 500 μm/ms.

Figure 8(A) shows how irregularities cover the entire surface of the substrates, as opposed to only along the irradiation zone as shown in **Figure 8(D)**. This agrees with the expectations.

4.2. Biocompatibility assessment

To see how influential the number of pulses is on bioactivity enhancement of titanium, a wider range of scanning speeds is used to assess the apatite-inducing ability of treated titanium substrates. Scanning speeds of 300 and 700 μm/ms are used to treat these substrates in order to more clearly show the differences between the two substrates. All other parameters remain the same (**Table 3**).

Scanning speed (μm/ms)	Frequency (kHz)	Average power (W)	Total number of laser pulses	Total delivered energy (mJ)
300	100	10	28	2.8
700	100	10	12	1.2

Table 3. Scanning speed and pulse numbers used in surface treating of Ti substrates (pulse width, 35 ns; pulse energy, 0.1 mJ.

Figure 9 displays the substrates immersed in SBF for 7 days.

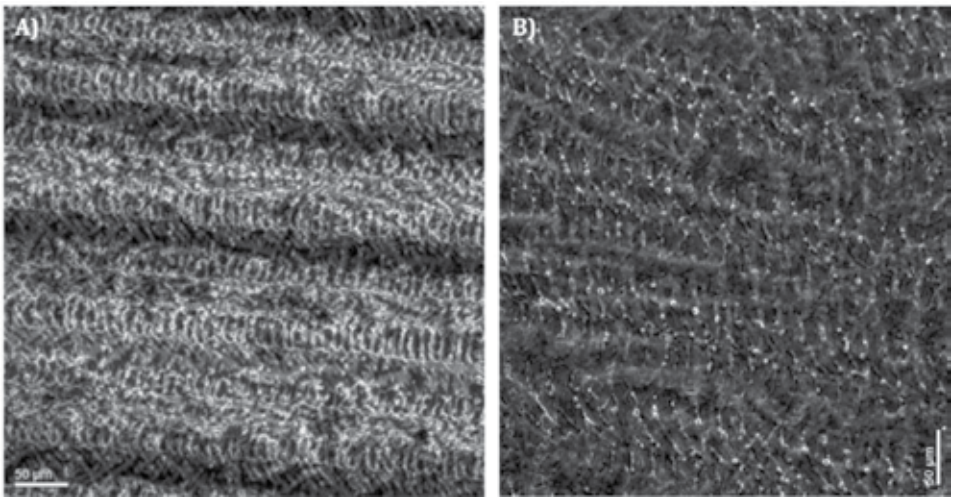

Figure 9. SBF-soaked substrates (A) 300 μm/ms, (B) 700 μm/ms.

As stated, a lower scanning speed delivers a larger number of pulses and therefore affects the surface topographic properties of the titanium more significantly. Additionally, with a larger number of pulses, the average surface temperature of the substrate increases, and therefore, a more ideal condition for the creation of titanium oxide is generated [25, 43]. **Figure 9** displays these effects clearly. Considering **Figure 9(A)**, more apatite deposition is observed across the surface as opposed to **Figure 9(B)**, which agrees with the expectations.

The apatite-inducing ability of these titanium substrates is further analyzed using EDX. **Figure 10** displays the results.

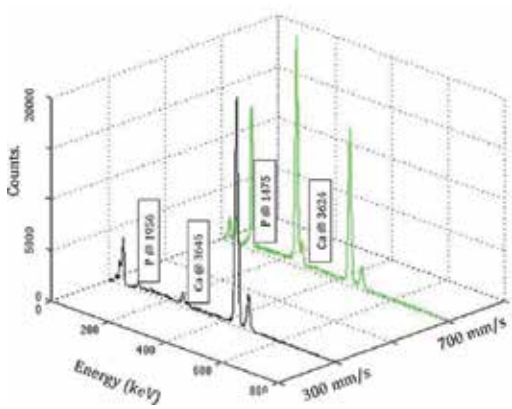

Figure 10. EDX analysis (A) 300 μm/ms, (B) 700 μm/ms.

It is evident in **Figure 10** that calcium and phosphorous concentrations detected across the surface are larger for the curve of 300 mm/s. This agrees with observations from **Figures 7** and **8**.

Overall, it was observed that with a larger number of laser pulses, more energy is delivered to the material, and therefore more surface topographic and oxidation changes take place across the surface of the treated substrates.

5. Effects of frequency

Lastly, the effects of frequency on surface of titanium substrates are examined.

A range of frequencies (25, 50, and 100 kHz) is used in surface treatment, while the average laser power and pulse width are held constant to 11 W and in the range of 15–35 nm, respectively, to ensure consistency of final results (**Table 4** introduces the parameters used in more detail).

Average laser power (W)	Laser frequency (kHz)	Pulse energy (mJ)
11	25	0.30
11	50	0.20
11	100	0.10

Table 4. Laser parameters used in surface treating of Ti substrates.

Figure 11 shows the untreated titanium substrates using laser frequencies of 25, 50, and 100 kHz.

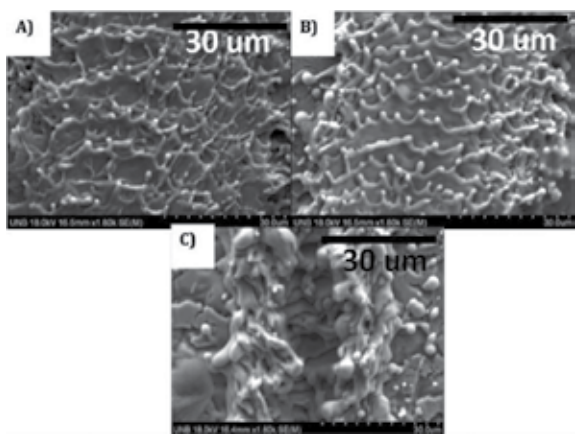

Figure 11. Non-SBF Ti substrates at laser frequency of (A) 25 kHz, (B) 50 kHz, (C) 100 kHz.

As evident in this figure, with a higher frequency, surface irregularities increase on the surface of the substrates. This enhances the surface topographic properties of the treated substrates and therefore increases the biocompatibility of the titanium [25, 41–43].

Furthermore, with a higher frequency, a larger amount of energy is delivered to the surface of the substrates, and the temperature increase causes more titanium oxide to form across the surface. This is similar to the results observed from the other parameters. Therefore, the substrates treated with a frequency of 100 kHz are expected to show the highest apatite-inducing ability across their surface.

5.1. Biocompatibility assessment

Figure 12 displays the EDX analysis of substrates immersed in SBF for 3 days.

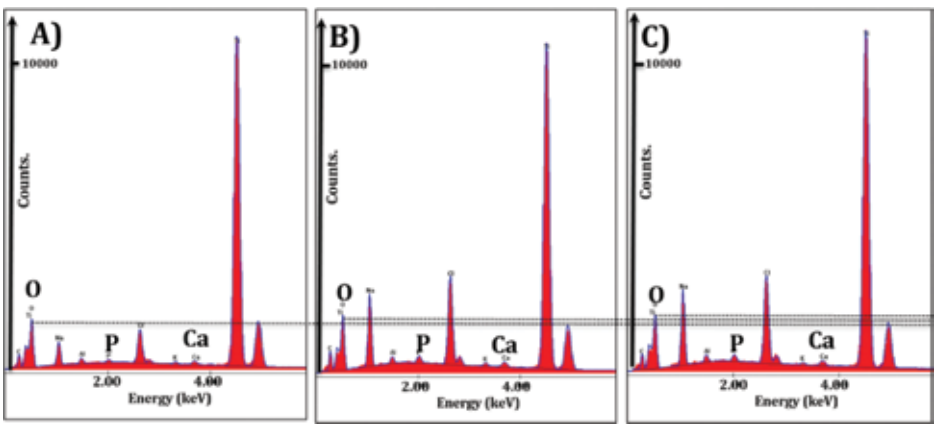

Figure 12. Ti substrates soaked in SBF for 3 days (A) 25 kHz, (B) 50 kHz, (C) 100 kHz.

As evident in **Figure 12**, oxygen concentration slightly increases with an increase in frequency, showing an increase in the concentration of titanium oxide. The higher oxidation level of titanium results in increased negative charge across the surface. Thus, positively charged CO_2, Ca^{2+}, NO_x, and H_2O atoms/ions are attracted to and absorbed by the negatively charged surface of the titanium (OH^-), and create an environment with excellent affinity to biomaterials, such as proteins. The attraction forces between the apatite and the negatively charged titanium oxides are increased through the laser treatment, which, in return, increases the biocompatibility of titanium [25, 42, 43].

This can be further observed by looking at the SEM photography of substrates immersed in SBF.

Figure 13 displays the result.

In this figure, the apatite deposition layer is evident across the irradiated area. As observed from the EDX analysis, the apatite-inducing ability of this substrate is high, which denotes the biocompatibility enhancement of the treated titanium.

http://dx.doi.org/10.5772/63770

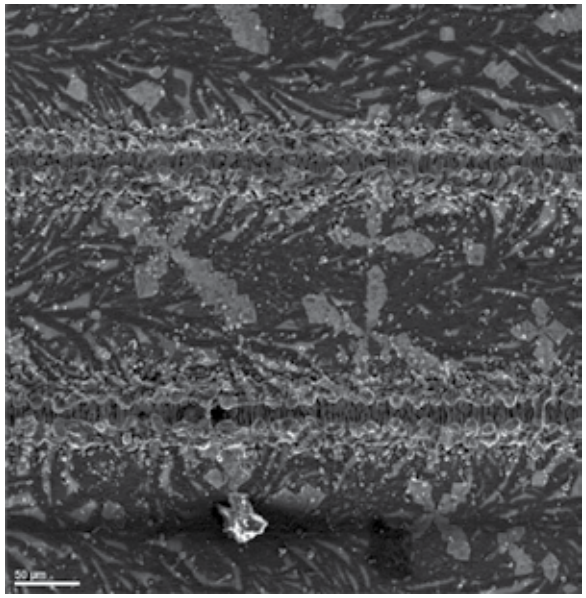

Figure 13. Substrate soaked in SBF for 3 days at 100 kHz.

6. Conclusion

In this chapter, a new method for micro/nano surface texturing of titanium was demonstrated using nanosecond laser irradiation. The application of this method in bone and tissue implant fabrication was explored. Systematic experimental and theoretical studies on effects of the laser parameters on biocompatibility and bioactivity of titanium were conducted. The effects of each parameter were explored individually while other parameters were held constant. Predetermined patterns were induced across thin sheets of titanium substrates to investigate the effects of power, scanning speed, and frequency on surface of the substrates.

Microscopy analysis determined that an increase in power increases the surface topography and ablation across the surface of the material. However, increasing the power within the oxidation limit of titanium can lead to generation of titanium oxide along the irradiation area. Using SBF and cell adhesion, it was found that bioactivity of titanium increases in areas with higher surface topography and higher concentration of titanium oxide.

Additionally, scanning parameters, including pulse number and scanning speed, were found to be influential on the biocompatibility enhancement of titanium substrates. Through a series of experimental and theoretical analysis, it was concluded that a higher pulse number increases the surface energy of titanium substrates, and hence increases the biocompatibility along the irradiation area.

Finally, a range of frequencies was used to examine the bioactivity along the irradiation areas. Microscopy photographs displayed the generation of structures with higher surface topogra-

phy along the laser-induced patterns that have high oxidation and topography properties. Upon biocompatibility assessment, concentrations of calcium, oxygen, and phosphorous are observed on the surface, which shows the bioactivity enhancement of titanium.

This chapter introduced the use of commercially used nanosecond laser systems for biocompatibility enhancement of titanium substrates for fabrication of bone and tissue implants. The key features of this method are described as following:

- Easy controllability
- Simple procedure with rapid processing (single step)
- Feasibility for micro/nano scales
- High efficiency and accuracy

These key features make laser surface texturing desirable for rapid prototyping and fabrication of biomedical devices, and can lead to improvements in cost and durability.

Author details

Amirkianoosh Kiani* and Mitra Radmanesh

*Address all correspondence to: a.kiani@unb.ca

Department of Mechanical Engineering, Silicon Hall: Laser Micro/Nanofabrication Facility, University of New Brunswick, NB, Canada

References

[1] Geetha, M., Singh, A. K., Asokamani, R. and Gogia, A. K. (2009). Ti based biomaterials, the ultimate choice for orthopaedic implants–a review. *Progress in Materials Science*, 54(3), 397–425.

[2] Burg, K. J. L.; Porter, S.; and Kellam, J. F. (2000) Biomaterials developments for bone tissue engineering. *Journal of Biomaterials,* 21, 2347–2359.

[3] Geetha, M.; Asokamani, S.; and Gogia, A. K. (2009) Ti based biomaterials, the ultimate choice for orthopaedic implants – a review. *Journal of Progress in Materials Science,* 54, 397–425.

[4] Ponsonnet, L.; Reybier, K.; Jaffrezic, N.; Comte, V.; Lagneau, C.; Lissac, M.; and Martelet, C. (n.d.)., Relationship between surface properties (roughness, wettability) of titanium and titanium alloys and cell behaviour. *Materials Science and Engineering.*

[5] Stevens, M. M. (2008) Biomaterials for bone tissue engineering. *Journal of Materials Today*, 11, 18–25.

[6] Taddei, E. B.; Henriques, V. A. R.; Silva, C. R. M.; and Cairo, C. A. A. (2004) Production of new titanium alloy for orthopedic implants. *Journal of Materials Science & Engineering*, 24, 683–687.

[7] Taimoor H.; Qazi, D.; Mooney, J.; Pumberger, M.; Geißler, S.; and Duda G. N (2015) Biomaterials based strategies for skeletal muscle tissue engineering: existing technologies and future trends. *Journal of Biomaterials*, 53, 502–521.

[8] Gristina, A (1987) Biomaterial-centered infection, microbial adhesion versus tissue integration. *Journal of* Science, 237, 1588–1595.

[9] Wang, H.; Liang, C.; Yang, Y.; and Li, C. (2010) Bioactivities of a Ti surface ablated with a femtosecond laser through SBF. *Journal of Biomedical Materials*, 5, 1–5.

[10] Majumdar, J.; and Manna, I. (2011) Laser material processing. *Journal of International Materials Reviews*, 56, 341–388.

[11] Pereira, A.; Cros, A.; Delaporte, P.; Georgiou, S.; Manousaki, A.; Marine, W.; and Sentis, M. (2004) Surface nano-structuring of metals by laser irradiation: effects of pulse duration, wavelength and gas atmosphere. *Journal of Applied Physics. A.*, 79, 1433–1437.

[12] Ahmmed, T.; Yang, T.; Ling, E. J.; Servio, P.; and Kietzig, A. (2014) Introducing a new optimization tool for femtosecond laser-induced surface texturing on titanium, stainless steel, aluminum and copper. *Journal of Optics and Lasers in Engineering*, 66, 258–268.

[13] Harooni, M.; Carlson, B.; Strohmeier, B. R.; and Kovacevic, R. (2014) Pore formation mechanism and its mitigation in laser welding of AZ31B magnesium alloy in lap joint configuration. *Journal of Materials & Design*, 58, 265–276.

[14] Mukherjee, S.; Dhara, S.; and Saha, P. (2013) Enhancing the biocompatibility of Ti6A14V implants by laser surface microtexturing: an in vitro study. *Journal of International Journal of Manufacturing Technolog*, 76(1–4), 5–15.

[15] Hutmacher, D. W. (2000) Scaffolds in tissue engineering bone and cartilage. *Journal of Biomaterials.* 21, 2529–2543.

[16] Venkatakrishnan, K.; Stanley, P.; Sivakumar, N.R.; Tan, B.; and Lim, L.E.N. (2003) Effect of scanning resolution and fluence fluctuation on femtosecond laser ablation of thin films. *Journal of Applied Physics*, 77, 655–658.

[17] Tong, W. Y., Y. M. Liang, Vivian Tam, H. K. Yip, Y. T. Kao, K. M. C. Cheung, K. W. K. Yeung, and Y. W. Lam. "Biochemical characterization of the cell-biomaterial interface by quantitative proteomics.(2010) Molecular & Cellular Proteomics 9 (10), 2089–2098.

[18] Tran, D. V.; Lam, Y. C.; Zhen, H. Y.; Murukeshan, V. M.; Chai, J. C.; and Hard, D. E. (2005) Femtosecond Laser Processing of Crystalline Silicon."http://dspace.mit.edu/bitstream/handle/1721.1/7449/IMST010.pdf

[19] Yilbas, B. S.; and Al-Aqeeli, N. (2009) Analytical Investigation Into Laser Pulse Heating and Thermal Stresses. *Journal of Optics & Laser Technology,* 41, 132–139.

[20] Kiani, A.; Venkatakrishnan, K.; and Tan, B. (2013) Optical absorption enhancement in 3D silicon oxide nano-sandwich type solar cell. Journal of Optics Express, 22, A120–A131.

[21] Ashby, M. F.; and Easterling, E. K. (1984) The transformation hardening of steel surfaces by laser beams; I. Hypo-eutectoid steels. *Journal of Acta Metallurgica*, 32, 1935–1937.

[22] Ion, J. C.; Scherclift, H. R; and Ashby, M. F. (1992) Diagrams for laser materials processing. *Journal of Acta Metallurgica et Materialia*, 40, 1539–1551.

[23] Kiani, A.; Venkatakrishnan, K.; and Tan, B. (2011) Enhancement of the optical absorption of thin-film of amorphorized silicon for photovoltaic energy conversion. *Journal of Solar Energy,* 85, 1817–1823.

[24] Woodard, p.; and Druden, J. (1998) Thermal analysis of a laser pulse for discrete spot surface transformation hardening. *Journal of Applied Science,* 85, 2488–2496.

[25] Radmanesh M.; Kiani A. (2015) Bioactivity enhancement of titanium induced by Nd: Yag laser pulses. *Journal of applied biomaterials & functional materials,* 0–0.

[26] Kokubo, T.; and Takadama, H. (2006) How useful is SBF in predicting in vivo bone bioactivity?. *Journal of Biomaterials,* 27, 2907–2915.

[27] Aza, De; Fernandez-Pradas, P. N.; and Serra, P. (2004). In vitro bioactivity of laser ablation pseudowollastonite coating. *Journal of Biomaterials*, 25, 1983–1990.

[28] Kurella, A., & Dahotre, N. B. (2005). Review paper: surface modification for bioimplants: the role of laser surface engineering. *Journal of biomaterials applications*, 20(1), 5–50.

[29] Egerton, R. F. (2005) Physical principles of electron microscopy: an introduction to TEM, SEM, and AEM. Springer, 202, New York, USA.

[30] Goldstein, J. (2012) Scanning Electron Microscopy and X-Ray Microanalysis, Springer, ISBN 978-0-306-47292-3, New York, USA.

[31] Albrektsson, T.; and Wennerberg, A. (2004). Oral implant surfaces: part 1 – review focusing on topographic and chemical properties of different surfaces and in vivo responses to them. *International Journal of Prosthodontics*, 17(5).

[32] Brady, J.; Newton, R.; and Boardman, S. (1995) New uses for powder x-ray diffraction experiments in the undergraduate curriculum. *Journal of Geological Education*, 43, 466–470.

[33] Trtica, M; Gakovic, B; Batani, D; Desai, T; Panjan, P; and Radak, B. (2006) Surface modifications of a titanium implant by a picosecond Nd: YAG laser operating at 1064 and 532nm. *Journal of Applied Surface Science,* 253, 2551–2556.

[34] Kiani, A.; Venkatakrishnan, K.; Tan, B.; and Venkataramanan, V. (2011) Maskless lithography using silicon oxide etch-stop layer induced by megahertz repetition femtosecond laser pulses. *Journal of Optics Express,* 19, 10834–10842.

[35] Colpitts, C.; and Kiani, A. (2016). Synthesis of bioactive three-dimensional silicon-oxide nanofibrous structures on the silicon substrate for bionic devices' fabrication. *Journal of Nanomater Nanotechnol*, 6:8. doi: 10.5772/62312

[36] Kiani, A.; Venkatakrishnan, K.; and Tan, B. (2010). Direct laser writing of amorphous silicon on Si-substrate induced by high repetition femtosecond pulses. *Journal of Applied Physics*, 108(7), 074907.

[37] Kiani, A.; Patel, N. B.; Tan, B.; and Venkatakrishnan, K. (2015). Leaf-like nanotips synthesized on femtosecond laser-irradiated dielectric material. *Journal of Applied Physics*, 117(7), 074306.

[38] Radmanesh, M.; and Kiani, A. (2015) ND:YAG laser pulses ablation threshold of stainless steel 304. *Journal of Materials Sciences and Applications*, 6, 634–645, doi: 10.4236/msa.2015.67065.

[39] Gamaly, E. G.; Rode, A. V.; and Luther-Davies, B. (1999). Ultrafast ablation with high-pulse-rate lasers. Part I: theoretical considerations. *Journal of Applied Physics*, 85(8), 4213–4221.

[40] Radmanesh, M.; and Kiani, A. (2015) Effects of laser pulse numbers on surface biocompatibility of titanium for implant fabrication. *Journal of Biomaterials and Nanobiotechnology*, 6, 168–175. doi:10.4236/jbnb.2015.63017.

[41] Zhao, G.; Schwartz, Z.; Wieland, M.; Rupp, F.; Geis-Gerstorfer, J.; Cochran, D. L.; and Boyan, B. D. (2005). High surface energy enhances cell response to titanium substrate microstructure. *Journal of Biomedical Materials Research Part A*, 74(1), 49–58.

[42] Tenner, F.; Brock, C.; Klampfi, F.; and Schmidt, M. (2014) Analysis of the correlation between plasma plume and keyhole behavior in laser metal welding for the modeling of the keyhole geometry. *Journal of Optics and Lasers in Engineering,* 64, 32–41.

[43] Radmanesh, M; and Kiani, A. (2015) "Enhancing biocompatibility of grade 4-titanium using laser surface texturing for bone and tissue transplant applications." 25th Canadian Congress of Applied Mechanics (CANCAM 2015), London, Ontario, Canada.

Chapter 16

Excimer Laser and Femtosecond Laser in Ophthalmology

Liang Hu, Yiqing Huang and Meng Lin

Additional information is available at the end of the chapter

http://dx.doi.org/10.5772/64238

Abstract

Laser technology is used in many basic and clinical disciplines and specialties, and it has played an important role in promoting the development of ophthalmology, especially corneal refractive surgery. We provide an overview of the evolution of laser technology for use in refractive and other ophthalmologic surgeries, mainly focusing on two types of lasers and their applications. First, we discuss the characteristics of the excimer laser and its application in corneal refractive surgery treating ametropia (e.g., photorefractive keratectomy (PRK), laser epithelial keratomileusis (LASEK), epipolis laser in situ keratomileusis (Epi-LASIK), and transepithelial photorefractive keratectomy (Trans-PRK) and presbyopia surgery). Second, we discuss the characteristics of the femtosecond laser and its application in corneal refractive surgery (e.g., femtosecond laser in situ keratomileusis (FS-LASIK), insertion of intracorneal ring segments, small-incision lenticule extraction (SMILE), and femtosecond lenticule extraction (FLEx)) and other ophthalmologic surgeries (e.g., penetrating keratoplasty (PKP), deep anterior lamellar keratoplasty, Descemet's stripping endothelial keratoplasty (DSEK), and cataract surgery). The patients studied received many benefits from the excimer laser and femtosecond laser technologies and were satisfied with their clinical outcomes.

Keywords: excimer laser, femtosecond laser, corneal refractive surgery, ophthalmology

1. Introduction

In the field of ophthalmology, laser technology is used in many basic and clinical disciplines and specialties. It has played an important role in promoting the development of ophthalmology. Advancements in technology have allowed measurable improvements in the surgical safety, efficacy, speed, and versatility of the laser, creating more operation methods to treat eye diseases, especially corneal refractive surgery. Because myopia is one of the most prevalent

ocular disorders, and high myopia may result in comorbidities associated with significantly increased risks of severe and irreversible loss of vision, it is always an important topic of research worldwide. Laser technology, including the excimer laser and the femtosecond laser, has brought an era of laser corneal refractive surgery. According to the location of ablation, corneal refractive surgery can be divided into two types: laser corneal surface refractive surgery and laser corneal lamellar refractive surgery. Because of the increasing numbers of applications in ophthalmology and their successful implementations, ophthalmic use of laser technology is expected to continue flourishing.

The aim of this chapter is to review the evolution of laser technology in refractive and other ophthalmologic surgeries, mainly focusing on the characteristics of two types of lasers and their applications: the excimer laser applied in laser corneal surface refractive surgery and presbyopia surgery and the femtosecond laser applied in laser corneal lamellar refractive surgery and other ophthalmologic surgeries.

2. Excimer laser in ophthalmology

2.1. Characteristics of the excimer laser

The *excimer* (comprising the terms *excited* and *dimer*) was named by the Russian, Nikolay Basov, in 1970, based on his work with a xenon dimer gas [1]. An *excimer* is a short-lived dimeric or heterodimeric molecule formed from two species (a noble gas and a halide), at least one of which has completely filled the valence shell by electrons. Excimers are only formed when one of the dimer components is in the excited state. When the excimer returns to the ground state, its components dissociate. The wavelength of an excimer's emission depends on the noble gas, such as ArF (193 nm), KrF (248 nm), XeCl (308 nm), or XeF (351 nm). The ultraviolet laser (193 nm) is commonly used to ablate tissue through ablative photodecomposition. The process of ablative photodecomposition involves three main components: absorption, bond breaking, and ablation. A large number of experiments have shown that the ArF excimer laser (193 nm) is the most optimal for corneal absorption and ablation because of its sufficient photon energy (6.4 eV) and precision (only penetrating the superficial layer; 0.3 μm). The tissue-ablation depth is positively correlated with the logarithm of laser density; 1-J/cm^2 energy can ablate approximately 1-μm corneal tissue. In addition, as a cold laser, the excimer laser can ablate the tissue accurately without thermal damage.

2.2. Photorefractive keratectomy (PRK)

Professor Jose I. Barraquer described his coined technique of "keratomileusis" to correct myopia in 1949, and this could be the original form of photorefractive keratectomy (PRK). A few years later, many researchers designed similar surgical procedures. In 1983, Stephen Trokel first started using the ArF (193 nm) excimer laser as a precise and safe tool of corneal shaping in calf eyes. He found that the excimer laser not only accurately ablated central corneal tissues but also did not do excessive damage to the peripheral corneal tissues. After a large number of animal experiments, in 1989, Marguerite McDonald, who first applied the technol-

ogy to human eyes, presented the first patency of using the excimer laser as a corneal refractive tool, and it was accepted. Since then, PRK has become the classic refractive surgery, and its safety and efficacy have been proven by abundant studies. China introduced this surgery in 1993, but the presence of postoperative complications has influenced its development [1].

Compared with the current, more popular lamellar corneal refractive surgery, PRK has shown similar postoperative visual quality but more intraoperative and postoperative complications, such as haze. Nevertheless, Wagoner et al. [2] proposed that PRK had better visual results compared with lamellar corneal refractive surgery. O'Brart [3] also thought PRK showed better cornea curvature and excellent visual quality compared with those of lamellar corneal refractive surgery.

2.3. Laser epithelial keratomileusis (LASEK)

Laser epithelial keratomileusis (LASEK), also called laser sub-epithelial keratectomy, was first proposed and named by Italian doctor Massimo Camellin in 1998. The first case of LASEK was performed by Azar at Massachusetts Eye and Ear Infirmary in 1996. It is a modified operation based on the PRK, which enabled the epithelium to be preserved as a flap (about 50–70 μm) using 20% ethanol to infiltrate and release the connection between the corneal epithelium and Bowman layer and then overturn the flap. The flap is then reset after ablating the stroma using the excimer laser.

Therefore, LASEK can be considered a kind of PRK that is "wearing flap." The key to success throughout the surgical procedure is the activity and good adhesion of the flap. Owing to the viable flap, it combines the advantages of laser in situ keratomileusis (LASIK) and PRK. Because LASEK is essentially a kind of surface ablation evolved from PRK; consequently, it reserves the features of safety, validity, simplicity, and stability in low to moderate ametropia and presbyopia correction. Moreover, its flap design, which is similar to that of LASIK, has several merits: postoperative discomfort can reduce within 2–8 h after the procedure; the epithelium of the optical region in the slit lamp after surgery is as complete and clear as it is before surgery within 12–24 h; there is no edema or postoperative haze; and early complications, such as corneal epithelium necrosis, are less common compared with PRK. These outstanding characteristics are likely to have provided the inspiration for the advent of LASIK.

Furthermore, LASEK preserves the corneal biomechanical integrity and results in good clinical outcomes. Scholars have indicated that LASEK shows better postoperative outcomes including postoperative corneal topography and contrast sensitivity, and faster postoperative recovery rate in low to moderate myopia correction compared with PRK. In addition, LASEK has a unique advantage for patients with retinal diseases, high myopia, or blepharophimosis. Lu Xiong conducted a study on the clinical outcomes in low to moderate myopia after LASEK treatment, and the results showed that LASEK has a good effect and better postoperative experience compared with PRK.

According to the principles of LASEK, it not only optimizes PRK but also avoids some disadvantages of laser lamellar corneal refractive surgery such as LASIK. First, it avoids the risk associated with the corneal flap (e.g., free flap, broken flap, and button flap) made by

microkeratome in LASIK. Second, it has less effect on the corneal nerve and less serious dry eye syndrome than LASIK. Third, LASEK creates less surgically induced wavefront aberration because of its thinner flap. In addition, it saves the cost of the microkeratome or femtosecond laser used in LASIK.

Nevertheless, LASEK has some common risks of surface ablation in high myopia correction, such as postoperative haze and side effects of corticosteroid eye drops required after surgery. What is more, LASEK is a complex surgical procedure that requires high surgical skill with a long learning curve for beginners.

2.4. Epipolis laser in situ keratomileusis (Epi-LASIK)

Epipolis laser in situ keratomileusis (Epi-LASIK) was first reported by the Greek doctor Pallikaris in 2003. Different from LASEK, Epi-LASIK uses a microkeratome instead of ethyl alcohol to bluntly separate the corneal epithelial from the Bowman layer. Therefore, Epi-LASIK avoids direct stimulation of alcohol and reserves the intact epithelial basement membrane, which results in good subjective feelings in patients as well as quick recovery and haze reduction.

Epi-LASIK surgery takes the activity of the flap as the core, which is crucial to the therapy effect. Compared with PRK, Epi-LASIK has an extra flap covering the corneal stromal bed, which can effectively protect the stroma below and also promotes corneal tissue healing. Epi-LASIK has different methods of flap creation than those of LASEK. Its flap basement membrane is intact, continuous integrity segments of stratum lucidum and a longer compact layer. The postoperative healing time of Epi-LASIK is shorter without alcohol stimulation or chemical damage to the corneal epithelium. Even though the flap of Epi-LASIK is closer to corneal natural state, the postoperative biomechanical change of the corneal flap and the effect on corneal healing are yet to be determined [4].

2.5. Transepithelial photorefractive keratectomy (Trans-PRK)

Transepithelial photorefractive keratectomy (Trans-PRK), where both the epithelium and stroma are removed in a single step, is a relatively new procedure of laser refractive error correction. It has become the focus in the refractive surgery field recently and the first choice to treat ametropia with or without an irregular cornea. The excimer laser has been developed to the sixth-generation lasers, targeting the goal of minimally invasive laser refractive surgery during the past 30 years. The latest laser system delivers more laser spots per second so as to reduce the treatment time [5]. Tran-PRK has brought a new revolution to excimer laser techniques for its bladeless surgery process [6] and superiority in efficiency and safety. Hence, it has been considered as the representative operation of the laser corneal surface refractive surgery, and it is a step closer to the perfect refractive surgery. Trans-PRK has been indicated in low to moderate myopia patients and a small number of high myopia patients (−8D below), but not in patients with a very low-degree myopia. Trans-PRK is currently regarded as an optimal safety choice for patients with a thin cornea. In addition, it is also the best choice for combat athletes, high-risk workers, and patients with ocular surgical history. For the second

operation and patients with irregular corneas, who need synergistic or customized surgery, Trans-PRK may be the only choice.

2.5.1. Advantages and disadvantages

Compared with other corneal refractive surgeries, Trans-PRK has the advantages of no chemical toxicity or mechanical damage, no corneal incision, no negative pressure suction, and less risk of infection, and it avoids the potential damage caused by negative pressure suction.

Trans-PRK was considered as a kind of minimally invasive surgery for its optimal safety. Without creating a corneal flap, Trans-PRK significantly reduces the postoperative corneal biomechanical change, and it has little effect on the structure of the cornea, without corneal flap mark and flap-related complications. In addition, Tran-PRK offers faster epithelial healing, lower postoperative pain, and significantly less haze formation. Kaluzny et al. [7] used optical coherence tomography to supervise the epithelial recovery time and found that Trans-PRK (3 days) has a significantly shorter recovery time than PRK does (4 days). Aslanides et al. randomly selected 60 eyes of 30 myopic patients who had undergone conventional alcohol-assisted PRK in one eye and Trans-PRK in the other eye. The postoperative follow-up showed that Trans-PRK offers faster epithelial healing and 64% lower average pain scores. The haze level was consistently lower after Trans-PRK from 1 to 6 months [8].

Trans-PRK is considered a minimal complication, maximum security single-laser surgery at present. There is no significant different between Trans-PRK and other laser surgery in final visual acuity [9, 10]. Patient satisfaction is not as high with Trans-PRK compared with the femtosecond laser-assisted laser in situ keratomileusis (FS-LASIK) and small-incision lenticule extraction (SMILE) soon after surgery because of the slightly higher incidence of haze, pain, and slower recovery of visual acuity. However, Trans-PRK has good long-term postoperative satisfaction.

2.5.2. Visual outcomes and visual quality

Many studies have shown that [8, 9, 11] Trans-PRK has high-precision visual outcomes and good stability in ametropia correction. A large retrospective comparison of transepithelial PRK with LASEK, Epi-LASIK, and LASIK detected better visual outcomes with Trans-PRK for high myopia [12]. In hyperopia correction, the effectiveness showed a substantial increase over the previous study, but there are still difficulties, such as the relatively high rate of secondary operation, residual refractive error, surgically induced negative spherical aberration, and astigmatism. In astigmatism correction, static cyclorotation component and dynamic cyclorotation component techniques greatly improve the effectiveness.

With the development of refractive surgery technology, its safety is high. Increasingly, researchers have focused on improving postoperative visual quality. The assessment of the visual quality is divided into two main aspects. The subjective part includes vision acuity (near, intermediate, and distance) and contrast sensitivity, whereas the objective part includes the objective wavefront aberration, point spread function, modulation transfer function, visual quality scale, and so on. Research shows that topography-guided Trans-PRK can

effectively correct the irregular astigmatism and improve the postoperative contrast sensitivity in patients. On the contrary, Trans-PRK simplifies the process, which reduces the potential higher order wavefront aberration caused by irregular ablation and decreases postoperative glare and night vision loss. Therefore, increasingly ophthalmologists choose Trans-PRK to improve postoperative visual quality.

Trans-PRK is the easiest laser refractive surgery for refractive surgeons to learn, and it is stable in techniques and cost-effective. As a result, it is considered an ideal corneal refractive operation for patients.

2.6. Excimer laser in presbyopia correction

Presbyopia is an age-related condition in which accommodation gradually decreases and the eyes are unable to focus and obtain clear near vision. There is one approach to correct presbyopia through laser refractive surgery commonly called PresbyLASIK. Synonymous with LASIK, PresbyLASIK contains the process of making a special ablation profile to either perform a multifocal cornea procedure or increase the depth of field.

PresbyLASIK has been described in three different approaches: central PresbyLASIK, peripheral PresbyLASIK, and transitional multifocality. In central PresbyLASIK, the central area is shaped for near vision and the mid-peripheral cornea is shaped for distant vision. On the contrary, in peripheral PresbyLASIK, the central area is shaped for distant vision and the mid-peripheral corneal area for near vision. Both central and peripheral techniques reportedly obtained adequate spectacle independence in both myopia and hyperopia. In addition, a neuroadaptation process is needed in peripheral techniques. The third approach combines depth of field increase and micro-monovision, which induces a certain degree of spherical aberration to each eye to increase the depth of field while making the nondominant eye slightly myopic [13].

Presbyopia remains the biggest challenge to be corrected: the mechanism of accommodation and the cause of presbyopia are complex to understand fully. Therefore, the efficacy of presbyopia correction even with the latest platform is still in dispute. However, there is enough scientific evidence to consider PresbyLASIK as a useful tool in presbyopia correction [14]. Epstein and Gurgos [15] reported that 89% hyperopia (25/28) patients and 91.3% myopia (94/103) patients who underwent peripheral PresbyLASIK were completely spectacle independent and with distance unaided visual acuity of 20/20 in 67.9% (19/28) in hyperopia patients and 70.7% (53/75) in myopia patients.

3. Femtosecond laser in ophthalmology

3.1. Characteristic of femtosecond laser

Femtosecond laser technology was first introduced by Dr. Kurtz in the early 1990s, and it has developed rapidly over the past two decades. “Laser power” is defined as energy delivered per unit time. The laser-related damage will reduce with the decrease of pulse duration. The

femtosecond laser for ophthalmology works at 1053-nm wavelength with a very short pulse duration of 10^{-15} s, minimizing the collateral damage [16]. The accuracy is 5 μm, allowing high precision in ophthalmic operations [17]. The use of the femtosecond laser has revolutionized the modern ophthalmic surgery.

3.2. Femtosecond laser in situ keratomileusis (FS-LASIK)

The concept of the lamellar refractive procedure was first introduced by Barraquer in the early 1960s. In the 1990s, an excimer laser ablation-assisted lamellar procedure was developed, as the foundation of modern laser in situ keratomileusis (LASIK). Compared with photorefractive keratectomy (PRK), visual recovery is faster and visual outcome is rapidly stable after LASIK. Flap-associated complications and increased incidence of dry eye after surgery, however, affect the quality of life. The safety, precision, and predictability of the femtosecond laser have changed LASIK over recent years.

Flap formation is critical to a successful LASIK surgery. Improper flap geometry, decentration, irregular cut, and epithelial damage lead to a large number of complications. Over the past decades, mechanical microkeratome has been performed in LASIK because of its reliability and safety. However, complications such as incomplete flap, free flap, and buttonhole continue to plague surgeons. Furthermore, because of the instability of mechanical microkeratome, corneas may be too steep, too flat, or too thin even after a successful operation [18].

The femtosecond laser became available for LASIK flap formation approximately 10 years ago. It reduced the risk of the above-mentioned complications. With mechanical microkeratome, the flap is thinner centrally and thicker peripherally (meniscus-shaped flap), which increases the incidence of buttonhole perforation. The femtosecond laser allows thin and uniform flaps, which improves the stability, safety, and precision of the flaps. It can also create thinner flaps with minimum effects on stromal architecture. Flap centration, diameter, and thickness are also more precise in femtosecond-created flaps. Another advantage of the femtosecond laser is that it allows the surgeon to select the cutting angle, position, and diameter of the hinge, as well as the flap diameter and flap thickness, which may provide better flap stability and reduce clinical epithelial ingrowth.

Though femtosecond lasers reduce the incidence of complications such as buttonhole perforation, incomplete flap, free cap, and irregular cuts, there are still some specific limitations in FS-LASIK. FS-LASIK requires two laser platforms—one for flap creation (femtosecond laser) and another for stromal bed ablation (excimer laser)—which increases the time and cost of the laser procedure. Because of the response of corneal keratocytes to the energy and inflammatory responses of adjacent tissues to gas bubbles, patients may encounter photophobia, called transient light-sensitivity syndrome (TLSS), early after FS-LASIK. With the development of the femtosecond laser, it needs less energy for flap formation, and thus reduces the incidence of TLSS [19]. The presence of cavitation gas bubbles during FS-LASIK, which originate from stray laser pulses into the aqueous humor, can impede the eye tracker of the excimer laser. An increased rate of diffuse lamellar keratitis, a sterile inflammatory reaction, was also observed in FS-LASIK because of the higher flap interface inflammatory response to

laser energy and gas bubbles. Revolution in femtosecond laser energy is expected to reduce the specific complications.

In our previous study, patients treated with a femtosecond laser showed better corneal regeneration than those with a microkeratome did. Because of its precision and predictability, the femtosecond laser makes a smoother flap and causes less damage to the corneal nerve [20]. However, different from others' opinions, our data showed that there were no significant differences in the tear meniscus parameters between the microkeratome and femtosecond laser [21].

3.3. Femtosecond lenticule extraction (FLEx)

A new approach called femtosecond lenticule extraction (FLEx) was introduced to correct myopia and astigmatism. FLEx does not require a microkeratome or an excimer laser. It uses only the femtosecond laser, which is more convenient than other procedures that require both excimer and femtosecond lasers. Two cuts (posterior and anterior) in the cornea are involved in the procedure, which thus create a lenticule that is ultimately removed. There is no significant difference between FLEx and conventional LASIK, both in efficacy and safety, which promotes FLEx to be a promising new corneal refractive procedure to correct refractive errors.

However, it has been reported that the visual outcome after FLEx was stable early after surgery, but visual recovery was slow [22]. As a corneal flap is necessary before lenticule extraction, associated complications such as dry eye and compromise of corneal biomechanical strength are inevitable. Therefore, the technique evolved into SMILE.

3.4. Small-incision lenticule extraction (SMILE)

SMILE, passing the Conformite Europeenne (CE) certification in 2009, is a novel technique to correct refractive errors. The procedure involves passing a dissector through a small incision to separate the lenticular interfaces and allow the lenticule to be removed, thus eliminating the need to create a flap [23]. Early or late complications associated with flaps, such as dislocations and buttonholes are avoided; therefore, patients' experience and visual outcomes improve.

The absence of flap creation minimizes the disruption of the stromal architecture because the corneal lenticule is extracted from the mid-stroma [24]. Fewer corneal nerve branches are disrupted compared with FS-LASIK, which preserves corneal biomechanical strength and maintains sensitivity. Thus, the risk of dry eye and patients' discomfort is reduced after surgery [25]. The minimal disruption of the anterior corneal surface epithelium, Bowman's layer, and anterior stroma is also associated with less risk of dry eye [26]. Laser fluence and difference in stromal hydration, which may affect stromal ablation, are avoidable in SMILE. Prospective and retrospective studies of SMILE have shown that in the terms of efficacy, predictability, and safety SMILE is similar to FS-LASIK.

However, there are still some difficulties in SMILE. Similar to a flap in FS-LASIK, a cap whose uniform regularity is essential to optimal visual outcome is created using a femtosecond laser.

In addition, the surface quality of the corneal lenticule can be irregular, causing tissue bridges, cavitation bubbles, scratches, or incomplete extraction of stromal lenticules [27]. At present, SMILE is mainly applied in mild myopia. It still needs more attempts and experience to be used in hyperopic eyes.

Complications such as epithelial erosion, suction loss, cap perforation, and lenticule extraction difficulty can all occur. Corneal haze, dry eye syndrome, keratitis, and interface inflammation have also been reported.

SMILE is a promising new technique for refractive error correction. With further development of the femtosecond laser, SMILE may gain greater acceptance in the future. However, we still have to pay more attention to its complications to verify its safety.

3.5. Femtosecond laser in presbyopia correction

3.5.1. Corneal inlay implantation

Corneal inlay implantation is performed for presbyopic correction. It changes the anterior corneal surface curvature, cornea refractive index, and depth of focus by placing a small inlay of suitable biocompatible material within the stroma. The benefits of inlays are the reversibility of the procedure by removal of the implant, implantation simplicity, and implant repositioning. The ability to perform ad hoc refractive procedures allows the simultaneous correction of ametropia. The most common complications after the surgery are glare and dry eye. The femtosecond laser advances flaps and tunnel creation to implant the inlays accurately on the line of sight, and thus result in remarkable improvements in uncorrected visual acuity (near and intermediate) and minimal change in uncorrected distance visual acuity. This procedure also provides good nonspectacle-corrected near vision for average daily activities [18, 28].

3.5.2. IntraCor surgery

IntraCor surgery is a new technique applicable for ametropic or low-degree hyperopic eyes (+0.5 to +1.5 D). It changes the topographic and refractive characteristics of the central portion of the cornea selectively with femtosecond laser. The procedure involves concentric intrastromal ring creation in the central portion of the cornea at different corneal depths (between the Bowman's and Descemet's boundaries). Other than the treatment failure in presbyopic correction, no major complications have been reported. IntraCor surgery is promising in the field of presbyopia correction [18].

3.6. Astigmatic keratotomy (AK)

To correct low to high astigmatism, astigmatic keratotomy (AK) is performed. The accuracy of length, optical zone, and incision depth are crucial in visual outcomes. However, the limitation of AK is the unpredictability of manual corneal incision. The application of femtosecond laser in AK provides accuracy and precision in corneal incision manufacturing and thus improves significantly in uncorrected and best-corrected visual acuity. The femtosecond laser can also be applied in case of high degrees of post-keratoplasty astigmatism. The

incisions within the graft button present precise geometry and reliable depth of incision. Specific complications associated with femtosecond laser-assisted AK such as self-healing micro-corneal perforations and low-grade inflammation at the incision site appeared [18, 29].

3.7. Intracorneal ring segments

Intracorneal ring segments were small and curved when first proposed in 1978. Clear ring segments made of polymethylmethacrylate are implanted in the deep corneal stroma with the aim of generating modifications of corneal curvature and refractive changes. Peripheral intracorneal implantation has been permitted to correct low to moderate astigmatism and myopia and keratoconus by Food and Drug Administration (FDA). Complications such as incomplete tunnel formation, corneal perforation, endothelial perforation, corneal melting, and uneven implant placement may occur with the traditional technique. The femtosecond laser can be programmed to create corneal channels at a specific depth and orientation with high predictability and precision to allow safer insertion of Intacs segments. In patients with keratoconus, the femtosecond laser can be programmed to cut tunnels for the implantation of intracorneal ring segments, and it results in better safety owing to greater consistency of depth and uniformity [29, 30].

3.8. Penetrating keratoplasty (PKP)

Penetrating keratoplasty (PKP) developed rapidly after first being introduced in the early 1900s. The surgical outcomes rely on a centered and perpendicular cut of cornea, a well-matched donor button, and a recipient bed [18]. Manual PKP requires a long learning curve and a lengthy procedure time, which can be optimize using the femtosecond laser. The femtosecond laser can also achieve a higher precision in surgical steps, such as the donor cornea cutting. Moreover, the choice of shapes and diameters in femtosecond laser-assisted PKP is dependent on individualized clinical requirement. It enables advanced shaped corneal cuts creation, eliminates manual dissection, thus minimizing misalignments, and increases the stability of the wound. Some pattern of incisions that are not compassable with conventional technique can be achieved by femtosecond laser. However, postoperative regular and irregular astigmatism remain a major challenge in full-thickness keratoplasty.

3.9. Anterior lamellar keratoplasty (ALK)

Anterior lamellar keratoplasty (ALK) is a partial thickness corneal transplantation indicated for management of anterior corneal dystrophies degenerations, ulcers, and scars. The advantages of ALK over PKP include being less invasive and having a decreased rate of rejection. Femtosecond laser-assisted suture less anterior lamellar keratoplasty (FALK), first described in 2008, has been reported to be safe, effective, and stable. The femtosecond laser has reduced irregular astigmatism and accelerated visual recovery by its precision of pre-programmed corneal dissections at a variety of depths and orientations. As the corneal incision is well shaped, it can be converted to full-thickness keratoplasty in case of Descemet membrane perforation. The donor and recipient tissue are better positioned because of highly precise cuts assisted by the femtosecond laser, and thus sutures are typically removed earlier.

Limitations of ALK include the high cost and the slow growth of the epithelium over the graft [18, 30].

3.10. Femtosecond laser-assisted endothelial keratoplasty

3.10.1. Descemet's stripping endothelial keratoplasty (DSEK)

DSEK has been the preferred approach for treating corneal endothelial diseases, such as bullous keratopathy, Fuchs dystrophy, congenital hereditary endothelial dystrophy, and endothelium failure in previous penetrating keratoplasty. It removes the diseased endothelium and leaves the posterior cornea intact. However, technical challenges always afflict corneal surgeons. The application of the femtosecond laser alleviates certain difficulties. Significant advantages over manual dissection are that the femtosecond laser allows for increased automation and standardization in donor tissue preparation. In addition, lamellar interface preparation can be performed up to 3 weeks before the surgery, making it feasible for conversion to PKP owing to complications during preparation of the donor disk. It also creates a smoother donor-recipient interface to minimize induced refractive astigmatism. However, whether the femtosecond laser has an effect on endothelial cell loss and visual acuity after donor tissue preparation has yet to be determined [18, 30].

3.10.2. Descemet's membrane endothelial keratoplasty (DMEK)

Descemet's membrane endothelial keratoplasty (DMEK) has been proven to result in faster visual recovery, fewer higher order aberrations, and lower rejection rates by abundant evidence. The crucial technique is selective endothelial transplantation. The femtosecond laser offers a precise and predictable means to create the uniform thickness of the posterior stromal rim and control big bubble expansion that cannot be achieved by manual operation. The femtosecond laser not only avoids energy-associated damage but also results in smooth stromal interface by closer spots, line separations, and a low energy level. Thus, the femtosecond laser can be a novel approach for the donor grafts preparation of DMEK, which may reduce intraoperative graft manipulation and postoperative detachments [29, 31].

3.11. Cataract surgery

At 2008, the femtosecond laser was first performed in Europe in cataract surgery and was approved by the FDA in 2010. It was applied in the steps of corneal incision, arcuate corneal incisions, capsulorhexis, lens fragmentation, and liquefaction. The short pulses duration (10^{-15} s) make it a promising tool in cataract surgery [32].

3.11.1. Corneal incisions

Clear self-sealing corneal incision is of most importance in cataract surgery. In terms of length and tunnel structure, manual incision is difficult to control. In addition, bacteria have a chance to enter at low intraocular pressure because of the instability of manual incision and thus lead to endophthalmitis. Compared with manual incisions, corneal incisions made using the

femtosecond laser are more precise in width, depth, and length. More consistency in the architecture is also achieved, which leads to better incision sealing without stromal hydration at the end of the surgery. The stability of the wound makes it more resistant to deformation and leakage. The femtosecond laser is used to create a clear corneal incision according to pre-programming, which requires a large amount of patient data to confirm, and definitive results. In cases of corneal astigmatism, an arcuate or a relaxing incision can be created, which has been reported to provide more stable and accurate long-term outcomes compared with toric intraocular lenses (IOLs). The femtosecond laser shows less damage by virtue of its construction and reduced mechanical stress during surgery, which may decrease corneal swelling after surgery.

3.11.2. Capsulotomy

A precise size and centration capsulorhexis are essential to optimize the IOL position. The IOL's longitudinal displacement per millimeter will lead to approximately 1.25-D refractive change, inducing myopia for an anterior shift and hyperopia for a posterior displacement. Capsulorhexis size is correlated with effective lens position. An insufficient overlap of the IOL, results in decentration, oblique astigmatism, and increased higher order aberration. A small capsulorhexis has been associated with anterior capsule fibrosis. Manual continuous curvilinear capsulorhexis (CCC) relies on the technique and proficiency of the surgeon. The femtosecond laser can be used to create a more precise, better-sized, and centered opening of the anterior capsule compared with the conventional CCC by dissecting it with a spiral laser pattern. Compared with the manual CCC group, the laser CCC group showed more accuracy and stability in anteroposterior and central IOL positioning. It is also more predictable in the refractive outcome, which is more important to patients with high expectation [33, 34].

3.11.3. Lens fragmentation and liquefaction

The increased energy for lens fragmentation and liquefaction delivered from the phacoemulsification probe to the eye can result in energy-associated capsule complications and corneal endothelial cell injury in manual phacoemulsification. The reduction in ultrasound energy can decrease the risk of such complications. It is reported that the femtosecond laser reduced the ultrasonic energy delivered during phacoemulsification significantly. However, its effect on endothelial damage is still unknown.

3.11.4. Limitation and complications

Although the femtosecond laser showed excellent advantages over manual operation in cataract surgery, there are still some inevitable limitations and complications.

1. Additional operating room shifting time

Patients need to be shifted under the operating microscope after application of laser treatment. This logistical issue results in increased time spent with each patient, which could lead to overall delay.

http://dx.doi.org/10.5772/64238

2. Applicability

   The femtosecond laser relies on good anterior chamber imaging. Patients with poor eyelid opening, nystagmus, poor pupillary dilatation, corneal opacities, and ocular surface disease are poor candidates. It is also not suitable for patients with tremors or dementia in the initial docking system. The femtosecond laser is not available for grade 4 cataract according to the Lens Opacities Classification System III (LOCS III).

3. Complications

   Capsular blockage syndrome: Large diameter hydrodissection cannula with high-speed fluid may inhibit a gas bubble that is formed from leaving the nucleus. Pressure elevation between the capsule leads to the rupture of the posterior capsule, and the lens may drop into the vitreous cavity. This is a learning curve-related complication, which can be avoided by a more cautious and skilled surgeon

   Pupillary constriction: Bubble formation and suction force can trigger pupillary constriction by releasing small amounts of free radicals. In addition, a delay between femtolaser pretreatment and cataract surgery may result in pupil diameter changes (5–10 min is recommended).

   Corneal incision sizing and positioning the initial docking of the laser ring is crucial to the accuracy of the intended femtolaser-created incision. Imperfect interface positioning causes inaccuracy of corneal incision sizing and positioning, which results in surgically induced astigmatism and complication in the manual final procedure [18, 35].

4. Summary

The surgery has gradually matured with the development of the modern excimer laser equipment and technology. Upgrading thermal control and ablation centration will achieve better corneal biomechanical results. We have reason to believe that a single excimer laser surgery would be the next breakthrough in refractive surgery, the next step toward the "perfection" of refractive surgery. Femtosecond laser advancements over the past two decades have brought revolutionary change in ophthalmic practice. It not only improves the safety and efficacy in corneal refractive surgery but also achieves remarkable advancement in the field of cataract surgery. Despite having certain limitations and complications, femtosecond lasers are promising in ophthalmology. Both excimer and femtosecond laser technology will serve for better human health as long as we apply it appropriately.

Author details

Liang Hu*, Yiqing Huang and Meng Lin

*Address all correspondence to: liang_hu@live.cn

School of Ophthalmology and Optometry, Wenzhou Medical University, Wenzhou, China

References

[1] Krueger RR, Rabinowitz YS,Binder PS. The 25th anniversary of excimer lasers in refractive surgery: historical review. J Refract Surg. 2010, 26(10): 749–760. 10.3928/1081597X-20100921-01

[2] Wagoner MD, Wickard JC, Wandling GR, Milder LC, Rauen MP, Kitzmann AS, Sutphin JE,Goins KM. Initial resident refractive surgical experience: outcomes of PRK and LASIK for myopia. J Refract Surg. 2011, 27(3): 181–188. 10.3928/1081597X-20100521-02

[3] O'Brart DPS. Excimer laser surface ablation: a review of recent literature. Clin Exp Optom. 2014, 97(1): 12–17. 10.1111/cxo.12061

[4] Pallikaris IG, Kalyvianaki MI, Katsanevaki VJ,Ginis HS. Epi-LASIK: Preliminary clinical results of an alternative surface ablation procedure. J Cataract Refract Surg. 2005, 31(5): 879–885. DOI 10.1016/j.jcrs.2004.09.052

[5] El Bahrawy M,Alio JL. Excimer laser 6(th) generation: state of the art and refractive surgical outcomes. Eye Vis (Lond). 2015, 2: 6. 10.1186/s40662-015-0015-5

[6] Wang DM, Du Y, Chen GS, Tang LS,He JF. Transepithelial photorefractive keratectomy mode using SCHWIND-ESIRIS excimer laser: initial clinical results. Int J Ophthalmol. 2012, 5(3): 334–337. 10.3980/j.issn.2222-3959.2012.03.16

[7] Kaluzny BJ, Szkulmowski M, Bukowska DM, Wojtkowski M. Spectral OCT with speckle contrast reduction for evaluation of the healing process after PRK and transepithelial PRK. Biomed Opt Express. 2014, 5(4): 1089–1098. 10.1364/BOE.5.001089

[8] Aslanides IM, Padroni S, Arba Mosquera S, Ioannides A,Mukherjee A. Comparison of single-step reverse transepithelial all-surface laser ablation (ASLA) to alcohol-assisted photorefractive keratectomy. Clin Ophthalmol. 2012, 6: 973–980. 10.2147/OPTH.S32374

[9] Fadlallah A, Fahed D, Khalil K, Dunia I, Menassa J, El Rami H, Chlela E,Fahed S. Transepithelial photorefractive keratectomy: clinical results. J Cataract Refract Surg. 2011, 37(10): 1852–1857. 10.1016/j.jcrs.2011.04.029

[10] Celik U, Bozkurt E, Celik B, Demirok A,Yilmaz OF. Pain, wound healing and refractive comparison of mechanical and transepithelial debridement in photorefractive keratectomy for myopia: results of 1 year follow-up. Contact Lens Anterior Eye. 2014, 37(6): 420–426. 10.1016/j.clae.2014.07.001

[11] Abdulaal MR, Wehbe HA,Awwad ST. One-step transepithelial photorefractive keratectomy with mitomycin C as an early treatment for LASIK flap buttonhole formation. J Refract Surg. 2015, 31(1): 48–52. 10.3928/1081597X-20141104-01

[12] Kanitkar KD, Camp J, Humble H, Shen DJ,Wang MX. Pain after epithelial removal by ethanol-assisted mechanical versus transepithelial excimer laser debridement. J Refract Surg. 2000, 16(5): 519–522.

[13] Pallikaris IG,Panagopoulou SI. PresbyLASIK approach for the correction of presbyopia. Curr Opin Ophthalmol. 2015, 26(4): 265–272. 10.1097/Icu.0000000000000162

[14] Alio JL, Amparo F, Ortiz D,Moreno L. Corneal multifocality with excimer laser for presbyopia correction. Curr Opin Ophthalmol. 2009, 20(4): 264–271. 10.1097/ICU.0b013e32832a7ded

[15] Epstein RL,Gurgos MA. Presbyopia treatment by monocular peripheral PresbyLASIK. J Refract Surg. 2009, 25(6): 516–523. 10.3928/1081597X-20090512-05

[16] Soong HK,Malta JB. Femtosecond lasers in ophthalmology. Am J Ophthalmol. 2009, 147(2): 189–197 e182. 10.1016/j.ajo.2008.08.026

[17] Lubatschowski H, Maatz G, Heisterkamp A, Hetzel U, Drommer W, Welling H,Ertmer W. Application of ultrashort laser pulses for intrastromal refractive surgery. Graefes Arch Clin Exp Ophthalmol. 2000, 238(1): 33–39.

[18] Aristeidou A, Taniguchi EV, Tsatsos M, Muller R, McAlinden C, Pineda R, Paschalis EI. The evolution of corneal and refractive surgery with the femtosecond laser. Eye Vis (Lond). 2015, 2: 12. 10.1186/s40662-015-0022-6

[19] Stonecipher KG, Dishler JG, Ignacio TS,Binder PS. Transient light sensitivity after femtosecond laser flap creation: clinical findings and management. J Cataract Refract Surg. 2006, 32(1): 91–94. 10.1016/j.jcrs.2005.11.015

[20] Liang Hu, Wenjia Xie, Lei Tang, Jia Chen, Dong Zhang, Peng Yu, Jia Qu. CorneaI subbasal nerve density changes after laser in situ keratomileusis with mechanical microkeratome and femtosecond laser. Chin J Ophalmol, 2015, 51(1):39–44. 10.3760/cma.j.issn.0412-4081.2015.01.010

[21] Xie W, Zhang D, Chen J, Liu J, Yu Y,Hu L. Tear menisci after laser in situ keratomileusis with mechanical microkeratome and femtosecond laser. Invest Ophthalmol Vis Sci. 2014, 55(9): 5806–5812. 10.1167/iovs.13-13669

[22] Shah R,Shah S. Effect of scanning patterns on the results of femtosecond laser lenticule extraction refractive surgery. J Cataract Refract Surg. 2011, 37(9): 1636–1647. 10.1016/j.jcrs.2011.03.056

[23] Reinstein DZ, Archer TJ,Gobbe M. Small incision lenticule extraction (SMILE) history, fundamentals of a new refractive surgery technique and clinical outcomes. Eye Vis (Lond). 2014, 1: 3. 10.1186/s40662-014-0003-1

[24] Zhang Y, Chen YG,Xia YJ. Comparison of corneal flap morphology using AS-OCT in LASIK with the WaveLight FS200 femtosecond laser versus a mechanical microkeratome. J Refract Surg. 2013, 29(5): 320–324. 10.3928/1081597X-20130415-03

[25] Demirok A, Ozgurhan EB, Agca A, Kara N, Bozkurt E, Cankaya KI,Yilmaz OF. Corneal sensation after corneal refractive surgery with small incision lenticule extraction. Optom Vis Sci. 2013, 90(10): 1040–1047. 10.1097/OPX.0b013e31829d9926

[26] Denoyer A, Landman E, Trinh L, Faure JF, Auclin F,Baudouin C. Dry eye disease after refractive surgery: comparative outcomes of small incision lenticule extraction versus LASIK. Ophthalmology. 2015, 122(4): 669–676. 10.1016/j.ophtha.2014.10.004

[27] Dong Z,Zhou X. Irregular astigmatism after femtosecond laser refractive lenticule extraction. J Cataract Refract Surg. 2013, 39(6): 952–954. 10.1016/j.jcrs.2013.04.016

[28] Charman WN. Developments in the correction of presbyopia II: surgical approaches. Ophthalmic Physiol Opt. 2014, 34(4): 397–426. 10.1111/opo.12129

[29] Liu HH, Hu Y,Cui HP. Femtosecond laser in refractive and cataract surgeries. Int J Ophthalmol. 2015, 8(2): 419–426. 10.3980/j.issn.2222-3959.2015.02.36

[30] Mian SI,Shtein RM. Femtosecond laser-assisted corneal surgery. Curr Opin Ophthalmol. 2007, 18(4): 295–299. 10.1097/ICU.0b013e3281a4776c

[31] Jardine GJ, Holiman JD, Galloway JD, Stoeger CG, Chamberlain WD. Eye bank-prepared femtosecond laser-assisted automated descemet membrane endothelial grafts. Cornea. 2015, 34(7): 838–843. 10.1097/ICO.0000000000000453

[32] Ali MH, Javaid M, Jamal S,Butt NH. Femtosecond laser assisted cataract surgery, beginning of a new era in cataract surgery. Oman J Ophthalmol. 2015, 8(3): 141–146. 10.4103/0974-620X.169892

[33] Friedman NJ, Palanker DV, Schuele G, Andersen D, Marcellino G, Seibel BS, Batlle J, Feliz R, Talamo JH, Blumenkranz MS,Culbertson WW. Femtosecond laser capsulotomy. J Cataract Refract Surg. 2011, 37(7): 1189–1198. 10.1016/j.jcrs.2011.04.022

[34] Abouzeid H,Ferrini W. Femtosecond-laser assisted cataract surgery: a review. Acta Ophthalmol. 2014, 92(7): 597–603. 10.1111/aos.12416

[35] Nagy ZZ. New technology update: femtosecond laser in cataract surgery. Clin Ophthalmol. 2014, 8: 1157–1167. 10.2147/OPTH.S3

Chapter 17

Diode Laser-Based Sensors for Extreme Harsh Environment Data Acquisition

Chayan Mitra and Rachit Sharma

Additional information is available at the end of the chapter

http://dx.doi.org/10.5772/63971

Abstract

The world has witnessed several step changes in living standards, productivity, growth, and innovation. We are currently witnessing a convergence of intelligent devices, intelligent networks, and intelligent decision making. Obtaining long-term accurate, in situ, and real time data from the machines is necessary for enabling the industrial Internet. This relies heavily on sensor systems. Development of robust sensors that can operate reliably in extreme environments will make it possible to gather data from previously inaccessible locations in the equipment. This will enable machine operators to monitor and optimize the performance of their machines. Diode laser-based diagnostics technology has found applications in a variety of areas and a versatile range of operating conditions. It has proven to be a strong and reliable technique for remote measurements of concentrations and temperatures in harsh environments. Some of the major challenges for implementation of these sensors in real world are machine vibrations, window clogging, cooling, etc. In this chapter, the authors discuss about the application details and specific technologies suitable for the applications. Few case studies are considered, and the theoretical approach, algorithm development, and experimental validation are also discussed.

Keywords: lasers, sensor, harsh environment, tunable diode laser, industrial Internet, optical sensor

1. Introduction

Prior to late eighteenth and early nineteenth century, the human society was primarily agrarian and rural. Then, a step change of innovation occurred: the Industrial Revolution, which gave us a shift from hand tools to steam engine, the internal combustion engine,

telegraph, telephone, and electricity. Productivity and economic growth accelerated sharply [1]. A key upside of the feature characterizing this period was that it harnessed the efficiencies of hierarchical structures, with centralization of controls. It led to reduction in cost as the machines and fleets got larger and production volumes increased. A major downside was that it was more resource intensive. Much of the incremental innovation at later stages was focused on improving efficiency, reducing waste, and enhancing the working environment. The second wave of Industrial Revolution started with the advent of the electronics, computers, and Internet. Here, the key feature was the design of standards and protocols to permit incompatible machines in diverse locations to connect and exchange information. The explosive growth was a result of the combination of speed and volume. Deeper integration, flexible operation, and distributed intelligence led to the creation of new platforms for commerce and social exchange by driving down the cost. Ability for rapid exchange of information and decentralized decision-making process led to open innovation and knowledge-intensive growth. Today, we are witnessing another transformation by melding of the global industrial system with open computing and communication system. The industrial Internet is enabled by the coming together of intelligent devices, intelligent systems, and intelligent decision-making systems [1]. The architecture consists of three technology elements: brilliant machines, advanced analytics, and people at work. A brilliant machine is self-aware of its performance, health condition, and capability. This enables the machine to operate close to its performance boundary. The machine communicates with other machines and operators or service personnel through the Internet.

The first step in this revolution is the generation of data from the machines assuring the real-time health condition information of the machine. Widespread instrumentation of the machines is a necessary factor in this case. A suite of sensors on each machine will enable performance monitoring on a real-time basis and help the operators make the most of their assets [2]. The challenge comes from the increasing technical complexity of the assets in service. Performance data from a sensor located in an unmonitored location in a machine along with powerful software analytics and visualization tools will enable the operator to diagnose the problem with greater confidence. **Table 1** provides a breakup of the value opportunity of industrial Internet for various industry segments [3].

Industry segment	Global base	Capacity	Labor-hours/Year	Value
Power	56,620 (Gas + Steam Turbines)	4156 GW	52M	$ 7B
Aviation	21,500 Commercial Jet Aircraft	43,000 Jet engines	205M	$ 10B
Rail	120,000 Freight	7M People + 9.6T Freight tonne-km	52M	$ 3B
Healthcare	105,000 (CT + MRI Machines)		4M	$ 250M

Table 1. Value opportunity of industrial Internet for various industry segments [3].

Similarly, in the oil and gas sector, reduction in asset downtime (asset performance management) and operations optimization through predictive analytics and condition-based maintenance can result in substantial cost savings for the oil well owners. For example, the cost for

http://dx.doi.org/10.5772/63971

surfacing a blowout preventer (BOP) from the seabed is around $10–$16 million and unplanned downtime costs a mid-size LNG facility $150 million per year [4]. Most of the downtime in deep sea drilling rig is caused by BOP-related problems, and it costs an oil company more than $ 1 million per day in lost productivity [5].

Therefore, nowadays when major industrial products, such as gas and steam turbines, aircraft engines, turbomachinery equipment, power transformers, and locomotives, are involved, the primary challenge is to keep the systems operating at peak performance to avoid unwarranted shutdowns. Continuous operation at peak performance not only demands high-fidelity system architecture and design, but also requires optimized operation and maintenance practices. This in-turn necessitates the usage of online sensor systems that can perform desired measurements for continuous monitoring of operational performance and overall system health. The idea is that measurements using multiple sensors in combination with environmental, operational, and performance-related parameters can provide a more accurate system health status. The sensor data can also be used along with statistical pattern recognition and machine-learning techniques to detect changes in machine parameter data, isolate faults, and estimate the remaining useful life (RUL) of the machines [6–9]. This approach assumes a product's loading and operating conditions, geometry, material properties, and failure mechanisms as the parameters to estimate RUL. The sensor systems are used to monitor these parameters for anomalies, faults, and failure predictions [10].

In an example provided in GE Report [11], the operators of Whitegate Power Station near Cork in Ireland placed more than 140 sensors throughout the plant. This allowed the operators to run the plant reliably and efficiently through round-the-clock monitoring and diagnostics of the plant. The sensors digitized the critical plant operating parameters (vibration, temperature, pressure, fuel mix, ambient temperature, and load) and helped to create a virtual dynamic model of the asset in the cloud, which is a mirror of the real asset. The model in conjunction with the sensor data gives us the ability to predict the plant's performance, understand tradeoffs (adjust hedging strategies to manage fuel cost volatility), and enhance efficiency. The modeling approach discussed above requires directly sensed parameters, design parameters, and operating condition uncertainties, as well as inspection and historical reliability data. Several techniques, such as stochastic models (which take into account randomness of the operating profiles, extreme operating events), physics-based models, neural networks, or real-time probabilistic models, are used for this purpose. To a large extent, the integrity of the measured parameters determines the fidelity of the models used [9].

It is obvious from the above discussion that robust and reliable online sensors that can accurately measure the desired system parameters are crucial toward optimizing asset performance and maximizing its lifetime. Most of the above-mentioned industrial assets, such as gas turbines or aircraft engines, involve extreme harsh environments such as high temperatures, high pressures, vibrations, shocks, dust and soot load, reacting flow, and thermal transients. Several industrial challenges and applications can be addressed through sensing of parameters under these harsh conditions. Conventional sensors do not work reliably here (or even fail to perform) because these harsh conditions often lie outside the operational envelope of traditional techniques. Therefore, development of new and advanced harsh

environment sensors is becoming increasingly important because such sensors can enable the industrial community to get enhanced value out of their assets. When classified broadly, harsh environment sensors serve the following key application areas: process optimization (or controls), prognostics/health management, better machine design, and monitoring/diagnostics. For all these applications, it is beneficial to have on-line/real-time, accurate, selective, and direct measurement of the harsh environment parameters. In addition, high measurement repeatability and ease of installation and maintenance are extremely desirable. As described in this chapter, optical harsh environment sensors can provide these major advantages over conventional techniques for a host of industrial applications.

Technology	Laser type	Detectors	Measured sample	Information
Laser-induced fluorescence	CW/pulsed, low power	Camera	Fluorescent molecules	Species concentration
Laser-induced incandescence	Pulsed, high power	Camera	Soot particles	Soot distribution
Laser Doppler anemometry	CW, low power	Photodiodes	Particles and droplets	Local flow velocity
Particle imaging velocimetry	Pulsed/modulated, high power	Camera	Seeding particles, fuel droplets	Flow field
Phase Doppler anemometry	CW, low power	Photodiodes	Droplets/Particles	Droplet/particle size
Laser-induced breakdown spectroscopy	Pulsed, high power	Spectrometer	Molecules	Elemental composition
Raman scattering	CW/pulsed, high power	Photodiodes/ spectrometer	Molecules	Concentration, temperature
Laser absorption spectroscopy	CW/pulsed, low power	Photodiode	Molecules	Concentration, temperature

Table 2. Overview of common optical techniques for industrial-sensing applications [12].

Laser-based optical sensors provide a unique method for measurement of fluid properties in industrial environments. Typical applications include flow or velocity measurement through techniques such as particle imaging velocimetry (PIV) or laser Doppler anemometry (LDA) and particle size measurement using phase Doppler anemometry (PDA). Laser-induced breakdown spectroscopy (LIBS) is commonly used where elemental composition measurement is required. Furthermore, for applications requiring concentration measurements, laser-induced fluorescence (LIF), Raman scattering, or laser absorption spectroscopy (LAS) is used depending on the type of sample. For fluorescing samples, LIF is preferred. On the other hand, Raman scattering is beneficial for measurements on di-atomics (H_2, N_2) or for analyzing gases at high pressures. Finally, LAS is used for applications where high sensitivity and selectivity

http://dx.doi.org/10.5772/63971

are crucial. A brief snapshot of the various laser-based industrial-sensing techniques is provided in **Table 2**, and the reader is encouraged to refer the literature [12] for more details on these techniques. To remain within scope, this chapter will remain focused on absorption-based techniques, especially diode laser sensing, which is most promising for harsh environment applications.

Common industrial applications of conventional absorption-based optical sensors include gas monitoring, sensing, and analysis through techniques, such as Fourier transform infrared (FTIR), ultraviolet spectroscopy (UV), nondispersive infrared (NDIR), and photo-acoustic spectroscopy (PAS) [13, 14]. For harsh environment applications, such as power generation and energy systems, these techniques typically require gas extraction to condition the sampled gas. This often leads to unwanted lag in the measurement and requires frequent maintenance of the sampling system [15]. For applications requiring fast response time, high resolution, and good selectivity, such as industrial controls and process optimization, LAS has immense potential that is why it is an active area of research across the industrial and academic community. Tunable diode laser absorption spectroscopy (TDLAS) [16] and quantum cascade laser absorption spectroscopy (QCLAS) [17] are the two most common modalities in which LAS-based optical solutions can be implemented in harsh environments. This is mainly because these techniques, as discussed later in the chapter, can be implemented using economical, robust, and compact diode lasers/quantum cascade lasers that are specifically designed for the required application. In addition, diode lasers/quantum cascade lasers can be mass produced, require minimal maintenance, and have long operation lifetimes (>20,000 h) [18]. In the past decade, the industrial community has been increasingly adopting novel technology solutions based on these lasers. This is acting as the driving force behind the rapid advancement of the diode laser manufacturing industry toward lower cost, higher performance, and increased reliability. As this trend continues, these lasers will become even better and cheaper in the future, which will open new avenues toward novel and affordable optical solutions to today's unsolved challenges. Therefore, diode laser-based sensing techniques, such as TDLAS and QCLAS, are of utmost importance to the industrial community.

TDLAS/QCLAS-based sensors have immense potential and advantages for in situ measurements of concentration of constituents, temperature, and other wide varieties of gas parameters in challenging real-world environments [19–21]. In most of these applications, light emitted from a tunable diode laser system is passed through a gaseous medium to a detector. The transmitted radiation is then used to measure the gas temperature, species concentration, or pressure using spectral absorption models for the target absorbing species [22]. When implemented in line-of-sight [23, 24] or standoff configuration [25], these techniques can offer true in situ measurement capability in harsh environments with high temperatures or pressures. This is because the sensor can make reliable measurements through one or more transmitting windows while being completely decoupled from the harsh environment.

This chapter discusses the technology background of TDLAS from an applied experimental perspective. The two most common methodologies, that is, direct absorption spectroscopy (DAS) and wavelength modulation spectroscopy (WMS), will be covered. Subsequently, the key design philosophy, optomechanical architecture, and instrumentation of a TDLAS sensor

will be presented. Finally, two harsh environment application examples will be provided to demonstrate the power of diode laser sensing toward solving complex real-world challenges. Please note that the implementation of QCLAS is essentially very similar to TDLAS, the only significant difference being that QCLAS uses mid-infrared quantum cascade lasers while TDLAS uses near-infrared tunable diode lasers. For the sake of simplicity, the term TDLAS is used in most places in this chapter but the concepts presented translate directly to QCLAS as well.

2. Technology background: tunable diode laser absorption spectroscopy

The fundamentals of molecular spectroscopy, including concepts such as vibration modes, absorption coefficient, line-shape, spectral width, and spectral broadening have been extensively studied and discussed in several books and articles [26, 27]. This section is presented from an applied experimental perspective and will use the aforementioned concepts assuming that the reader is equipped with basic understanding of molecular spectroscopy.

The absorption of optical radiation by gaseous medium is governed by the Beer–Lambert law. The law describes the optical transmission losses associated with a uniformly absorbing medium. When a narrow spectral radiation of frequency υ passes through a gaseous medium of length L [cm], the incident intensity $I_{0,}$ and the transmitted intensity I_1 are related as,

$$I_1 = I_0 e^{(-k_\upsilon L)} \tag{1}$$

where k_υ [cm^{-1}] is the spectral absorption coefficient. It should be noted that for a mixture in pure gaseous phase (devoid of particulates, water droplets or condensed phases), the Beer–Lambert law assumes the optical scattering of the medium to be negligible. The spectral absorption coefficient k_υ is defined as below for an isolated (interference-free) vibrational transition,

$$k_\upsilon = PcS_i(T)\varphi_\upsilon \tag{2}$$

where P [atm] is the total gas pressure, c is the mole fraction of the species of interest, S_i (T) [cm^{-2} atm^{-1}] is the temperature dependent line strength of the transition at temperature T [K], and φ_υ is the normalized line-shape function, such that

$$\int_{\infty}^{-\infty} \varphi_\upsilon d\upsilon = 1 \tag{3}$$

Using the above equations, the concentration c of the species of interest can be calculated.

http://dx.doi.org/10.5772/63971

The quantity $k_\upsilon L$, called absorbance, is of critical importance in deciding the capability and performance of a tunable diode laser-based gas sensor. For typical laser-based gas-sensing applications, trace concentrations need to be detected, and therefore, the absorbance to be detected is <<1. In such cases, the Eq. (1) reduces to

$$\frac{I_0 - I_1}{I_0} = \frac{\Delta I}{I_0} \sim k_\upsilon L \tag{4}$$

The quantity $\Delta I/I_0$ is a known as the fractional absorbance. The minimum fractional absorbance detectable by a TDLAS system is known as the minimum detectable absorbance (MDA). For a given TDLAS system, MDA is characteristically a function of the different system-level noises (such as laser excess noise, detector thermal noise, optical interference noise, or etalon noise) and does not depend on the species to be measured with that system. For a given path length, the MDA of the system can be used to calculate the minimum detectable concentration (or detection limit) for a measurable species using Eqs. (2) and (4). For most practical TDLAS applications, the MDA is around 10^{-5} to 10^{-6} and is often limited by the optical interference noise or etalon noise of the system [13, 28]. The two most common methodologies in which TDLAS is implemented are direct absorption spectroscopy (DAS) and wavelength modulation spectroscopy (WMS), which are discussed in the following subsections.

2.1. Direct laser absorption spectroscopy (DLAS/DAS)

A key requirement for both DAS and WMS is that the laser source must have a spectral width much narrower (at least 1–2 orders of magnitude) than the gas absorption feature to be measured. Distributed feedback diode lasers (DFB) in the near-infrared (NIR) and quantum cascade lasers (QCL) in the mid-infrared (MIR) can meet this requirement and serve as excellent sources for a majority of applications [18]. These lasers are generally available in both pulsed and continuous wave (cw) modes. The emitted wavelength of a diode laser is a function of the diode temperature and the injection current. Typically, a thermoelectric controller (TEC) is used to set (and control) the diode-operating temperature to a value where there desired wavelength can be reached at the desired injection current. For implementation of DAS [29], the injection current of the diode laser is scanned periodically in a sinusoidal, ramp, or sawtooth fashion. This leads to a related wavelength scanning of the laser. The scan current range has to be selected such that the resulting wavelength scan covers the absorption transition of interest. Typical scan frequencies are in the range of 5–200 Hz. It is highly advisable to use a wavelength-appropriate etalon to characterize the current–wavelength transfer function of the laser at the scan frequency [30].

The scanned laser is made to pass through an absorption cell where it interacts with the species of interest. The transmitted signal is measured using a photodiode (usually DC coupled). Most common detector types are indium gallium arsenide (InGaAs) for near-infrared and mercury cadmium telluride (MCT) for mid-infrared regions, respectively. The basic components and schematic of a direct absorption spectroscopy system are shown in **Figure 1**. In the absence of

absorption, the detector signal will essentially represent the power vs current behavior of the laser. This behavior is typically linear when in small current ranges but could also be of higher order depending on the laser nonlinearity. In the presence of absorption, a typical DAS spectrum looks similar to the embedded graph in **Figure 1**, where a dip in transmission is observed as the laser wavelength scans through the absorption feature. The magnitudes of the photodiode signal at the absorption line center, with absorption and without absorption, are proportional to I_1 and I_0 in the Beer–Lambert law, respectively, and can be used to estimate the species concentration. A common way to calibrate a DAS system involves analyzing and plotting the photodiode signal as a function of the laser wavelength using the aforementioned current–wavelength transfer function. Subsequently, the integrated area under the absorption curve (which is directly proportional to the species number density) is used to correlate the DAS signal to species concentration [13].

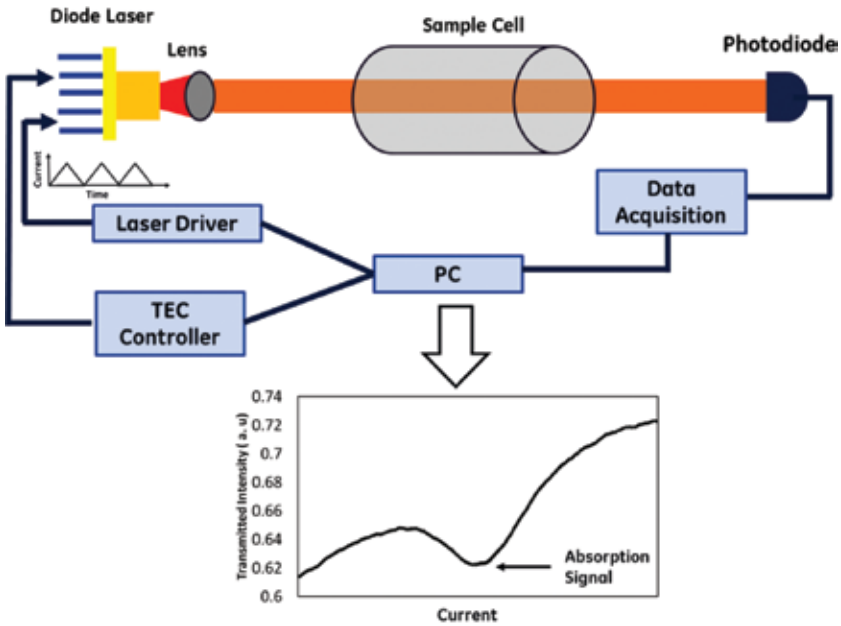

Figure 1. Schematic of a typical direct absorption spectroscopy system.

2.2. Wavelength modulation spectroscopy (WMS)

For TDLAS applications requiring high sensitivity, wavelength modulation spectroscopy (WMS) is a very effective technique [29, 31–33]. A typical WMS setup is shown in **Figure 2**. In addition to the laser scan (as in DAS), a fast current modulation (at a frequency f and amplitude a) is added to the injection current of the laser. The frequency f of the modulation signal is typically in the range 1–20 kHz. As in the case of direct absorption, the wavelength tuning properties of the laser, for both the scan and modulation frequencies, have to be well characterized with an appropriate etalon [30]. The transmitted signal measured by the photodiode

http://dx.doi.org/10.5772/63971

is fed into a lock-in amplifier. As shown in **Figure 2**, it is critical that the reference signal of the lock-in amplifier is the same as the laser's modulation signal. It should be noted that this is a general requirement and applies differently depending on the type of lock-in amplifier. For example, in case the reference is internally generated in the lock-in, the reference signal from the lock-in can be scaled appropriately to modulate the laser. Or, if a software lock-in is used, then the PC generated reference can be used for this purpose. The lock-in analysis frequency is set to twice the modulation frequency of the laser (2f) and the spectrum is analyzed in a narrowband around the 2f frequency. This is known as second harmonic spectroscopy, and a typical second harmonic (2f) signal is shown in the inset of the **Figure 2**. As the modulated laser (at f) is scanned across a typical absorption line profile (Lorentzian, Gaussian, or Voigt), the transmitted on-absorption signal (at absorption line center) changes at a frequency of 2f, and the transmitted off-absorption signal changes at a frequency of 1f. Therefore, setting the lock-in band around 2f ensures that the system becomes more sensitive and selectively extracts the on-absorption signal. Also, choosing a higher f ensures a lower 1/f noise. Hence, the WMS technique is generally more suitable for high sensitivity applications compared to DAS. The typical absorbance limits achievable through WMS in the field are around 10^{-4} for standard WMS and 10^{-5}–10^{-6} for balanced detection-based WMS (compared to 10^{-2}–10^{-3} in typical DAS) [28].

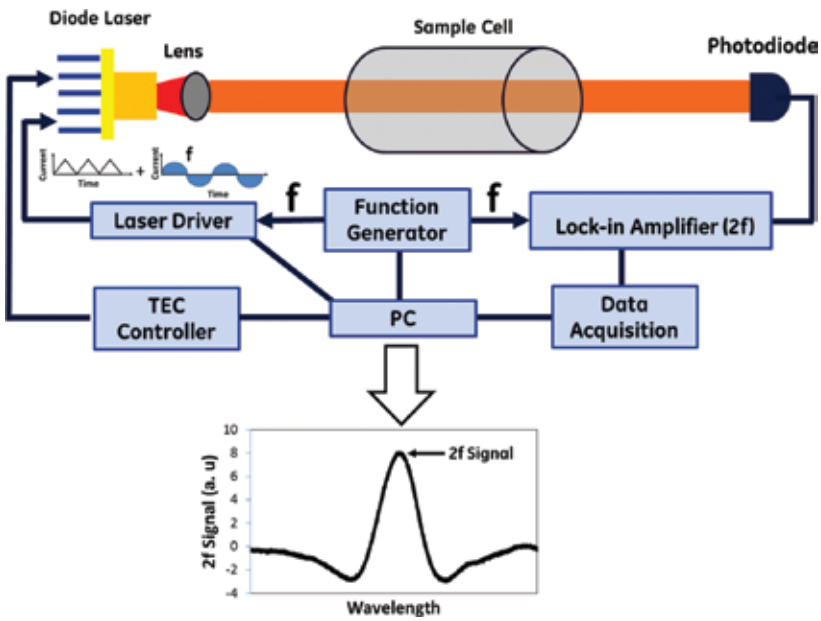

Figure 2. Schematic of a typical wavelength modulation spectroscopy system.

For WMS applications where the transmitted laser intensity fluctuates due to factors other than species concentration, an additional lock-in system is used to extract the 1f signal. The 2f and 1f signals are directly proportional to the transmitted laser intensity. Therefore, the 1f normal-

ized 2f signal, also known as 2f/1f, is a good way to desensitize the WMS system to transmission intensity fluctuations caused by external influences [14]. This is a major advantage of WMS that makes it robust and field deployable in environments with high vibrations, dust load, fogged windows, and beam steering.

Another key advantage of WMS is that it is more sensitive to spectrally sharp absorption features. This is because the on-absorption 2f signal is stronger for larger absorption gradients around the absorption line center. The concept of modulation index (m), which is the ratio of the modulation amplitude (a) to the half-width half-maximum of the spectral line ($\Delta\upsilon$), is important to understand this. For a given absorption line, the optimized 2f and 1f signals are obtained at m = 2.2 [34]. For a single absorption line of interest, the appropriate m is chosen to meet this criterion. This makes the WMS system selectively more sensitive to spectral features of that particular width and the 2f contribution from broad spectral features and from molecules like water or heavy hydrocarbons that are significantly diminished. Hence, WMS is a powerful tool to overcome spectral interferences and to measure trace concentrations in complex gas mixtures.

The WMS signals are a strong function of the temperature and pressure of the sample gas, and therefore the calibration of such systems is a critical step toward ensuring accuracy and reliability. For sampling-based TDLAS measurements, sample is often filled in an absorption cell. These cells can be single pass, dual pass, or long path multipass cells [13]. The temperature and pressure of the absorption cell are controlled at fixed values, and calibration is performed at these conditions. For applications where temperature and pressure may vary, calibration is done for multiple operating conditions. Dynamic measurements of temperature and pressure combined with spectral models are then used to estimate the gas concentration as the conditions vary. For in situ applications with wide temperature and pressure fluctuations, the calibration-free WMS technique [35], pioneered by the Hanson group at Stanford University, has become widely acceptable. This technique involves thorough characterization of the instrumentation (lasers, detectors, amplifiers, etc.) and combining these details with the quantitative spectroscopy model. This semi-empirical model, where most of the real-world noise sources are accounted or corrected for, is then used to calculate the expected 2f/1f signal for an operating condition (known or measured temperature and pressure). The calculated signal is compared with the experimentally measured 2f/1f signal. The optimized concentration value in the model, which gives the best match between the two signals, is stated as the in situ concentration of the species.

3. Designing the TDLAS sensor

The design of a TDLAS system, especially for harsh environments, involves several critical steps. Details of the required detection limit, sample gas conditions, sample accessibility, installation methodology, and data reporting frequency are crucial toward designing a reliable, accurate, and robust sensor. The following subsections discuss these in more detail.

http://dx.doi.org/10.5772/63971

3.1. Wavelength selection

Selection of a suitable absorption line for a particular application is the first and the most important step in the sensor design process. The choice of the line is strongly dependent on the species of interest, the sample temperature and pressure, available path length, and background gas composition (background gas constitutes all the other species in the gas mixture apart from the species of interest). The HITRAN molecular spectroscopic database [36] is a fairly comprehensive database and is commonly used for simulations to assist in the spectral line selection process.

To begin, the selected spectral line should have sufficient absorbance to reach the required Lower detection limit (LDL) for the application path length, without considering interference. Absorbance values of 10^{-4}–10^{-5} are typically achievable in industrial TDLAS systems. Coarse spectral simulations, at the appropriate sample temperature and pressure, can be used to identify the potential candidate lines in the NIR and MIR regions that can meet the detection limit requirements. It should be noted that for very low detection limits (<1 ppm), the MIR region is more promising as it covers the intense fundamental absorption bands of most molecules. Subsequently, for each of the candidate lines, a rigorous background gas interference analysis needs to be done to investigate cross-sensitivity issues and potential LDL degradation. It is critical to perform the interference analysis for the full range of background gas composition variations. A specific case is discussed below to throw more light on the spectral line selection process.

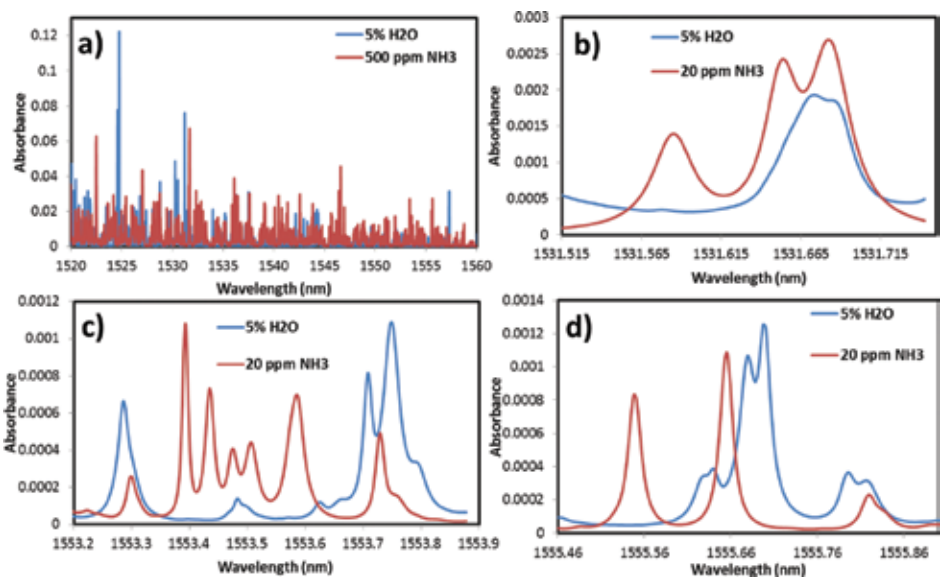

Figure 3. Spectroscopic absorbance simulations at 1.5 μm for pressure = 1 Bar, temperature = 500 K and path length = 10 m. (a) H_2O = 5%, NH_3 = 500 ppm. (b) H_2O = 5%, NH_3 = 20 ppm. (c) H_2O = 5%, NH_3 = 20 ppm. (d) H_2O = 5%, NH_3 = 20 ppm. Figures taken with permission from SPIE (From our published paper).

Assume a typical power plant emissions control application which requires measurement of ammonia (NH_3) with a sensitivity of <1 ppm at a path length of 10 m and sample gas temperature of 500 K. The average moisture level in the exhaust stream can be up to 5%. **Figure 3** shows the HITRAN spectral simulations for absorption line selection for this particular application. The spectral region around 1500 nm is good for ammonia detection because it covers strong absorption bands of ammonia. Also, this region allows for remote sensing as wavelengths around 1500 nm can be transmitted over fiber optics with low loss. **Figure 3a** shows a coarse simulation of ammonia lines (at the application conditions), with the appropriate moisture concentration. It is clear that many moisture lines are present which can potentially worsen the ammonia measurement fidelity. High-resolution simulations in shorter wavelength spans are conducted to identify three spectral lines at 1531.59, 1553.4, and 1555.56 nm where the spectral contribution of moisture is minimal. These are shown in **Figure 3b–d**, respectively. It should be noted that in all these regions, the moisture absorbance is nonzero but the spectra are relatively broader than the ammonia line. This is an acceptable solution when regions of zero background gas absorbance cannot be found. This is because, as explained in Section 2.2, WMS has the capability to be more sensitive toward sharp spectral features and can reject contributions from broad background gas features, like in this case. Once the absorption line is selected, the process of instrument development can be started as explained in the next subsection.

3.2. Optomechanical assembly and instrumentation

A well designed optomechanical assembly is crucial toward obtaining the optimum performance out of a TDLAS system and involves the following key considerations. All optical surfaces through which the laser passes, such as the laser window, the absorption cell window, and detector window, should have the appropriate antireflection (AR) coating for the laser wavelength. This ensures minimization of backscattering of photons into the laser which can severely increase the laser's excess noise. In case of fiber-coupled lasers, incorporation of an optical isolator in laser package (or right after the laser) is often a good idea to keep the excess noise in check. Furthermore, effort should be made to keep all windows wedged and tilted. This decreases the interference noise created by multiple reflections from parallel surfaces. In addition, in case of dual-pass or multipass systems, care should be taken to avoid the overlap of the different passes. This can also lead to significant interference noise in the system. Finally, all optical surfaces should be kept clean to the extent allowed by the application. It should be noted that some level of interference noise (also known as etalon noise [28]) will always be present in any practical TDLAS system as it cannot be completely avoided. However, if proper care is taken, as mentioned above, the absorbance noise level can typically be brought down to 10^{-4}–10^{-5}, which is sufficient for most industrial applications.

On the instrumentation, front, low noise laser current drivers are recommended. However, one must remember that the system noise level is often limited by the etalon noise. So, it is often sufficient if the stability of the current driver is enough to keep itself from becoming the dominant noise source. Typically, it is acceptable to have the noise induced by current drivers at about two orders of magnitude lower than etalon noise. Similar requirements apply to the

http://dx.doi.org/10.5772/63971

detector as well where the thermal noise should be at least 10^{-7}–10^{-8} in equivalent absorbance or less.

The harsh environment implementation of the system depends on the application. Free space systems [23, 24] employ a transmitter (or pitch) to launch the laser into the harsh environment and a receiver (or catch) to collect the transmitted radiation. The design of the transmitter assembly can include refractive or reflective optics to ensure that the laser is launched with the required diameter and divergence. Similarly, the design of the receiver includes optics to collect the transmitted laser and direct it to the detector. Multiple lasers can be incorporated into the transmitter through optical multiplexing. On the receiver side, these lasers can be demultiplexed using dichroic mirrors or beam splitters or other similar optical elements. Other advanced techniques, such as time division multiplexing (TDM) and frequency division multiplexing (FDM), are also employed when demanded by the application [37]. In some free space configurations, the transmitter and receiver are packaged into a single assembly, and the laser is reflected back using a retroreflector located across the sample on the other side. This typically enables a dual pass system. While free space TDLAS systems are generally used to measure the line-of-sight average species concentration or temperature, some applications toward temperature profiling have also been reported [38, 39].

Applications where a line of sight or retroreflector is not possible, TDLAS in standoff mode [25] is often employed. This approach is similar to the retroreflector configuration described above except that the return signal is due to the backscattering from the sample gas. One expected challenge in the standoff mode is to get enough backscattered signal to do a meaningful analysis. Narrowband filters are often used in front of the detector to selectively separate the detection laser from the ambient radiation. Also, large area optics (typical diameter 2–4 inches) is often employed for optimum collection of the backscattered signal. Similar to free space systems, standoff systems also measure path average concentration or temperature value.

Sampling-based systems, which use multipass absorption cells, are also used for harsh environment applications. Herriott-type [40], White-type [41], and Chernin-type [42] cells are the most well-known ones. When absorption cells are used to analyze harsh environment gases, it is a key requirement to maintain the properties of the gas mixture (to the extent possible) during sampling and analysis. This is because the change in gas properties, such as cooling, can change the concentration of the species of interest. For example, if an exhaust gas sample is allowed to cool, then the water vapor would condense out taking with it a significant amount of exhaust gases. High-temperature multipass cells [43], in combination with a heated sampling line, serve as a good solution in such cases.

Since most TDLAS applications require fast response, a real-time data acquisition system can be highly beneficial. In WMS, the detector data are collected at a high sampling frequency, at least 20–50 times the modulation frequency (f) of the system. In case of DAS, as expected, this requirement is relaxed based on the scan frequency. In WMS, the acquired data can be processed using a hardware or software lock-in amplifier to generate the 2f and 1f signals. The choice of hardware vs software lock-in amplifier depends on the application. For applications with 1 or 2 lasers, a compact hardware lock-in amplifier can be optimal. However, for

applications involving multiple lasers, the use of hardware lock-in amplifiers can be cumbersome and bulky. In such cases, an onboard PC/processor with software lock-in feature can be a much better solution. It should be noted that software lock-in features are commonly implemented in development environments such as National Instruments Labview and MATLAB. This concludes the basic overview of TDLAS sensor design and the following section will discuss some examples of how this technology is enabling real-world solutions to challenging industrial problems.

4. Harsh environment applications and examples

The applications of TDLAS and QCLAS techniques in harsh environment conditions are well known and widely discussed in the literature. The most common applications include measurement of trace gas concentrations [44–46], temperature [19, 47], combustion control [48], and plasma diagnostics [49]. It is beyond the scope of this chapter to discuss all these applications in detail. In the following subsections, two specific examples will be discussed which demonstrate the power of this technology in tackling real-world challenges where conventional techniques fail to perform well.

4.1. Steam quality sensor for steam turbine applications

This subsection is a summarized excerpt of the work published in reference [22]. Steam quality or steam wetness fraction is a critical operational parameter in steam turbines and is used in estimation of turbine efficiency and remaining life. It is a quantitative measure of the amount of water vapor and liquid water (usually microdroplets) present in the process steam. Steam quality or wetness fraction (X) is defined as follows

$$X = \frac{m_{vapor}}{m_{vapor} + m_{liquid}} \tag{5}$$

where m_{vapor} and m_{liquid} are the mass of vapor phase and mass of liquid phase, respectively.

The steam quality in a steam turbine needs to be closely monitored as an indicator of wear and tear of the machinery. The architecture of a steam turbine mainly includes three sections: HP (high pressure), IP (intermediate pressure), and LP (low pressure) respectively. The steam in HP and IP sections has little liquid water content, and therefore, the efficiency of these sections can be measured using standard temperature and pressure measurements. The LP section, however, can have steam with significant liquid water content (also known as wet steam), which can cause significant erosional damage to the rotating components [50, 51]. Therefore, the accurate measurement of steam wetness in the LP section becomes extremely critical. Most conventional methods are either based on steam sampling or based on calculations involving machine parameters (such as power output), both of which have low accuracy [22].

http://dx.doi.org/10.5772/63971

Therefore, a diode laser-based sensor capable of direct in situ measurement of steam quality in the hot and harsh LP section would be an ideal solution to this challenge.

As shown in Eq. (5), estimation of steam quality requires a quantitative measurement of water in liquid and vapor phases. **Figure 4** shows the schematic of a steam quality measurement system designed using two fixed wavelength broadband diode lasers. A laser at 945 nm (power 20 mW, spectral width ~2 nm) is used to probe the absorption of water vapor. Similarly, a laser at 1560 nm (20 mW, spectral width ~10 nm) is used for liquid water. Both lasers are passed through a steam chamber, which is capable of generating known vapor/liquid ratios. The path length of the steam chamber is predetermined. The intensities of both lasers before and after passage through the steam chamber are measured with Indium Gallium Arsenide (InGaAs) detectors. A comparison of the intensity loss is used to generate a quantitative measurement of the vapor and liquid concentrations respectively and hence, to estimate the steam quality, according to Eqs. (1) and (4).

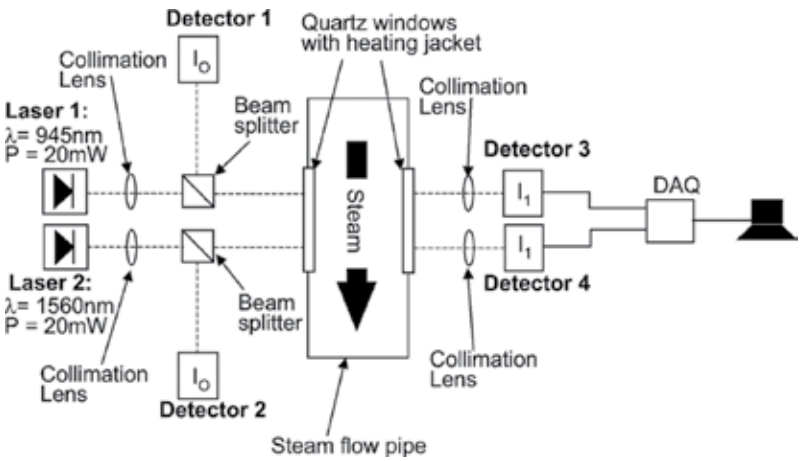

Figure 4. Schematic of the experimental setup for steam quality measurement. Figure taken with permission from IEEE (From our published paper).

Figure 5a and **b** shows a comparison of the laser-based steam quality measurement with the mass flow rate-based method under different water spray conditions. A reasonably good match is found between the two techniques and further improvements are possible through improvement of analysis algorithms for different temperature, pressure, and flow conditions. However, these results certainly demonstrate the power of laser-based techniques and the three main advantages offered in this particular application. First, this is a direct measurement of steam quality without any extraction or conditioning of the sample. The only inputs required in the method are temperature, pressure, and other standard operating parameters of the steam turbine. Second, the steam quality can be measured over a wide range (100–10%). This is a unique capability over conventional steam calorimeters which have a much smaller range of a (100–80%). Last but not the least, the measurement is real-time and can be used for better process optimization and steam turbine prognostics.

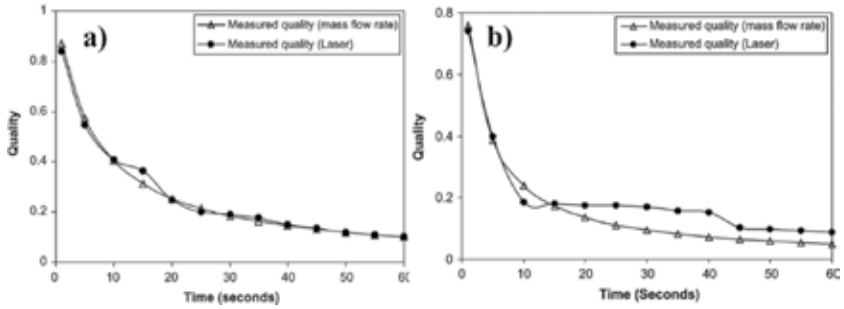

Figure 5. (a) Variation of steam quality with water spray in the in the steam flow pipe and comparison with calculation using mass flow rate. (b) Variation of steam quality with water spray in the steam flow pipe and comparison with calculation using mass flow rate at a different temperature, pressure, and flow rate condition. Figures taken with permission from IEEE (From our published paper).

4.2. Ammonia slip sensor for gas turbine applications

This subsection is a summarized excerpt of the work published in reference [14]. Gaseous emissions, such as NO_x, SO_x, and CO are strictly regulated by the environmental protection agency (EPA) in the United States and similar agencies around the world. To minimize NO_x emissions, a selective catalytic reduction (SCR) unit is commonly introduced in the exhaust gas path [52]. The gas temperatures in the harsh SCR exhaust environment are typically of the order of 250–380°C. The functioning of an SCR unit includes injection of ammonia (NH_3) gas to cause chemical reactions leading to reduction of NO_x into N_2 and H_2O. This process is depicted in **Figure 6**.

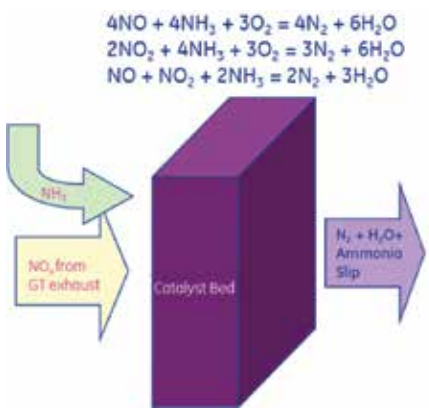

Figure 6. Schematic showing the function of a selective catalytic reduction unit in a power plant. (Figure taken with permission from Sharma et al. [14]).

The equations embedded in **Figure 6** suggest that the optimal performance of an SCR would require ammonia injection amount to vary with the NOx generated. Too much ammonia injection leads to incomplete reaction and too little leads to residual ammonia (ammonia slip)

http://dx.doi.org/10.5772/63971

in the exhaust. The amount of ammonia injected is typically controlled by monitoring and minimizing the ammonia slip. The conventional sampling-based continuous emissions monitoring system (CEMS) [15] is the state-of-the art for this application and is often believed to be suboptimal due to sampling-related measurement lags of up to 2–3 min. The most efficient and desired way of controlling the SCR is to directly measure the ammonia slip in the harsh SCR environment (without sampling). An example of how a TDLAS-based sensor can address this highly challenging real-world problem follows here.

The TDLAS sensor discussed here is designed for direct operation in an SCR exhaust so that measurement lag time is minimized. The sensor is based on a free space line-of-sight methodology employing a laser transmitter (pitch) to emit the laser radiation and a receiver (catch) to collect the radiation after passage through the SCR exhaust. A diode laser around 1.5 μm is chosen to sense ammonia. Details on spectral analysis and line selection have been presented in the Section 3.1. In a combined cycle power plant, the SCR exhaust is usually into a heat recovery steam generator (HRSG). The environment inside a HRSG is fairly harsh due to high temperatures, engine vibrations, and floating dust or impurities. The challenges around beam steering caused by temperature gradients and transmission losses due to dust particles are addressed using the 2f/1f WMS methodology described in the Section 2.2. A major challenge specific to this application is the thermally induced misalignment of the beam since the typical line-of-sight path length in a HRSG can be up to 10 m. Therefore, maintaining alignment through all engine-operating conditions is critical toward achieving long-term reliability.

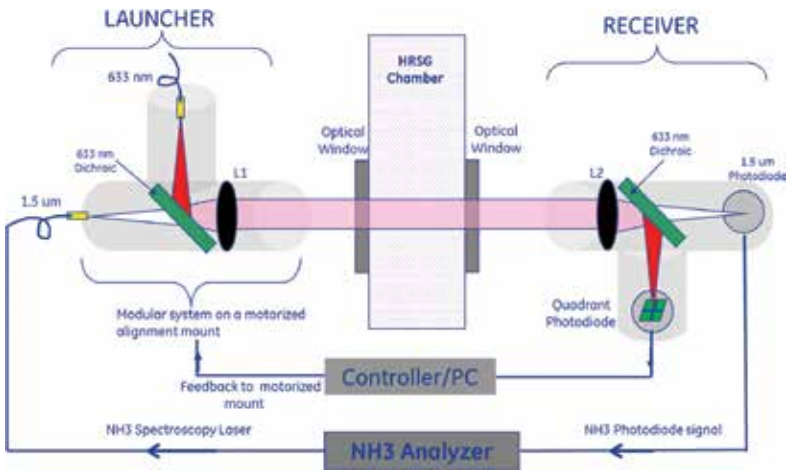

Figure 7. Schematic showing the hybrid ammonia slip sensor with alignment control and implementation in a HRSG. Figure taken with permission from SPIE (From our published paper).

The hybrid sensor, shown in **Figure 7**, is developed to address the misalignment challenge. A 633 nm fixed wavelength laser is multiplexed with the 1.5 μm ammonia spectroscopy laser at the transmitter (launcher) and demultiplexed at the receiver by using appropriate dichroic mirrors. The 633 nm laser wavelength is chosen because of two reasons: no absorption by exhaust gases and visibility to the human eye (helps in initial alignment of the system). As

shown, the launcher optical assembly is mounted on a motion control stage. The demultiplexed red laser is made incident on a quadrant photodiode which serves as a position sensitive detector. The error signal generated by the quadrant photodiode is used as a feedback signal to actively align the motion control stage to keep the red beam centered on the quadrant photodiode. As a consequence, the ammonia spectroscopy beam also remains centered on the 1.5 μm photodiode. This leads to overcoming of measurement errors induced by thermal misalignment and enables long-term reliable operation of the sensor.

Experimental results demonstrating the performance and value of the alignment control system are shown in **Figure 8**. **Figure 8a** shows the scenario with no vibrations/misalignments. As expected, the 2f/1f signal stability is the same with the alignment control system on or off. This is a key check to ensure that the alignment control system does not introduce any artifacts or errors by itself. **Figure 8b** shows the scenario under induced vibrations/misalignments. With the alignment control off, the total normalized transmitted power drops close to zero in a matter of seconds, hence indicating a severe misalignment of the system. However, with the alignment control on, the system is able to actively maintain alignment over time. About 20–25% power fluctuations are still observed which are experimentally found to be well within the correction capability of the 2f/1f WMS technique. For more details on the tests demonstrating performance of the hybrid sensor, the reader is advised to refer to reference [14].

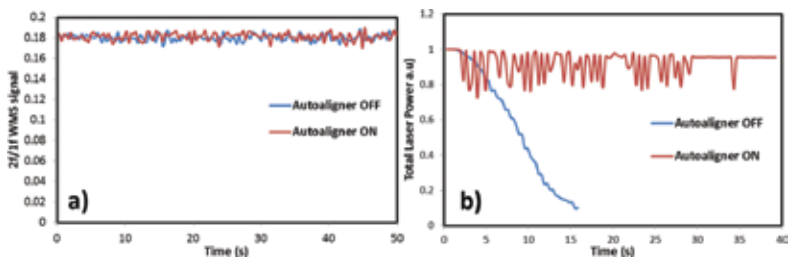

Figure 8. Experimental results showing the performance of the alignment control system. (a) 2f/1f WMS signals (with and without alignment control) as a function of time under no vibrations. (b) Transmitted spectroscopy laser power (with and without alignment control) as a function of time under induced vibrations. Figure taken with permission from SPIE (From our published paper).

5. Summary

In summary, this chapter presented the value and potential benefits of diode laser-based industrial harsh environment sensors. The chapter started with an overview of the industrial Internet and discussed the importance of sensors toward achieving enhanced output from industrial assets such as gas turbines, aircraft engines, and turbomachinery equipment . The discussion showed that real-time decision making through online sensors (that monitor the desired machine parameters) can enable optimized operation, performance enhancement, and extension of asset life. Subsequently, optical harsh environment sensors were introduced and the capabilities of diode laser-based techniques, that is TDLAS and QCLAS, were discussed.

http://dx.doi.org/10.5772/63971

The discussion was kept focused on these two most promising techniques (compared to other optical techniques) to remain within the scope of this chapter. The common implementation of TDLAS/QCLAS methodologies, that is direct absorption spectroscopy (DAS) and wavelength modulation spectroscopy (WMS), were discussed from an applied experimental perspective. The intention was to equip the reader with just the right level of information required to set up and carry out application-specific experiments. Appropriate references were provided for readers who wish to go deeper into these techniques. Next, the design philosophy and methodology behind a TDLAS sensor were discussed. Laser wavelength selection was presented as a crucial step where careful consideration to process temperature, pressure, and background gas interference needs to be given. Optomechanical configurations, namely line of sight, standoff, and extractive sampling, were then discussed followed by instrumentation and data acquisition basics. Finally, the power of diode laser technology in tackling real-world challenges was discussed using real-world examples. An in situ sensor for measurement of steam quality in the hot and harsh low pressure (LP) section of a steam turbine was presented. A solution based on two diode lasers, each targeted toward water in liquid phase and vapor phase, respectively, was discussed. Last but not the least, the chapter concluded with the discussion on a hybrid in situ ammonia slip sensor for power plant SCR control applications. A novel alignment control methodology in combination with a 2f/1f WMS scheme was shown to be an effective tool toward measuring gas concentrations in hot and harsh vibrating environments.

The field of optical and diode laser-based harsh environment sensing is rapidly evolving and is currently an area of active research in academia as well as industry. The various aspects of this technology space are being studied in details by different groups around the world and this chapter has, by no means, touched upon all of them. However, the authors do hope that this chapter has motivated the reader to think of new ideas and concepts that can advance the state-of-the art and application areas in this space and help the industrial community realize the full potential of their valuable assets.

Acknowledgements

The authors would like to acknowledge R&D support from the General Electric Company. The authors would also like to thank the Optics & Instrumentation team at GE Global Research, Bangalore for their contributions to the work presented in sections 4.1 and 4.2.

Author details

Chayan Mitra* and Rachit Sharma

*Address all correspondence to: chayan.mitra@ge.com

GE Global Research Center, Bangalore, India

References

[1] P. C. Evans and M. Anunziata, Industrial Internet: Pushing the Boundaries of Minds and Machines, 26 November 2012. [Online]. Available: www.ge.com/docs/chapters/Industrial_Internet.pdf. [Accessed 18 March 2016].

[2] J. Bruner, Industrial Internet – The Machines are Talking, O'Reilly Media, 2013 (Ebook ISBN:978-1-4493-6587-5).

[3] M. Annunziata and P. C. Evans, The Industrial Internet@Work, 2013. [Online]. Available: https://www.ge.com/sites/default/files/GE_IndustrialInternetatWork_WhitePaper_20131028.pdf. [Accessed 18 March 2016].

[4] M. Annunziata, Digital future of oil & gas & energy, [Online]. Available: http://gereports.cdnist.com/wp-content/uploads/2016/02/22094804/GE_Digital_Future_WP-02191611.pdf. [Accessed 18 March 2016].

[5] M. Egan, Deep Learning: New Subsea Service Model Helps Oil Drillers Limit Costs, 24 February 2016. [Online]. Available: http://www.gereports.com/deep-learning-new-subsea-service-model-helps-oil-drillers-limit-costs/ [Accessed 18 March 2016].

[6] B. Zhang, C. Sconyers, C. Byington, R. Patrick, M. Orchard and M. Vachtsevanos, Anomaly detection: a robust approach to detection of unanticipated faults, in: *International Conference on Prognostics and Health Management*, Denver, CO, 2008 (doi: 10.1109/PHM.2008.4711445).

[7] S. Mathew, D. Das, R. Rossenberger and M. Pecht, Failure mechanisms based prognostics, in: *International Conference on Prognostics and Health Management*, Denver, CO, 2008 (doi:10.1109/PHM.2008.4711438).

[8] A. Saxena, K. Goebel, D. Simon and N. Eklund, Damage propagation modeling for aircraft engine run-to-failure simulation, in: *International Conference on Prognostics and Health Management*, Denver, CO, 2008 (doi:10.1109/PHM.2008.4711414).

[9] M. J. Roemer and G. J. Kacprzynski, Advanced diagnostics and prognostics for gas turbine engine risk assessment, in: *IEEE Aerospace Conference Proceedings*, Big Sky, MT, 2000 (doi:10.1109/AERO.2000.877909).

[10] S. Cheng, M. H. Azarian and M. G. Pecht, Sensor systems for prognostics and health management, *Sensors,* vol. 10, p. 5774, 2010.

[11] T. Kellner, Here's How Digital Electricity Will Change The Power Industry All The Way To Your Home, 13 March 2016. [Online]. Available: http://www.gereports.com/heres-how-digital-electricity-will-change-the-power-industry-all-the-way-to-your-home/ [Accessed 18 March 2016].

[12] M. Lackner, Lasers in Chemistry, vol 1., Wiley, Weinheim, ISBN 978-3-527-31997-8, 2008.

[13] J. Hodgkinson and R. P. Tatam, Optical gas sensing: a review, *Measurement Science and Technology,* vol. 24, p. 012004, 2013.

[14] R. Sharma, S. Maity, A. Bekal, S. Vartak, A. K. Sridharan and C. Mitra, Optical sensors for harsh environment applications, in: *Proc. of SPIE,* vol. 9491, pp. 94910D-1, 2015.

[15] J. A. Jahnke, Continuous Emissions Monitoring,New York, USA, John Wiley & Sons, 2000.

[16] M. Lackner, Tunable diode laser absorption spectroscopy (TDLAS) in the process industries—a review, *Reviews in Chemical Engineering,* vol. 23.2, p. 65, 2007.

[17] L. Zhang, G. Tian, J. Li and B. Yu, Applications of absorption spectroscopy using quantum cascade lasers, *Applied Spectroscopy,* vol. 68, p. 1095, 2014.

[18] W. Zeller, L. Naehle, P. Fuchs, F. Gerschuetz, L. Hildebrandt and J. Koeth, DFB lasers between 760 nm and 16 μm for sensing applications, *Sensors,* vol. 10, p. 2492, 2010.

[19] R. K. Hanson and P. K. Falcone, Temperature measurement technique for high temperature gases using a tunable diode laser, *Applied Optics,* vol. 17, p. 2477, 1978.

[20] M. G. Allen, Diode laser absorption sensors for gas dynamic and combustion flows, *Measurement Science and Technology,* vol. 9, p. 545, 1998.

[21] V. Nagali and R. K. Hanson, Design of a diode laser sensor to monitor water vapor in high pressure combustion gases, *Applied Optics,* vol. 36, p. 3296, 1997.

[22] C. Mitra, S. Maity, A. Banerjee, A. Pandey, A. Behera and V. Jammu, Development of steam quality measurement and monitoring technique using absorption spectroscopy with diode lasers, *IEEE Sensors Journal,* vol. 11, p. 1214, 2011.

[23] S. T. Sanders, J. Wang, J. B. Jeffries and R. K. Hanson, Diode-laser absorption sensor for line-of-sight gas temperature distributions, *Applied Optics,* vol. 40, p. 4404, 2001.

[24] J. Wang, M. Maiorov, D. S. Baer, D. Z. Garbuzov, J. C. Connolly and R. K. Hanson, In situ combustion measurements of CO with diode-laser absorption near 2.3 μm, *Applied Optics,* vol. 39, p. 5579, 2000.

[25] M. B. Frish, R. T. Wainner, M. C. Laderer, B. Green and M. G. Allen, Standoff and miniature chemical vapor detectors based on tunable diode laser absorption spectroscopy, *IEEE Sensors Journal,* vol. 10, p. 639, 2010.

[26] C. N. Banwell and E. M. McCash, Fundamentals of Molecular Spectroscopy, 4th Edition, McGraw-Hill, London, 1994.

[27] J. D. Ingle and S. R. Crouch, Spectrochemical Analysis, Prentice Hall, London, 1988.

[28] J. Hodgkinson, D. Masiyano and R. P. Tatam, Gas cells for tunable diode laser absorption spectroscopy employing optical diffusers. Part 1: single and dual pass cells, *Applied Physics B,* vol. 100, p. 291, 2010.

[29] A. Klein, O. Witzel and V. Ebert, Rapid, time-division multiplexed, direct absorption- and wavelength modulation-spectroscopy, *Sensors,* vol. 14, p. 21497, 2014.

[30] X. Chao, J. B. Jeffries and R. K. Hanson, Wavelength-modulation-spectroscopy for real-time, in situ NO detection in combustion gases with a 5.2 μm quantum-cascade laser, *Applied Physics B,* vol. 106, p. 987, 2012.

[31] J. Reid and D. Labrie, Second-harmonic detection with tunable diode lasers—comparison of experiment and theory, *Applied Physics B,* vol. 26, p. 203, 1981.

[32] S. Schilt, L. Thevenaz and P. Robert, Wavelength modulation spectroscopy: combined frequency and intensity laser modulation, *Applied Optics,* vol. 42, p. 6728, 2003.

[33] P. Kluczynski, J. Gustafsson, A. M. Lindberg and O. Axner, Wavelength modulation absorption spectrometry—an extensive scrutiny of the generation of signals, *Spectrochimica Acta Part B: Atomic Spectroscopy,* vol. 56, p. 1277, 2001.

[34] G. Hancock, J. H. van Helden, R. Peverall, G. A. D. Ritchie and R. J. Walker, Direct and wavelength modulation spectroscopy using a cw external cavity quantum cascade laser, *Applied Physics Letters,* vol. 94, p. 201110, 2009.

[35] G. B. Rieker, J. B. Jeffries and R. K. Hanson, Calibration-free wavelength-modulation spectroscopy for measurements of gas temperature and concentration in harsh environments, *Applied Optics,* vol. 48, p. 5546, 2009.

[36] L. S. Rothman et al., The HITRAN2012 molecular spectroscopic database, *Journal of Quantitative Spectroscopy and Radiative Transfer,* vol. 130, p. 4, 2013.

[37] R. J. Muecke, P. W. Werle, F. Slemr and W. Prettl, Comparison of time and frequency multiplexing techniques in multicomponent FM spectroscopy,in: *Proc. SPIE Measurement of Atmospheric Gases,* vol. 1433, p. 136, 1991.

[38] X. Liu, J. B. Jeffries and R. K. Hanson, Measurement of nonuniform temperature distributions using line-of-sight absorption spectroscopy, *AIAA Journal,* vol. 45, p. 411, 2007.

[39] X. Yu, F. Li, L. Chen and X. Zhang, Spatial resolved temperature measurement based on absorption spectroscopy using a single tunable diode laser, *Acta Mechanica Sinica,* vol. 26, p. 147, 2010.

[40] D. R. Herriott, H. Kogelnik and R. Kompfner, Off-axis paths in spherical mirror interferometers, *Applied Optics,* vol. 3, p. 523, 1964.

[41] J. U. White, Long optical paths of large aperture, *Journal of Optical Society of America,* vol. 32, p. 285, 1942.

[42] S. M. Chernin and E. G. Barskaya, Optical multipass matrix systems, *Applied Optics,* vol. 30, p. 51, 1991.

[43] R. Bartlome, M. Baer and M. W. Sigrist, High-temperature multipass cell for infrared spectroscopy of heated gases and vapors, *Review of Scientific Instruments,* vol. 78, p. 013110, 2007.

[44] X. Chao, J. B. Jeffries and R. K. Hanson, Absorption sensor for CO in combustion gases using 2.3 μm tunable diode lasers, *Measurement and Science Technology,* vol. 20, 2009.

[45] R. Sur, K. Sun, J. B. Jeffries, R. K. Hanson, R. J. Pummill, T. Waind, D. R. Wagner and K. J. Whitty, TDLAS-based sensors for in situ measurement of syngas composition in a pressurized, oxygen-blown, entrained flow coal gasifier, *Applied Physics B,* vol. 116, p. 33, 2013.

[46] J. C. Wormhoudt, M. S. Zahniser, D. D. Nelson, J. B. McManus, R. C. Miake-Lye and C. E. Kolb, Infrared tunable diode laser measurements of nitrogen oxide species in an aircraft engine exhaust, in: *Proc. SPIE, Optical Techniques in Fluid, Thermal, and Combustion Flow,* vol. 2546, p. 552, 1995.

[47] M. G. Allen and W. J. Kessler, Simultaneous water vapor concentration and temperature measurements using 1.31-micron diode lasers, *AIAA Journal,* vol. 34, p. 483, 1996.

[48] E. R. Furlong, D. S. Baer and R. K. Hanson, Real-time adaptive combustion control using diode-laser absorption sensors, in: *Symposium (International) on Combustion,* vol. 27, p. 103, 1998.

[49] J. Röpcke, G. Lombardi, A. Rousseau and P. B. Davies, Application of mid-infrared tuneable diode laser absorption spectroscopy to plasma diagnostics: a review, *Plasma Sources Science and Technology,* vol. 15, 2006.

[50] B. Stanisa and V. Ivusic, Erosional behavior and mechanisms for steam turbine rotor blades, *Wear,* Vols. 186–187, p. 395, 1995.

[51] B. Stanisa and Z. Schauperl, Erosional behavior of turbine blade in nuclear power plant, *Wear,* vol. 254, p. 735, 2003.

[52] P. Forzatti, Present status and perspectives in de-NOx SCR catalysis, *Applied Catalysis A: General,* vol. 222, p. 221, 2001.

Edited by Richard Viskup

This book gives the readers an introduction to experimental and theoretical knowledge acquired by large-scale laser laboratories that are dealing with extra-high peak power and ultrashort laser pulses for research of terawatt (TW), petawatt (PW), or near-future exawatt (EW) laser interactions, for soft X-ray sources, for acceleration of particles, or for generation of hot dense thermal plasma for the laser fusion. The other part of this book is dealing with the small-scale laser laboratories that are using for its research on commercial sources of laser radiation, nanosecond (ns), picosecond (ps), or femtosecond (fs) laser pulses, either for basic research or for more advanced applications.

This book is divided into six main sections dealing with short and ultrashort laser pulses, laser-produced soft X-ray sources, large-scale high-power laser systems, free-electron lasers, fiber-based sources of short optical pulse, and applications of short pulse lasers. In each chapter readers can find fascinating topics related to the high energy and/or short pulse laser technique.

Individual chapters should serve the broad spectrum of readers of different expertise, layman, undergraduate and postgraduate students, scientists, and engineers, who may in this book find easily explained fundamentals as well as advanced principles of particular subjects related to these phenomena.

ISBN 978-953-51-5078-7

Photo by IgOrZh / CanStock

IntechOpen